Adam Wittek · Karol Miller
Poul M.F. Nielsen *Editors*

Computational Biomechanics for Medicine

Models, Algorithms and Implementation

Springer

Computational Biomechanics for Medicine

Adam Wittek • Karol Miller • Poul M.F. Nielsen
Editors

Computational Biomechanics for Medicine

Models, Algorithms and Implementation

Springer

Editors
Adam Wittek
Intelligent Systems for Medicine Lab.
School of Mechanical & Chem. Engineering
The University of Western Australia
Crawley-Perth, Western Australia, Australia

Karol Miller
Intelligent Systems for Medicine Lab.
School of Mechanical & Chem. Engineering
The University of Western Australia
Crawley-Perth, Western Australia, Australia

Poul M.F. Nielsen
Auckland Bioengineering Institute
The University of Auckland
Auckland, New Zealand

ISBN 978-1-4614-6350-4 ISBN 978-1-4614-6351-1 (eBook)
DOI 10.1007/978-1-4614-6351-1
Springer New York Heidelberg Dordrecht London

Library of Congress Control Number: 2013935499

© Springer Science+Business Media New York 2013
This work is subject to copyright. All rights are reserved by the Publisher, whether the whole or part of the material is concerned, specifically the rights of translation, reprinting, reuse of illustrations, recitation, broadcasting, reproduction on microfilms or in any other physical way, and transmission or information storage and retrieval, electronic adaptation, computer software, or by similar or dissimilar methodology now known or hereafter developed. Exempted from this legal reservation are brief excerpts in connection with reviews or scholarly analysis or material supplied specifically for the purpose of being entered and executed on a computer system, for exclusive use by the purchaser of the work. Duplication of this publication or parts thereof is permitted only under the provisions of the Copyright Law of the Publisher's location, in its current version, and permission for use must always be obtained from Springer. Permissions for use may be obtained through RightsLink at the Copyright Clearance Center. Violations are liable to prosecution under the respective Copyright Law.
The use of general descriptive names, registered names, trademarks, service marks, etc. in this publication does not imply, even in the absence of a specific statement, that such names are exempt from the relevant protective laws and regulations and therefore free for general use.
While the advice and information in this book are believed to be true and accurate at the date of publication, neither the authors nor the editors nor the publisher can accept any legal responsibility for any errors or omissions that may be made. The publisher makes no warranty, express or implied, with respect to the material contained herein.

Printed on acid-free paper

Springer is part of Springer Science+Business Media (www.springer.com)

Preface

A novel partnership between surgeons and machines, made possible by advances in computing and engineering technology, could overcome many of the limitations of traditional surgery. By extending surgeons' ability to plan and carry out surgical interventions more accurately and with less trauma, Computer-Integrated Surgery (CIS) systems could help to improve clinical outcomes and the efficiency of health-care delivery. CIS systems could have a similar impact on surgery to that long since realized in Computer-Integrated Manufacturing (CIM). Mathematical modeling and computer simulation have proved tremendously successful in engineering. Computational mechanics has enabled technological developments in virtually every area of our lives. One of the greatest challenges for mechanists is to extend the success of computational mechanics to fields outside traditional engineering, in particular to biology, biomedical sciences, and medicine.

Computational Biomechanics for Medicine Workshop series was established in 2006 with the first meeting held in Copenhagen. The seventh workshop was held in conjunction with the Medical Image Computing and Computer Assisted Intervention Conference (MICCAI 2012) in Nice on 01 October 2012. It provided an opportunity for specialists in computational sciences to present and exchange opinions on the possibilities of applying their techniques to computer-integrated medicine.

Computational Biomechanics for Medicine VII proceedings are organized into three parts: "Computational Biomechanics of Soft Organs," "Computational Biomechanics for Image-Guided Surgery," and "Musculoskeletal System and Injury Biomechanics." The application of advanced computational methods to the following areas was discussed:

- Medical image analysis
- Image-guided surgery
- Surgical simulation
- Surgical intervention planning
- Injury mechanism analysis
- Implant and prostheses design

After rigorous review of full (nine-to-fifteen pages) manuscripts we accepted 15 papers, collected in this volume. The proceedings also include abstracts of two invited lectures by world's leading researchers Professor Stéphane P.A. Bordas from Cardiff University, UK and Yohan Payan from Université Joseph Fourier—Grenoble 1, CNRS and TIMC-IMAG UMR in Grenoble, France.

Information about Computational Biomechanics for Medicine Workshops, including proceedings of previous meetings, is available at http://cbm.mech.uwa.edu.au/.

We would like to thank the MICCAI 2012 organizers for help with administering the workshop, invited lecturers for deep insights into their research fields, the authors for submitting high quality work, and the reviewers for helping with paper selection.

Perth, Western Australia, Australia — Adam Wittek
Perth, Western Australia, Australia — Karol Miller
Auckland, New Zealand — Poul M.F. Nielsen

Contents

Part I
Invited Lectures

Cutting in Real Time in Corotational Elasticity and Perspectives on Simulating Cuts

Hadrien Courtecuisse, Pierre Kerfriden, and Stéphane P.A. Bordas

Abstract We focus here on the simulation of surgical acts of types similar to cutting and needle insertion in soft tissue, in real time (500 Hz), where the scale of the surgical instrument is several orders of magnitude smaller than that of the organ.

We review the state of the art and make propositions (Fig. 1) to address some of the main difficulties in this area:

- Complex geometries—implicit boundaries, XFEM, meshless, advanced meshing
- Multiple scales (large gradients)—domain decomposition and model reduction [1–3]
- Error control and adaptivity [4]
- Parallel implementation Graphical Processing Units (GPUs) [5, 6]

Finally, we present preliminary work on a semi-implicit method for real-time deformation, topological changes, and contact of soft tissues, which relies on the asynchronous preconditioner proposed in [6] and extends the work to sharp topological modifications and contact arising during cutting. Time integration is performed semi-implicitly and can handle heterogeneous corotational elastic solids.

The use of implicit methods is a way forward in the direction of "error control" at each time step. To treat problems of realistic sizes, mesh adaptivity, enrichment and model reduction are fruitful avenues of investigation. Finally, material non-linearities should be considered, which is on-going work.

H. Courtecuisse • P. Kerfriden • S.P.A. Bordas (✉)
Cardiff University, School of Engineering, Institute of Mechanics and Advanced Materials, The Parade, CF24 3AA Cardiff Wales, United Kingdom
e-mail: hadrien.courtecuisse@gmail.com; kerfridenP@cardiff.ac.uk; stephane.bordas@alum.northwestern.edu

A. Wittek et al. (eds.), *Computational Biomechanics for Medicine: Models, Algorithms and Implementation*, DOI 10.1007/978-1-4614-6351-1_1,
© Springer Science+Business Media New York 2013

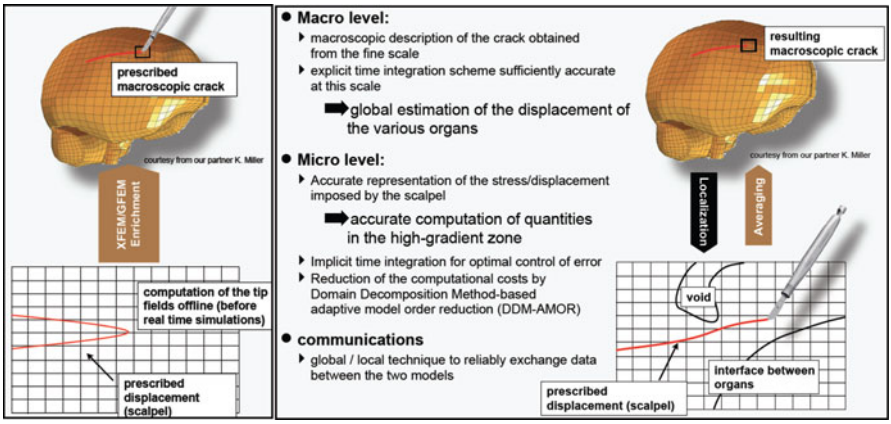

Fig. 1 Two proposed methods for the multiscale simulation of cutting: [*Left*: two-scale description] Macroscopic crack problem enriched with microscopic fields around the virtual scalpel through XFEM. Enrichment functions obtained by solving a local (micro) problem. [*Right*: Global/Local (Macro/Micro)]semi-concurrent multiscale method: the macroscopic crack is obtained through a microscopic simulation. Coarse scale: geometry and material properties of the brain represented crudely (away from the cut), the cut is incorporated without remeshing using XFEM. Fine scale ("micro") representation of the geometry (zoom) in the vicinity of the cut with implicit representation of the cut and internal organ boundaries by the XFEM, implicit representation of the interfaces (perfect bonding or contact) between organs and of the voids: regular meshes are sufficient thanks to enrichment. (*Note*: micro is used here abusively to denote a scale 10–1,000 times smaller than the macroscopic scale (mm)

Acknowledgment Acknowledgment of S. Bordas for the financial support of The European Research Council Starting Independent Research Grant entitled "Towards real time multiscale simulation of cutting in heterogeneous materials with applications to surgical simulation and computer guided surgery" (ERC Stg grant agreement No. 279578) and of the UK Engineering and Physical Science Research Council (EPSRC) for partial support of his time under grant: EP/I006494/1 Sustainable domain-specific software generation tools for extremely parallel particle-based simulations

References

1. Kerfriden, P., Passieux, J.C., Bordas, S.: Local/global model order reduction strategy for the simulation of localised failure. Int. J. Numer. Meth. Eng. **89**(2), 154–179 (2012)
2. Niroomandi, S., Alfaro, I., Cueto, E., Chinesta, F.: Real-time deformable models of non-linear tissues by model reduction techniques, Computer Methods and Programs in Biomedicine, Elsevier, **91**(3), 223–231 (2008)
3. Kerfriden, P., Gosselet, P., Adhikari, S., Bordas, S.P.-A.: Bridging proper orthogonal decomposition methods and augmented Newton–Krylov algorithms: an adaptive model order reduction for highly nonlinear mechanical problems, Computer Methods in Applied Mechanics and Engineering, **200**(5):850–866 (2011)

4. Wu, X., Downes, M.S., Goktekin, T., Tendick, F.: Adaptive nonlinear finite elements for deformable body simulation using dynamic progressive meshes. Comput. Graph. Forum. **20**(3), 349–358 (2001)
5. Joldes, G.R., Wittek, A., Miller, K.: Real-time nonlinear finite element computations on GPU-application to neurosurgical simulation. Comput. Meth. Appl. Mech. Eng. **199**(49–52), 3305–3314 (2010)
6. Courtecuisse, H., Junga, H., Allard, J., Duriez, C., Lee, D.Y., Cotin, S.: GPU-based real-time soft tissue deformation with cutting and haptic feedback. Prog. Biophys. Mol. Biol. **103**(2–3), 159–68 (2010)

Why Most of the Intra-Operative Medical Robotic Devices Do Not Use Biomechanical Models? Some Clues to Explain the Bottlenecks and the Needed Research Breakthroughs

Yohan Payan

Abstract This invited lecture addresses the frontier that biomechanics is now facing with the development of computer-assisted devices that can provide intra-operative assistance of the surgical gesture. The underlying idea is to use patient-specific biomechanical models during surgery, i.e. in the operating theatre. In that case, three main challenges need to be solved to be compatible with the clinical constraints: (1) a very fast generation of patient-specific models, (2) an in vivo estimation of the patient-specific constitutive equations of the soft tissues, and (3) interactive numerical simulations

TIMC-IMAG Laboratory (www-timc.imag.fr) is a 250 people laboratory devoted to translational and fundamental research at the intersection between Medicine and Information Science and Technology (from Applied Mathematics to Computer Science and Robotics). In that lab, since the 1980s, the Computer-Assisted Medical Intervention group has been developing devices to assist the physician or the surgeon in the successful execution of diagnostic or therapeutic gestures by minimizing invasiveness whilst improving accuracy.

Computer-assisted surgery (CAS) is now a mature domain. Researchers, clinicians and industrial partners have developed CAS applications by building links with classical domains such as computer science, robotics, image processing and mathematics. Orthopaedics was the first clinical domain mainly addressed by the pioneer CAS applications [1]. The reason for this was probably that bones are the human body structures which were considered as the most easily includable into a CAS application: they were assumed to be rigid, i.e. with a fixed 3D geometry, they are strongly identifiable onto computed tomography exams, and their relative

Y. Payan (✉)
UJF-Grenoble 1/CNRS/TIMC-IMAG UMR 5525, Grenoble F-38041, France
e-mail: Yohan.Payan@imag.fr

A. Wittek et al. (eds.), *Computational Biomechanics for Medicine: Models, Algorithms and Implementation*, DOI 10.1007/978-1-4614-6351-1_2,

© Springer Science+Business Media New York 2013

position during surgery is easily tractable by fixing rigid bodies onto their external surfaces (these rigid bodies being, for example, tracked with the use of an optical device, thus providing "surgical navigation").

The connection to biomechanics (i.e. the mechanics of living tissues) is more recent. Biomechanicians were first asked to work onto CAS applications when orthopaedic surgeons were looking for tools able to predict risks of fractures in the case of prosthetic implants. In that case, bony structures could no more be considered as rigid but on the contrary had to be modeled as a deformable continuum with a nonhomogeneous distribution of the internal stresses. For example, a patient-specific finite element model of the femur could be designed to estimate the internal stresses generated by a hip prosthesis and therefore to help limit fracture risks [2]. In these continuous biomechanical models, bones were usually considered as linear elastic material that underwent small deformations, which permitted easy calculation of numerical solutions.

More recently, CAS has addressed a larger spectrum of clinical domains such as cardiology, neurosurgery, urology or abdominal surgery. For these applications, biomechanics faces a new challenge since the involved tissues are required to move and be deformed by stress generated by clinical actions. Moreover, soft tissues are difficult to model accurately since they typically exhibit complex, time dependent, non-linear, inhomogeneous and anisotropic behaviors. Most of the corresponding biomechanical models need to include large deformation effects and visco-hyperelastic constitutive laws. Such models are very computationally demanding and are therefore limited to pre-operative use, since the simulations often require many minutes or hours to compute.

Our group did contribute to such pre-operative use of biomechanical models, for example in the domain of orthognatic surgery [3], tongue cancer treatment [4] and orbital surgery [5].

More recently, we have addressed the new frontier that biomechanics is now facing with the development of CAS devices that can provide *intra-operative* assistance [6]. The underlying idea is to use patient-specific biomechanical models during surgery, i.e. in the operating theatre. In that case, three main challenges need to be solved to be compatible with the clinical constraints:

1. Patient-specific models should be easily generated (no more than some minutes to elaborate such a model).
2. Patient-specific constitutive equations of the soft tissues have to be estimated through in vivo experiments, some of them only being possible during surgery if the organs are not accessible pre-operatively (e.g. the brain tissues).
3. The implementation of the models should provide real-time (or at least interactive) numerical simulations.

During this talk, we will try to address these new challenges and discuss the reason why most of the intra-operative medical robotic devices provided by industrial companies still do not use biomechanical models.

References

1. Taylor, R., Lavallée, S., Burdea, G., Mosges, R.: Computer-integrated surgery. Technology and Clinical Applications. MIT, Cambridge (1996)
2. Weinans, H., Huiskes, R., Grootenboer, H.J.: Effects of fit and bonding characteristics of femoral stems on adaptive bone remodeling. J. Biomech. Eng. **116**, 393–400 (1994)
3. Chabanas, M., Luboz, V., Payan, Y.: Patient specific finite element model of the face soft tissue for computer-assisted maxillofacial surgery. Med. Image Anal. **7**(2), 131–151 (2003)
4. Buchaillard, S., Brix, M., Perrier, P., Payan, Y.: Simulations of the consequences of tongue surgery on tongue mobility: implications for speech production in post-surgery conditions. Int. J. Med. Robot. Comput. Assist. Surg. **3**(3), 252–261 (2007)
5. Luboz, V., Swider, P., Ambard, D., Boutault, F., Payan, Y.: Intra-operative quantification of the surgical gesture in orbital surgery: application to the proptosis reduction. Clin. Biomech. **22**, 298–303 (2007)
6. Payan, Y. (ed.): Soft Tissue Biomechanical Modeling for Computer Assisted Surgery. Springer, Berlin (2012). ISBN 978–3–642–29013–8

Part II
Computational Biomechanics of Soft Organs and Flow

Numeric Simulation of Fluid–Structure Interaction in the Aortic Arch

Suzie Brown, Jing Wang, Harvey Ho, and Stephen Tullis

Abstract This paper presents a numeric simulation for a fully coupled fluid–structure interaction (FSI) of an anatomically accurate aortic arch from the aortic root immediately distal of aortic valve to the junction of the renal arteries. The aortic wall was simplified as a shell structure and assumed to be supported by virtual springs with adjustable stiffness. A structural finite element analysis of the vessel wall and a finite volume-based computational fluid dynamics model of the blood flow were used for the simulation. The blood flow was assumed to be turbulent and a $k-\varepsilon$ / $k-\omega$ blended shear stress transport used for the turbulent flow. A pulsatile flow rate waveform (adopted from ultrasonic measurements) was prescribed at the inlet, and a pulsatile pressure waveform was imposed at the outlets. The wall shear stress and three-dimensional flow velocity, as well as the wall deformation and von-Mises stress distributions on the aortic wall over a cardiac cycle are presented. The flow pattern in the aortic arch is laminar at the ascending phase of systole but turbulent flow develops during the descending phase of systole. This phenomenon is consistent with in vivo measurements in canine and human models. It is concluded that the fluid–structure interaction model can provide physiological insight into the biomechanics of the aortic arch.

S. Brown • J. Wang • S. Tullis (✉)
Department of Mechanical Engineering, McMaster University, Hamilton, Ontario, Canada
e-mail: browns6@mcmaster.ca; wangj73@mcmaster.ca; stullis@mcmaster.ca

H. Ho
Bioengineering Institute, The University of Auckland, Auckland, New Zealand
e-mail: harvey.ho@auckland.ac.nz

A. Wittek et al. (eds.), *Computational Biomechanics for Medicine: Models, Algorithms and Implementation*, DOI 10.1007/978-1-4614-6351-1_3,
© Springer Science+Business Media New York 2013

1 Introduction

Blood flow patterns in the aorta are highly complex but may be characterized by two basic features. First, after receiving intermittent jet-like flows from the left heart ventricle, the aortic flow is highly pulsatile, and second, the pulsatile aortic flow is dampened and partly "contained" in the elastic aorta. These two effects, i.e. the vascular resistance and compliance, were modeled in a simple WindKessel model by Frank more than one century ago and its variants are still being used to this day [1].

This simple lumped parameter model, of course, cannot be used to simulate the extremely complicated three-dimensional (3D) flow patterns in the aorta, which is supported by surrounding tissue and organs [2]. This is due to a number of reasons, particularly the complex vascular anatomy and the nonlinear properties of the arterial wall [2, 3]. Consequently most computational studies of aorta (or elastic arteries) have made substantial simplifications, either by treating the vessel wall as rigid [3, 4] or by using ideal arterial wall geometries (e.g. cylinders [5]). From a physiological perspective, the rigid wall assumption is too simplified for the aorta, where compliance/elasticity plays a major role in the WindKessel effects.

The fluid–structure interaction (FSI) problem considers effect of the fluid forces (pressure and wall shear stresses) as loads on the vessel walls and the effects of the subsequent vessel deformations as a change in the geometry of the fluid flow. This necessitates the use of a mesh deforming process for the fluid region. A basic computational technique to address this problem is the Arbitrarily Lagrangian–Eulerian (ALE) method [2, 6]. However, the ALE method is computationally expensive because updating of the fluidic and structural geometry is required at each time step. Various approaches have been proposed to alleviate the computational load, e.g., Figueroa et al. [2] proposed a coupled momentum method, which applied a conventional finite element formulation of the Navier–Stokes equations to the rigid fluid domain, and treated the blood vessel as a linear elastic membrane. This method was applied to an anatomically accurate model of the abdominal aorta [2].

The aim of this work is to develop a fully coupled FSI model of an anatomically accurate aortic arch, whose geometry is digitized directly from a 3D CT image. A commercial ANSYS FSI framework is used to address the complex interactions between the pulsatile aortic flow and elastic wall.

2 Methods

2.1 Geometric Model of the Aortic Arch

The geometry of a patient-specific aortic arch was adopted from the public vascular model repository of cardiovascular simulation, Inc. (www.vascularmodel.org) and is shown in Fig. 1. The three branches arising from the arch are the right

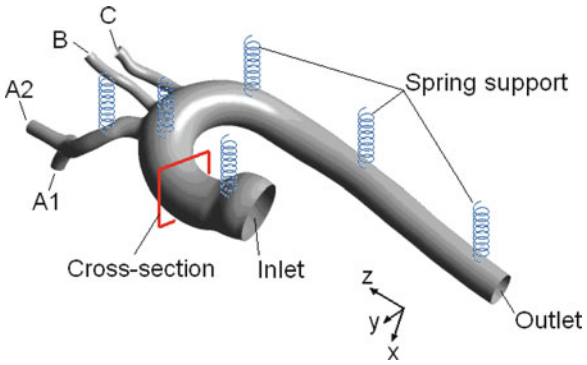

Fig. 1 Schematic diagram of aortic arch geometry: the aortic arch is supported by a virtual spring system whose stiffness is adjustable; the *red square* indicates an ascending aorta cross section whose velocity streamlines will be visualized in Fig. 4

brachiocephalic artery (with outlets A1 and A2), the left common carotid artery (with outlet B) and the left subclavian artery (with outlet C). These arteries supply blood to the head, neck, and upper limbs. The distal end of the arch is truncated proximal to the renal hepatic arteries. The descending aorta, which receives more than 70% of the cardiac output, supplies blood to the torso, abdominal organs, and lower limbs. The unloaded diameters of the ascending aorta (inlet) and descending aorta (outlet) are 25.8 mm and 14.0 mm, respectively.

Since the aortic arch is supported by tissues, body fluids, and organs inside the chest, the arterial wall is assumed to be supported by virtual springs (as seen in Fig. 1) to simulate this scenario. The spring support is applied uniformly over the surface of the vessel walls with a stiffness of 135 kPa/m used here—this value is low enough that these backing spring supports do not act to constrain the vessel dilatation and compliance (this is effectively determined only by the vessel wall stiffness) but is adequate to resist large lateral displacements of the entire vessel. It should be noted that the main results are not particularly sensitive to the exact value of this spring support. The wall thickness is taken as 1.5 mm, which is approximately 6% of the aortic diameter.

The aortic geometry of Fig. 1 requires computational grid generation for both structure and fluid domains. The computational mesh of the solid domain contains approximately 11,000 quadrilateral elements; the grid for the fluid domain contains approximately 550,000 tetrahedral elements with 15 near-wall layered cells to provide good resolution of the boundary layer. The resulting meshes are shown in Fig. 2.

2.2 Fluid–Structure Interaction

The commercial structural finite element analysis code ANSYS and computational fluid dynamics (CFD) code CFX (ANSYS Inc., Canonsburg, PA) are used in the coupled FSI analysis. The solution is obtained in a time-marching manner, and within each time step there are a series of stagger loops, which allows coupling

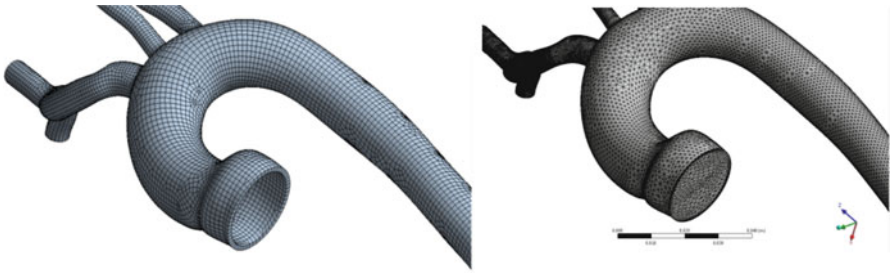

Fig. 2 Computational grid generation for the aorta arch: (*left*) quadrilateral elements for the solid wall domain; and (*right*) tetrahedral elements with layered boundary cells for the fluid (blood) domain

of the load fields from the CFD intermediate solutions to a deflected geometry from the structural code. The deflection is assumed to be relatively small so that the fluid mesh is simply stretched and deformed by the deflection of the wall surface (i.e. no remeshing of either the structural or fluidic meshes takes place). Convergence of the FSI coupling in the stagger loops is determined by monitoring changes in the displacement variants, after which the solution progresses to the following time step.

2.3 Turbulence Modeling for the Blood Flow

While the blood flow in most blood vessels in the human cardiovascular system is laminar, turbulence can occur in the aortic arch [7]. The peak Reynolds number in the aorta can reach 4,000, exceeding the critical value (∼2,300) for turbulent flow in straight pipes. Because adverse pressure gradients and possible flow separation occur at the arch portion of aorta as well as aortic bifurcations, the $k-\omega$ / $k-\varepsilon$ blended shear stress transport (SST) turbulence model [8, 9] is used to capture the flow behavior in the aorta, similar to that used by Tan [10] (for aortic flow without fluid structure coupling). In such eddy-viscosity models, a turbulent viscosity μ_t is used to account for the turbulent transport of fluid momentum. In the SST model, it is determined as: $\mu_t = \frac{\rho k}{\omega}$, where ω is determined from a blend of the $k-\omega$ model using the standard constants [11] near the wall, and that using constants based on the $k-\varepsilon$ model farther from the wall [8]. Limiters are also used to improve near wall performance in adverse pressure gradients and separated flows [8, 9] both in the production term of the transport equation for the turbulent kinetic energy k, and in the equation for eddy viscosity itself:

$$\mu_t = \frac{\rho k}{\max\left[\omega, C\Omega F\right]} \tag{1}$$

where Ω is the vorticity magnitude, C a constant, and F a near wall blending function. Detailed description of the model and its various terms and their physical/mathematical definitions are lengthy, and so we refer the interested reader to literature [8, 9] for more details.

2.4 Linear Elastic Shell Model for the Aortic Wall

The arterial wall is assumed to behave like a linear elastic shell because the wall thickness is relatively small (∼6%) compared to the artery diameter. In the finite element analysis, shell elements governed by the Kirchhoff–Love theory are used due to the thin aortic wall as well as its small bending deformation. The applied shell elements are 4-noded with six degrees of freedom at each node: translation in the x, y, and z directions, and rotation about the x, y, and z axes.

The behaviour of aortic wall is nonlinear; however, here a linear constant elasticity assumption is made as the range of pressure loading is small compared to the nonlinear behaviour seen in tensile testing of cadavar samples. A Young's modulus of 2 MPa is used, approximately in the middle of the wide range of aorta wall Young's moduli that have been reported [2, 5]. Much of the literature variation is apparently due to real differences along the length of the aorta [5], as well as the wide range of loadings imposed on the samples (i.e. where a linear fit is made to the nonlinear behaviour). A Poisson's ratio of 0.45 was used, typical of arterial walls [12].

2.5 Boundary and Initial Conditions

The inlet volumetric flow rate waveform of the pulsatile blood flow is adopted from [13], as shown in Figs. 3 and 6, and implemented as a uniform velocity profile at the inlet. In this waveform, a cardiac cycle was one second, with the division between systole and diastole at approximately 0.48 s. The mean flow rate of this waveform is 4.94 l/min, which is the approximate cardiac output of a healthy adult [14]. Fourier analysis was performed for this periodic function, and the first ten harmonics of the waveform are taken to prescribe a function defining the inflow velocity boundary condition in the fluids solver.

For the outlets' boundary conditions, a real time back pressure from a previous hemodynamic study in a large arterial tree [4] is imposed on each outlet synchronized to the inlet flow cycle. The back pressure differences between outlets in this model are assumed to be small enough that the same back pressure can be used at each outlet. The outflow pressure data was prescribed in the fluids solver as a function of time using a Fourier analysis similar to the inlet flowrate. It is recognized that this assumption is valid only for this geometry with its limited lengths, and in

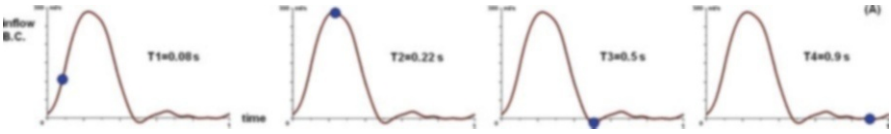

Fig. 3 Time points T1–T4 identified through the cardiac cycle shown as a trace of the time-varying inlet velocity

particular is sensitive to the lengths of the three branch artery stubs; however, the split in the bulk (time-averaged) flow rate between the descending aorta and the branch arteries is realistic.

The inlet of the aorta is assumed to be clamped to aid numerical convergence, similar to that of Gerbeau et al. [6]. The outlet of the descending aorta is fixed in the z (caudal) direction and in the x and y directions (i.e. on the transverse plane), representative of the rigid attachment of the aorta by the intercostal arteries (see Fig. 1). The branch outlets were set to be fixed to avoid large oscillations induced by the pulsatile blood flow in the vessel and is consistent with the anatomy of branch artery attachments. The internal surface of the aorta was defined as the FSI interface, across which structural FEA code and fluid CFD code transfer load and boundary deflection data to each other. Structural damping was imposed to ensure convergence. In vivo structural damping is expected to be very high, due to both the vessel wall structure and the adjacent tissue and fluid outside the aorta.

3 Results

The blood is assumed to be a Newtonian fluid (valid for these larger Reynolds numbers) with a dynamic viscosity and density of 0.00388 Pas and 1,050 kg/m^3, respectively. The simulation was run for 3 s (i.e. three complete cardiac cycles) with a time step of 0.02 s, and an initial flow at $t = 0$ of zero. After two full cardiac cycles, the flow exhibits cycle-to-cycle consistency (there is less than a 2% difference in all local velocities between the third and fourth cycles). Flow data in the third cardiac cycle was used for post-processing. Four time points (t =0.08 s, 0.22 s, 0.5 s, 0.9 s) that span both systole and diastole were selected for post-processing the simulation results, as shown in Fig. 3.

Flow velocity streamlines were visualized for these specific time steps. From Fig. 4 we see that the flow pattern is essentially laminar at the ascending phase of systole with, turbulent flow developing during the descending phase of the systole. Helical blood flow is evident during diastole. The streamline visualization of the blood flow on crosssection of the ascending aorta (Fig. 4 at the location indicated by the red square in Fig. 1) shows the start of the development of the vortices at the descending phase of systole. The highest instantaneous velocity in the aorta, which occurs at systole, reaches 1.5 m/s. At the end phase of diastole, the aortic

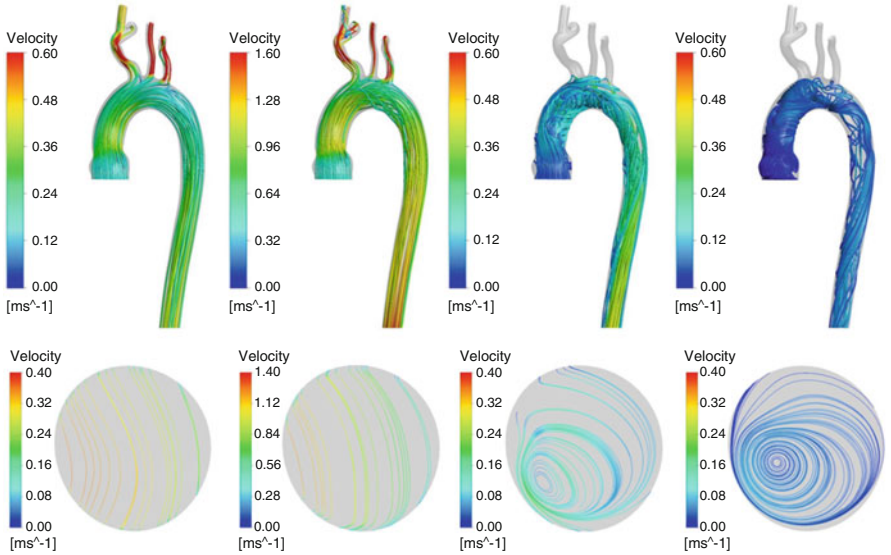

Fig. 4 Velocity streamlines at the 4 time points T1–T4 *from left to right*: (*top row*) streamlines throughout the entire computational domain; (*bottom row*) the velocity streamlines on the cross-section plane identified in Fig. 1

wall recoils to push blood downstream, albeit at a much lower velocity (less than 0.15 m/s). These phenomena are consistent with in vivo canine [7] and human [15] observations.

Figure 5(left) shows the calculated principal stress distributions on the aortic arch surface at the time points T2 and T4. The cross-section area averaged stress at T2 of systole is approximately 1.5 times that of the trough point T4. These stresses are dominated by the pressure loading (rather than the wall shear stress). Figure 5(right) also shows the displacement contours of the aortic surface at the corresponding times T2 and T4. The stresses and deformations are largest in the ascending aorta and smallest in the descending aorta. The cross-sectional area of the slice through the ascending aorta (shown in Figs. 1 and 4) is 442 mm^2 at T2 and 405 mm^2 at T4. The model is predicting the elastic chamber behaviour of the aorta (i.e. Windkessel effects) [7] in the 10% area increase from diastole to systole seen. Stress concentrations and large displacements occur at the transition between the aortic sinuses and the ascending aorta where the geometry has its largest deviation from a cylindrical pipe. Stress concentrations can also be seen at the proximal ends of subclavian and common carotids arteries. The displacement of these points is large through the cycle, although the stress concentrations seen here are exaggerated by the assumed uniform spring attachment of all of the vessel walls (in reality, the arteries are relatively stiffly attached at their distal ends of the lengths in the model, and much less stiffly from the aortic arch to these outlet points.

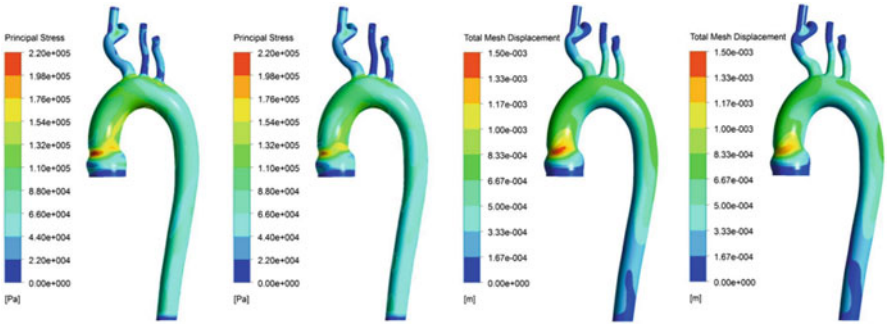

Fig. 5 Principal stress at T2 and T4 (*left*) and mesh displacement at T2 and T4 (*right*)

Temporal flow rate waveforms are shown in Fig. 6 for each outlet and the inlet over a cardiac cycle. Given the boundary conditions used, the split between the descending aorta outflow (taking over 78% of the total cardiac output) and the common carotid and subclavian arteries (almost equally dividing the remainder) are realistic. A comparison can also made between the time-varying flow rates simulated by the elastic wall model and the same model but with a rigid wall, also shown in Fig. 6. We observe that the waveform differences between the outlets A1, A2, B and C are small—mainly consisting of a delay in the time of peak flow. This makes physiological sense as the aortic wall is dilated by the high blood pressure in systole, and thus a portion of blood is "contained" by the aorta in systole and released in diastole. Interestingly, a decrease in peak flow rates is not seen—there is a delay in the peak, but no peak broadening is seen.

Figure 7 shows the variation of the wall shear stress (WSS) during a cardiac cycle due to the pulsatility of blood flow. The highest WSS in the aorta itself approaches 17 Pa at the narrowing of the ascending aorta at systole (t =0.24 s). High values are also seen on the inner arch wall of the aorta at systole. The highest WSS in the aorta at diastole was about 0.5 Pa, also located at the inner arch wall. Low WSS regions form at the outer wall of the arch as well as the inner wall of the descending aorta immediately after the arch. The WSS with the turbulent model used here was much higher (2–3x) than that seen in an earlier purely laminar model due to the turbulence viscosity reducing the thickness of the boundary layers (the unpublished laminar results are not shown here). The highest WSS levels naturally occur when the flow rate (and so Reynolds number and turbulence level) is highest, showing the importance in including the turbulent nature of the flow in the aorta. Locations of high and low WSS were similar in both the turbulent model here and the earlier laminar model.

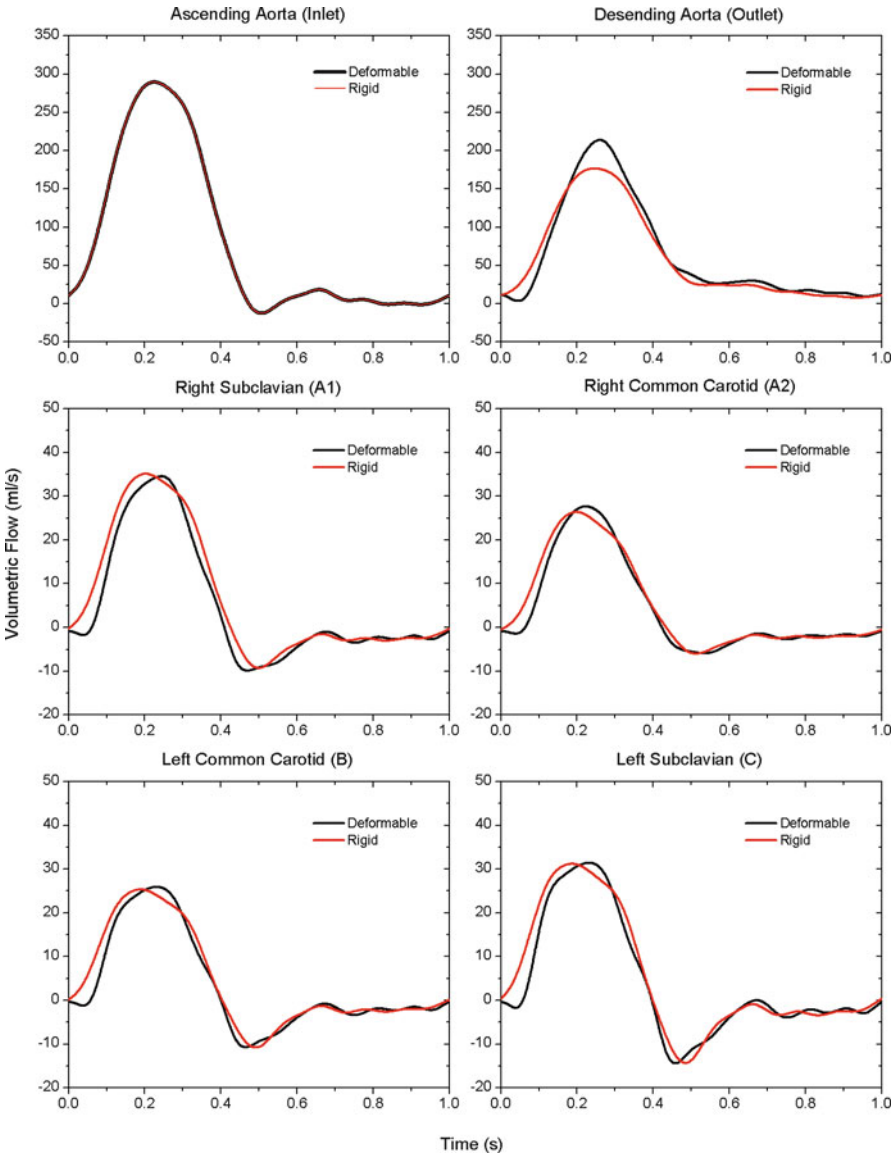

Fig. 6 Volumetric flow rate vs. time at each outlet

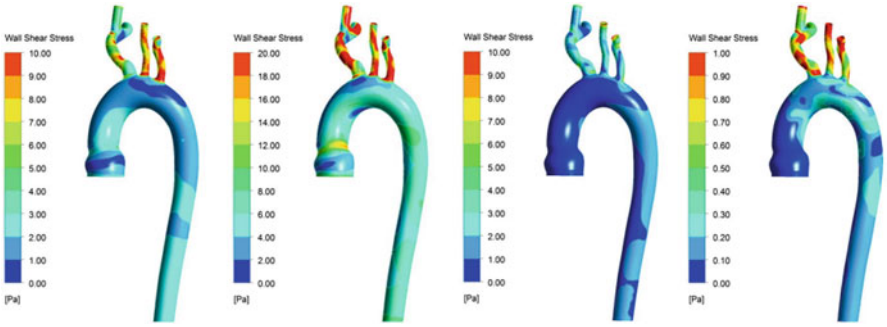

Fig. 7 Wall shear stress distributions on the vessel walls at the four time points T1–T4 *from left to right*

4 Discussion and Conclusions

The purpose of this study was to simulate fluid–structure interaction in the aortic arch with realistic pulsatile inlet blood flow and a realistic 3D aortic arch geometry. A 3D computational fluid dynamics simulation of the blood flow in the aorta was performed and the resulting fluid pressures and wall shear stresses used as input to a structural finite element analysis of the vessel walls. The resulting deformation of the walls due to these forces was then applied as new boundary conditions to the fluids solver.

Using such an approach, the WSS, velocity, mass/volume flow rate and total pressure in the fluid domain, as well as the von-Mises stress distributions and elastic wall deflections in the solid domain were calculated throughout a cardiac cycle. Since in vivo measurements for these quantities is sparse (and variable between test subjects and studies), validation was mainly made by qualitative comparison with aortic arch studies [3, 5, 6, 12, 15]. The comparison shows that the computational results such as flow transition from laminar to turbulence, the high and low WSS regions, and the wall displacement are consistent with that reported in literature. Limitations of the current model include the linearly elastic wall model, which should be anisotropic and nonlinear. Also, the uneven vessel thickness and supporting issues distributions around the aorta arch were not considered. Moreover, the outflow boundary condition was simply treated as real time back pressure—future work is needed to consider the downstream truncated arterial tree as a combined resistance and compliance (Windkessel) boundary condition. Nevertheless, the 3D FSI aortic model presented in this paper has established an initial platform to conduct further physiological/pathological flow analysis in the aorta

References

1. Westerhof, N., Lankhaar, J., Westerhof, B.: The arterial windkessel. Med. Biol. Eng. Comput. **47**(2), 131–141 (2009)
2. Figueroa, C.A., Baek, S., Taylor, C.A., Humphrey, J.D.: A computational framework for fluid-solid growth modeling in cardiovascular simulations. Comput. Meth. Appl. Mech. Eng. **198**(45-46), 3583–3602 (2009)
3. Taylor, C.A., Hughes, T.J.R., Zarins, C.K.: Finite element modeling of Three-Dimensional pulsatile flow in the abdominal aorta: Relevance to atherosclerosis. Ann. Biomed. Eng. **26**(6), 975–987 (1998)
4. Ho, H., Sands, G., Schmid, H., Mithraratne, K., Mallinson, G., Hunter, P.: A hybrid 1D and 3D approach to hemodynamics modelling for a Patient-Specific cerebral vasculature and aneurysm. In: Medical Image Computing and Computer-Assisted Intervention - MICCAI, 323–330 (2009)
5. Gao, F., Watanabe, M., Matsuzawa, T.: Stress analysis in a layered aortic arch model under pulsatile blood flow. Biomed. Eng. OnLine **5**(1), 25 (2006)
6. Gerbeau, J., Vidrascu, M., Frey, P.: Fluid structure interaction in blood flows on geometries based on medical imaging. Comput. Struct. **83**(2-3), 155–165 (2005)
7. Fung, Y.C.: Biomechanics: Mechancial Properties of Living Tissues, 2nd edn. Springer, New York (1993)
8. Menter, F.R.: Improved two-equation k-omega turbulence models for aerodynamic flows. NASA STI/Recon Technical Report N **93**, 22809 (1992)
9. Menter, F.R.: Two-equation eddy-viscosity turbulence models for engineering applications, AIAA Journal., **32**(8), 1598–1605 (1994)
10. Tan, F., Borghi, A., Wooda, R.M.N., Thom, S., Xu, X.: Analysis of flow patterns in a patient-specific thoracic aortic aneurysm model. Comput. Struct. **87**, 680–690 (2009)
11. Wilcox, D.: Multiscale model for turbulent flows. AIAA 24th Aerospace Sciences Meeting, Reno, Nevada, pp. 1311–1320 (1986)
12. Giannakoulas, G., Giannoglou, G., Soulis, J., Farmakis, T., Papadopoulou, S., Parcharidis, G., Louridas, G.: A computational model to predict aortic wall stresses in patients with systolic arterial hypertension. Med. Hypotheses **65**, 1191–1195 (2005)
13. Olufsen, M.E., Peskin, C.S., Kim, W.Y., Pedersen, E.M., Nadim, A., Larsen, J.: Numerical Simulation and Experimental Validation of Blood Flow in Arteries with Structured-Tree Outflow Conditions. Ann. Biomed. Eng. **28**(11), 1281–1299 (2000)
14. Levick, J.: An Introduction to Cardiovascular Physiology, 4th edn. Arnold, Great Britain (2003)
15. Morbiducci, U., Ponzini, R., Rizzo, G., Cadioli, M., Esposito, A., De Cobelli, F., Del Maschio, A., Montevecchi, F., Redaelli, A.: In vivo quantification of helical blood flow in human aorta by time-resolved three-dimensional cine phase contrast magnetic resonance imaging. Ann. Biomed. Eng. **37**(3), 516–531 (2009)

Patient-Specific Computational Models: Tools for Improving the Efficiency of Medical Compression Stockings

L. Dubuis, C.P.-Y. Rohan, S. Avril, P. Badel, and J. Debayle

Abstract Compression therapy is used in the management and the treatment of various forms of venous insufficiency ranging from the relief of heavy and achy legs to the treatment of more severe forms such as acute venous ulceration. However, the pressure needed to achieve clinical benefit is a matter of debate. The purpose of this study was to examine the transmission of pressure within the soft tissues to improve current understanding of the mechanism of action of medical compression stockings (MCS). Three-dimensional patient-specific finite element models were developed for six subjects. The geometry was obtained from CT scans. Because experimental data on the mechanical properties of healthy adipose tissues and passive muscle are scarce in literature, an inverse method was setup to identify the constitutive properties of the said anatomical elements. This constitutes the original contribution of this work. The main outcome of this study is that the mean pressure applied by the MCS onto the skin is of the same order of magnitude as that applied by the compressed tissues onto the wall of the main deep veins, thereby suggesting that the mean pressure applied can be used as an indicator of the efficiency. Likewise, the maximal hydrostatic pressure in fat can be used to estimate the comfort.

1 Introduction

Compression therapy is a highly effective modality for treating venous disorders of the lower leg. It is traditionally employed to achieve a variety of therapeutic goals

L. Dubuis (✉)
Chris Barnard Division of Cardiothoracic Surgery, University of Cape Town, Cardiovascular Research Unit, Cape Town, South Africa
e-mail: dubuis.biomecha@gmail.com

C.P.-Y. Rohan • S. Avril • P. Badel • J. Debayle
École Nationale Supérieure des Mines, CIS, CNRS: UMR 5146, LCG, Saint-Étienne F-42023, France
e-mail: rohan@emse.fr; avril@emse.fr; badel@emse.fr; debayle@emse.fr

A. Wittek et al. (eds.), *Computational Biomechanics for Medicine: Models, Algorithms and Implementation*, DOI 10.1007/978-1-4614-6351-1_4,
© Springer Science+Business Media New York 2013

which mainly fall under three categories: prevention of vein-related diseases such as varicose veins and deep vein thrombosis, the relief of symptoms associated with various forms of venous insufficiency and the treatment of venous-related diseases such as the treatment of active venous ulcerations [1].

It has been observed in practice, however, that the response of the calf to external compression is highly variable [2, 3]. Conflicting results have also been reported in the case of injection sclerotherapy for varicose veins combined with external compression [4, 5]. This highlights the current lack of knowledge regarding exact nature of the mechanical and biological responses of the leg to external compression.

One explanation brought forward by many authors is that the pressure performance of the MCS, which condition the effectiveness of the therapy, is particularly dependent on the morphology of the leg of each individual [6]. Much work has been done in that regard in order to evaluate the contact pressure performance of elastic stockings and to develop new tools to help manufacturers improve the medical functions and comfort of compression hosieries [7, 8].

Yet, very little is known on the biomechanical response of the leg to this interface pressure and the implications for the venous return. The resulting redistribution of pressure is known to be non-uniform and is likely to be of paramount importance in the evaluation of MCS and to better comprehend the mechanisms by which it achieves its medical functions.

The purpose of this study was to simulate the three-dimensional distribution of pressure in the calf resulting from external compression on a significant number of patients. In order to address the issue of identifying the elastic properties of the soft tissues, a Finite Element Model Updating-based approach was developed and applied to six subjects. We have recently reported the results of the developed methodology on three subjects in [9].

2 Method

2.1 Leg Imaging Protocol

The right leg of six healthy volunteers was imaged using CT scan (computed tomography scans) according to the following procedure. First, informed consent was obtained from all the volunteers according to a protocol approved by the local institutional ethics committee. A medical examination was then carried out to make sure that none of them suffered from venous insufficiency. Their leg perimeters were measured to prescribe the correct MCS in agreement with the manufacturer's recommendations. Finally, a CT scan was done on one of each subject leg with and without MCS. The sizes of the images were $512^{*}512^{*}376$ voxels and the resolution was $0.93^{*}0.93^{*}1\,\text{mm}^3$. The principal characteristics of each subject are summarised in Table 1 below.

Table 1 Subject characteristics

Subjects	1	2	3	4	5	6
Age (years old)	42	25	30	35	35	25
Weight (kg)	60	58	73	55	60	58
Height (m)	1.6	1.7	1.8	1.7	1.7	1.6
Sex	Female	Female	Male	Female	Female	Female

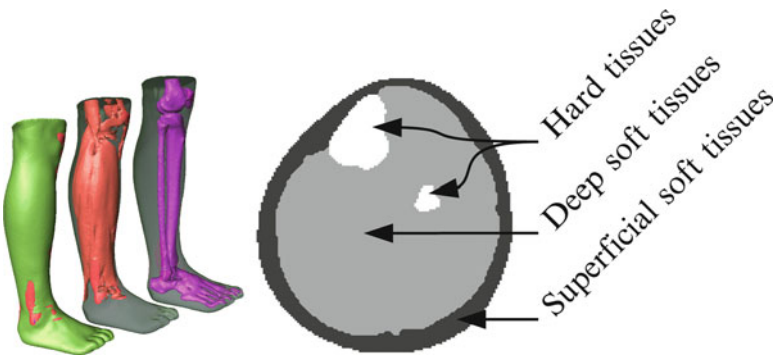

Fig. 1 Segmentation results: three-dimensional visualisation (*left*) and a cross section with the three main regions (*right*)

2.2 Definition of the Model Geometry

2.2.1 Segmentation Step

The three-dimensional CT scan images were segmented into three main regions:

1. Superficial soft tissues, composed principally of adipose tissues, skin and some veins.
2. Deep soft tissues, composed principally of muscles, tendons and blood vessels.
3. Hard tissues, consisting of the two bones (the tibia and the fibula).

The segmentation was performed using the image processing program, ImageJ©. A three-dimensional visualisation of the segmentation for one subject is shown in Fig. 1 below.

2.2.2 Image Warping

Both the images of the legs with and without MCS need to be in the same reference so that the inverse method can be applied. This is achieved by performing a rigid transformation of the two geometries. The correct transformation is calculated from

the formula (1) below which computes the smallest distance in the least-squares sense to superimpose the hard tissues of both legs:

$$\left[\hat{R}, \hat{T}\right] = \arg_{(R,T)} \min \sum_{i}^{N} \|Q_i - RP_i - T\| \tag{1}$$

where R and T are the optimal rotation and translation, respectively, to superimpose the two images, N is the pixel number assigned to the bones in the images, Q_i and P_i are the coordinates of the bones in the leg without and with MCS, respectively. Only the two bones were used to perform image warping because it is assumed that they are not deformed under external compression.

2.3 Finite Element (FE) Model

2.3.1 Meshing

The segmented images were meshed using AVIZO© with linear tetrahedral elements (approximately 500,000 elements and 60,000 nodes for each model).

2.3.2 Boundary Conditions

The tibia and fibula are considered as infinitely rigid materials with respect to the elastic properties of soft tissues and hence were fixed in this model.

The interface pressure delivered the MCS on the skin was computed from Laplace law given in Eq. (2) below:

$$P = \text{Stiff}\frac{\varepsilon}{Rc} \tag{2}$$

where Stiff is the stiffness of the sock textile (estimated from a previous study [10]), Rc the curvature radius of the leg with MCS (to have the pressure in the final state) in the horizontal plane, and ε is the strain of the sock in the horizontal plane. The latter was derived knowing leg and sock perimeters from the CT scans.

2.3.3 Constitutive Equation

Both soft tissues were assumed to be homogeneous, isotropic, quasi-incompressible and governed by a Neo-Hookean strain energy function, φ defined in Eq. (3) as follows:

$$\varphi = c_{10}\left(\bar{I}_1 - 3\right) + \frac{\kappa}{2}(J-1)^2 \tag{3}$$

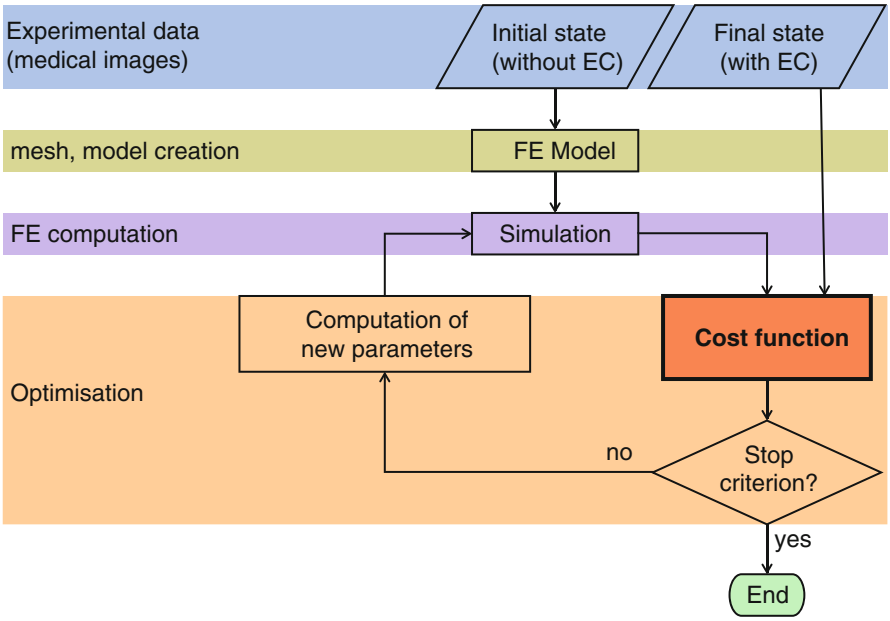

Fig. 2 Inverse method

where c_{10} and κ are the Neo-Hookean parameters driving the constitutive equation, $\overline{I}_1 = Tr(\overline{F}.\overline{F}^t)$ is the first deviatoric strain invariant, and $J = \det(F)$ is the volume ratio. Due to incompressibility, the κ parameter was fixed at 1 MPa for both soft tissues (as estimated by the volume change between the two configurations, i.e. with and without external compression) and the parameter c_{10} was identified by an inverse method.

2.4 Identification

2.4.1 Inverse Method

Finite Element Model Updating is used for the identification process. The principle is outlined in the diagram given in Fig. 2 below. First, the patient-specific FE model is created from the initial imaging data (CT scans of legs without external compression). The result of the simulation is then compared to the final experimental data (CT scans of legs with MCS) based on a cost function, detailed below, which estimates the difference between the target leg contour (experimental images of leg under external compression) and the simulated leg contour. If the match between the two contours is not satisfactory, new constitutive parameters are calculated by an optimisation algorithm and the process is reiterated. When the cost function's

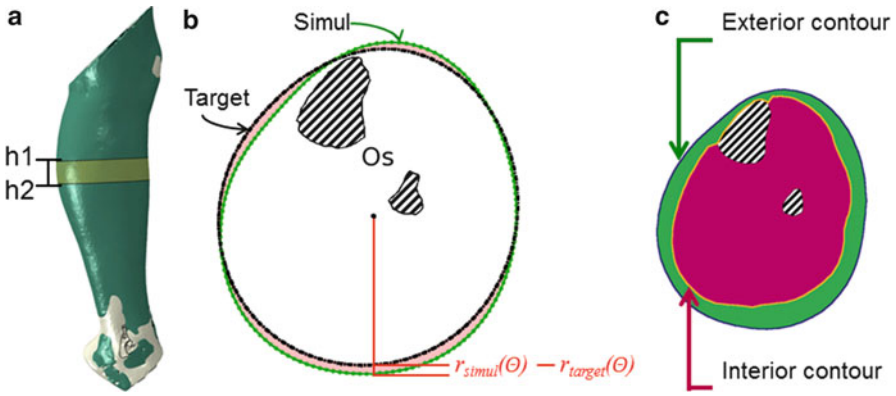

Fig. 3 Cost function. Minimisation of the difference of the target and simulation radius for all the contour of the leg (**b**) (minimisation of the red area on the scheme), for five slices between the heights h_1 and h_2 (**a**), and for the interior and exterior contours (**c**)

minimum is reached, the constitutive parameters are considered to be identified. The optimisation algorithm employed here is the Nelder Mead algorithm implemented in Matlab® as the *fminsearch* function. Also, the starting value for the c_{10} parameter was 3 kPa.

2.4.2 Cost Function

The cost function evaluates the average distance between the target leg contour and simulated deformed leg contour for five consecutive slices taken at the calf according to the formula (4) given below:

$$C = \frac{\sum_{z=h1}^{h2} \sum_{\theta} \left(\left[\frac{r_{\text{simul}}(z,\theta) - r_{\text{target}}(z,\theta)}{r_{\text{target}}(z,\theta)} \right]^2_{\text{ext.}} - \left[\frac{r_{\text{simul}}(z,\theta) - r_{\text{target}}(z,\theta)}{r_{\text{target}}(z,\theta)} \right]^2_{\text{int.}} \right)}{\sum_{z=h1}^{h2} \sum_{\theta} \left(\left[\frac{r_{\text{initial}}(z,\theta) - r_{\text{target}}(z,\theta)}{r_{\text{target}}(z,\theta)} \right]^2_{\text{ext.}} - \left[\frac{r_{\text{initial}}(z,\theta) - r_{\text{target}}(z,\theta)}{r_{\text{target}}(z,\theta)} \right]^2_{\text{int.}} \right)} \tag{4}$$

where $r_{\text{simul}(z,\theta)}$ and $r_{\text{target}(z,\theta)}$ in the numerator are, respectively, the simulation and the target radius at the θ angle of the contours (Fig. 3b), for the outer (exterior) and inner (interior) contours of the superficial soft tissues (Fig. 3c) at the height z of the leg; $h1$ and $h2$ are the boundary heights for the identification (Fig. 3a). In the denominator, $r_{\text{initial}(z,\theta)}$ represents the simulation contour at the beginning of the identification process.

The cost function takes values between 1 (at the first iteration of the Identification step) and 0 (when the simulated contours match the target experimental contours). The five slices covered a height of 3 cm.

3 Results

3.1 Identification Results

The average c_{10} value identified for the deep soft tissue and for the six subjects was 3.25 ± 0.93 kPa. The values of the cost function corresponding to the optimised constitutive parameter are given for each subject in the Table 2 below.

3.2 Interface Pressure Distribution

The interface pressure distribution for the six subjects, calculated from Laplace law, is illustrated in Fig. 4 below. It can be observed that the order magnitude of the applied pressures is highly non-uniform across the height of the leg. This highlights the inter-subject interface pressure variations and the need for patient-specific treatment of the simulation of the treatment.

3.3 Pressure Distribution

The elastic properties of the soft tissues identified were used in the FEA to determine the pressure distribution in the calf when external compression is applied. The results for the hydrostatic pressure are shown for all the six subjects in Fig. 5 below.

Table 2 Values of the cost function at the end of the identification step for each subject

Subjects	1	2	3	4	5	6
Cost function C	0.85	0.73	0.44	0.19	0.21	0.44

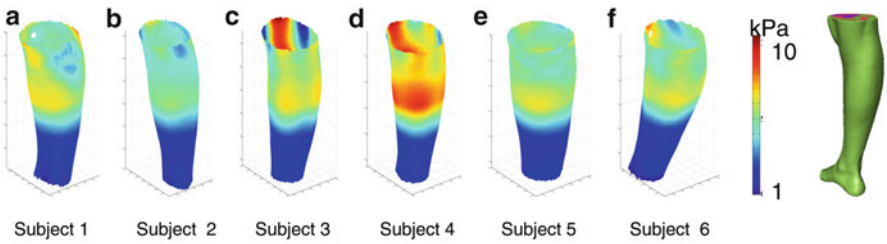

Fig. 4 Magnitude of the interface pressure distribution for each of the six subjects. A three-dimensional rendering of the geometric model oriented in the same direction as six pressure maps is given in the Right Hand Side (R.H.S.) of the figure

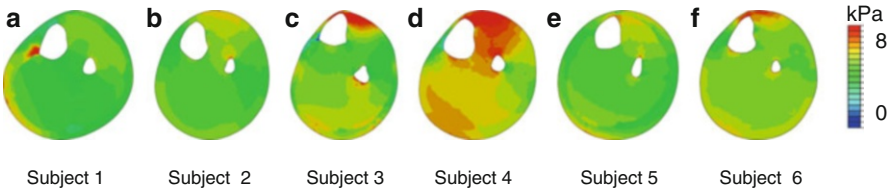

Fig. 5 Hydrostatic pressure field for six subjects at mid-calf in the leg cross section

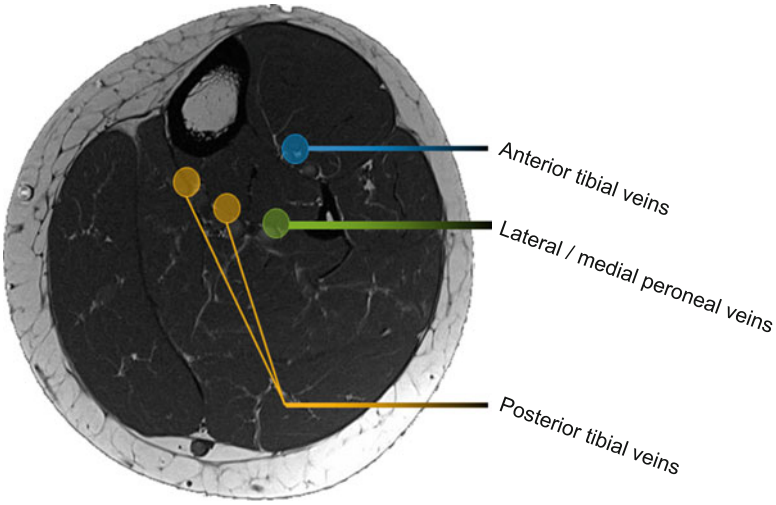

Fig. 6 Position in the calf of the major deep veins. The hydrostatic pressure predicted by the developed model was extracted in these locations to have an estimate of the pressure transmitted to the deep veins

Hydrostatic pressure was chosen for the analysis because it does not depend on the coordinate system and can be used to predict local fluid flows. Although the appropriate MCS was used for each subject to ensure that comparable interface pressure was delivered from one subject to another, large inter-individual variability of the pressure field was observed in the results as illustrated in Fig. 5 below:

Results also show that the pressure transmitted to the deep vein location is of the order of the average interface pressure delivered by the compression garment for most of the subjects. We can infer from this that the pressure delivered on the skin can be used as an indicator of the pressure effectively transmitted to the deep veins, and therefore of the efficiency of the MCS. The position of the main deep veins of the calf where the pressure transmitted was measured is illustrated in Fig. 6 below.

Moreover, due to the presence of pain receptors in the adipose tissue, it seems reasonable to think that the maximum hydrostatic pressure has a major contribution in the comfort sensed by patients wearing MCS. Our computational results

(not shown here) suggest that there exists a relationship between the thickness of the adipose tissue and the maximum hydrostatic pressure. A direct clinical application of this is that thickness of the adipose tissue can be used as a gross evaluation of the comfort of the MCS.

4 Discussion

4.1 Interface Pressure Prediction Using Laplace Law

In this study, Laplace law has been used to compute the pressure exerted by the MCS on the surface of the skin and thus to define the natural loading conditions of the numerical model. The theoretical pressures derived from Laplace law have been shown to provide a good estimate of the real interface pressures measured using pressure transducers [7].

However, Laplace law is valid only insofar as solid non-deformable bodies are concerned. In the case of deformable bodies, as is the case here, it is crucial to take into account the mechanical interaction between the leg and the sock which results in variations of both the local radius of curvature of the limb and the local tension of the fabric. This particular point has been accounted for in the model by computing the surface pressure from the deformed geometry, i.e. the CT scans of the leg under compression.

Another approach consists in integrating the sock in the model and simulating the application of the latter on the leg [8, 11]. The simulation of the application of the sock has been developed in two dimensions and results show that the distribution of pressure fit the one predicted by Laplace law.

In three dimensions, Laplace law was preferred to reduce the complexity of the problem, all the more so that Finite Element Updating requires a large number of simulations to determine the optimal material parameters.

4.2 Choice of Material Behaviour Law for the Soft Tissues

The superficial and deep soft tissues constituting the model (i.e., the adipose tissue and muscle, respectively) are defined as homogeneous, isotropic, compressible, and hyperplastic materials.

The first assumption (homogeneity) stems from the fact that we are interested only in the deformation of the fat and muscle contours, respectively, because they are the only point of comparison between the predictions of the simulation and the experimental results. It follows that the local heterogeneities in the superficial and deep soft tissues are of no interest presently and are not considered in our model.

The second assumption originates chiefly from the experimental conditions: (1) the experimental protocol has been developed to evaluate the passive response of the muscle only and (2) the leg is loaded in compression, essentially in a horizontal plane. Under these conditions, the muscle fibres have but a minor contribution in the response of the leg to external compression and have been considered as isotropic for the sake of simplicity. A more complex material behaviour—such as transverse isotropic, for example—would have been more realistic, but the benefits would not have outweighed the high cost of identifying the optimised material parameter set.

Moreover, due to their high water content soft biological tissues can be approximated as nearly incompressible materials [12, 13].

Finally, soft tissues are known to be highly nonlinear materials exhibiting finite deformations. Under elastic compression, it has been observed that the deformation predicted by the model can be as high as 10 % especially in calf region, as the soft tissues readjust and deform until the internal and exterior forces are balanced. A nonlinear elastic model was therefore chosen to adequately reproduce experiments. The Neo-Hookean hyper-elastic material behaviour law was preferred because of the small number of parameters which simplify the identification process but yet is still a fully nonlinear material. For small deformations, the Neo-Hookean model also reduces to the linear material model, which makes comparison with values from the literature easier.

4.3 Identification Results

This result is in the same order of magnitude as that reported by [11] for in vivo indentation of pig muscle (4.25 kPa). For the superficial soft tissue, the average identified value was 8.17 ± 7.22 kPa, which is also close to the results reported in the literature by [12] for the buttock fat (11.7 kPa).

4.4 Cost Function

The cost function presented above provides a measure of the gap between the experimental contour of the leg under compression and the contour predicted by the model under loading.

Although the uniqueness of the solution cannot be guaranteed, it has been tested for different algorithms and for different sets of initial parameters and the optimised parameter set was always the same (not show here).

The cost function has been defined for a slice of the leg taken in the calf instead of the whole leg to make sure that the assumption of homogeneity remains valid. Indeed, the constitutions of the soft tissues vary across the height of the leg. In the ankle, the presence of the tendons in the deep soft tissue makes the average stiffness higher than in the calf, for example. If the identification had been made over the

whole leg, the resulting identified material parameters would have been an average between the stiffness at the different heights.

Besides, the three-dimensional model also accounts for the out-of-plane displacements and assures a realistic restitution of the leg response in the region where the cost function is applied. This constitutes an added value of the present model over the previous 2D model in which plane strain assumption was made [14].

4.5 Comfort

Comfort is a very important issue in the treatment of vein-related diseases by MCS. Indeed, if the patient cannot endure the treatment prescribed by the doctor because of pain issues, he/she will be inclined to neglect the treatment even if it has a positive impact.

Although the issue of comfort is not very well understood, recent studies on the underlying mechanical principles of discomfort have shown that mechanical loads (pressure as well as shear) influences discomfort [15, 16]. In particular, the Pain Pressure Threshold (PPT) is an index widely used to evaluate the perceived pain caused by high local pressure [17–19].

Our simulation results show that the maximum hydrostatic pressure in the soft tissues is related to the maximum contact pressure on the skin. In addition, according to Laplace law, the contact pressure is inversely proportional to the curvature radius for a given sock tension. We can therefore deduce from Laplace law that in a round leg there is no concentration of interface pressure on the skin. Besides, a high proportion of fat always results in a round leg. It is therefore sound to suppose that the morphology of the fat tissue can be used to estimate the comfort of the MCS. This statement, however, deserves further investigation.

5 Conclusions

In order to provide a quantitative insight into the mechanical response of soft tissues of the leg to elastic compression and to address the essential question of the transmission of pressure, three-dimensional patient-specific FE models of the leg was developed for six subjects. In order to identify the nonlinear properties of the soft tissues, an inverse method based on Finite Element Model Updating has been presented. This constitutes the original contribution of this work.

The material properties identified for the superficial and deep soft tissues are in good agreement with the values reported in the literature for fat and muscles.

Our results show that the mechanical response of the leg to external compression results in a non-homogeneous pressure field which supports the relevance of a patient-specific treatment of the evaluation of the performance of MCS. It has also been shown that the mean interface pressure applied by the MCS can be used as an

indicator of the efficiency of the MCS and that the thickness of the adipose tissue in the leg can be used to estimate the comfort of the MCS.

Yet, the relationship between the hydrostatic pressures measured in the vicinity of the veins using the developed model and the impact on vein-related diseases needs to be further investigated to improve our current understanding of the mechanisms of action of MCS. To address the latter point, a more realistic model will be implemented in 2D to analyse the local response of the vein wall. Refinement of the muscle models is also under progress.

References

1. Nehler, M.R., Moneta, G.L., Woodard, D.M., Defrang, R.D., Harker, C.T., Taylor Jr., L.M., Porter, J.M.: Perimalleolar subcutaneous tissue pressure effects of elastic compression stockings. J. Vasc. Surg. **18**(5), 783–788 (1993)
2. Ibegbuna, V., Delis, K.T., Nicolaides, A.N., Aina, O.: Effect of elastic compression stockings on venous hemodynamics during walking. J. Vasc. Surg. **37**(2), 420–425 (2003)
3. Mayberry, J.C., Moneta, G.L., De Frang, R.D., Porter, J.M.: The influence of elastic compression stockings on deep venous hemodynamics. J. Vasc. Surg. **13**(1), 91–100 (1991)
4. Hamel-Desnos, C.M., Guias, B.J., Desnos, P.R., Mesgard, A.: Foam sclerotherapy of the saphenous veins: randomised controlled trial with or without compression. Eur. J. Vasc. Endovasc. Surg. **39**(4), 500–507 (2010)
5. Kern, P., Ramelet, A.-A., Wütschert, R., Hayoz, D.: Compression after sclerotherapy for telangiectasias and reticular leg veins: a randomized controlled study. J. Vasc. Surg. **45**(6), 1212–1216 (2007)
6. Wildin, C.J., Hui, A.C.W., Esler, C.N.A., Gregg, P.J.: In vivo pressure profiles of thigh]length graduated compression stockings. Br. J. Surg. **85**(9), 1228–1231 (1998)
7. Gaied, I., Drapier, S., Lun, B.: Experimental assessment and analytical 2D predictions of the stocking pressures induced on a model leg by medical compressive stockings. J. Biomech. **39**(16), 3017–3025 (2006)
8. Dai, X., Liu, R., Li, Y., Zhang, M., Kwok, Y.: Computational Textile, vol. 55, pp. 301–309. Springer, Berlin (2007)
9. Avril, S., Badel, P., Dubuis, L., Rohan, P.-Y., Debayle, J., Couzan, S., Pouget, J.-F.: Patient-specific modeling of leg compression in the treatment of venous deficiency. In: Gefen, A. (ed.) Patient-Specific Modeling in Tomorrow's Medicine, vol. 09, pp. 217–238. Springer, Berlin (2011)
10. Dubuis, L., Avril, S., Debayle, J., Badel, P.: Identification of the material parameters of soft tissues in the compressed leg. Comput. Meth. Biomech. Biomed. Eng. **15**(1), 3–11 (2012)
11. Liu, R., Kwok, Y.-L., Li, Y., Lao, T.-T., Zhang, X., Dai, X.: A three-dimensional biomechanical model for numerical simulation of dynamic pressure functional performances of graduated compression stocking (GCS). Fibers Polymer **7**(4), 389–397 (2006)
12. Carter, T.J., Sermesant, M., Cash, D.M., Barratt, D.C., Tanner, C., Hawkes, D.J.: Application of soft tissue modelling to image-guided surgery. Med. Eng. Phys. **27**(10), 893–909 (2005)
13. Kauer, M., Vuskovic, V., Dual, J., Szekely, G., Bajka, M.: Inverse finite element characterization of soft tissues. Med. Image Anal. **6**(3), 275–287 (2002)
14. Avril, S., Bouten, L., Dubuis, L., Drapier, S., Pouget, J.-F.: Mixed experimental and numerical approach for characterizing the biomechanical response of the human leg under elastic compression. J. Biomech. Eng. **132**(3), 31006–31014 (2010)
15. Goossens, R.H.M.: Fundamentals of pressure, shear and friction and their effects on the human body at supported postures. In: Gefen, A. (ed.) Bioengineering Research of Chronic Wounds, vol. 1, pp. 1–30. Springer, Berlin (2009)

16. Moreno, J.C., Brunetti, F.J., Pons, J.L., Baydal, J.M., Barbera, R.: Rationale for multiple compensation of muscle weakness walking with a wearable robotic orthosis. In: Robotics and Automation, 2005. ICRA 2005. Proceedings of the 2005 IEEE International Conference, pp. 1914–1919, 2005
17. Fischer, A.A.: Pressure tolerance over muscles and bones in normal subjects. Arch. Phys. Med. Rehabil. **67**(6), 406–409 (1986)
18. Fischer, A.A.: Pressure algometry over normal muscles. Standard values, validity and reproducibility of pressure threshold. Pain **30**(1), 115–126 (1987)
19. Ylinen, J., Takala, E.-P., Kautiainen, H., Nykänen, M., Häkkinen, A., Pohjolainen, T., Karppi, S.-L., Airaksinen, O.: Effect of long-term neck muscle training on pressure pain threshold: a randomized controlled trial. Eur. J. Pain **9**(6), 673–681 (2005)

Intraoperative Damage Monitoring of Endoclamp Balloon Expansion Using Real-Time Finite Element Modeling

Nele Famaey, Vukašin Štrbac, and Jos Vander Sloten

Abstract Endovascular clamping can be achieved by means of intraluminal occlusion with an Endoclamp balloon. Circumventing the need for opening the thoracic cage provides significant benefits in terms of reducing trauma for the patient. This procedure, however, induces risks of damage to the aortic lumen by way of over-expansion of the balloon, exposing the aortic tissue to unsafe levels of loading. Accurate estimates of the induced stress and consequent damage are required intraoperatively to warn the surgeon and mitigate the risk of injury.

This paper proposes a method for intraoperative monitoring of the inflicted damage to the arterial tissue, by means of finite element modeling. The Total Lagrangian Explicit Dynamic (TLED) finite element (FE) formulation, capable of handling geometric and material nonlinearities, is used. A 2D plane strain formulation is used to additionally simplify and speed up the execution time by reducing the number of degrees of freedom involved, meanwhile retaining sufficient accuracy for the proposed application. A material model incorporating damage as an internal variable allowed tracking of the degree of injury to the artery. The large amount of computation needed to solve for the stress field is relieved by using dedicated massively parallel hardware. An Nvidia CUDA GPGPU (General Purpose Graphics Processing Unit) is employed to parallelize critical portions of the TLED algorithm. The accuracy of the solution is verified against an industry-proven FE package Abaqus. Results show significant speed-ups compared to Abaqus, thereby retaining a sufficient degree of accuracy.

N. Famaey (✉) • V. Štrbac • J. Vander Sloten
Biomechanics Section, KU Leuven, Heverlee, Belgium
e-mail: nele.famaey@mech.kuleuven.be; www.mech.kuleuven.be/en/BMe

A. Wittek et al. (eds.), *Computational Biomechanics for Medicine: Models, Algorithms and Implementation*, DOI 10.1007/978-1-4614-6351-1_5,
© Springer Science+Business Media New York 2013

1 Introduction

The clamping of the aorta by means of intraluminal occlusion is an important part of a minimally invasive full cardiopulmonary bypass procedure. The device is inserted through the femoral artery and positioned in the ascending aorta. The subsequent filling of the balloon with a saline solution expands the endoclamp balloon and the aorta, thus occluding the lumen and stopping blood flow [1, 2]. Aside from leaks around the balloon, additional risks exist in the form of balloon movement. For this reason, endovascular surgeons tend to overexpand the balloon to enhance apposition between the balloon and the aortic lumen. This ensures better stability and sealing but increases the probability of damage if the aorta is strained excessively [3].

In this regard, monitoring of stresses and consequent damage is necessary in order to reduce risk of injury to the patient. For the most accurate estimate of stresses and strains, the Finite Element method is to be used [4]. This approach, however, proves to be very slow for real-time applications, even more so for nonlinear implementations. This paper presents an adaptation and implementation of the computational scheme proposed by Miller et al. [5] to enable the computation of stresses and consequent damage inside the aorta in real time, using a nonlinear finite element formulation.

Successful real-time implementations of nonlinear finite elements have been sparse in publications, mostly likely due to the limited computational power of hardware and the high arithmetic intensity of conventional FE algorithms. The Total Lagrangian Explicit Dynamic (TLED) algorithm [5] tackles this problem in part by using the total Lagrangian spatial discretization scheme. It ensures that shape function derivatives do not need to be recomputed every time step, thus additionally reducing the number of operations. By using explicit time integration (the central difference method), the nonlinearities are handled in a simple way, provided a small enough time step is selected. Another benefit of explicit integration is that per-element computations can be done somewhat independently, adding individual contributions gradually to form the global force matrix. This feature along with the per-node fully independent computations lends itself well to parallelization.

Nvidia CUDA [6] technology enables us to use the massively parallel architecture of modern GPUs to conduct general-purpose floating-point computations in an accessible and simplified way. By distributing the computations over the cores of the card, most calculations of the same time step can be done at the same time, providing significant speed-up to the algorithm.

A nonlinear material model incorporating damage by means of an energy-driven internal variable is implemented into the computational scheme. Monitoring of this damage variable enables us to track the amount of injury that is being inflicted by expansion of the Endoclamp balloon. Ideally, this damage variable can be directly coupled to the control system inflating the balloon, thereby automatically protecting the artery from overexpansion.

In the next section, we present more details on the algorithm implementation and used hardware, followed by results and a discussion on the topic.

2 Materials and Methods

2.1 Mechanical Model

We use a plane strain formulation to describe the mechanical system. By disregarding the out of plane stresses we omit one dimension from the computation and thus significantly reduce the computational load. The mesh, therefore, is a ring-shaped cross section of the aorta. The simulation is driven by a prescribed displacement loading of 4 mm in radial direction on the inner nodes of the model. All other nodes are unconstrained.

A planar mesh comprising of 150 nodes and 240 elements is used. The aortic cross section is meshed using linear triangular elements with a single integration point. After meshing, a hyperelastic nearly incompressible constitutive model is assigned to the elements. The strain-energy density function of the material model, composing of a deviatoric and volumetric part is expressed as:

$$\Psi = \overbrace{(1-d)\frac{\mu}{2}(\bar{I}_1 - 3)}^{\Psi^{\text{dev}}} + \overbrace{\frac{\kappa}{2}(J-1)^2}^{\Psi^{\text{vol}}}, \tag{1}$$

where μ and κ are material constants—shear and bulk modulus, respectively. $\bar{I}_1$ is the first invariant of the right Cauchy–Green deformation tensor $\mathbf{C}$. The first part of the deviatoric energy contains the damage variable d is the actual damage variable, indicating the integrity of the material on a scale from 0 to 1. Following the approach of Simo et al. [7], this damage is defined as:

$$d = \gamma[1 - \exp(-\beta/m)], \tag{2}$$

where $\gamma \in]0, 1]$ is a weighting factor and m is a parameter of the damage model. β is the maximum value of energy in the interval $0 < t < \tau$:

$$\beta = \max_{0<t<\tau} (\Psi(t) - \Psi_0) \tag{3}$$

The value for Ψ_0, which is the threshold value for which damage initiates, is set to systolic pressure since no damage is assumed in the physiological range.

The second Piola–Kirchoff stress tensor $\mathbf{S}$ can be derived from the SEDF as:

$$\mathbf{S} = 2(1-d)\frac{\partial \Psi}{\partial \mathbf{C}} = \mu J^{-1}\left(\mathbf{I} - \frac{tr(\mathbf{C})}{2}\mathbf{C}^{-1}\right) + \kappa J(J-1)\mathbf{C}^{-1}. \tag{4}$$

In spite of more viable and detailed models [8–10] for the aorta, this model was chosen due to its simplicity and ease of implementation, making it easier to evaluate the performance of the FE algorithm.

2.2 Total Lagrangian Explicit Dynamic Algorithm

The system to be solved is:

$$\mathbf{M}\ddot{\mathbf{u}} + c_d\mathbf{M}\dot{\mathbf{u}} + \mathbf{P}(\mathbf{u}) = \mathbf{R}, \tag{5}$$

where $\mathbf{M}$ is the diagonalized mass matrix, c_d is the damping coefficient, $\mathbf{u}$ are the nodal displacements, $\mathbf{P}$ are the internal forces and $\mathbf{R}$ are the external forces. Miller et al. [5], Joldes et al. [11], and Belytchko and Hughes [12], for example, provide additional detail on the topic. A pseudo-code of the solution of the system in Eq. (5) is provided below.

Precomputation phase:

1. Shape Function Derivatives: $\nabla\mathbf{N}_i \; i = 1,2,3$
2. Diagonalized mass matrix $\mathbf{M} = M_e\mathbf{I}$
3. Gaussian integration weights: $w(e)$
4. Central difference method coefficients:

$$a = -\frac{2(\Delta t^2)}{2t\Delta t M_e};\; b = \frac{1+(2-q\Delta t)}{2+q\Delta t}; \tag{6}$$

$$c = -\frac{2-q\Delta t}{2+q\Delta t};\; q = \frac{2(1-{C_r}^2)}{\Delta t(1+C_r)} \tag{7}$$

Iteration phase:

4. Deformation gradient:

$${}^t\mathbf{F}_e = \mathbf{I} + \nabla\mathbf{N}{}^t\mathbf{u}_e \tag{8}$$

5. Cauchy–Green strain tensor, Jacobian determinant:

$${}^t\mathbf{C}_e = {}^t\mathbf{F}_e^T{}^t\mathbf{F}_e \;,\; {}^tJ_e = det({}^t\mathbf{F}_e) \tag{9}$$

6. Second Piola–Kirchoff stress:

$${}^t\mathbf{S}_e = 2\frac{\partial^t\mathbf{\Psi}_e}{\partial^t\mathbf{C}_e} \tag{10}$$

7. Force contribution:

$${}^t\mathbf{P}_e = \nabla\mathbf{N}_e{}^t\mathbf{S}_e{}^t\mathbf{F}_e w(e) \tag{11}$$

8. Summation of elemental contributions into the global force vector:

$${}^t\mathbf{P} = \sum{}^t\mathbf{P}_e \tag{12}$$

9. New displacements:

$${}^t\mathbf{u} = a({}^t\mathbf{P} - {}^t\mathbf{R}) + b{}^t\mathbf{u} + c\,{}^{t-\Delta t}\mathbf{u} \tag{13}$$

10. Loading for next step:

$$^{t+\Delta t}\mathbf{u}_{BC_d} = \mathbf{d}_{BC_d}(t+\Delta t) \tag{14}$$

and/or

$$^{t+\Delta t}\mathbf{R}_{BC_n} = \mathbf{R}_{BC_n}(t+\Delta t) \tag{15}$$

In the above notation the left superscript denotes the time step, the right subscript denotes element scope. C_r is the convergence rate of the central difference scheme, and set close to 1, as relaxation effects were not considered and a small enough time step was used.

In light of increasing the speed of the algorithm, precomputing all possible values is essential. Due to the spatial discretization scheme chosen, the shape function derivatives do not change across the time steps, therefore we compute them here. For the chosen elements, the weight computation reduces to a simple division of the area by 3 and is performed in the precomputation phase, step 3. The central difference method coefficients are also precomputed as they too do not change throughout.

Single point Gaussian integration is used to obtain element nodal forces from element stress in step 7, which was in turn computed from the right Cauchy–Green tensor and deformation gradient in steps 4–6. Depending on the material model used, the stress computation in step 7 can vary. In our implementation, the nonlinear damage material according to Eq. (4) is used. After assembly of the global force vector in step 8, the nodal displacements are calculated using the central difference scheme. Finally, new displacement boundary conditions and/or nodal force boundary conditions are assigned to the boundary nodes to prepare for the next iteration step. For a more detailed discussion on TLED, the reader is encouraged to refer to [5].

2.3 Hardware and Implementation

The pseudocode described in Sect. 2.2 is implemented using Nvidia Compute Unified Device Architecture (CUDA). The GPGPU card used for this purpose is an Nvidia Tesla C2075 that has 448 lightweight computing cores capable of running thousands of threads concurrently. For a detailed overview of CUDA, the reader is referred to [6].

The two most important factors in speeding up a program by using a GPGPU is replacing loops with parallel functions (kernels) and the precomputation of all possible values for later use in the algorithm. Albeit, the former can be used only if iterations are independent from one another. For this reason we can parallelize over elements and nodes and not over time steps. The most suitable portions of code to implement in parallel are: obtaining the global force matrix (steps 4–8), updating of displacements (step 9) and loading for the next step (10), which have been implemented as three kernels.

Table 1 Material parameters

Parameter	Value	Parameter	Value
μ	1006.7 MPa	γ	0.9 [−]
κ	50e3 MPa	m	1e3 MPa

The granularity of parallelization in the computation of force contributions in the global force matrix assembly is one element, meaning that each thread run by the hardware computes the values of force for one element. The interconnectivity of elements mandates storage problems when summing force contributions on a node from surrounding elements in a parallel setting. A reduction scheme has been implemented for this reason that avoids the serialization of storage writes.

In the second kernel, we obtain per-node displacements using coefficients computed in the precomputation phase. Using the central difference method we compute future displacements of nodes based on the global force matrix and the precomputed coefficients in step 3. Here, the granularity is one node.

The last kernel executes the loading of the nodes under boundary conditions. Much like the previous kernel, it is executed per-node and it is an embarrassingly parallel task due to no communication requirements between nodes.

Due to the limited volume of computation on a single value in the memory of the Tesla for this simulation, floating-point truncation errors do not compound excessively. For this reason, single-precision number representation is warranted and significant speed-ups are retained.

An Abaqus finite element simulation code was used to verify the newly implemented code. Identical boundary conditions and loading curve were used in both solution regimes. The same material model with identical parameters according to Table 1 was implemented by means of a custom user material implementation (UMAT). The Abaqus job was run on a Xeon E5620 processor on one core. To investigate the effect of incorporating damage in the material model, the simulations were repeated in Abaqus and in our CUDA implementation for a simple Neo-Hookean material.

3 Results

The results obtained through simulation in Abaqus implicit are regarded as a benchmark. The accuracy of the newly implemented algorithm was evaluated by comparing the percentage of discrepancy of the final displacement of a chosen outermost node, shown in Table 2. This table also shows the computation time for each of the solution schemes. The duration of the Abaqus solution was taken from its output files, while timing CUDA code was performed on a high-accuracy hardware clock accessed through the Nvidia CUDA profiling tool.

Figure 1 shows color plots of the solutions obtained with the CUDA TLED algorithm. Figure 1a shows the initial configuration of the domain. The following Fig. 1b shows the loaded damaged configuration. The induced damage is displayed in a

Table 2 Nodal displacement of a node x on the outer boundary of the ring-shaped segment and calculation time, for each of the solution schemes and for the Neo Hookean and the Neo-Hookean material model including damage

Method	Material model	Displacement of node x (mm)	% deviation	Calculation time (ms)
Abaqus implicit	Neo Hookean	1.8125		400
	Damage	1.8109		500
CUDA TLED	Neo Hookean	1.8163	0.21%	81
	Damage	1.8147	0.21%	87

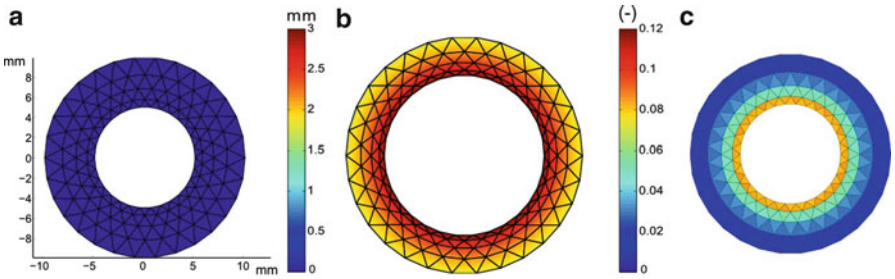

Fig. 1 Initial configuration, deformed configuration and damage map. The *left most image* shows the starting conditions of the system, the *middle image* shows the damaged final configuration with a displacement color map. The *right-most image* shows the damage itself and its color map

color map in Fig. 1c Note that this damage is, by definition, irreversible. Hence, even when relaxed back to the unloaded configuration, the damage remains, weakening the material. From Table 2 it is clear that significant speed-ups are achievable with the newly implemented solution scheme. Implementing damage does not induce significant delays to the calculations. Moreover, all CUDA displacement and stress results fall within 0.2% of the Abaqus implicit benchmark value.

4 Discussion and Future Work

The newly implemented TLED CUDA algorithm solved our problem in roughly 85 ms, without losing a significant amount of accuracy compared to the Abaqus solution. This translates to about 11 frames per second and is well within the requirements of the surgical theater, additional time to retrieve results from the device notwithstanding. The damage model implemented does not significantly impact the solution times, and thus efficiently tracks damage over re-inflations.

Note that the achieved computational speed and the achieved speed-up with respect to the Abaqus implicit solver are not fixed values. Firstly, they depend on the problem size. Due to the hardware specifics of the GPGPU used in this research (number of cores, multiprocessors, etc.) the relative speed-ups will vary with the

problem size. More elements and nodes will increase the occupancy of the GPU and thus achieve better speed-ups. This will hold true up to problems of very large size, where the increase of speed-up will stop. This study of performance scaling of the algorithm is planned as future work for this research. Secondly, they depend on the degree of nonlinearity of the problem, as an implicit solver will by far outperform an explicit solver for a relatively linear problem. For this particular problem, the Abaqus explicit solution time is in the order of magnitude of minutes.

Despite the well-known complexity of arterial tissue, a simple Neo Hookean damage material model was implemented, to enable a clear evaluation of the performance of the algorithm. As a next step, the typical arterial constituents, collagen fibers and smooth muscle cells will be incorporated into the material description, thereby also allowing for degradation of each of these individual constituents, following the approach of [10]. Realistic material parameters should be obtained from experiments as, for example, described in [13] and [14] .

Due to the large difference in the length of the aorta compared to its thickness, we used a plane strain formulation of the problem. This reduces the volume of computation and, therefore, increases the speed of the simulation. However, when axial residual stretches are taken into account, the plane strain assumption no longer holds. Future work will involve an upgrade to a fully 3D parallel solver. An extension to hexahedral elements and tackling accompanying problems like spurious energy modes are planned. A 3D implementation will also allow for more complex out-of-plane loading situations and the use of more complex patient-specific geometries, as, for example, described in [15]. Parallel contact algorithms will allow a more detailed simulation of the balloon–tissue interaction as well as interaction with other surgical instruments.

5 Conclusion

We have presented an integral part of a computer integrated system for monitoring of damage during the expansion of an Endoclamp Balloon. The algorithm and the computational scheme fully support both geometric an material nonlinearities, in addition to meeting the speed requirements for intra-operative use. Future work will be directed towards upgrading the algorithm to a fully 3D solver with contact capabilities and towards incorporating it into a robust computer integrated surgery system.

Acknowledgements The authors would like to thank Prof. K. Miller, Prof. A. Wittek and Dr. G. Joldes for considerable instruction and assistance with the details of the TLED algorithm. This research was funded by an FP7 STREP project, SCATh (www.scath.net), by an interdisciplinary research project of KU Leuven (IDO) and by the Research Foundation Flanders (FWO).

References

1. Carpentier, A., Loulmet, D., Le Bret, E., Haugades, B., Dassier, P., Guibourt, P.: [open heart operation under videosurgery and minithoracotomy. first case (mitral valvuloplasty) operated with success]. Comptes rendus de lAcadmie des sciences. Srie III, Sciences de la vie., vol. 319(3), pp. 21923 (1996)
2. Casselman, F.P., Van Slycke, S., Wellens, F., De Geest, R., Degrieck, I., Van Praet, F., Vermeulen, Y., Vanermen, H.: Mitral valve surgery can now routinely be performed endoscopically. Circulation **108**(Suppl 1), II48–II54 (2003). [Online]. Available: http://dx.doi.org/10.1161/01.cir.0000087391.49121.ce
3. Farhat, F., Metton, O., Thivolet, F., Jegaden, O.: Comparison between 3 aortic clamps for video-assisted cardiac surgery: a histological study in a pig model. Heart Surg. Forum **9**(3), E657–E660 (2006). [Online]. Available: http://dx.doi.org/10.1532/HSF98.2005-1101
4. Zienkewicz, O., Taylor, R.: The Finite Element Method for Solid and Structural Mechanics, 6th edn. Elsevier, Butterworth Heineman (2005)
5. Miller, K., Joldes, G., Lance, D., Wittek, A.: Total Lagrangian explicit dynamics finite element algorithm for computing soft tissue deformation. Comm. Numer. Meth. Eng. **23**(2), 121–134 (2007). [Online]. Available: http://dx.doi.org/10.1002/cnm.887
6. Nvidia, CUDA C Programming Guide 4.2, Nvidia Corporation (2012). [Online]. Available: http://developer.nvidia.com/nvidia-gpu-computing-documentation
7. Simo, J., Ju, J.: Strain- and stress-based continuum damage models. Int. J. Solid Stuct. **23**, 821–840 (1987)
8. Holzapfel, G.A., Gasser, T.C., Ogden, R.W.: A new constitutive framework for arterial wall mechanics and a comparative study of material models. J. Elasticity **61**, 1–48 (2000)
9. Gasser, T.C., Ogden, R.W., Holzapfel, G.A.: Hyperelastic modelling of arterial layers with distributed collagen fibre orientations. J. R. Soc. Interface **3**(6), 15–35 (2006)
10. Famaey, N., Vander Sloten, J., Kuhl, E.: A three-constituent damage model for arterial clamping in computer-assisted surgery. Biomech. Model Mechanobiol. 12(1), 123–36 (2013). [Online]. Available: http://dx.doi.org/10.1007/s10237-012-0386-7
11. Joldes, G.R., Wittek, A., Miller, K.: Suite of finite element algorithms for accurate computation of soft tissue deformation for surgical simulation. Med. Image Anal. **13**(6), 912–919 (2009). [Online]. Available: http://dx.doi.org/10.1016/j.media.2008.12.001
12. Belytschko, T., Hughes, T.J.R. (eds.): Computational Methods for Transient Analysis. In Computational Methods in Mechanics. Amsterdam-New York, North-Holland Publ. Co. ISBN 0-444-86479-2, **1**, (1983)
13. Famaey, N., Verbeken, E., Vinckier, S., Willaert, B., Herijgers, P., Vander Sloten, J.: In vivo soft tissue damage assessment for applications in surgery. Med. Eng. Phys. **32**(5), 437–443 (2010). [Online]. Available: http://dx.doi.org/10.1016/j.medengphy.2010.04.002
14. Famaey, N., Sommer, G., Vander Sloten, J., Holzapfel, G.A.: Arterial clamping: Finite element simulation and in vivo validation. J. Mech. Behav. Biomed. Mater. **12C**, 107–118 (2012). [Online]. Available: http://dx.doi.org/10.1016/j.jmbbm.2012.03.010
15. Wittek, A., Joldes, G., Couton, M., Warfield, S.K., Miller, K.: Patient-specific non-linear finite element modelling for predicting soft organ deformation in real-time: application to non-rigid neuroimage registration. Prog. Biophys. Mol. Biol. **103**(2–3), 292–303 (2010). [Online]. Available: http://dx.doi.org/10.1016/j.pbiomolbio.2010.09.001

3D Algorithm for Simulation of Soft Tissue Cutting

Xia Jin, Grand Roman Joldes, Karol Miller, and Adam Wittek

Abstract Modelling and simulation of soft tissue cutting in 3D remain one of the most challenging problems in surgery simulation, not only because of the nonlinear geometric and material behaviour exhibited by soft tissue but also due to the complexity of introducing the cutting-induced discontinuity. In most publications, the progressive surgical cutting is modelled by conventional finite element (FE) method, in which the high computational cost and error accumulation due to re-meshing constrain the computational efficiency and accuracy. In this paper, a meshless Total Lagrangian Adaptive Dynamic Relaxation (MTLADR) 3D cutting algorithm is proposed to predict the steady-state responses of soft tissue at any stage of surgical cutting in 3D. The MTLADR 3D algorithm features a spatial discretisation using a cloud of nodes. With the benefits of no meshing and no re-meshing, the cutting-induced discontinuity is modelled and simulated by adding nodes on the cutting faces and implementing the visibility criterion with the aid of the level set method. The accuracy of the MTLADR 3D cutting algorithm is verified against the established nonlinear solution procedures available in commercial FE software Abaqus.

X. Jin • G.R. Joldes • A. Wittek
Intelligent Systems for Medicine Laboratory, The University of Western Australia, Perth, Australia
e-mail: jinxiach@gmail.com; grand.joldes@uwa.edu.au; adam.wittek@uwa.edu.au

K. Miller (✉)
Intelligent Systems for Medicine Laboratory, The University of Western Australia, Perth, Australia

Institute of Mechanics and Advanced Materials, Cardiff School of Engineering, Cardiff University, Wales, UK
e-mail: karol.miller@uwa.edu.au

A. Wittek et al. (eds.), *Computational Biomechanics for Medicine: Models, Algorithms and Implementation*, DOI 10.1007/978-1-4614-6351-1_6,
© Springer Science+Business Media New York 2013

1 Introduction

Surgery simulation has great significance in extending surgeons' ability to learn, plan and carry out surgical interventions more accurately and less invasively. Potential applications include surgical simulators for highly realistic surgical training and planning, non-rigid registration in image-guided surgery systems and computer-aided design of medical devices and procedures.

Modelling and simulation of soft tissue cutting remain one of the most challenging problems in surgery simulation. The challenges exist in the complexity of introducing cutting-induced discontinuity and the capability of handling the nonlinear geometric and material behaviour of soft tissue [1–3] while reducing the high computational cost of 3D simulation.

So far, the progressive surgical cutting has been modelled and simulated by subdivision of elements of the volumetric mesh using conventional finite element (FE) method [4–7]. Even when using sophisticated re-meshing technologies, the FE method tends to become unstable and its accuracy deteriorates when the mesh undergoes distortion and fragmentation due to large deformations and cutting [8]. Despite the exploration of speed-up technologies [7, 9, 10], the high computational cost constrains the computational efficiency of FE method in surgical cutting simulation.

In this paper, a meshless Total Lagrangian Aadaptive Dynamic Relaxation (MTLADR) 3D cutting algorithm is developed to provide robust solution for modelling and simulation of soft tissue responses during cutting in 3D. This algorithm belongs to the Element-Free Galerkin (EFG) family and is a generalisation of the 2D version presented in [11]. A cloud of points is used for discretisation and approximation of the deformation field within the continuum which eliminates the need for time-consuming generation of FE meshes and avoids the shortcomings of the distortion and fragmentation of finite elements. In the MTLADR 3D cutting algorithm, the cutting path is geometrically represented as a series of cutting planes. The discontinuities induced by surgical cutting are modelled and traced using nodes with specific level set values and appropriate field values (the nodal displacements and the size of influence domain). The update of the level set values is performed using simple and fast algebraic computations based on the geometry of the cutting path. The effect of cutting is entirely reflected in the changes of the shape and size of the influence domain of the nodes by efficiently implementing visibility criterion with the aid of level set values.

Using adaptive dynamic relaxation, MTLADR 3D cutting algorithm offers a fast convergence to the deformed state of deformation for problems with nonlinear geometric and material behaviour. The application of Total Lagrangian (TL) formulation eliminates the error accumulation due to the stress/strain update associated with the Updated Lagrangian (UL) formulation. The accuracy of the algorithm is well controlled by the stringent convergence criteria of dynamic relaxation. A range of numerical experiments were conducted for verification of the results.

This paper is organised as follows. The methods for modelling and simulation of surgical cutting in 3D are presented in Section 2. The numerical experiments and result verification are given in Section 3. Section 4 contains discussion and conclusions.

2 Methods

2.1 Governing Equation and Solution

The deformed state of soft tissue at any stage of cutting is solved using dynamic relaxation with optimal time stepping to obtain steady-state solution of the deformed continuum [12]. Details of the solution method are given in our previous papers [11, 13, 14].

2.2 Modelling of Surgical Cutting in 3D

In this study, we geometrically represent the progressing surgical cut in 3D as a series of cutting planes as shown in Fig. 1. We adapt the level set method proposed by Osher and Sethian [15] and developed by Stolarska et al. [16] to mathematically describe the signed distances of all the nodes and integration points relative to the cutting path. The discontinuities induced by surgical cutting are modelled and traced using pairs of nodes which are created by adding two new nodes or splitting the existing node at the point of discretisation. Every pair of discretising nodes on the cutting faces is assigned specific level set values in order to be allocated into the opposite sides of the cutting path. The appropriate field values (the nodal

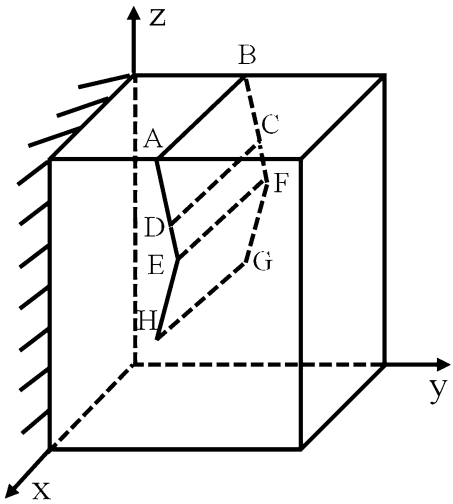

Fig. 1 The cutting path in 3D problem domain is represented by a series of cutting planes (ABCD, CDEF and EFGH)

displacement and the size of domain of influence) of the newly added node can either be interpolated by the existing nodal field parameters or be inherited from the existing node. The effect of cutting is entirely reflected in the changes of the shape and size of the influence domain of the nodes by implementing visibility criterion with the help of the level set values of the nodes and integration points.

2.2.1 Initialisation of the Level Set Values of the Nodes and Integration Points

When the first cut (e.g. the cutting plane ABCD illustrated in Fig. 1) is made, the cutting face and its extension plane are mathematically represented as the zero level set of function $\psi(x,y,z)$ as defined in (1). The bottom line of the cut is defined as the intersection of the cutting face and its orthogonal plane, which is mathematically represented by the zero level set of function $\phi(x,y,z)$ as defined in (2):

$$\psi(x,y,z) = \left(x - x_{\text{ep}}\right)\frac{K_x}{\|K\|} + \left(y - y_{\text{ep}}\right)\frac{K_y}{\|K\|} + \left(z - z_{\text{ep}}\right)\frac{K_z}{\|K\|} \tag{1}$$

$$\phi(x,y,z) = \left(x - x_{\text{ep}}\right)\frac{T_x}{\|T\|} + \left(y - y_{\text{ep}}\right)\frac{T_y}{\|T\|} + \left(z - z_{\text{ep}}\right)\frac{T_z}{\|T\|} \tag{2}$$

where (x,y,z) is the coordinate of a given point in the problem domain; $\left(x_{\text{ep}}, y_{\text{ep}}, z_{\text{ep}}\right)$ is the coordinate of an arbitrary point located at the end-line/endpoint of the cutting plane; K represents the normal vector of the cutting plane; K_x, K_y, and K_z are the x, y, z components of vector K respectively; $\|K\|$ is the length of vector K; T represents the normal vector of the orthogonal plane of the cutting face which points to the cutting direction; T_x, T_y, and T_z are the x, y, z components of vector T respectively; $\|T\|$ is the length of vector T.

The values of both level set functions ψ and ϕ are calculated and stored for all the nodes and integration points to indicate their positions relative to the cutting path. The value of the level set function ψ at a given point is the signed distance from this point to the cutting face. As illustrated in Fig. 2, the points with positive values of the level set function ψ are all located on the same side of the cutting plane P and its extension plane P1, while the points with negative values are all on the other side. Zero value of function ψ indicates that the point is located right on the cutting plane P or its extension plane P1. Following the same principle, the value of the level set function ϕ indicates the signed distance from a given point to the plane P2 which is orthogonal to the cutting face at the end-line of cutting L. If a point is judged to be located on the cutting plane P (zero value of function ψ and negative value of function ϕ), the associated value of function ψ is set to a small positive or negative value in order to allocate the point to one of the sub-domains S1 or S2 (Fig. 2).

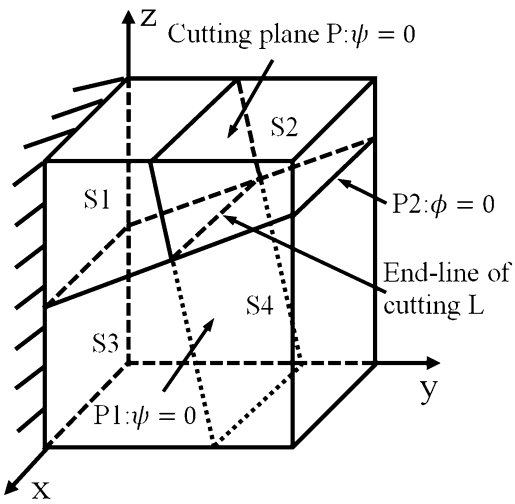

Fig. 2 The initialisation of level set values of functions ψ and ϕ. The 3D problem domain is divided into four subdomains: subdomain S1: $\psi < 0$ and $\phi < 0$; subdomain S2: $\psi > 0$ and $\phi < 0$; subdomain S3: $\psi < 0$ and $\phi > 0$; subdomain S4: $\psi > 0$ and $\phi > 0$. $\psi = 0$ on the cutting plane P and its extension plane P1. $\phi = 0$ on the orthogonal plane P2

2.2.2 Spatial Discretisation of the Cutting Planes

The cutting planes representing the cutting path are discretised using nodes spaced at the average nodal interval of the computational grid. If the computational grid obtained by discretising the geometry of the analysed continuum contains no node at the discretised position of the end-line of the cut, we add one node there with zero values of level set functions ψ and ϕ. If there is no node at the discretised position of the rest of the cutting planes, two nodes (having the same coordinates) are added at this position. If there is an existing node at the discretised position or elsewhere on the cutting planes, we split this node into two nodes having the same coordinates.

2.2.3 Update of Level Set Values of Nodes and Integration Points During Progressing Cutting

When cutting progresses from one cutting plane to the next, the level set values of functions ψ and ϕ at the nodes and the integration points need to be updated. In the following algorithm, ψ^n and ϕ^n denote the values of functions ψ and ϕ at step n; ψ^{n+1} and ϕ^{n+1} denote the values of functions ψ and ϕ at step $n+1$; (x, y, z) are the coordinates of a given node or integration point; $(x_{\text{ep}}^n, y_{\text{ep}}^n, z_{\text{ep}}^n)$ and $(x_{\text{ep}}^{n+1}, y_{\text{ep}}^{n+1}, z_{\text{ep}}^{n+1})$ are the coordinates of an arbitrary point located at the end-line/endpoint of the cutting plane at step n and $n+1$ respectively; T^{n+1} denotes the normal vector of the orthogonal plane of the cutting face at step $n+1$ which points in the cutting direction; T_x^{n+1}, T_y^{n+1}, T_z^{n+1} are the x, y, z components of the normal vector T^{n+1}; $\|T^{n+1}\|$ is the length of the normal vector T^{n+1}; K^{n+1} denotes the normal vector of the cutting face at step $n+1$; K_x^{n+1}, K_y^{n+1}, K_z^{n+1} are the x, y, z components of the

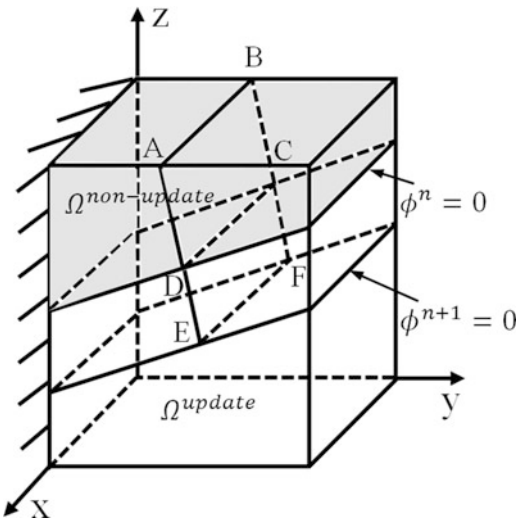

Fig. 3 Progression of cutting without direction change (cutting plane ABCD and CDEF are co-linear). The *shaded space*, where $\phi^n < 0$, is a non-update space $\Omega^{\text{non-update}}$ while the rest of the domain is an update space Ω^{update}

normal vector K^{n+1} respectively; $\|K^{n+1}\|$ is the length of the normal vector K^{n+1}; Ω represents the whole region of the problem domain.

1. Cutting direction does not change. When cutting progresses from one cutting plane to the next without direction change, the values of level set function ϕ of the nodes and integration points whose $\phi^n \geq 0$ need to be updated. The update process is illustrated in Fig. 3. No update is done in the space where $\phi^n < 0$ (indicated as non-update space $\Omega^{\text{non-update}}$ in Fig. 3) while the rest of the analysed domain (where $\phi^n \geq 0$) is an update space

$$\psi^{n+1} = \psi^n \text{ in } \Omega \tag{3}$$

$$\phi^{n+1} = \phi^n \text{ in } \Omega^{\text{non-update}} \tag{4}$$

$$\phi^{n+1}(x,y,z) = (x - x_{\text{ep}}^{n+1}) \frac{T_x^{n+1}}{\|T^{n+1}\|} + (y - y_{\text{ep}}^{n+1}) \frac{T_y^{n+1}}{\|T^{n+1}\|} + \left(z - z_{\text{ep}}^{n+1}\right) \frac{T_z^{n+1}}{\|T^{n+1}\|} \text{ in } \Omega^{\text{update}} \tag{5}$$

   where Ω is the union of $\Omega^{\text{non-update}}$ and Ω^{update} regions.
2. Cutting direction changes. If the cutting direction changes, the update region Ω_c^{update} is defined as the space where $\bar{\phi}^n > 0$ while the rest of the analysed domain is defined as the non-update region $\Omega_c^{\text{non-update}}$ (Fig. 4).

   (a) Level set function $\bar{\phi}^n$ is obtained by rotating function ϕ^n around the end-line/endpoints of the cutting plane at step n (e.g. end-line CD of cutting plane ABCD in Fig. 4) until orthogonal to the cutting plane at step $n+1$ (e.g. cutting plane CDEF in Fig. 4):

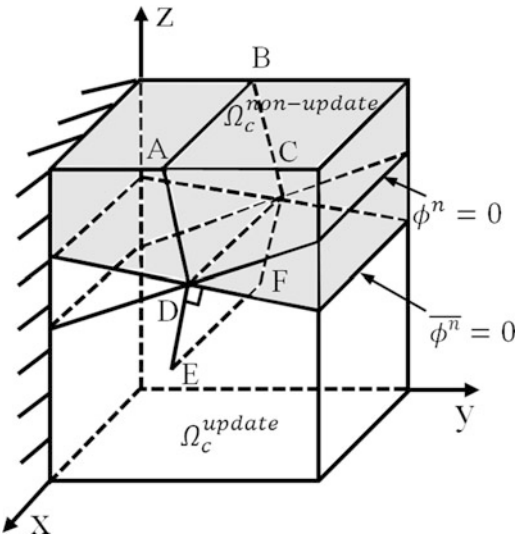

Fig. 4 Progression of cutting with direction change: the cutting proceeds from cutting plane ABCD to cutting plane CDEF with direction change. Level set function $\bar{\phi}^n$ is obtained by rotating level set function ϕ^n until it is orthogonal to the current cutting plane CDEF. The *shaded space*, where $\bar{\phi}^n \leq 0$, is non-update region $\Omega_c^{\text{non-update}}$ while the rest of the problem domain is an update region Ω_c^{update}

$$\bar{\phi}^n(x,y,z) = \left(x - x_{\text{ep}}^n\right)\frac{T_x^{n+1}}{\|T^{n+1}\|} + \left(y - y_{\text{ep}}^n\right)\frac{T_y^{n+1}}{\|T^{n+1}\|} + \left(z - z_{\text{ep}}^n\right)\frac{T_z^{n+1}}{\|T^{n+1}\|} \text{ in } \Omega \tag{6}$$

(b) Following changes in the cutting direction, the values of function ψ^{n+1} of the nodes and integration points in the update region Ω_c^{update} are re-computed while no re-computation is needed in the non-update region

$$\psi^{n+1} = \psi^n \text{in } \Omega_c^{\text{non-update}} \tag{7}$$

$$\psi^{n+1}(x,y,z) = \left(x - x_{\text{ep}}^{n+1}\right)\frac{K_x^{n+1}}{\|K^{n+1}\|} + \left(y - y_{\text{ep}}^{n+1}\right)\frac{K_y^{n+1}}{\|K^{n+1}\|} + \left(z - z_{\text{ep}}^{n+1}\right)\frac{K_z^{n+1}}{\|K^{n+1}\|} \text{ in } \Omega_c^{\text{update}} \tag{8}$$

(c) Re-computation of function ϕ^{n+1} is conducted in the entire analysed space

$$\phi^{n+1}(x,y,z) = \left(x - x_{\text{ep}}^{n+1}\right)\frac{T_x^{n+1}}{\|T^{n+1}\|} + \left(y - y_{\text{ep}}^{n+1}\right)\frac{T_y^{n+1}}{\|T^{n+1}\|} + \left(z - z_{\text{ep}}^{n+1}\right)\frac{T_z^{n+1}}{\|T^{n+1}\|} \text{in } \Omega \tag{9}$$

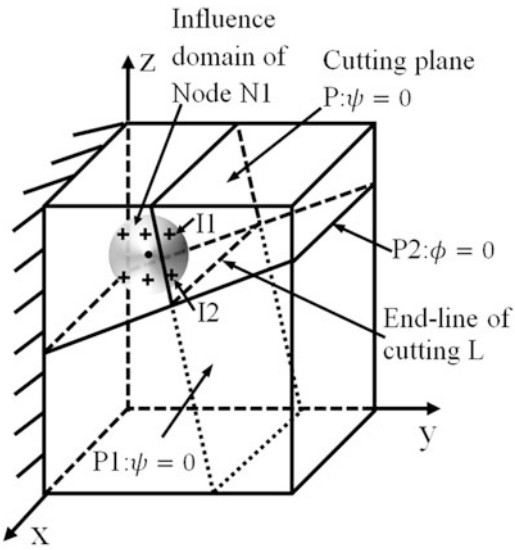

Fig. 5 The influence domain of node N1 intersects the cutting plane P; points I1 and I2 should be eliminated from the influence domain of this node

2.2.4 Update of Influence Domains During Progressing Cutting

The update of the influence domains of every node in the vicinity of the cutting faces is implemented by finding and eliminating the points that are no longer influenced by the node due to the cutting path. In the following algorithm, ψ_i and ϕ_i denote the values of the level set functions ψ and ϕ at node i while ψ_{pt} and ϕ_{pt} denote the values of level set functions ψ and ϕ at an integration point/node in the influence domain of node i.

1. The influence domain of a node, which is defined as a sphere in our algorithm, is updated if it intersects the cutting path (Fig. 5). The selection criterion for the node whose influence domain needs to be updated is

$$|\psi_i| \leq R_i \quad \text{AND} \quad \phi_i < R_i \tag{10}$$

   where R_i is the size (radius) of the influence domain of node i.
2. If the point and the node are located at the opposite sides of the cutting faces and the line segment linking the node and the point intersects the cutting plane (Fig. 5),

$$\psi_i \times \psi_{\text{pt}} < 0 \quad \text{AND} \quad \phi_{\text{pt}} < -\phi_i \times \left| \frac{\psi_{\text{pt}}}{\psi_i} \right| \tag{11}$$

   the point is removed from the influence domain of the node. Otherwise, the node remains to be the supporting node of the point for interpolation.

3. The following updates are made to account for the changes in influence domains:
   - For the points that are eliminated from the influence domains of the nodes, the shape functions and their derivatives are re-calculated.
   - The global 3D mass matrix is updated.

3 Numerical Results and Algorithm Verification

3.1 Numerical Experiment

The large deformation preceding cutting is simulated by the elongation of a cube ($0.1 \times 0.1 \times 0.1\,\text{m}$). One face of the cube (at $y = 0\,\text{m}$) is rigidly constrained in x,y,z axes directions. The opposite face (at $y = 0.1\,\text{m}$) is elongated by 20% of the initial length along y axis while the displacements in x and z axis direction are constrained. The cube is spatially discretised into nodes to create the computational grid for meshless algorithm. The soft tissue-like material property of the specimen is modelled as soft and nearly incompressible continuum using Neo-Hookean material model (Young's modulus $= 3,000\,\text{Pa}$, Poisson's ratio $= 0.49$, mass density $= 1,000\,\text{kg/m}^3$) that approximates the mechanical response of brain tissue [2]. Cutting is conducted in the deformed soft tissue-like specimen via three sequential steps with arbitrary direction as shown in Fig. 6a, b, and c respectively. The strain energy, the reaction force at the rigidly constrained face of the specimen, and the nodal displacements are predicted at every stage of the simulation.

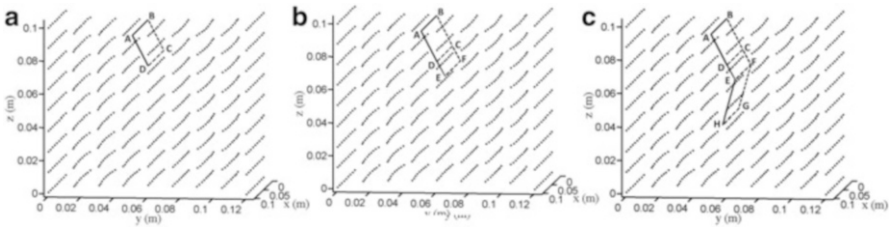

Fig. 6 Model for verification of the MTLADR 3D cutting algorithm (shown using 729 nodes for discretisation). Cutting is carried out in the stretched specimen of soft tissue-like material along the pre-defined path shown using thick line segments. (**a**) The first cutting plane ABCD: A(0.0953,0.05,0.095), B(0.0047,0.05,0.095), C(0.005,0.06,0.077) and D(0.095,0.06,0.077). Cutting starts with arbitrary angle; (**b**) The second cutting plane CDEF: E(0.095,0.065,0.068) and F(0.005,0.065,0.068). Cutting progresses without direction change; (**c**) The third cutting plane EFGH: G(0.0053,0.058,0.041) and H(0.095,0.058,0.041). Cutting progresses with direction change. Dimensions are in meters (m)

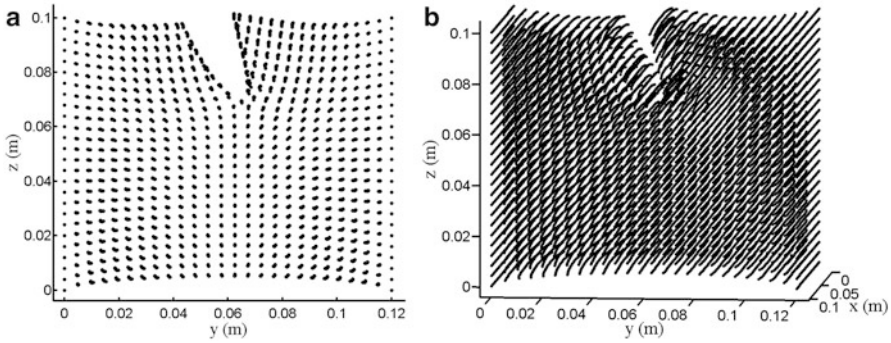

Fig. 7 The deformed model of the 3D specimen of soft tissue-like material before the change of cutting direction obtained using the MTLADR 3D cutting algorithm (converged solution shown using 17,576 nodes): (**a**) the projection of the deformed model on the YOZ plane; (**b**) 3D view of the deformed model

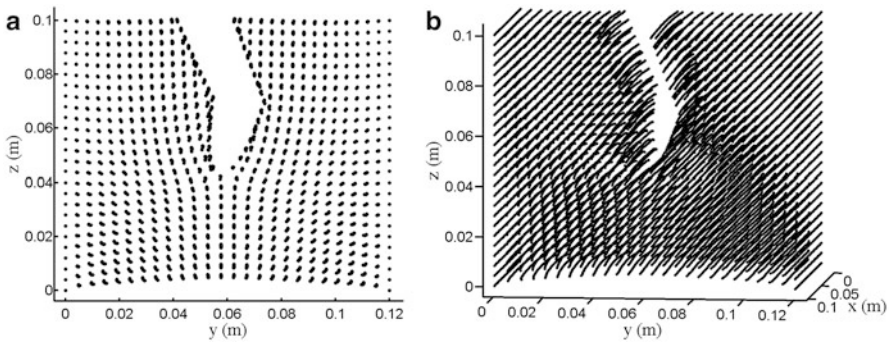

Fig. 8 The deformed model of the 3D specimen of soft tissue-like material at the end of 3-step arbitrarily angled cutting obtained using the MTLADR 3D cutting algorithm: (**a**) the projection of the deformed model on the YOZ plane; (**b**) 3D view of the deformed model

3.2 Numerical Results

Careful convergence studies were conducted. The deformed state of the specimen before the change of cutting direction (converged solution) is shown in Fig. 7. The deformed shape of the specimen at the end of cutting (converged solution), i.e. after the change in cutting direction is introduced, is shown in Fig. 8.

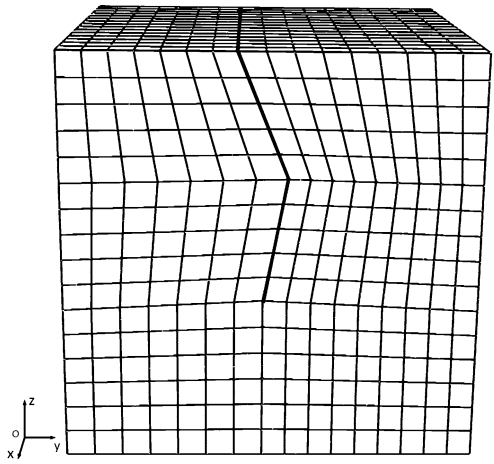

Fig. 9 The mesh of elements of the FE model analysed to obtain the reference solution in Abaqus (18,133 nodes). The edges of the elements were aligned and separated along the pre-cut face, which is shown as *thick line* segments, in order to assure the good aspect ratio of the elements

3.3 Reference Solution for Verification of MTLADR 3D Cutting Algorithm

The results of MTLADR 3D cutting algorithm were verified against the well-tested nonlinear FE analysis procedure available in commercial software Abaqus 6.10–1. As simulation of cutting is not supported by Abaqus, we computed only the deformed configuration of the specimen with pre-introduced discontinuity corresponding to the cutting path (Fig. 9).

3.4 Comparison of MTLADR 3D and Abaqus Solutions

The strain energy, reaction force and nodal displacements obtained using the MTLADR 3D cutting algorithm agree well with the reference solution obtained using the commercial FE solver Abaqus. The relative differences for strain energy and the reaction force between the two methods are 0.34% and 0.29% respectively. To enable verification of the predicted deformations, the nodal displacements obtained using the MTLADR 3D cutting algorithm were re-calculated (through interpolation using the MLS shape functions) for the nodal positions of the Abaqus model. For the nodal displacement magnitudes, the maximum absolute difference between the results obtained using the MTLADR 3D cutting algorithm and Abaqus is 0.78 mm (3.9% of the imposed elongation) and the average difference (averaging over all model nodes) is only 0.039 mm (0.19% of the imposed elongation). The absolute difference at most of the nodal positions (95.76%) is less than 0.1 mm (0.5% of the imposed elongation).

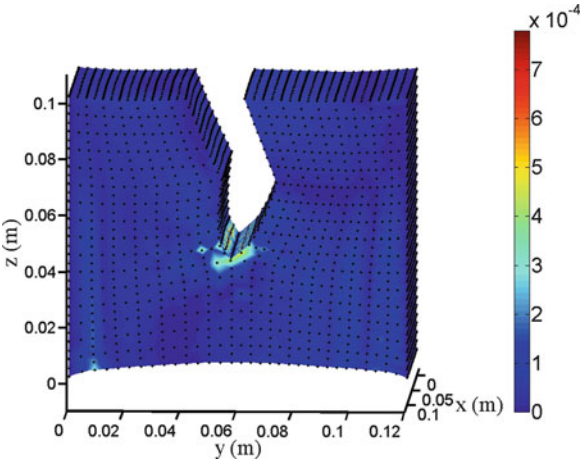

Fig. 10 Verification results for the proposed MTLADR 3D cutting algorithm. Distribution of the absolute differences between the nodal displacement magnitudes computed using the MTLADR 3D cutting algorithm and the reference results from the established nonlinear static solution procedures available in commercial finite element software Abaqus

As shown in the distribution of the absolute differences demonstrated in Fig. 10, the maximum differences are located at the vicinity of the endpoints of the cutting plane while the differences in the other areas are extremely small (well below 0.1 mm). It is probable that the maximum differences may be caused by the deterioration of the finite element solution accuracy caused by mesh distortion at large strains in the vicinity of the endpoints of the cutting plane rather than by our meshless algorithm. Considering that the accuracy of the state-of-the-art image-guided neurosurgery techniques is not better than 1 mm [17], the accuracy of the proposed MTLADR 3D cutting algorithm can be regarded as satisfying the requirements of computer-integrated surgery.

4 Discussion and Conclusions

We developed the MTLADR 3D cutting algorithm, which belongs to the EFG family, to predict the steady-state responses of soft tissue at any stage of surgical cutting in 3D. The algorithm is capable of modelling both large deformations and nonlinear material properties of soft tissues that are necessary in simulating surgery. Since the spatial discretisation is in a form of a cloud of nodes, the burdensome mesh generation and re-meshing in 3D required by the FE method are effectively alleviated. The application of TL formulation eliminates the accumulation of errors due to the reference frame update that occurs in UL formulation, which is typically utilised in commercial FE codes. The privilege of pre-computing the shape functions and their spatial derivatives greatly reduces the number of numerical operations as compared to UL formulation. Furthermore, the strategy of dynamic relaxation offers excellent performance in terms of computation speed while preserving good

accuracy by controlling errors using stringent convergence criteria. These features make our MTLADR method faster than FEM using tetrahedra.

The trajectory of cutting in 3D is geometrically represented as a series of cutting planes. The cutting-induced discontinuity is modelled by creating a pair of nodes at each discretised position of the cutting faces and introducing one node at each discretised position of the end-line of the cutting. The nodes of each nodal pair on the cutting faces are allocated to the opposite sides of the cutting path by using specific level set values. For explicit time integration, the field variable values at these nodes (i.e. the nodal displacements at the current and previous time step and the size of the influence domain) are either inherited or interpolated (using MLS shape functions) from the surrounding nodes. The effect of the cutting in the deformation of the continuum is modelled solely through the changes in the nodal domains of influence, which is effected through the efficient implementation of the visibility criterion using the level set method.

The accuracy of the proposed MTLADR 3D cutting algorithm is verified against the well-established nonlinear solution procedures available in the commercial finite element software Abaqus. Numerical experiments were carried out to predict the behaviour of a deformed (stretched) specimen of soft tissue-like material during surgical cutting in 3D. The computed strain energy, reaction force, and the nodal displacements agree very well with the reference solution obtained using the nonlinear static solution procedures in Abaqus.

The key factor determining the computational cost of the proposed MTLADR 3D cutting algorithm is the number of iterations associated with dynamic relaxation rather than modelling of cuts through the visibility criterion and level set method. We have already completed a prototype implementation of the dynamic relaxation part of our 3D cutting algorithm on graphics processing unit (GPU) (from within Matlab) and achieved more than two orders of magnitude improvement in computational speed in comparison with the Matlab implementation on CPU alone. We are confident that our approach is sufficiently computationally efficient to offer the prospect of surgical simulation within the time constraints of the operating theatre.

Acknowledgements The first author was supported by William & Marlene Schrader Postgraduate Scholarship. The financial support of the Australian Research Council (Discovery Grants No DP1092893 and DP120100402) and the National Health and Medical Research Council (Grant No. APP1006031) is gratefully acknowledged.

References

1. Fung, Y.C.: Biomechanics: Mechanical Properties of Living Tissues. Springer, New York (1993)
2. Miller, K., Chinzei, K., Orssengo, G., Bednarz, P.: Mechanical properties of brain tissue in-vivo: experiment and computer simulation. J. Biomech. **33**, 1369–1376 (2000)

3. Wittek, A., Dutta-Roy, T., Taylor, Z., Horton, A., Washio, T., Chinzei, K., Miller, K.: Subject-specific non-linear biomechanical model of needle insertion into brain. Comput. Meth. Biomech. Biomed. Eng. **11**, 135–146 (2008)
4. Mor, A.B.: Progressive Cutting with Minimal New Element Creation of Soft Tissue Models for Interactive Surgical Simulation. Carnegie Mellon University, Pittsburgh (2001)
5. Bruyns, C.D., Senger, S., Menon, A., Montgomery, K., Wildermuth, S., Boyle, R.: A survey of interactive mesh-cutting techniques and a new method for implementing generalized interactive mesh-cutting using virtual tools. J. Visualization Comput. Anim. **13**, 21–42 (2002)
6. Bielser, D., Glardon, P., Teschner, M., Gross, M.: A state machine for real-time cutting of tetrahedral meshes. Graph. Model. **66**, 398–417 (2004)
7. Courtecuisse, H., Jung, H., Allard, J., Duriez, C.: GPU-based real-time soft tissue deformation with cutting and haptic feedback. Prog. Biophys. Mol. Biol. **103**, 159–168 (2010)
8. Belytschko, T., Tabbara, M.: Dynamic fracture using element-free Galerkin methods. Int. J. Numer. Meth. Eng. **39**, 923–938 (1996)
9. Cotin, S., Delingette, H., Ayache, N.: A hybrid elastic model for real-time cutting, deformations, and force feedback for surgery training and simulation. Vis. Comput. **16**, 437–452 (2000)
10. Wu, W., Heng, P.A.: An improved scheme of an interactive finite element model for 3D soft-tissue cutting and deformation. Vis. Comput. **21**, 707–716 (2005)
11. Jin, X., Joldes, G.R., Miller, K., Yang, K.H., Wittek, A.: Meshless algorithm for soft tissue cutting in surgical simulation. Comput. Meth. Biomech. Biomed. Eng. 12 pages (in press) (2012)
12. Underwood, P.: Dynamic relaxation. In: Belytschko, T., Hughes, T.J.R. (eds.) Computational Methods for Transient Analysis, pp. 245–265. Elsevier Science Publishers B. V., Amsterdam, the Netherlands (1983)
13. Joldes, G.R., Wittek, A., Miller, K.: An adaptive dynamic relaxation method for solving nonlinear finite element problems. Application to brain shift estimation. Int. J. Numer. Meth. Biomed. Eng. **27**, 173–185 (2011)
14. Joldes, G.R., Wittek, A., Miller, K.: Computation of intra-operative brain shift using dynamic relaxation. Comput. Meth. Appl. Mech. Eng. **198**, 3313–3320 (2009)
15. Osher, S., Sethian, J.A.: Fronts propagating with curvature-dependent speed: Algorithms based on Hamilton-Jacobi formulations. J. Comput. Phys. **79**, 12–49 (1988)
16. Stolarska, M., Chopp, D.L., Moes, N., Belytschko, T.: Modelling crack growth by level sets in the extended finite element method. Int. J. Numer. Meth. Eng. **51**, 943–960 (2001)
17. Bucholz, R., MacNeil, W., McDurmont, L.: The operating room of the future. Clin. Neurosurg. **51**, 228–237 (2004)

Simulation of Congenital Heart Defect Corrective Surgeries Using Thin Shell Elements

Stefan Kislinskiy, Tomáš Golembiovský, Christian Duriez, Eugénie Riesenkampff, Titus Kuehne, Hans-Peter Meinzer, and Tobias Heimann

Abstract Congenital heart defect (CHD) corrective interventions in infants are extremely challenging due to commonly complex and heterogeneous disease patterns. At present, cardiac surgeons can only rely on non-invasive imaging prior to surgery. Critical decisions regarding the surgical procedure of choice and its execution must be made during the actual surgery and are strongly dependent on experience. We want to improve surgery planning by providing a simulation system that is able to accurately predict patient-specific results for different surgical procedures preoperatively. Therefore we use a sophisticated simulation model based on thin shell elements. We present a novel joining approach that allows for implementing all necessary surgical low-level procedures, e.g. incising and suturing, independent from the simulation model. No modifications of previously verified thin shell implementations are necessary, thus our simulation system can

S. Kislinskiy (✉) • H.-P. Meinzer
German Cancer Research Center (DKFZ), Heidelberg, Germany
e-mail: s.kislinskiy@dkfz.de; h.p.meinzer@dkfz.de

T. Golembiovský
Masaryk University, Brno, Czech Republic

Inria Lille – Nord Europe, Lille, France
e-mail: nyoxi@ics.muni.cz

C. Duriez
Inria Lille – Nord Europe, Lille, France
e-mail: christian.duriez@inria.fr

E. Riesenkampff • T. Kuehne
German Heart Institute Berlin (DHZB), Berlin, Germany
e-mail: riesenkampff@dhzb.de; titus.kuehne@dhzb.de

T. Heimann
German Cancer Research Center (DKFZ), Heidelberg, Germany

Siemens AG, Corporate Technology, Erlangen, Germany
e-mail: tobias.heimann@siemens.com

A. Wittek et al. (eds.), *Computational Biomechanics for Medicine: Models, Algorithms and Implementation*, DOI 10.1007/978-1-4614-6351-1_7,
© Springer Science+Business Media New York 2013

instantaneously benefit from further improved simulation models in the future. By reducing computationally expensive simulations to a minimum during a virtual surgery, we can achieve a fluent workflow for surgeons. However, a specialized mesh resampling algorithm is required to fully utilize our simulation system.

1 Introduction

Surgical interventions in infants with congenitally malformed great arteries and hearts are extremely challenging due to the complex and heterogeneous nature of their disease patterns. Cardiac surgeons rely on non-invasive imaging for patient-specific examination and preoperatively sketch varying surgical procedures. However, the most promising approach is often chosen during the actual open-heart surgery, when surgeons get a more concrete idea of possible outcomes for different surgical procedures. Finalizing this decision during an on-pump cardiac surgery is further complicated by deflated blood vessels since it is difficult to imagine their exact change of shape caused by the intervention. Accordingly, important decisions have to be made in very short time and are strongly dependent on the surgeon's experience.

Planning of pediatric cardiac surgeries can be improved by using three-dimensional heart models based on patient-specific image data as input for surgical simulation systems. Most present simulation systems focus on execution of low-level surgical procedures, e.g. incising and suturing [1, 2]. In these reactive simulation systems it is more important to enable simulations in real time than accurate simulation of tissue and blood vessel deformation in response to simulated interventions.

To be able to predict results of complex surgical procedures a physically more sophisticated simulation is necessary. In [3], a predictive surgical simulation system for bidirectional Glenn shunts and similar surgeries is presented. The authors use a hybrid model to simulate deformations of blood vessels by elastically binding surface meshes to reference Cosserat rods. Although the results are promising, the method is limited to operations on uniform tubular structures and does not allow for arbitrary manipulations of the surface meshes. Suturing of blood vessel walls and patches is accomplished by attaching infinitely contracting springs to split meshes. However, these infinite contraction forces break fundamental physical laws and equations of the simulation model have to be modified accordingly to be able to deal with surplus energy that arises during infinite spring contraction.

In this paper we introduce a novel method for predictive simulation of congenital heart defect (CHD) corrective surgeries which is based on elastic thin shell elements and allows for joining of meshes without using springs. A specific relaxation process during simulation enables our approach to be completely independent from a concrete thin shell elements implementation, i.e. no additional constraints are introduced to the underlying equations. By using SOFA [4], a modular medical simulation framework, we can greatly benefit from this independence as the simulation model can be quickly replaced without any adaption.

2 Methods

Finite element methods (FEM) are a well-known tool for physically accurate simulations of deformable bodies [5]. Shell elements are two-dimensional finite elements with a certain thickness specified as parameter of the simulation. While they are naturally well suited for simulation of blood vessel walls and are computationally less expensive than volumetric elements, their computational expense is still higher compared to simple mass-spring methods. However, we achieve a fluent workflow of the surgical planning by reducing the actual simulation to a minimum—instead of executing surgical low-level procedures during simulation, surgeons specify essential properties of the next task before the actual simulation, i.e. both incising and suturing are treated as purely topological manipulations and only induced deformations must be simulated. Complex interventions are simulated by consecutive simulation runs while interactions by surgeons occur in between.

Since our method is independent from a concrete simulation model we only provide essential information of our model of choice in the next subsection for the sake of completeness. In-depth descriptions can be found in the referenced literature, i.e. [6,7]. The novel joining approach for meshes, which can be separated into rest shape mapping prior to simulation and rest shape relaxation during simulation, is described subsequently and its limitations regarding possibly necessary mesh preprocessing conclude this section. The whole process is depicted in Fig. 1.

2.1 Thin Shell Elements

Shell elements (see Fig. 2) combine forces from in-plane deformations, i.e. stretching and shearing, with bending forces. These internal forces $\mathbf{f}$ are a function of current displacement measured as difference of the current element shape $\mathbf{x}$ to its rest shape $\mathbf{x}_0$.

We accelerate computation by using a corotational formulation that is based on the definition of local frames for each element. In these local frames computation of internal forces is linear:

$$\mathbf{f} = \mathbf{K}_\mathrm{e} \left(\mathbf{x} - \mathbf{x}_0 \right)$$

where $\mathbf{K}_\mathrm{e}$ is the stiffness matrix of the shell element computed by Kirchhoff–Love's equations. This approach is similar to the model presented in [6, 7].

During assembly of simulation meshes, contributions of each shell element are computed in a global frame using different rotation matrices $\mathbf{R}_\mathrm{e}$ for each element:

$$\mathbb{K} = A_{\mathrm{e}=0}^{N} \left(\mathbf{R}_\mathrm{e}^\mathrm{T} \mathbf{K}_\mathrm{e} \mathbf{R}_\mathrm{e} \right)$$

$$\mathbb{F} = A_{\mathrm{e}=0}^{N} \left(\mathbf{R}_\mathrm{e}^\mathrm{T} \mathbf{K}_\mathrm{e} \left(\mathbf{x} - \mathbf{x}_0 \right) \right)$$

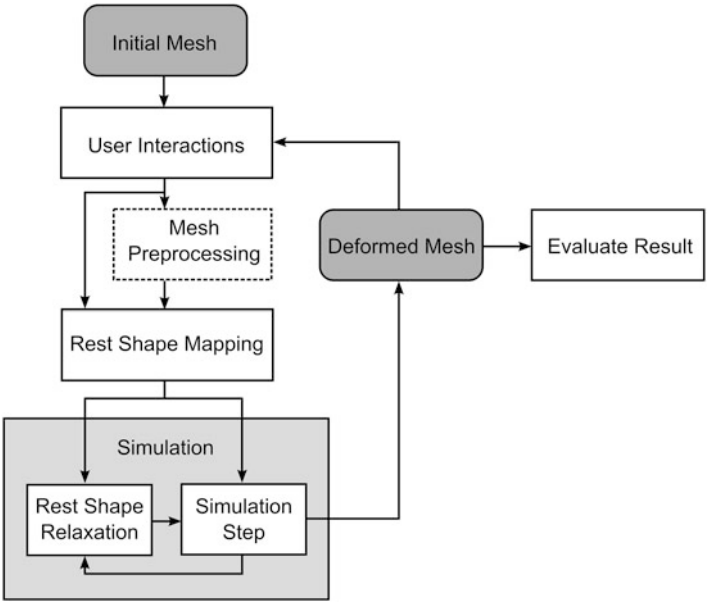

Fig. 1 The complete simulation process. Surgeons interact with the mesh prior to simulation by specifying new incisions and edges they wish to join. Especially in case of low shell element count the mesh may be preprocessed to refine and align its vertices along new incisions. Before the actual simulation can start our joining approach requires creation of a rest shape mapping. During simulation, rest shape relaxation is executed in between simulation steps to join split meshes. The deformed mesh may be further manipulated by the surgeon or evaluated in case the simulated surgical procedure is complete

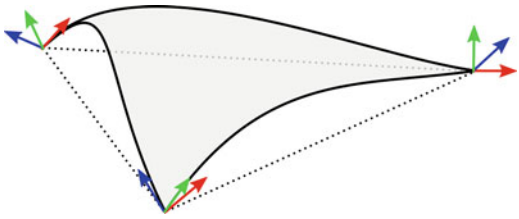

Fig. 2 A thin shell element. At each of its 3 nodes 6 degrees of freedom are defined (3 translations, 3 rotations). The shape function of the element allow for smooth interpolation of surface behavior. Shell elements can be bent, twisted, compressed, and stretched

where A is the assembling operator over N elements, $\mathbb{K}$ is the global stiffness and $\mathbb{F}$ the internal forces of the entire shell element mesh structure. Computation of shell element node motion $\mathbb{U} = \mathbb{K}^{-1}\mathbb{F}$ is performed using a conjugate gradient algorithm.

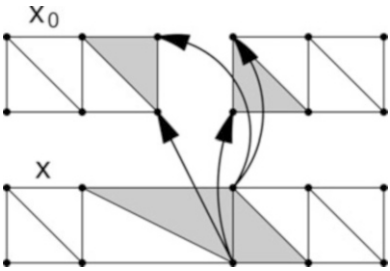

Fig. 3 Creation of a topologically joined initial shape x and the mapping to its rest shape $\mathbf{x}_0$ it originates from. The mapping of vertices along the joined edge is explicitly indicated by *arrows*

2.2 Rest Shape Mapping Prior to Simulation

We topologically connect the rest shape $\mathbf{x}_0$ of an object prior to simulation by joining its vertices along split edges. This connected mesh defines the initial shape $\mathbf{x}$ of the simulated object and has fewer vertices as well as a different topology than rest shape $\mathbf{x}_0$. Consequently, the 1:*n*-vertex-mapping needs to be preserved so that adjacent mesh faces which share a vertex can still refer to their distinct vertices of rest shape $\mathbf{x}_0$.

The creation of an initial shape $\mathbf{x}$ and the mapping to its rest shape $\mathbf{x}_0$ is shown in Fig. 3. For clarity reasons, it represents a minimal scenario (the same concept can be applied to arbitrarily complex real-world scenarios), where two two-dimensional elastic stripes are about to be joined. While most of the vertices in the example have a 1:1-mapping, vertices along the split edges have a 1:2-mapping as indicated by arrows in Fig. 3. The shaded shell elements share two vertices in initial shape $\mathbf{x}$ and each of them references two distinct vertices of rest shape $\mathbf{x}_0$.

2.3 Rest Shape Relaxation during Simulation

Depending on the simulated joining scenario, the simulation starts with a large difference between rest shape $\mathbf{x}_0$ and the initial shape $\mathbf{x}$. This provokes extremely high internal energies and forces in the affected shell elements. To prevent excessive deformation and numerical instabilities we create a second rest shape $\mathbf{y}_0$ which is congruent to the initial shape $\mathbf{x}$ but still has split edges. During simulation we linearly interpolate differing shell element node positions between rest shape $\mathbf{y}_0$ and the original rest shape $\mathbf{x}_0$. Orientations of affected shell element nodes are aligned by spherical linear interpolation (Slerp). As soon as rest shape $\mathbf{x}_0$ is reached the simulation is in a state where the actual joining is complete and continues until the resulting deformation is complete as well.

The example of Fig. 3 is continued in Fig. 4 to visualize the relaxation process during simulation. The opposite sides of the elastic stripes are fixed so that stretching will occur during simulation. Rest shape and shape of the simulated objects are shown side-by-side for three time steps t_0 to t_2. At time t_0, which represents the very

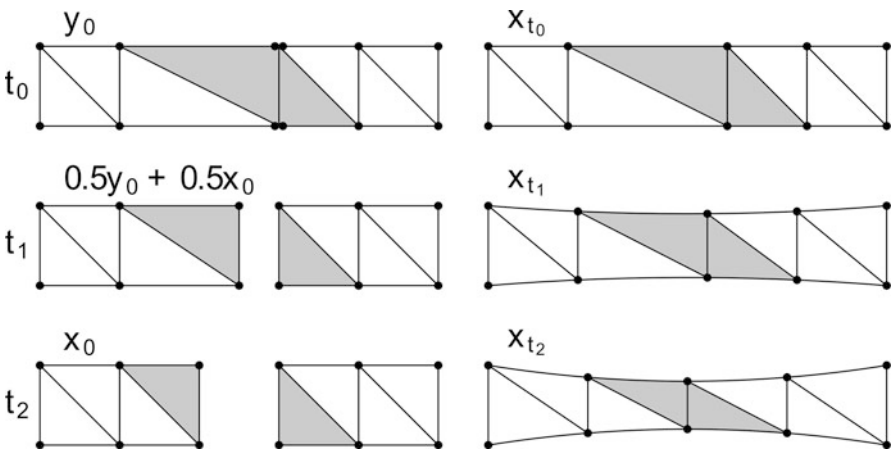

Fig. 4 Current rest shape (*left*) and actual shape (*right*) are displayed for three time steps t_1 to t_2 of the simulation. The stripes are fixed at their opposite ends

beginning of the simulation, the current rest shape equals $\mathbf{y}_0$. It is spatially congruent to shape $\mathbf{x}_{t0}$ but differs in topology (this is emphasized in Fig. 4 by contiguous dots at the split edge). At time t_1 the relaxation of the initial rest shape $\mathbf{y}_0$ towards the original rest shape $\mathbf{x}_0$ is halfway through. Accordingly, the current rest shape is equally interpolated between rest shapes $\mathbf{y}_0$ and $\mathbf{x}_0$. Shape $\mathbf{x}_{t1}$ converges to its energy equilibrium since it differs spatially from the current rest shape. At time steps t_0 and t_1, shapes $\mathbf{x}_{t0}$ and $\mathbf{x}_{t1}$ temporarily have no correlation with reality in which the shape would still be split. However, at time t_2, when the relaxation process is finished, the joining is truly complete.

Both rest shape mapping and relaxation can be directly applied to arbitrary complex scenarios. Figure 5 demonstrates the concept during a patch aortoplasty, where a patch is used to widen a coarctation of a blood vessel. While this example is still readily comprehensible, a real world pre-post comparison of a patch aortoplasty is included in Fig. 7 besides a subclavian flap aortoplasty and an end-to-end anastomosis. All former examples have in common that the joining requires only a 1:2-mapping. However, our mapping is defined as a 1:*n*-mapping which allows to combine multiple surgical tasks in a single simulation run. This capability is especially advantageous in case of overlapping incisions which are about to be sutured. Figure 6 shows such a scenario during an end-to-end anastomosis, where one of the blood vessels is widened by a patch to fit the other circumference.

2.4 Mesh Preprocessing

As our joining method is solely based on vertices there are important restrictions. On both sides of an incision or edges that are about to be joined there must be the

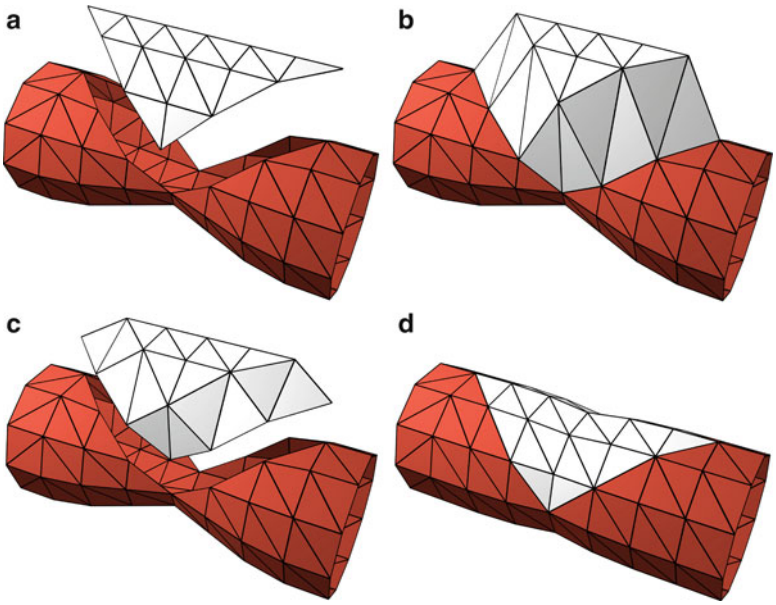

Fig. 5 Joining during a patch aortoplasty. The size of the applied patch is larger than the removed piece of vessel wall to widen the coarctation. (**a**) rest shape $\mathbf{x}_0$, (**b**) initial shape $\mathbf{x}$/rest shape $\mathbf{y}_0$ (split edges), (**c**) rest shape during relaxation process, (**d**) final shape after simulation

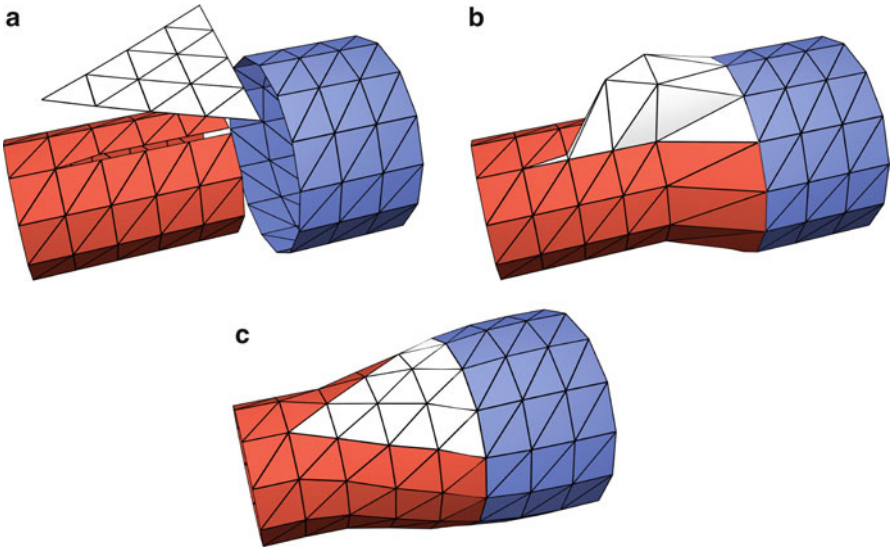

Fig. 6 Joining during an end-to-end anastomosis. The circumference of one blood vessel must be widened by a triangular patch. Vertices that are shared between both blood vessels and the patch have a 1:3-mapping to the rest shape: (**a**) rest shape $\mathbf{x}_0$, (**b**) initial shape $\mathbf{x}$/rest shape $\mathbf{y}_0$ (split edges), (**c**) final shape after simulation

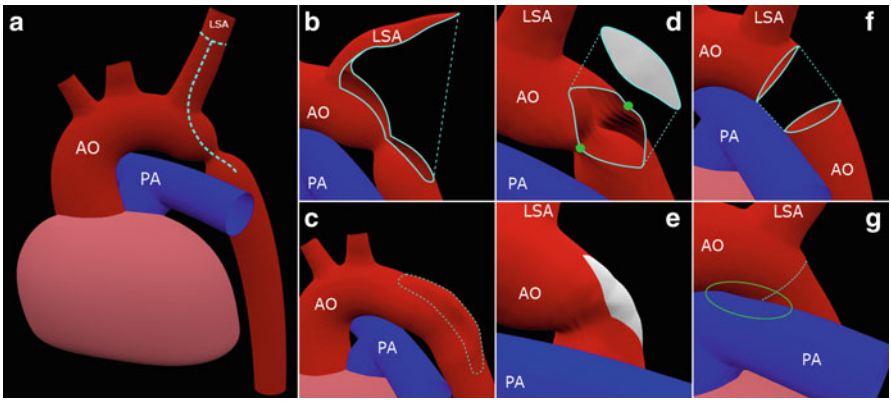

Fig. 7 Screenshots of our simulation system prototype for different surgical procedures used to repair a coarctation of an aortic arch. For all scenarios our novel joining approach was used. The screenshots are enriched with overlay delineations for clarification. (**a**) Overview of the simulation scene consisting of an aortic arch (AO), the left subclavian artery (LSA) and the pulmonary artery (PA). The coarctation can be seen next to the LSA and the *dashed line* indicates where the aorta will be incised for a subclavian flap aortoplasty. The vertical image pairs display the scene before and after different surgical interventions. (**b, c**) Subclavian flap aortoplasty: the subclavian flap is used as an organic patch to widen the coarctation. (**d, e**) Patch aortoplasty: a patch is sutured into an incision along the coarctation. The *green dots* represent springs that were attached to widen the incision for visualization purposes. (**f, g**) End-to-end anastomosis: the coarctation is resected and the loose ends of the AO are sutured together. Due to deformation of the AO it slightly collides (we utilize the default collision model of the SOFA framework based on Coulomb frictional Signorini contact mechanics to emphasize straightforward combinability of our method with other simulation components due to its independence from a concrete simulation model) with the PA which causes additional deformations on both blood vessels

same amount of vertices. To prevent artificial stretching and compression forces along individual joining edges, vertices should be aligned so that all edge pairs have similar length each. These constraints have major impact on the resampling of meshes. It is well known that the convergence of FEM greatly depends on the quality of the mesh, e. g. regularity of element extent and neighborhood. All these restrictions combined with the requirement of minimizing element count while keeping simulations accurate is a challenging task. The additional requirements originating from our joining approach for a mesh resampling algorithm can be summarized as follows:

- Local alignment of elements along prespecified lines, e.g. incisions.
- Usage of locally prespecified fixed vertices, e.g. along joining edges.

While these constraints are hard constraints at their exact locations, there must be smooth transitions of element alignment and size between them to still produce high quality simulation meshes. For our simulation system prototype (see Fig. 7) we currently elude mesh resampling completely by using relatively dense meshes

and by snapping incisions along element edges. Joining is restricted on split edges with the same amount of vertices and we provisionally rely on very regular and clean meshes to guarantee similar edge lengths of shell elements along incisions.

3 Results and Discussion

In order to show an improvement on existing simulation systems for CHD corrective surgeries we want to demonstrate that our blood vessel model based on thin shell elements

- physically meets the requirements for predictive simulation results
- converges to these results with a moderate number of elements
- is able to simulate surgical procedures in practice

We close this section with a discussion about the constraints of our method compared to present simulation systems.

3.1 Predictive Simulation Results

A quantitative validation by means of a comparison to real pre- and post-surgery image data is impossible at present. This is mainly due to ethical issues that arise during image acquirement of infants, i.e. necessary heart rate lowering medications or exposure to radiation. To our knowledge there is no image data available that is obtained soon enough after relevant interventions in infants, where the growth of the patient does not interfere comparison. However, a qualitative comparison with real image data acquired months after a surgical intervention, which confirms at least a principal applicability of predictive simulations for surgery planning, can be found in [3].

At present we can only provide a rudimentary qualitative validation shown in Fig. 8, where bending and twisting of an elastic tube manipulated by hand is compared to the simulation results of [3] and our shell model. Both deformations are likely to occur during surgery and our results are visually very close to the real deformations as expected due to the physically formulation of shell elements. Minor differences in shape are probably owed to the lack of knowledge of material properties and thickness of the reference model.

3.2 Convergence of Thin Shell Elements

We set up an evaluation for the convergence of shell elements for large deformations of blood vessels in order to gather valuable hints for reasonable mesh resampling

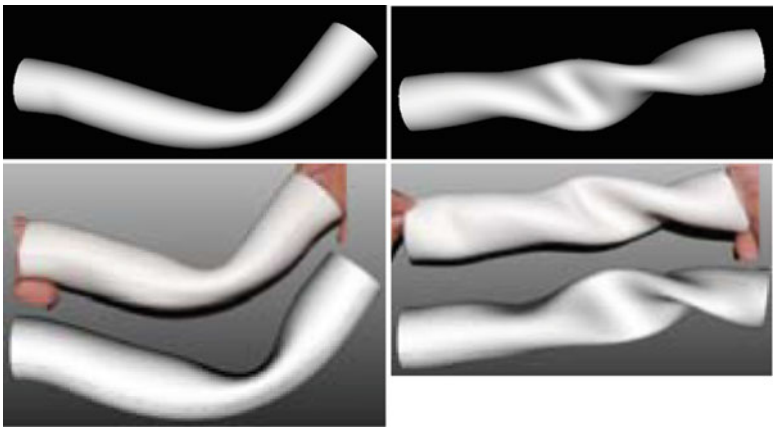

Fig. 8 Simulation of bending and twisting of an elastic tube. *Top row*: Our thin shell element model. *Bottom row*: Real elastic tube manipulated by hand and Cosserat rod based hybrid model [3] (credits for the bottom images: Li et al.)

while keeping appropriate simulation accuracy (see Fig. 9). Therefore we simulated the same deformation on the same mesh sampled at different levels of detail and measured the Hausdorff distance between them. We continuously increased the element count during mesh sampling until the Hausdorff distance between simulation results was negligible. This simulation result was taken as reference and all Hausdorff distances were finally computed against it. To minimize the measuring error we mapped each simulation result to the same dense mesh which in turn was used for comparison.

Although the results of the evaluation can only be used to illustrate tendencies, it is remarkable that despite the large deformation its shape is preserved very well even for a reduction of the shell element count to 25 % of the reference. While the mean distance is generally low, the maximal distances always occur at locally high curvature, which is expected behavior since the high rate of change in curvature cannot be mapped by the shape functions of relatively large shell elements. This effect can be clearly seen in Fig. 9d.

3.3 Simulation of Virtual Surgeries in Practice

As mentioned in Sect. 2.4 we implemented a basic prototype of our simulation system which is shown in Fig. 7 for different surgical procedures. While its usability is restricted due to a missing mesh resampling algorithm, it is convenient for a proof of concept. We created a three-dimensional model of a malformed aortic arch based on real image data and simulated three fundamentally different surgical approaches to repair the coarctation. Especially the subclavian flap aortoplasty is a complex

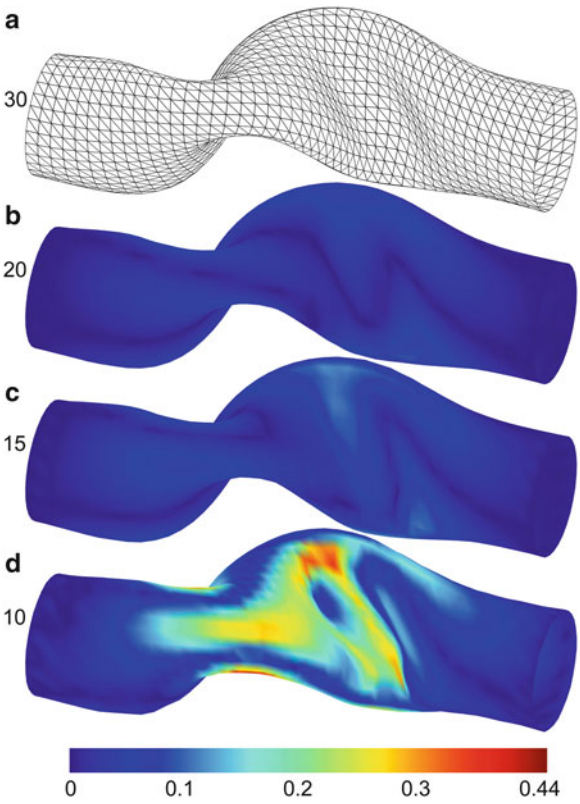

Fig. 9 Hausdorff distances between a deformed reference tube with 30 vertices along its circumference and meshes with lower levels of detail: (**b**) 20, (**c**) 15, (**d**) 10 vertices. Relative shell element count: (**a**) 100 %, (**b**) 44 %, (**c**) 25 %, (**d**) 11 %. The tube has radius 10 mm, length 100 mm, shell thickness 2 mm, Young's modulus 2 MPa, and Poisson's ratio 0.5

intervention which heavily changes topology. However, it makes no difference for our novel joining approach which is universally applicable for arbitrarily split meshes.

3.4 Limitations

Although our novel joining method can be universally used for joining of arbitrarily split meshes, it enforces special requirements on a suitable mesh resampling algorithm (see Sect. 2.4). However, simulation systems based on joining by contracting springs must include mesh resampling as well in case a surgeon wants to continue an intervention after joining, whereas there are no additional constraints for the resampling.

Regarding the speed of shell element-based simulations we observed an inversely proportional dependency to the shell element count. At approximately 1,000 shell elements, simulation time of our reference implementation elapses faster than

real time on average consumer-level hardware. Considering our observations of convergence in Sect. 3.2, a fast yet predictive simulation system should be feasible with today's hardware and an optimized implementation of a shell element model.

4 Conclusion

We presented a modular and independent method for joining meshes in the context of an efficient surgical simulation system for CHD corrective surgeries. There are two major advantages of our approach: Firstly, simulations of virtual surgeries are accelerated despite the usage of a sophisticated simulation model which enables a fluent workflow for surgeons. Secondly, the loose coupling between low-level surgical procedures and the simulation model allows for instantaneous utilization of alternative or newly developed and improved shell element implementations in the future. Furthermore, the modularity of our method eases its combination with other simulation models, e.g. volumetric finite element models for heart simulations, especially in the environment of SOFA, an open source framework for medical simulations. However, our simulation system can only be fully utilized in case a specialized mesh resampling algorithm is provided. Development of such an algorithm is consequently the next step towards applicability of our methods in clinical workflow.

References

1. Mosegaard, J.: LR-spring mass model for cardiac surgical simulation. MMVR 256–258 (2004)
2. Sørensen, T.S., Greil, G.F., Hansen, O.K., Mosegaard, J.: Surgical simulation – a new tool to evaluate surgical incisions in congenital heart disease? Interact. CardioVasc. Thorac. Surg. **5**, 536–539 (2006)
3. Li, H., Leow, W.K., Chiu, I.S.: Predictive simulation of bidirectional Glenn shunt using a hybrid blood vessel model. MICCAI **5762**, 266–274 (2009)
4. Allard, J., Cotin, S., Faure, F., Bensoussan, P.J., Poyer, F., Duriez, C., Delingette, H., Grisoni, L.: SOFA – an open source framework for medical simulation. MMVR **15** (2007)
5. Reddy, J.N.: Introduction to the Finite Element Method. McGraw-Hill, New York (1993)
6. Comas, O., Cotin, S., Duriez, S.: A shell model for real-time simulation of intraocular implant deployment. Biomed. Simul. **5958**, 160–170 (2010)
7. Comas, O., Duriez, C., Cotin, S.: Shell model for reconstruction and real-time simulation of thin anatomical structures. MICCAI **6362**, 371–379 (2010)

Efficient Suturing of Deformable Models

Georges Younes, Julien abi-Nahed, and George Turkiyyah

Abstract Suturing is a fundamental operation in surgical procedures. Simulation of suturing involves the simulation of needle–tissue and thread–tissue interaction, as well as contact between sutured boundaries. In this work, robust methods are proposed for an efficient finite element-based suture simulation. Contact conditions are modeled using complementarity relations. By exploiting adjacency relationships inherent to simplicial meshes and decomposing rigid body motion into sliding and bulk-deforming components, needle driving can be simulated in real time without introducing any new mesh elements. In addition, a computationally efficient formulation of thread pulling is presented. These techniques are implemented and tested in a prototype system which allows for interactive simulation of suturing with high resolution models.

1 Introduction

Suturing is a fundamental operation in surgical procedures. It is an ever-present task in procedures ranging from the closing of lacerations and stitching of wounds in open surgery, to anastomosis and closing of incisions after tissue removal in laparoscopic and robotic-assisted procedures. The techniques for planning suturing

G. Younes (✉)
Department of Computer Science, American University of Beirut, Beirut, Lebanon

Qatar Robotic Surgery Centre, Qatar Science & Technology Park, Qatar Foundation, Doha, Qatar

J. abi-Nahed
Qatar Robotic Surgery Centre, Qatar Science & Technology Park, Qatar Foundation, Doha, Qatar

G. Turkiyyah
Department of Computer Science, American University of Beirut, Beirut, Lebanon

A. Wittek et al. (eds.), *Computational Biomechanics for Medicine: Models, Algorithms and Implementation*, DOI 10.1007/978-1-4614-6351-1_8,
© Springer Science+Business Media New York 2013

tasks and the manual dexterity involved in executing them are essential skills that student surgeons and practitioners develop through training and practice. In the context of laparoscopic and robotic-assisted surgery, with their constrained workspace due to instrument kinematics, this practice often has a steep learning curve, and it takes a substantial amount of training to perfect the necessary skills. The practice generally takes place on suturing boards, phantom models, or live animals (w/o on), but there has been significant interest in the use of simulation-based training tools because of the flexibility in the training scenarios that the simulators can provide, their convenience, and their ultimate cost-effectiveness.

The development of surgical training simulators and procedure-rehearsal systems requires reliable models for suture simulation that can pass the tests of face and content validity. The importance of this problem has led to a number of efforts for modeling various aspects of the suturing task. In particular, finite element models for needle insertion and steering inside soft tissue have been described in [1, 2]. In these works, node repositioning, additions, and local remeshing are performed in a two-dimensional or three-dimensional volumetric finite element mesh to support the compatible sliding and sticking movements of a needle inside the mesh. Duriez et al. [3] describe a flexible needle insertion model that does not remesh locally but instead uses complementarity constraints to tie points on the needle to the elements of the tissue mesh. This strategy has obvious computational savings and allows realistic biopsy and brachytherapy simulations to be performed. Another set of research efforts [4, 5] has focused on experiments intended to produce realistic in vivo and in vitro values for friction forces, puncture thresholds, and other parameters needed in validated simulations. Contact involving rigid tools and deformable models have been studied in physically based surgical simulations and related haptic environments. Laycock and Day [6] survey some early models that have been proposed for generating contact forces. More recent works have successfully used models involving linear complementarity relations between gaps and reaction forces [7, 8] to handle contact. Methods for collision detection for deformable models have been described in [9, 10].

In the context of suturing simulations, an early work [11] used constraints to model suture closing in a finite element model. A model that uses a spline endowed with a continuum dynamic model and sliding constraints was proposed in [12]. Wittek et al. [13] simulate needle insertion into the brain with high fidelity and precision using a predictive nonlinear biomechanical tissue model that accounts for large deformations, but it is not clear if it can produce haptic rates of interaction for realistic models. Guébert et al. [7] propose a promising simulation based on complementarity constraint modeling of all interactions between surgical threads and the embedding soft tissue. Choi et al. [14] describe a suturing system using the physics available in a commodity physics engine including line springs and chained linear segments. Mass-spring chains have also been proposed for thread modeling. Despite these and related efforts however, there is not yet a satisfactory suturing simulation model that has sufficient realism and interactive response rate, suitable for training medical students and related professionals.

The difficulties of modeling of suturing operations come from a number of factors. An inextensible thread, essentially massless, with almost negligible bending

stiffness is driven by a rigid tool in a highly deformable anatomically complex, heterogeneous, anisotropic soft tissue environment. The topology of the environment is continuously changing because of the needle movement and the general contact conditions between the deforming tissue being sutured as well as between tools, threads, and tissue. These simulations have to be performed in a limited computational budget to allow for interactive use operations that support real-time visual feedback and haptic interaction.

The main contribution of this chapter is a computationally effective model that allows threads to be inserted into neighboring soft tissue volumes and pulled at two points to close an opening in real time and in a mechanically plausible fashion. The model introduces efficient geometric operations to allow needle and thread to traverse multiple boundaries and builds the appropriate constraints to use in a finite element model. We take advantage of the rigid nature of the needle to decompose driving motion into sliding and bulk-deforming components and handle them separately. We also introduce a new thread pulling constraint model and demonstrate it on a realistic example of an anastomosis procedure involving a fine mesh with multiple puncture points.

The rest of this chapter is organized as follows. In Sect. 2 we describe how three-dimensional inter-boundary contact is handled in the context of a finite element model. In Sect. 3, we describe how we model needle driving and puncturing of multiple tissue boundaries. Section 4 presents a thread pulling model, suitable for single stitches as well as running sutures, to close openings between two boundaries. Section 5 shows results and concludes.

2 Interaction Modeling and Contact Handling

In this chapter, deformable models are simulated using a quasi-static finite element model. At every step of the simulation $\mathbf{Kx} = \mathbf{f}$ is solved, where $\mathbf{x}$ is a vector with the geometric positions of the n_0 nodes, $\mathbf{K}$ is a $3n_0 \times 3n_0$ (stiffness) matrix, and $\mathbf{f}$ contains the external forces.

The solution $\mathbf{x}$ can be constrained with the aid of algebraic constraints of the form $\mathbf{C}_i\mathbf{x} = \mathbf{b}_i$. The constraints linearly couple a subset of $\mathbf{x}$ and are solved by augmenting the original system:

$$\begin{bmatrix} \mathbf{K} & \mathbf{C}^t \\ \mathbf{C} & \mathbf{0} \end{bmatrix} \begin{Bmatrix} \mathbf{X} \\ \lambda \end{Bmatrix} = \begin{bmatrix} \mathbf{f} \\ \mathbf{b} \end{bmatrix} \tag{1}$$

where $\mathbf{C} = [\mathbf{C}_0; \mathbf{C}_1; \ldots; \mathbf{C}_m]$ and $\mathbf{b} = [\mathbf{b}_0; \mathbf{b}_1; \ldots; \mathbf{b}_m]$. This system can be solved efficiently by precomputing the Cholesky decomposition of $\mathbf{K}$ at the start of the simulation and reusing it with backward/forward passes and different right-hand sides.

This constraint framework allows us to model complex interactions between the different objects that are being simulated, for example, a vertex v can be fixed at position $\mathbf{v}_0$ by adding a constraint of the form: $g(v) = \mathbf{v}_0$, where $g(s)$ returns the geometric positions of the vertices of a simplex s. In addition, Vertex–

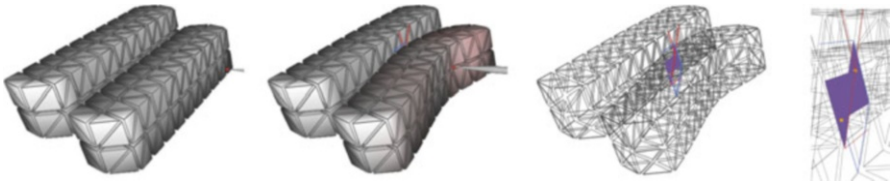

Fig. 1 A sequence of interaction demonstrating the handling of contact. The contact complex is zoomed in the rightmost figure (VF in *orange and purple* EE in *red and blue*)

Face (VF) and Edge–Edge (EE) contact collisions can be handled by properly imposed constraints to prevent interpenetration. A VF contact between a point with barycentric coordinates γ in face f and a vertex v is represented using $g(f) \cdot \gamma = g(v)$ and an EE collision between two points with barycentric coordinates α and β in edges e_0 and e_1, respectively, is represented using $g(e_0) \cdot \alpha = g(e_1) \cdot \beta$. Figure 1 shows an example of contact handling with this formulation.

These constraints are activated and deactivated dynamically based on their Lagrange multipliers. For example, for a VF constraint, the associated Lagrange multipliers represent the force being exerted by the vertex on the face. When the normal component of the multiplier is negative, the corresponding constraint is deactivated. In order to prevent sticking of the two boundaries when they get into contact, the tangential components of the constraints are released to allow tangential movement of the two boundaries with respect to each other using $\hat{\mathbf{n}}_f \cdot g(f) \cdot \gamma = \hat{\mathbf{n}}_f \cdot g(v)$, where $\hat{\mathbf{n}}_f$ is the face normal. A similar equation is used for EE constraints. Note that the coefficients have to be updated at every step because the normal vectors are changing.

3 Needle Driving

In this section we describe the needle–tissue interaction model. The most common types of needles are handled, namely straight and circular. The end goal is to efficiently and robustly simulate the driving of a needle into soft tissue. The different steps of our approach are depicted in Fig. 3.

3.1 Motion Decomposition

Let the positions and orientations of the needle at two successive time steps be denoted by $\mathbf{R}^{[k]}$ and $\mathbf{R}^{[k+1]}$, respectively, and $\mathbf{T}$ be the transformation between them: $\mathbf{R}^{[k+1]} = \mathbf{T}\,\mathbf{R}^{[k]}$. It is convenient to decompose the motion $\mathbf{T}$ into two components: a sliding component where the needle moves along its natural axis with every point moving tangentially along the axis and a normal component where the needle translates and rotates to reach its final position.

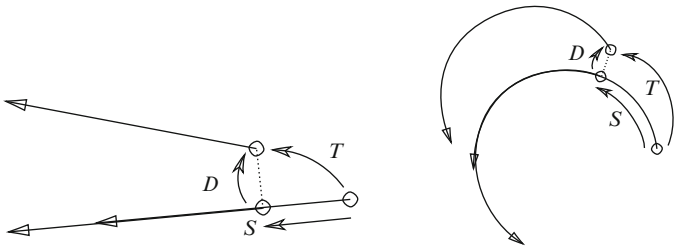

Fig. 2 Decomposition of inter-frame motion into sliding and sticking components

$$\mathbf{R}^{[k+1]} = \mathbf{T}\mathbf{R}^{[k]} = \underbrace{\mathbf{D}}_{\text{sticking}}\ \underbrace{\mathbf{S}}_{\text{sliding}}\ \mathbf{R}^{[k]} \tag{2}$$

These two components are used in updating the displacements and forces in the system in two fractional steps. This decomposition is primarily motivated by the different types of tool–tissue mechanical behavior that take place when the needle displaces in the embedding tissue.

When the needle is sliding in the tissue, it is essentially gliding unimpeded except by the (typically small) dynamic friction forces along its path. The tissue deformation induced is small since it is only caused by the frictional forces tangential to the path. On the other hand, when the needle is sticking to the tissue, its motion causes significant bulk deformation of the embedding tissue. Larger forces are induced because of the strain energy build up in the tissue and these forces are needed to maintain the deformed shape.

Both types of motion take place simultaneously during interaction and it is convenient computationally to divide an update step into a sliding step with minimal (or no) friction and tissue deformation, and a step where the needle sticks to the tissue and deforms it in its motion. While the motion takes place, the haptic forces felt by the user are the resultants of the stresses on the needle due to both the sliding and non-sliding steps. If at any point the needle's motion is halted, the forces felt by the user will be only the resultants of the needle contact stresses due to the non-sliding component. This is essentially a viscous model of the frictional phenomenon.

Note that both factors in the decomposition include rotational as well as translational components. Moreover, the **DS** decomposition of the transformation matrix **T** is not unique. Our decomposition strategy is to define the sliding component to be the transformation that causes the needle to move the closest to its final position (Fig. 2), followed by the transformation that causes bulk deformations.

3.2 Needle Tracking

In what follows, we present a strategy for incrementally tracking the cells intersected by the needle to be able to generate the constraints representing sticking motion later on. The strategy relies on using a list of *history* cells and incrementally updating it

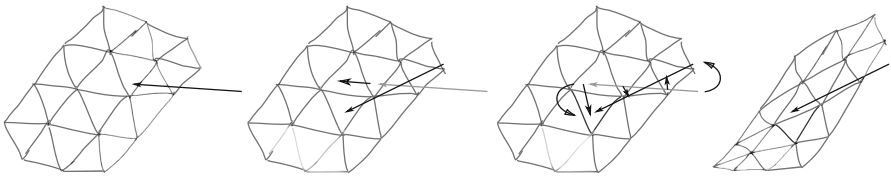

Fig. 3 Example of tracking a straight needle inside a two-dimensional mesh that depicts the general idea behind our proposed approach. Inter-frame needle motion is decomposed into two separate components: sliding (non-deforming) and sticking (deforming), then the needle is slid and its position in the mesh is updated. The new needle position is coupled to the midpoints of the previous cell intersections and the system is solved and updated

using the sliding components and the simplicial adjacency operators provided by the supporting data structure.

The sliding component ($\sigma^{[k]}$), from the inter-frame motion of the needle at step k, is used to incrementally track the position of the needle inside the mesh as it slides. A history of the cells' indices that have been intersected by the needle is saved in a list (Λ) along with the indices of the intersected faces and the barycentric coordinates of their respective intersection points—they are used in imposing needle–tissue interaction constraints. The needle points that correspond to these interaction points are also saved. The entries of Λ are tagged as either active (the needle intersects the corresponding cell) or inactive (there is no intersection).

The first element of Λ always references the cell that contained the tip at the previous step and is used as a starting point when searching for the new location of the tip. The tip is displaced by $\sigma^{[k]}$ and the curve joining its previous and current (slid) position is tested for intersection with the current cell's faces. If there is no intersection, the tip remained in the same cell and only its barycentric coordinates are updated, otherwise, the tip has crossed a face. If the adjacent cell (that shares the same intersected face) is already present in the list, the tip has moved *backward* and the current entry is deleted from Λ, otherwise, the tip is moving *forward* and the adjacent cell is added to Λ along with the needle–tissue interaction points. This process is repeated using the intersected adjacent cell, if any, until the tip is located (inside or outside the mesh). Whenever the tip lies outside the mesh, its path is tested for intersection with the mesh's boundary; this allows for multiple boundary crossing.

After locating the tip inside or outside the mesh using its new position, Λ is traversed backwards to update the parametric coordinates of the needle points and to mark cells that are no longer being intersected by the needle. This fully tracks the position of the needle inside the mesh.

For the sticking motion, we compute for every point of the needle, $s(\alpha)$, that is associated with an active cell, its sticking component ($\tau^{[k]}(\alpha)$) by subtracting the sliding component from $s(\alpha)$'s inter-frame motion. The vertices are driven into their new positions by imposing constraints of the following form:

$$g(t) \cdot \xi = s(\alpha) + \tau^{[k]}(\alpha), \tag{3}$$

where ξ are the barycentric coordinates of the midpoints of the needle segment inside one of Λ's cells with tetrahedron index t. The Lagrange multipliers associated with these constraints are used to compute the resultant forces.

4 Thread Pulling

The needle path inside the body serves to define the topological path in the mesh. The mesh elements crossed by the needle, and the puncture points introduced while entering and exiting the mesh, define an ordered data structure that is used to model the thread–tissue interaction while the thread is pulled to close an opening. Consider, for example, the thread in Fig. 4 that shows a running suture with entry and exit points numbered sequentially from 1 to n. Under displacement control, the user is pulling on the pieces of the thread at points 1 and n. For simplicity of the presentation, we consider here the case of a frictionless interaction between the thread and tissue. The induced tissue deformation and internal stresses are due to the tensile forces in the thread and the contact forces from the closing boundaries.

The pull of the thread is modeled by a constraint equation that constrains the length of the thread portion that is outside the tissue,

$$\sum_{j=1}^{n/2-1} \left(\mathbf{x}_{2j}^{[k+1]} - \mathbf{x}_{2j+1}^{[k+1]} \right) \cdot \hat{\mathbf{d}}_{2j,2j+1}^{[k]} = \sum_{j=1}^{n/2-1} \ell_{2j,2j+1}^{[k]} - \Delta\ell^{[k+1]}, \tag{4}$$

where $\mathbf{x}^{[k]}$ denotes the positions of tissue points at puncture locations at the kth time step. The sum on the left-hand side is over the segments that join successive exit and entry points along the thread. Every term in the sum represents the length of such a segment as described below. $\ell^{[k]}$ is the length of the corresponding portion of the engaged straight thread at time step k and $\Delta\ell^{[k+1]}$ is the incremental pull enacted by the user at time step $k+1$. This constraint presumes and is active only

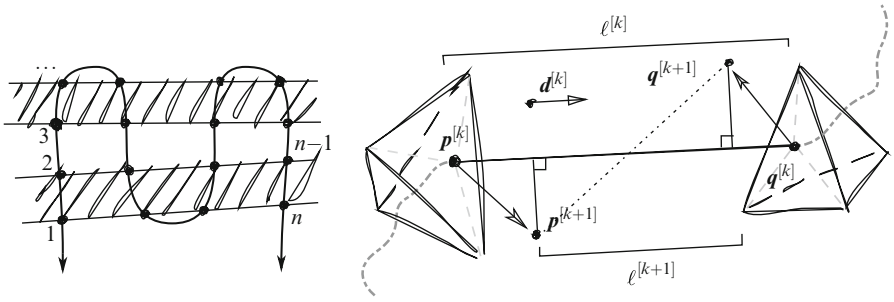

Fig. 4 Sequence of puncture points in a running suture (*left*) and linearization of pulling distance constraint (*right*)

when the thread is fully engaged and has no slack. As long as the right-hand side is less than the actual length of the thread between the two end points, pulling causes pure sliding until the thread is fully engaged. The scalar Lagrange multiplier of this constraint corresponds to the tensile force in the thread as it is pulled. This force may be rendered haptically as needed. Another way of expressing this pull constraint that makes its complementarity clearer is:

$$\sum_{j=1}^{n/2-1} (\mathbf{x}_{2j}^{[k+1]} - \mathbf{x}_{2j+1}^{[k+1]}) \cdot \hat{\mathbf{d}}_{2j,2j+1}^{[k]} + (\mathbf{r}_0 - \mathbf{x}_1^{[k]}) \cdot \hat{\mathbf{d}}_{0,1}^{[k]} + (\mathbf{x}_n^{[k]} - \mathbf{r}_{n+1}) \cdot \hat{\mathbf{d}}_{n,n+1}^{[k]} \leq \ell^{[0]}. \quad (5)$$

$\mathbf{r}_0$ and $\mathbf{r}_{n+1}$ are thread points at locations before first entry (point 1) and after last exit (point n) of the suture. These points are under direct user positional control. $\ell^{[0]}$ is the actual thread length outside the tissue between points 0 and $n+1$. When the left-hand side of (5) is satisfied with strict inequality, the thread has slack and the corresponding Lagrange multiplier is zero. Only when it is satisfied with equality, the thread gets engaged and applies forces to deform the tissue and bring the sutured boundaries together. As the suture closes, additional contact constraints are introduced as described in Sect. 2.

For efficient computations with the pull constraint of (4), we linearize it by measuring the length of every segment as the projection on its direction at the previous step. The justification for this linearization may be explained with reference to Fig. 4. Let $\mathbf{p}$ and $\mathbf{q}$ be two sequential puncture points in the volumetric mesh and $\hat{\mathbf{d}} = (\mathbf{q}-\mathbf{p})/\|\mathbf{q}-\mathbf{p}\|$ be the direction of the line joining $\mathbf{p}$ and $\mathbf{q}$. When $\mathbf{p}$ and $\mathbf{q}$ are pulled close together, the length of the line segment, $\ell = \|\mathbf{q}-\mathbf{p}\|$, joining the two punctures points decreases. At every iteration $\hat{\mathbf{d}}^{[k+1]} \cdot (\mathbf{q}^{[k+1]} - \mathbf{p}^{[k+1]})$ is linearized as $\hat{\mathbf{d}}^{[k]} \cdot (\mathbf{q}^{[k+1]} - \mathbf{p}^{[k+1]})$. The computation of $\hat{\mathbf{d}}$ is also suitably stabilized as the distance between $\mathbf{p}$ and $\mathbf{q}$ becomes small to avoid the near-zero denominator.

5 Results and Conclusion

Figure 5 shows snapshots of an anastomosis procedure using our prototype simulator. The first row shows the initiation of the procedure with the needle puncturing (and deforming) the two vessels at four puncture points. In the second and third rows, running sutures are simulated using a variant number of punctures. Contact constraints prevent the two vessels from interpenetrating and allow the closure of the separating gap. Notice the high principal stress in the regions near the suture.

In order to avoid the small time steps required for the stability of explicit methods [15], we solve the system of constrained equilibrium equations at every step. Our efficient incremental solution strategies, which we will report on in future publications, allow us to achieve haptic rates for medium-sized models with 1,650 nodes and 5,853 linear tetrahedrons. Each step in these simulations takes an average of 30 ms to compute and render using a single 3.3 GHz core, resulting in a refresh rate of 33 FPS on average.

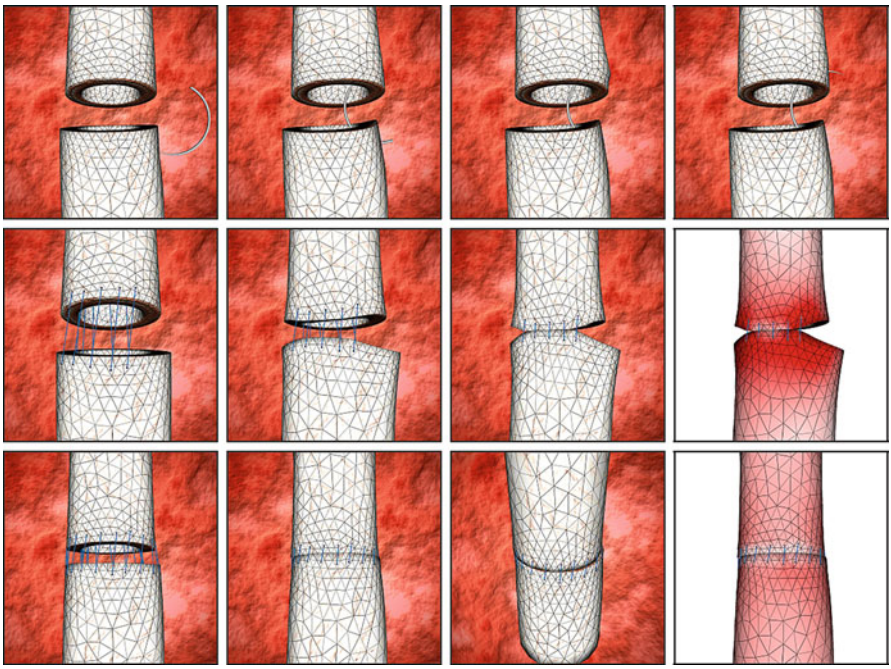

Fig. 5 Needle driving using a $1/2$-circle round body needle (top) and thread pulling with 20 (middle) and 50 (bottom) puncture points. The vessels have different diameters and are discretized with 1,650 nodes and 5,853 tetrahedrons

We believe the techniques presented here form a robust basis for simple and efficient suturing simulation and are currently being used as building blocks for a full-fledged surgical simulator.

Acknowledgments We thank the Lebanese National Council for Scientific Research (LNCSR) for providing support for this project.

References

1. Chentanez, N., Alterovitz, R., Ritchie, D., et al.: Interactive simulation of surgical needle insertion and steering. ACM Trans. Graph. **28**(1), 88:1–10 (2009)
2. DiMaio, S., Salcudean, S.: Needle steering and motion planning in soft tissues. IEEE Trans. Biomed. Eng. **52**(6), 965–974 (2005)
3. Duriez, C., Guébert, C., Marchal, M., et al.: Interactive simulation of flexible needle insertions based on constraint models. Lect. Note Comput. Sci. **5762**, 291–299 (2009)
4. O'Leary, MD., Simone, C., Washio, T et al.: Robotic needle insertion: effects of friction and needle geometry (2003). doi:10.1109/ROBOT.2003.1241851
5. Rosen, J., Brown, J., De, S., et al.: Biomechanical properties of abdominal organs in vivo and postmortem under compression loads. J. Biomech. Eng. **130**(2), 021020 (2008)

6. Laycock, S., Day, A.: A survey of haptic rendering techniques. Comput. Graph. Forum **56**(1), 50–65 (2007)
7. Guébert, C., Duriez, C., Cotin, S., et al.: Suturing simulation based on complementarity constraints. Proc. SCA (Poster) (2009)
8. Otaduy, M.A., Tamstorf, R., Steinemann, D., et al.: Implicit contact handling for deformable objects. Comput. Graph. Forum **28**(2), 559–568 (2009)
9. Tang, M., Manocha, D., Tong, R.: Fast continuous collision detection using deforming non-penetration filters (2010). doi:10.1145/1730804.1730806
10. Teschner, M., Kimmerle, S., Heidelberger, B., et al.: Collision detection for deformable objects. Comput. Graph. Forum **24**(1), 61–81 (2005)
11. Berkley, J., Turkiyyah, G., Berg, D., et al.: Real-time finite element modeling for surgery simulation: an application to virtual suturing. IEEE Trans. Vis. Comput. Graph. **10**(3), 314–325 (2004)
12. Lenoir, J., Meseure, P., Grisoni, L.: A suture model for surgical simulation. Lect. Notes Comput. Sci. **3078**, 105–113 (2004)
13. Wittek, A., Dutta-Roy, T., Taylor, Z., et al.: Subject-specific non-linear biomechanical model of needle insertion into brain. Comput. Meth. Biomech. Biomed. Eng. **11**(2), 135–146 (2008)
14. Choi, K.S., Chan, S.H., Pang, W.M.: Virtual suturing simulation based on commodity physics engine for medical learning. J. Med. Syst. **36**(3), 1781–1793 (2012)
15. Miller, K., Joldes, G., Lance, D., et al.: Total Lagrangian explicit dynamics finite element algorithm for computing soft tissue deformation. Comm. Numer. Meth. Eng. **23**(2), 121–134 (2007)

Part III
Computational Biomechanics for Image-Guided Surgery

Objective Evaluation of Accuracy of Intra-Operative Neuroimage Registration

Revanth Reddy Garlapati, Grand Roman Joldes, Adam Wittek, Jonathan Lam, Neil Weisenfeld, Arne Hans, Simon K. Warfield, Ron Kikinis, and Karol Miller

Abstract Pre-operative brain images that are registered onto relevant intra-operative images can enhance navigation during image-guided neurosurgery. One of the crucial steps in the process of image registration is assessment of its accuracy. The accuracy of an image registration procedure was evaluated in one of our previous studies, for five cases of neurosurgery, using a manual segmentation-based method that is subjective and prone to human errors. The aim of this study is to develop an evaluation method that is objective and automatic. An edge-based Hausdorff Distance (HD) metric based on Canny edges was developed for evaluation. Subsequently, the accuracy of non-rigid registration (NRR) results was evaluated using intra-operative images as ground truth and compared with those

R.R. Garlapati • G.R. Joldes • A. Wittek • J. Lam
Intelligent Systems for Medicine Laboratory, The University of Western Australia, Perth, Australia
e-mail: revanth@mech.uwa.edu.au; grandj@mech.uwa.edu.au; adwit@mech.uwa.edu.au; jonathan.lam.03@gmail.com

N. Weisenfeld • A. Hans • S.K. Warfield
Computational Radiology Lab, Children's Hospital, Harvard Medical School, Boston, MA, USA
e-mail: neil.weisenfeld@childrens.harvard.edu; arne.hans@childrens.harvard.edu; Simon.Warfield@childrens.harvard.edu

R. Kikinis
Surgical Planning Laboratory, Brigham and Women's Hospital, Harvard Medical School, Boston, MA, USA
e-mail: kikinis@bwh.harvard.edu

K. Miller (✉)
Intelligent Systems for Medicine Laboratory, The University of Western Australia, Perth, Australia

Institute of Mechanics and Advanced Materials, Cardiff School of Engineering, Cardiff University, Wales, UK
e-mail: kmiller@mech.uwa.edu.au

A. Wittek et al. (eds.), *Computational Biomechanics for Medicine: Models, Algorithms and Implementation*, DOI 10.1007/978-1-4614-6351-1_9,
© Springer Science+Business Media New York 2013

from the previous study. The obtained results compared well despite the differences in the methods employed. The edge-based HD metric provides an objective measure for image registration accuracy evaluation.

1 Introduction

Neurosurgical resection is the primary therapeutic intervention in the treatment of cerebral gliomas [1]. Near-total surgical removal with the goal of minimising the number of infiltrating glioma cells in the adjacent brain tissue is desirable for several reasons: it prolongs patient's survival, increases time to malignant progression [2] and decreases risk of seizures [3]. Therefore, the knowledge of white matter tract locations and their relationship to the glioma is as important as defining the tumour's relationship with eloquent cortex, where the functional significance is clustered. Moreover, damage in certain areas will cause permanent neurological deficits. For example, the functions of primary motor, somatosensory and visual cortex could get affected.

Maximising surgical removal of gliomatous tissue, while minimising neurological deficits, is challenging because functional brain tissue may reside close to or even within gliomas [4]. This is further complicated due to the brain shift, which occurs during surgery. The shift distorts the pre-operative anatomy and progressively decreases the utility of pre-operatively acquired data [5, 6]. However, maximal resection requires precise localisation of the anatomic features of the tumour and the individual functional organisation of adjacent brain. Therefore, it is necessary to register high-quality pre-operative images onto the intra-operative configuration, as it is not feasible to obtain high-quality images during surgery. In order to perform this registration, the deformations undergone by the brain during surgery are needed.

It has been shown that the deformations undergone by the brain during craniotomy can be predicted using biomechanical models [7–14]. These deformations can be used to warp the pre-operative images onto their intra-operative configuration [15,16]. The usage of warped pre-operative images in surgical planning can improve neuronavigation [17]. However, it is necessary to perform a quantitative assessment of this registration, in order to establish its accuracy [18]. This makes the assessment of accuracy of image alignment, a crucial step in the image registration process.

In this work, the registration accuracy is evaluated using intra-operative brain images as ground truth. Some of the previous studies suggest that such evaluation can be performed by computing the overlap between corresponding anatomical regions or by comparing their outlines [19–21]. In one of our recent studies [13], the ventricles were segmented from the registered pre-operative image and the intra-operative image for five cases of neurosurgery. Subsequently, the point sets representing the surfaces of both segmentations were compared during evaluation using a HD metric [13]. Such methods are time-consuming, labour-intensive, subjective and prone to human errors [18], and therefore they are not well suited for performing evaluation on large number of cases.

In order to facilitate the validation of image registration algorithms, it is necessary to develop an automatic, fast and objective method for measurement of misalignment between images. Hence, automatically generated Canny edges [22] of two-dimensional images are compared in this study for assessment of registration accuracy.

Although similarity metrics such as mutual information and correlation ratio are available for fast and automatic assessment of registration quality, they do not provide the alignment error in terms of physical (Euclidean) distance [18]. In contrast, similarity metrics based on HD can be used to compute the alignment error in terms of physical distance, in a fast and automated manner. Therefore, a method based on HD metric was developed to evaluate the registration results. This paper is organised as follows: in Sect. 2 the edge-based HD metric used in the evaluation of image registration results is defined; the verification of the proposed metric on both artificial and real image data is presented in Sect. 3; evaluation results for five patient-specific brain image registration cases are presented in Sect. 4, and Sect. 5 contains the discussion and conclusions.

2 Methods

2.1 Round-Trip Distance and Consistent Pixels

The round-trip distance and consistent pixels, defined in this subsection, are needed for the definition of the edge-based HD metric and for preprocessing of edges. We consider two sets of Canny edges, **A** and **B**, extracted from registered images. Each pixel and the corresponding point in space will be identified using the same notation in this sub-section. For each non-zero pixel p in the binary edge image **A**, we find the closest non-zero pixel q in the other image **B** (Fig. 1). If the same procedure is followed from this point q in image **B**, we expect to reach the starting point $p$from image **A**, if the images are perfectly aligned. However, in reality the registered images are not perfectly aligned, and therefore we reach an end point r which is different from the starting point p. The distance between the starting point and the end point in image **A** is defined as the round-trip distance (Fig. 1).

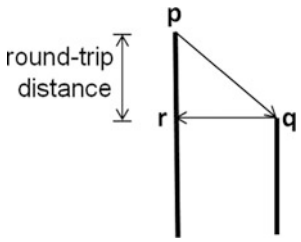

Fig. 1 Illustration of the round-trip distance computation. The starting point p is in image **A**, the intermediate point q is in image **B** and the final point r is in image **A**. The round-trip distance for point p is $\|p - r\|$, where $\|\cdot\|$ represents the Euclidean distance

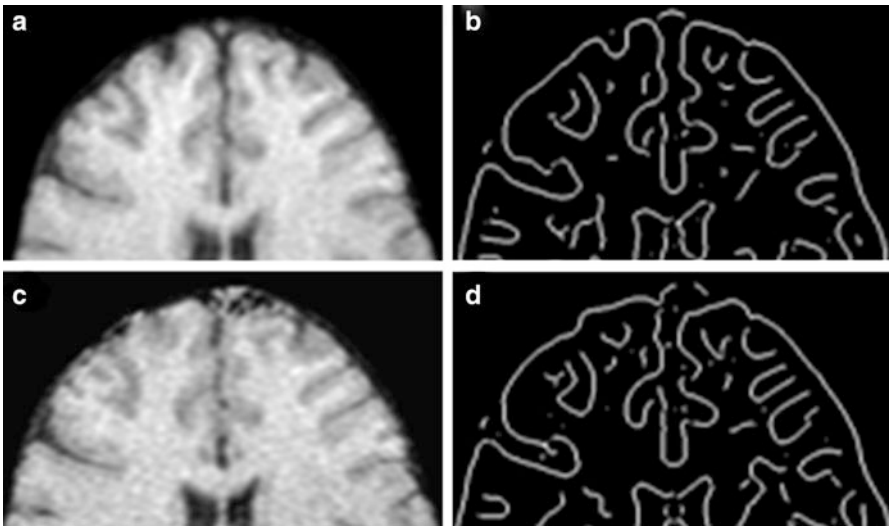

Fig. 2 The Canny edges of a deformed pre-operative and the corresponding intra-operative images. (**a**) Deformed pre-operative image. (**b**) Canny edges of deformed pre-operative image. (**c**) Intra-operative image. (**d**) Canny edges of intra-operative image

The pixels that have a round-trip distance greater than a prescribed threshold are excluded from the evaluation process, as they are less likely to have corresponding pixels in the other image. This threshold is called the round-trip consistency threshold criterion, while the pixels that are not excluded are termed consistent pixels. If a round-trip threshold criterion of zero is used to make two images consistent with respect to each other, only the edges that are parallel to each other are not excluded. Since pixels that have a round-trip distance greater than the threshold criterion get excluded from the evaluation process, it is important to choose an optimal threshold such that the consistency is maximised, while minimising the number of features removed. The round-trip threshold criterion for computing the edge-based HD metric was chosen as 1 mm, that is, twice the in-plane resolution of the analysed images. Only the consistent pixels are included in the computation of directed distance for each edge while computing the HD metric.

2.2 Definition of the Consistent Edge-Based HD Metric

Let the elements of images $\mathbf{A} = \{\mathbf{a_1}, \ldots, \mathbf{a_m}\}$ and $\mathbf{B} = \{\mathbf{b_1}, \ldots, \mathbf{b_n}\}$ denote finite edge sets, with each element of the set a Canny edge (Fig. 2). The HD is the maximum directed distance computed using the edge sets as indicated in Eq. (1). The procedure for computing the directed distance between edge sets is different from the point-based directed Euclidean distance, as indicated in Eqs. (2)–(4).

$$\mathrm{H}(\mathbf{A},\mathbf{B}) = \max\left(\mathrm{h}(\mathbf{A},\mathbf{B}),\mathrm{h}(\mathbf{B},\mathbf{A})\right) \tag{1}$$

$$\mathrm{h}(\mathbf{A},\mathbf{B}) = \max_{\mathbf{a}\in\mathbf{A}}\min_{\mathbf{b}\in\mathbf{B}}\mathrm{h}'(\mathbf{a},\mathbf{b}) \tag{2}$$

Let edges $\mathbf{a}$ and $\mathbf{b}$ belong to edge sets $\mathbf{A}$ and $\mathbf{B}$, respectively. The point sets $\mathbf{a} = \{\mathbf{a'}_1,\ldots,\mathbf{a'}_m\}$ and $\mathbf{b} = \{\mathbf{b'}_1,\ldots,\mathbf{b'}_n\}$ contain the points that form these edges. The point sets are made consistent with respect to each other prior to the computation of edge-based HD using the round-trip threshold criterion. Therefore, only the consistent subsets of edges $\mathbf{a}$ and $\mathbf{b}$ are used to compute the edge-based directed distance. Let the consistent point subsets be represented by $\tilde{\mathbf{a}} = \{\mathbf{a'}_1,\ldots,\mathbf{a'}_{\tilde{m}}\}, \tilde{m} \leq m$ and $\tilde{\mathbf{b}} = \{\mathbf{b'}_1,\ldots,\mathbf{b'}_{\tilde{n}}\}, \tilde{n} \leq n$. The edge-based directed distance is computed using the point-based HD metric between the consistent point subsets $\tilde{\mathbf{a}}$ and $\tilde{\mathbf{b}}$:

$$\mathrm{h}'(\mathbf{a},\mathbf{b}) = \max\left(\mathrm{h}''(\tilde{\mathbf{a}},\tilde{\mathbf{b}}),\mathrm{h}''(\tilde{\mathbf{b}},\tilde{\mathbf{a}})\right) \tag{3}$$

$$\mathrm{h}''(\tilde{\mathbf{a}},\tilde{\mathbf{b}}) = \max_{a'\in\tilde{\mathbf{a}}}\min_{b'\in\tilde{\mathbf{b}}}\left\|a'-b'\right\| \tag{4}$$

2.3 Preprocessing

The edges shorter than 5 mm are deleted from the analysed images as their dimension is insignificant in comparison with the relevant brain dimension, which is approximately 150 mm. The edges are also made consistent with respect to each other using the round-trip threshold. The round-trip threshold criterion for preprocessing is selected as 2 mm, that is, four times the in-plane resolution of the resampled images. The purpose of this round-trip threshold during preprocessing is to remove features that have no correspondence in the other image (Fig. 3). During preprocessing, the usage of a lower (stringent) threshold causes some of the features with correspondence in the other image to be removed. The threshold during preprocessing is larger (less stringent) than during the HD metric computation, because pixels that are not consistent are only ignored during the computation of HD metric between the edges, whereas such pixels are removed from the images during preprocessing. The larger (less stringent) threshold during preprocessing enables us to remove inconsistent features while retaining most of those that actually have correspondence. When edges are made consistent with respect to each other using the round-trip threshold, more short edges are created. The short edges are removed from the images and the consistency procedure is applied one more time. The remaining edges were found to represent features that better correspond to each other in the two images (Fig. 3).

2.4 Application to Three-Dimensional MRI Images

In this study a two-dimensional (2D) image sequence was created in the axial plane from each of the three-dimensional (3D) MRI images using Slicer3 (http://www.slicer.org/). The edge-based HD metric is used to evaluate the registration

Fig. 3 The Canny edges of corresponding representative 2D slices from the deformed pre-operative image and intra-operative image overlaid on each other before (**a**) and after (**b**) preprocessing, for five analysed cases of craniotomy-induced brain shift. The *green* portion represents overlapping edges, the *blue* part identifies non-overlapping edges of the deformed pre-operative image and the *red* part identifies non-overlapping edges of the intra-operative image

accuracy by comparing each warped pre-operative 2D image with the corresponding intra-operative image. The images that are located in the same axial plane are considered to correspond to each other.

Fig. 4 Visualisation of an outlier pair of Canny edges. The *green* portion represents overlap between the edges in the two images being compared, the *blue* part identifies the non-overlapping edges from the deformed pre-operative image and *red* part identifies the non-overlapping edges from the intra-operative image

The original resolution of the images is $0.859 \times 0.859 \times 2.5\,\text{mm}^3$. Subsequently, the pre-operative and intra-operative images were re-sampled to a resolution of $0.5 \times 0.5 \times 2.5\,\text{mm}^3$, in order to increase the precision in locating the Canny edges in each 2D axial image.

The algorithm was programmed in Matlab (www.mathworks.com). The built-in Canny edge detector is used for edge detection. The standard deviation for the Gaussian filter used by the Canny edge detector is set to (4), so that only the major features are extracted (Fig. 2). The edge-based HD was used to assess the degree of misalignment between each 2D image pair. The results of all associated image pairs are combined together for the percentile-HD metric analysis. The n percentile-HD metric is defined as the value that is greater than n percent of the total number of directed distances belonging to edges of either image.

The preprocessing stage ensures that most edges used for HD computation have a corresponding edge in the other image. Nevertheless, some pairs of edges do not represent the same anatomical feature in the two images, and thus lack correspondence (Fig. 4). The presence of such pairs of edges (outliers) leads to large values of the edge-based HD distance, which are not representative of the registration accuracy. In order to eliminate such outliers, the registration accuracy analysis involves the computation of percentile-HD metric values in conjunction with visualisation of edges.

3 Verification of the Evaluation Method

3.1 Verification Using Artificial Images

The first step in the verification of the evaluation algorithm was the creation of an artificial brain-like image. A new image was created by translating this artificial image by 5 pixels along the y-axis. The percentile-HD metric values were computed by comparing the two images. The HD metric values between percentiles 70 and 100 were found to be equal to the actual alignment error, that is, 5 pixels. A repeat of this process using a 5 pixel translation along the x-axis led to a similar result.

3.2 Verification Using MRI Images and Known Deformation Fields

Five cases of neurosurgery involving tumour removal are considered in this study. These are the same cases that were analysed for registration accuracy in a previous study [13]. In that study, patient-specific biomechanical models enabled the computation of the deformation fields used to warp the pre-operative images into their intra-operative configurations.

A representative 2D pre-operative image from each of the five real MRI image sets is warped with three different known 2D deformation fields. The three different deformation fields for each case are obtained by scaling known deformation fields by factors 0.5, 1.0, and 1.5. The proposed edge-based HD metric is used to evaluate the difference between the warped pre-operative images and the original pre-operative image.

The percentile-HD metric plots associated with the various deformation fields are presented for the five cases in Fig. 5. It can be observed that the HD metric values at higher percentiles (70–100) generally increase with an increase in the value of the maximum deformation. This shows that a good correlation exists between the percentile-HD metric and the maximum deformation, and therefore the percentile-HD metric (at high percentiles) can be utilised as an indicator of the degree of misalignment. However, in general, the percentile-HD metric values deviate from the applied maximum deformation, as the definition of HD metric does not include point-to-point correspondence [18].

4 Analysis of Registration Accuracy Using the Proposed Method

We analysed the registration accuracy for five cases of craniotomy-induced brain shift (previously used in [13]) by comparing the warped pre-operative images with the corresponding intra-operative images using the proposed method. Only the half of the brain image (in the axial plane) that contained the tumour is used for evaluation, because most of the brain deformation occurs in this region. The percentile-HD metric values obtained for the five cases are presented in Fig. 6. The steep rise in the percentile-HD metric value noticed between percentiles 95 and 100 is attributed to outliers. Based on the visualisation of edges, it was observed that most outliers are included in the top 5% of HD values. It was also found that the relevant edges have to be plotted before they can be classified as outliers with certainty (Fig. 4).

It is difficult to avoid an alignment error smaller than 2 pixels when performing non-rigid registration [18]; therefore, the success criterion for registration was defined as 1.7 mm. This distance is approximately twice the in-plane resolution of the original intra-operative image (Fig. 6). The edges that have a directed distance

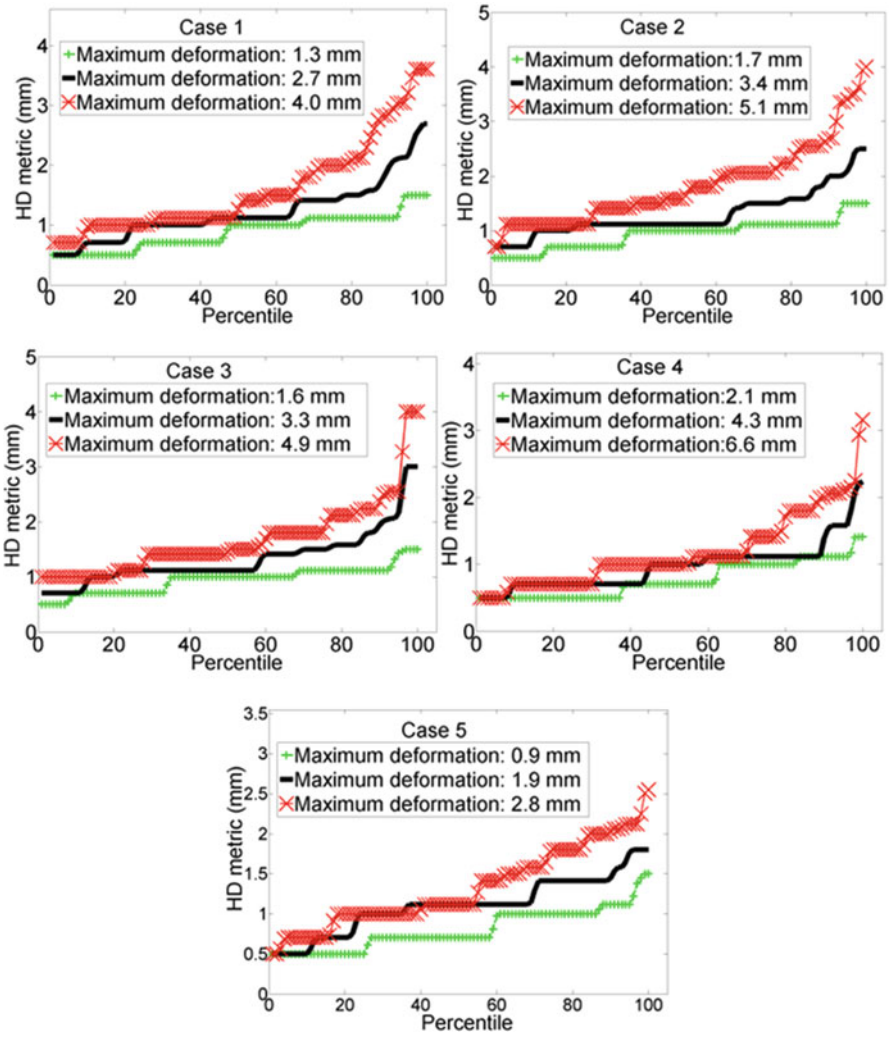

Fig. 5 Percentile-HD metric plots corresponding to various deformation fields for five cases

value smaller than 1.7 mm can be considered to be successfully registered. For the analysed cases, 82%, 64%, 64%, 74%, and 72% of the directed distance values are less than 1.7 mm, respectively. This implies that the same percentages of edges were successfully registered.

The 99 percentile-HD metric values for cases 1–5 are relatively high and greater than 3 mm (Table 1), as they include outliers, according to visualisation of edges. Hence, these values should not be used as a registration error measure, in general, as they tend to over-estimate the alignment error. On the other hand, the 90 percentile-HD metric values range between 2.1 and 2.5 mm (Table 1). Based on visualisation,

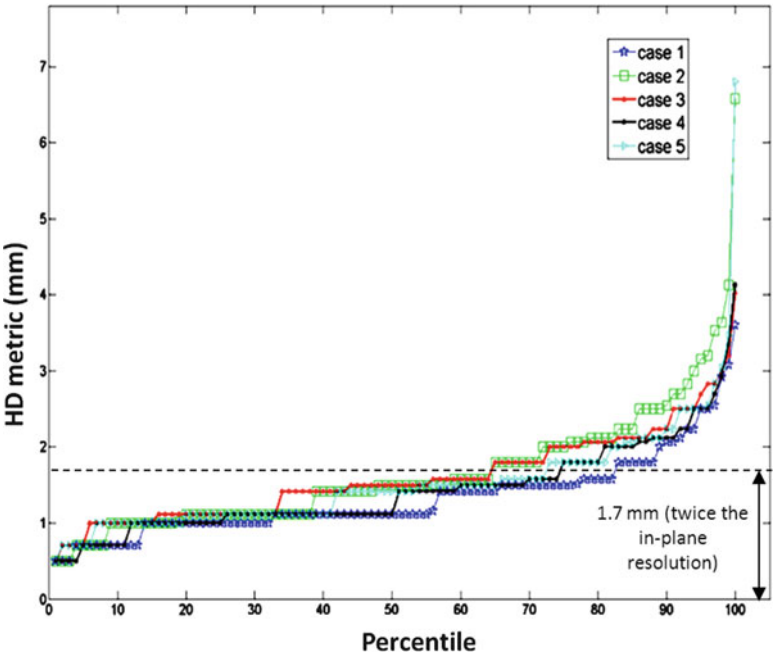

Fig. 6 The edge-based percentile-HD metric for the five cases analysed

Table 1 99-, 95-, 90- and 75-percentile HD metric computed using the Canny edges from the warped pre-operative images and intra-operative images for the analysed cases

	99-percentile HD metric (mm)	95-percentile HD metric (mm)	90-percentile HD metric (mm)
Case 1	3.1	2.5	2.1
Case 2	4.1	3.2	2.5
Case 3	3.2	2.7	2.2
Case 4	3.3	2.5	2.1
Case 5	3.5	2.5	2.2

the 90 percentile-HD metric values were found to exclude all outliers for the analysed cases. However, it should not be used as a registration error measure, as it excludes some of the edges that actually correspond to each other, and therefore it is likely to underestimate the degree of alignment error.

The 95 percentile-HD metric is generally used as a measure of alignment error, as it is believed to be an accurate indicator of the alignment error [18]. Nevertheless, we found that the 95 percentile-HD metric values sometimes include a few outliers. Hence, the percentile-HD metric that is used as a measure of alignment error should be decided using the percentile-HD metric plot and visualisation of edges for each individual case.

5 Discussion

This paper presents several improvements to the image registration accuracy evaluation procedure, compared to a previous study that involved the same five neurosurgery cases [13]. The segmented contours of the ventricles, obtained by manual segmentation of pre-operative and intra-operative images, were used during the evaluation process in the earlier study. Segmentation of the lower resolution intra-operative images is especially difficult, leading to unavoidable uncertainties. The current study does not suffer from this limitation, as it uses Canny edges which are extracted automatically from images. Therefore the current evaluation method is more objective.

The misalignment in our previous study [13] was computed using point-based HD. The 95 percentile-HD obtained for the five cases are 1.3, 2.8, 1.9, 0.9, and 1.5 mm, respectively [13]. The new edge-based 95 percentile-HDs metric presented in this paper leads to values of 2.5, 3.2, 2.7, 2.5, and 2.5 mm, for the same cases. The corresponding values from the studies compare reasonably well, considering the differences between methodologies. In fact, the alignment errors from the previous study are expected to be lower, as evaluation was performed using only ventricle surfaces, where deformations are relatively low compared to the deformations on the brain's surface. This study involves a region of interest that includes the tumour and the craniotomy area, where the maximum deformation occurs.

The evaluation method developed in this study was applied slice by slice in 2D. Therefore, misalignments that occur in the direction perpendicular to the plane of evaluation may not be captured accurately. Nevertheless, the 2D method can be used for conducting 3D evaluations, if it is applied in two perpendicular planes. The qualitative differences between the various images reflected well in the HD metric results obtained using the 2D evaluation method. We plan to extend the current 2D evaluation method to 3D in future studies.

Acknowledgments The first author is a recipient of the SIRF scholarship and gratefully acknowledges financial support of The University of Western Australia (Research Collaboration Award). The financial support of National Health and Medical Research Council (Grant No. APP1006031), National Institute of Health (Grants R01 EB008015 and R01 LM010033) and Children's Hospital Boston Translational Research Program is gratefully acknowledged. In addition, the authors also gratefully acknowledge the financial support of Neuroimage Analysis Center (NIH P41 EB015902), National Center for Image Guided Therapy (NIH U41 RR019703) and the National Alliance for Medical Image Computing (NAMIC), funded by the National Institutes of Health through the NIH Roadmap for Medical Research, Grant U54 EB005149. Information on the National Centers for Biomedical Computing can be obtained from http://nihroadmap.nih.gov/bioinformatics.

References

1. Black, P.: Management of malignant glioma: role of surgery in relation to multimodality therapy. J. Neurovirol. **4**, 227–236 (1998)
2. Nakamura, M., Konishi, N., Tsunoda, S., et al.: Analysis of prognostic and survival factors related to treatment of low-grade astrocytomas in adults. Oncology **58**, 108–116 (2000)
3. Luyken, C., Blümcke, I., Fimmers, R., et al.: The spectrum of long-term epilepsy-associated tumours: long-term seizure and tumour outcome and neurosurgical aspects. Epilepsia **44**, 822–830 (2003)
4. Schiffbauer, H., Ferrari, P., Rowley, H.A., et al.: Functional activity within brain tumours: a magnetic source imaging study. Neurosurgery **49**, 1313–1320 (2001)
5. Miga, M.I., Paulsen, K.D., Lemery, J.M., et al.: Model-updated image guidance: Initial clinical experiences with gravity-induced brain deformation. IEEE Trans. Med. Imag. **18**, 866–874 (1999)
6. Nabavi, A., Black, P.M., Gering, D.T., et al.: Serial intraoperative magnetic resonance imaging of brain shift. Neurosurgery **48**, 787–797 (2001)
7. Hu, J., Jin, X., Lee, J.B., et al.: Intraoperative brain shift prediction using a 3D inhomogeneous patient-specific finite element model. J. Neurosurg. **106**, 164–169 (2007)
8. Joldes, G.R., Wittek, A., Miller, K.: Computation of intra-operative brain shift using dynamic relaxation. Comput. Meth. Appl. Mech. Eng. **198**, 3313–3320 (2009)
9. Joldes, G.R., Wittek, A., Miller, K.: Real-time nonlinear finite element computations on GPU - Application to neurosurgical simulation. Comput. Meth. Appl. Mech. Eng. **199**, 3305–3314 (2010)
10. Joldes, G.R., Wittek, A., Miller, K.: Suite of finite element algorithms for accurate computation of soft tissue deformation for surgical simulation. Med. Image Anal. **13**, 912–919 (2009)
11. Miller, K., Wittek, A., Joldes, G.: Biomechanical modelling of the brain for computer-assisted neurosurgery. In: Miller, K. (ed.) Biomechanics of the Brain, pp. 111–136. Springer, New York (2011)
12. Miller, K., Wittek, A., Joldes, G., et al.: Modelling brain deformations for computer-integrated neurosurgery. Int. J. Numer. Method Biomed. Eng. **26**, 117–138 (2010)
13. Wittek, A., Joldes, G., Couton, M., et al.: Patient-specific non-linear finite element modelling for predicting soft organ deformation in real-time; application to non-rigid neuroimage registration. Prog. Biophys. Mol. Biol. **103**, 292–303 (2010)
14. Wittek, A., Miller, K., Kikinis, R., et al.: Patient-specific model of brain deformation: application to medical image registration. J. Biomech. **40**, 919–929 (2007)
15. Joldes, GR., Wittek, A., Warfield, SK., et al.: Performing brain image warping using the deformation field predicted by a biomechanical model. In: Nielsen, P.M.F., Miller, K., Wittek, A. (eds.) Computational Biomechanics for Medicine VI Workshop, MICCAI. pp. 89–96. Springer, Toronto (2011)
16. Warfield, S.K., Talos, F., Tei, A., et al.: Real-time registration of volumetric brain MRI by biomechanical simulation of deformation during image guided neurosurgery. Comput. Visual Sci. **5**, 3–11 (2002)
17. Warfield, S.K., Haker, S.J., Talos, I.F., et al.: Capturing intraoperative deformations: research experience at Brigham and womens's hospital. Med. Image Anal. **9**, 145–162 (2005)
18. Fedorov, A., Billet, E., Prastawa, M., et al.: Evaluation of brain MRI alignment with the robust Hausdorff distance measures. In: 4th international symposium on advances in visual computing. pp. 594–603. Springer, Las Vegas (2008)
19. Klein, A., Andersson, J., Ardekani, B.A., et al.: Evaluation of 14 nonlinear deformation algorithms applied to human brain MRI registration. Neuroimage **46**, 786–802 (2009)
20. Rogelj, P., Kovacic, S., Gee, J.C.: Validation of a nonrigid registration algorithm for multimodal data. In: Sonka, M., Fitzpatrick, J.M. (eds.) Medical Imaging 2002. Proceedings of SPIE, pp. 299–307, San Diego (2002)

21. Wei, Y., Christensen, G.E., Song, J.H., et al.: Evaluation of five non-rigid image registration algorithms using the NIREP framework. In: Dawant, B.M., Haynor, D.R. (eds.) Medical Imaging 2010. Proceedings of the SPIE, pp. 76232L-76232L-10, San Diego (2010)
22. Canny, J.: A computational approach to edge detection. IEEE Trans. Pattern Anal. Mach. Intell. **8**, 679–698 (1986)

Registration of Brain Tumor Images Using Hyper-Elastic Regularization

Andac Hamamci and Gozde Unal

Abstract In this paper, we present a method to estimate a deformation field between two instances of a brain volume having tumor. The novelties include the assessment of the disease progress by observing the healthy tissue deformation and usage of the Neo-Hookean strain energy density model as a regularizer in deformable registration framework. Implementations on synthetic and patient data provide promising results, which might have relevant use in clinical problems.

1 Introduction

Registration of brain volumes with tumors is important to track the changes between two instances in order to assess the progression of the tumor and the treatment response. The first step is a rigid/affine registration between volumes. Although this is a challenging problem due to the changes caused by the tumor, various approaches on the problem reported successful results in the literature [4, 13, 15]. The total deformation caused by the tumor growth can be taught as the combination of infiltration to the healthy tissue and mass effect components. Our aim in this work is to separate the mass effect and infiltration components, so that malignancy and the reversibility of the destruction can be determined. The healthy brain tissue in one of the images can be warped onto the other ignoring the tumor tissue regions, as the latter may contain uncertainty due to highly complex tumor growth and therapy processes. Hence, matching only the healthy tissues in baseline and follow-up tumor images provides an estimation of the intracranial pressure caused by the tumor growth plus the mass effect.

A. Hamamci • G. Unal (✉)
Faculty of Engineering and Natural Sciences, Sabanci University, Istanbul, Turkey
e-mail: gozdeunal@sabanciuniv.edu

A. Wittek et al. (eds.), *Computational Biomechanics for Medicine: Models, Algorithms and Implementation*, DOI 10.1007/978-1-4614-6351-1_10,
© Springer Science+Business Media New York 2013

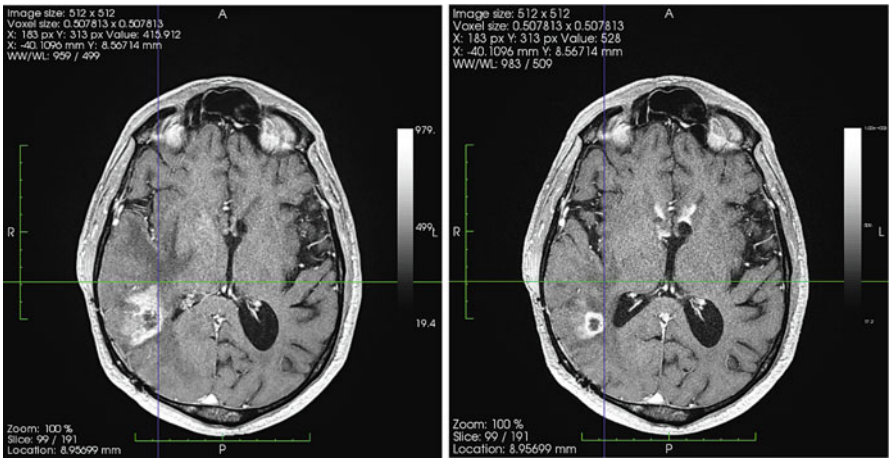

Fig. 1 A sample axial slice from baseline (*on the right*) and follow-up (*on the left*) MRI

A similar problem arises in deformable registration of the brain with tumors to a healthy population atlas. The main difference to the intra-subject registration problem is that the deformation also includes inter-subject variations. Hence, a general strategy to solve this problem is to iterate the forward model by simulating the tumor growth on the atlas and refining the parameters of the simulation model by comparing it to the tumor image [6]. This requires strong models, which rely on realistic models of tumor growth and deformations due to the mass effect [2, 6, 8, 14]. The main problem with those approaches is that the growth of the tumor is mostly affected by the uncontrolled parameters such as treatment and requires sophisticated tumor growth models even without treatment. In "Geometric Metamorphosis" paper, Niethammer et al., proposed an interesting approach to the problem using a weak model by separating the foreground, hence the tumor growth, and the background changes [11].

For the problem of intra-subject registration, our approach is based on the assumption that the deformations except around the tumor volume are caused by the mass effect of the tumor, hence obey the bio-mechanical rules. This is different from the atlas matching problem, since there is also inter-subject variations between the images. Sample baseline and follow-up MRI slices are shown in Figs. 1 and 2. Deformation of the ventricles and sulci due to the mass effect of the growing tumor can be clearly observed on the right hemisphere. Although a mapping of the tumor tissue between the baseline and the follow-up is not well defined due to the uncertain growth pattern and therapy effects, a mapping between the healthy tissues can be estimated. Therefore, our aim is to find a mapping between the healthy tissues of the brains, which obeys the nonlinear elastic finite deformation models.

The results of the experimental studies on animals suggest to model the brain with a homogeneous hyper-viscoelastic non-isotropic material [9]. In the image analysis literature, simplified hyper-elastic or linear models are used: Neo-Hookean

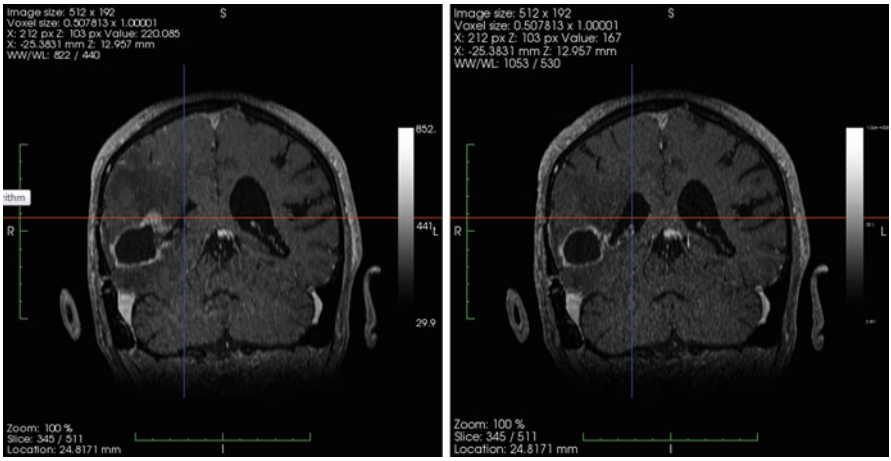

Fig. 2 A sample coronal slice from baseline (*on the right*) and follow-up (*on the left*) MRI

[7], Ogden type [10,16], Saint-Venant Kirchhoff model [18], linear elastic [3], linear viscoelastic type [2]. In their work, comparing viscoelastic, hyper-elastic and linear elastic models on brain simulations, Wittek et al. report no significant difference on the results obtained [17]. In "Nonlinear Elastic Registration with Unbiased Regularization in Three Dimensions", Saint-Venant Kirchhoff model was used as a regularizer in the registration of serial magnetic resonance images [18].

Our novel contributions in this paper are: (a) Matching healthy tissue to healthy tissue of the brain using a dedicated image data term; (b) Using the hyper-elastic Neo-Hookean strain energy density as a regularizer in deformable registration framework; (c) Derivation of displacement field update equations based on the Neo-Hookean model.

2 Methods

2.1 Background

The mechanical properties of a hyper-elastic material are characterized completely by a scalar strain-energy density function W. Specifying the strain energy density W as a function of deformation gradient tensor F: $W = W(F)$ ensures that the material is perfectly elastic. The general form of the strain energy density is guided by experiment [1].

Let us define the displacement field from the un-deformed to deformed configuration as $u : \Omega \longrightarrow \mathbb{R}^3$ where $\Omega \in \mathbb{R}^3$. In addition to the strain energy density

$W = W(x, \nabla u)$, let $f = f(x, u(x))$ denote the external energy, then the equilibrium configurations can be determined as the minima of the total energy functional:

$$I(u) = \int_{\Omega} W(x, \nabla u) \mathrm{d}x - \int_{\Omega} f(x, u) \mathrm{d}x \tag{1}$$

The Euler–Lagrange system associated with the functional I is precisely the equilibrium equations:

$$\mathrm{div}\left(\frac{\partial W}{\partial F}(x, \nabla u(x))\right) + \frac{\partial f}{\partial u}(x, u(x)) = 0 \tag{2}$$

where $F_{ij} = \sigma_{ij} + \frac{\partial u_i}{\partial x_j}$ and $\frac{\partial W}{\partial F}^T$ is called the First Piola–Kirchhoff tensor. Common constitutive hyper-elastic strain energy density models include [12]:

- St Venant–Kirchhoff material:

$$W(F) = \alpha(trE)^2 + \beta tr(E^2) \text{ where } E = \frac{1}{2}(F^T F - I) \tag{3}$$

- Neo-Hookean material:

$$W(F) = a\|F\|^2 + g(detF) \text{ where } a > 0 \tag{4}$$

2.2 Hyper-Elastic Registration for Tumor Follow-Up

Let $R(x)$ and $T(x)$ denote the brain tissue maps (White Matter + Gray Matter + Tumor) of reference (undeformed) and target (deformed) volumes, respectively. We are assuming the mechanical properties of white matter and gray matter are similar. The problem is to find the displacement u from the volume R to T, which minimizes the given functional:

$$u^* = \arg\min_u \int_{\Omega} f(R(x), T(x - u(x))) + \alpha W(x, \nabla u) \mathrm{d}x \tag{5}$$

where f is the external energy density term calculated as a similarity measure between the two volumes and α is the weighting parameter of the regularizer term W.

Distance maps to the binary segmentations are used, instead of common image similarity measures, such as mutual information. In this way, state-of-the art segmentation methods specific to the problem could be used to obtain reliable image forces. Reliability of the image term is especially important for the proposed regularizer dominant approach.

2.3 Volumetric Data Term

Since a mapping between the two solid body is needed, all the displacements from the reference should point towards inside of the target body. This is ensured by the following external energy density term:

$$f_V(x,u(x)) = \chi_R(x) D_T(x+u(x)) \tag{6}$$

where χ_R is the indicator function of the reference body, with the value of 1 for the points inside and 0 for the outside. D_T is the distance function to the target body, where D_T is zero inside the target body and takes the distance values outside the target body. The goal is that the displacement vectors can move freely inside the target volume. To derive the Euler–Lagrange condition for this energy density, the derivative of the functional in Eq. (6) is written as:

$$\frac{\partial}{\partial u} f_V(x,u(x)) = \chi_R(x) \frac{\partial}{\partial u} D_T(x+u(x)) \tag{7}$$

This is simply the gradient of the distance function of the target body:

$$\frac{\partial}{\partial u} f_V(x,u(x)) = \chi_R(x) \nabla D_T(x+u(x)) \tag{8}$$

2.4 Boundary Data Term

In addition, a solution that matches the outside surfaces of the two bodies is required. Therefore, another external energy density is added which penalizes the distance from the surface of the reference body to the surface of the target. We note that displacement vectors can still move on the target surface freely. This is ensured by the following energy term:

$$f_B(x,u(x)) = \chi_{\partial R}(x) D_{\partial T}(x+u(x)) \tag{9}$$

where $\chi_{\partial R}$ is the indicator function of the boundary of the reference body, having the value of 1 for the points on the boundary and 0 elsewhere. $D_{\partial T}$ is the distance function to the boundary of the target body. The Euler–Lagrange condition for this energy density is:

$$\frac{\partial}{\partial u} f_B(x,u(x)) = \chi_{\partial R}(x) \frac{\partial}{\partial u} D_{\partial T}(x+u(x)) = \chi_{\partial R}(x) \nabla D_{\partial T}(x+u(x)) \tag{10}$$

2.5 Hyper-Elastic Regularizer

For simplicity, assuming nonlinear hyper-elastic model in Ogden form as in [10]:

$$W = \frac{2\mu}{\alpha^2}(\bar{\lambda_1}^{\alpha} + \bar{\lambda_2}^{\alpha} + \bar{\lambda_3}^{\alpha} - 3) + \frac{1}{D_1}(J-1)^2 \tag{11}$$

where principal strains $\bar{\lambda_i} = \lambda_i / J^{1/3}$, $\lambda_i = e_i^{1/2}$, e_i's are eigenvalues of $B = FF^T$, J is the determinant of the deformation $J = \det(F)$ and deformation gradient tensor $F_{ij} = \frac{\partial u_i}{\partial x_j} + \delta_{ij}$. In [9], α parameter of the model for the brain tissue is determined as $\alpha = -4.7$. For simplicity, in this work we will use $\alpha = 2$, which is known as the Neo-Hookean model. By replacing $Tr(B) = \lambda_1^2 + \lambda_2^2 + \lambda_3^2$, the strain energy density function becomes:

$$W = \frac{\mu}{2}\left(\frac{Tr(B)}{J^{2/3}} - 3\right) + \frac{1}{D_1}(J-1)^2 \tag{12}$$

Let us derive the Euler–Lagrange condition on the displacement field u for minimizing the given strain energy functional in terms of the trace and determinant. The derivative of the energy density W with respect to u_i is given by:

$$\nabla_{u_i} W = \frac{\partial W}{\partial u_i} - \sum_j \frac{\partial}{\partial x_j} \frac{\partial W}{\partial (\partial u_i / \partial x_j)} \tag{13}$$

The first term drops, as the energy density functional W is not dependent on the u but its derivatives. The derivative with respect to $\partial u_i / \partial x_j$ is identical to the derivative with respect to F_{ij}, therefore, rewriting Eq. (13) results in:

$$\nabla_{u_i} W = -\sum_j \frac{\partial}{\partial x_j} \frac{\partial W}{\partial F_{ij}} \tag{14}$$

Now, we need the derivatives $\frac{\partial W}{\partial F_{ij}}$, which is also known as the 1st Piola–Kirchhoff tensor in mechanics literature. After a set of manipulations, the following derivative is obtained:

$$\begin{aligned} \nabla_{u_i} W = &-\frac{\mu}{J^{2/3}} \sum_j \left(\frac{\partial F}{\partial x_j}\right)_{ij} + \frac{2\mu}{3J^{2/3}} \sum_j F_{ij} Tr\left(F^{-1}\frac{\partial F}{\partial x_j}\right) \\ &- \left(\frac{\mu Tr(B)}{3J^{2/3}} - \frac{2J(J-1)}{D1}\right) \sum_j \left(F^{-1}\frac{\partial F}{\partial x_j} F^{-1}\right)_{ji} \end{aligned}$$

$$-\left(\frac{2\mu Tr(B)}{9J^{2/3}}+\frac{2J(2J-1)}{D1}\right)\sum_j (F^{-1})_{ji} Tr\left(F^{-1}\frac{\partial F}{\partial x_j}\right)$$
$$+\frac{2\mu}{3J^{2/3}}\sum_j (F^{-1})_{ji} Tr\left(\frac{\partial F}{\partial x_j}F^T\right) \quad (15)$$

2.6 Implementation Details

A multi-resolution approach is implemented to increase the convergence speed. Volumes are down-sampled using trilinear interpolation and the obtained displacement field is interpolated to the higher resolution at the end of each stage.

The update equation for the displacement field u is obtained by the gradient descent method as:

$$\frac{\partial u}{\partial t} = -(\text{Eq.}(8)+\text{Eq.}(10)+\text{Eq.}(15)) \quad (16)$$

If the maximum change due to the regularizer is greater than 1, the update of the displacement is normalized by dividing to the maximum update:

$$\nabla_u W = \begin{cases} \frac{\nabla_u W}{\max(\nabla_u W)} & \text{if } \nabla_u W > 1 \\ \nabla_u W & \text{otherwise} \end{cases} \quad (17)$$

Scaling of the strain energy density function of the regularizer term is arbitrary. Therefore, instead of having two independent parameters μ and D_1 for the energy functional in Eq. (12), the algorithm is affected mainly by the ratio $\frac{\mu}{1/D_1} = \mu D_1$.

The effect of a μD_1 at a higher limit is shown on the sub-figure at the center of Fig. 4, which corresponds to the first term in Eq. (12), whereas the effect of a zero μD_1 is shown on the right sub-figure of Fig. 4, which corresponds to the second term. In this work, our aim is to estimate the cause (tumor deformation) by observing the result (displacement at the boundaries). Therefore, we assure the reversibility by enforcing a highly incompressible behavior to prevent the energy to be stored in the material, which we cannot observe by MRI. This is achieved by penalizing the local volume changes more by setting a low μD_1. We also assume that the total volume increase of the brain parenchyma is mostly caused by the increase of the tumor volume. Therefore, by setting the tumor region as a hole for the regularizer, which does not contribute to the external energy, and using an incompressible strain energy density, the observed local volume changes at the boundaries of the parenchyma are carried to the tumor area. We also note that, by decreasing the μ, the dependence of the strain energy density to the model parameter α in Eq. (11) is decreased, which strengthen our simplification approach of using Neo-Hookean model ($\alpha = 2$) instead of Ogden form with $\alpha = -4.7$.

Starting with an initial time step δt for the regularizer, the value is halved if the strain energy is not decreased by updating the displacement field.

The first derivatives are calculated by using central difference finite differencing scheme as:

$$V_x(x,y,z) = \frac{V(x+h,y,z) - V(x-h,y,z)}{2h} \tag{18}$$

The derivative $\frac{\partial F}{\partial x_j}$ is given by the following matrix:

$$\frac{\partial F}{\partial x_j} = \begin{pmatrix} \frac{\partial^2 u_1}{\partial x_1 \partial x_j} & \frac{\partial^2 u_1}{\partial x_2 \partial x_j} & \frac{\partial^2 u_1}{\partial x_3 \partial x_j} \\ \frac{\partial^2 u_2}{\partial x_1 \partial x_j} & \frac{\partial^2 u_2}{\partial x_2 \partial x_j} & \frac{\partial^2 u_2}{\partial x_3 \partial x_j} \\ \frac{\partial^2 u_3}{\partial x_1 \partial x_j} & \frac{\partial^2 u_3}{\partial x_2 \partial x_j} & \frac{\partial^2 u_3}{\partial x_3 \partial x_j} \end{pmatrix}$$

Its components are calculated by second order finite difference discretization as:

$$\begin{aligned} V_{xx}(x,y,z) &= \frac{V(x-h,y,z) - 2V(x,y,z) + V(x+h,y,z)}{h^2} \\ V_{xy}(x,y,z) &= \\ &\times \frac{V(x+h,y+h,z) - V(x+h,y-h,z) - V(x-h,y+h,z) + V(x-h,y-h,z)}{4h^2} \end{aligned} \tag{19}$$

Other derivative components are calculated similarly. At the boundaries, one-sided differences are used, for both the first and the second order derivatives.

3 Experiments and Results

3.1 Regularizer Test

To test the regularizer initially, the algorithm is run on 10×10×10 mask on a 20×20×20 lattice with a single constant displacement vector (0.0001,0.0001,0.0) and zero boundary conditions. The central *xy*-plane of the input and the result obtained with $\mu = 0.8$ and $D_1 = 1.0$ is given in Fig. 3 with a closer look at Fig. 4. The effect of setting the parameters of the model at the lower and higher limits is shown on the middle and the right sub-figures of Fig. 4. Although incompressibility is a necessity for our problem as discussed in the method, setting a nonzero value to μ helps to increase the stability of the solution.

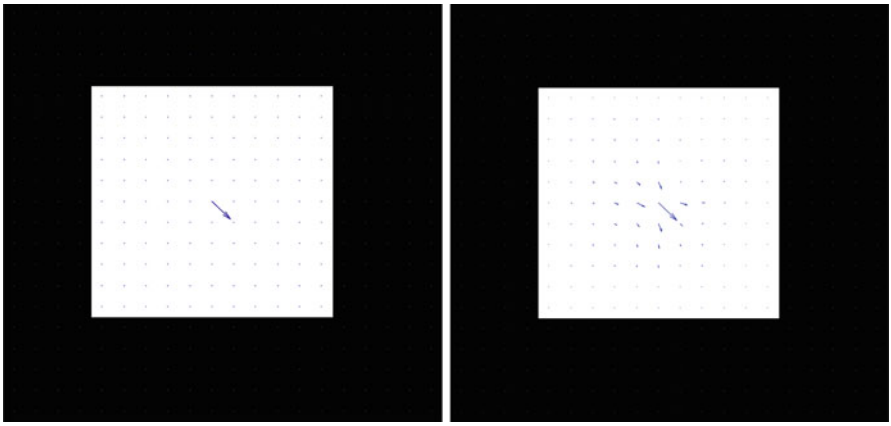

Fig. 3 *Left*: Input phantom for the regularizer test. *Right*: Output of the regularizer test

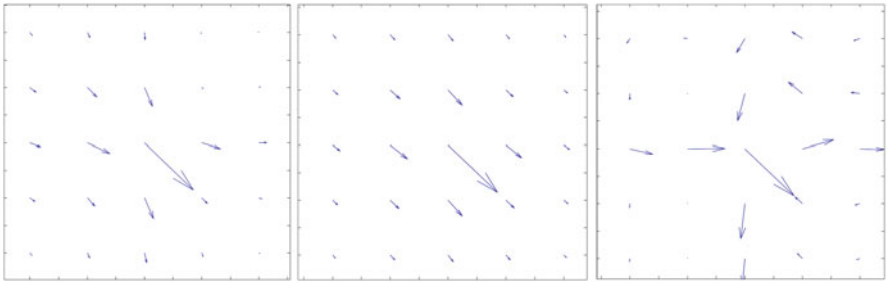

Fig. 4 *Left*: A closer view of the output of the regularizer test on phantom. *Middle*: The result obtained on phantom by increasing μ in the strain energy density model in Eq. (12). *Right*: The result obtained on phantom by setting the μ as zero in the strain energy density model in Eq. (12)

3.2 Phantom Results

To test the algorithm, two synthetic volumes are created as a sphere and an ellipsoid. Firstly, the method is run to determine the displacement field from sphere to ellipsoid by considering only the image terms, without the regularization. The results obtained with these external energies alone are shown in Fig. 5.

The central *xy*-plane of the result obtained by considering both image terms and the regularizer with $\mu = 0.4$ and $D_1 = 1.0$ is given in Fig. 6. Since the target volume is larger than the reference, the incompressibility, enforced by a low μ, results curled field to minimize the change of the volume. Shortfall appearance of the vectors is due to the 2D slice visualization of the 3D vector field.

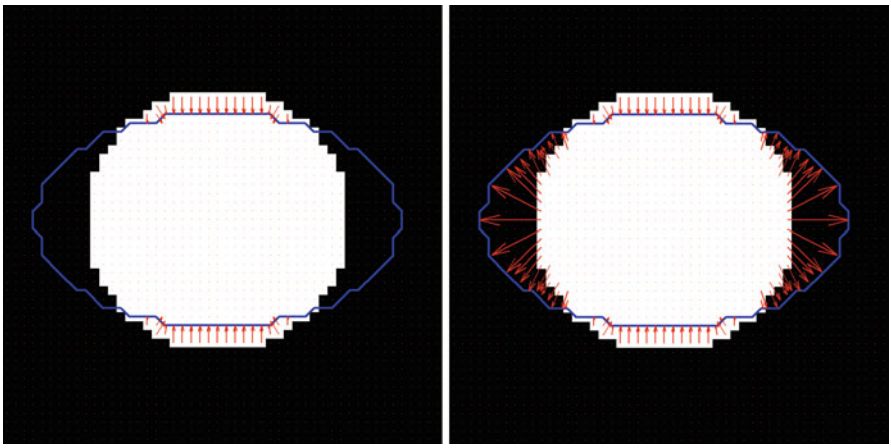

Fig. 5 The central slices of the results obtained on synthetic volumes by applying the volumetric data term only (*on left*) and boundary data term only (*on right*) without regularization

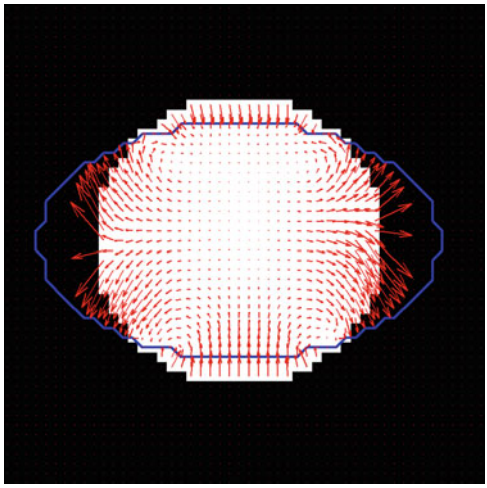

Fig. 6 The result obtained on the synthetic volumes. Reference spherical volume is labeled with *white color*, the *blue contour* represents the boundary of the target ellipsoid, and the displacement field from sphere to ellipsoid is indicated with *arrows in red color*

3.3 Experiments on MRI Brain Tumor Follow-up Volumes

3.3.1 The Data

MR images of a brain tumor patient (Glioblastoma Multiforme), obtained by 1.5T MRI scanner at high resolution ($\approx 0.5 \times 0.5 \times 1.0$ mm) contiguous axial T1 weighted 3D SPGR (TE/TR=3.16s/8.17s, FA=25°) sequence acquired after IV injection of 10cc 0.5M Multihance Gd, is used for validation study. The sample slices of the baseline and the follow-up volume, obtained 35 days after, are given in Figs. 1 and 2.

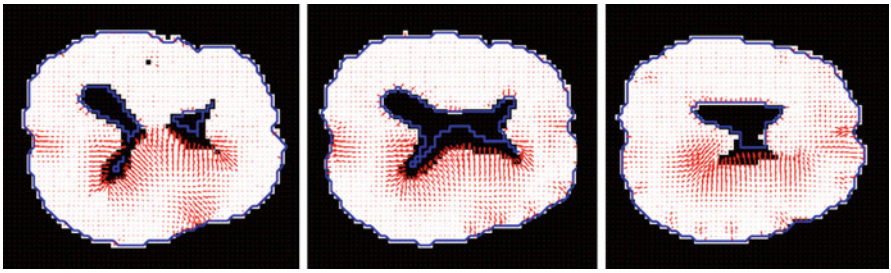

Fig. 7 Sample slices of the result obtained on tumor patient data in $3\times3\times3$ mm voxel size. Binarized brain tissue of the reference volume is labeled in *white color*, the *blue contour* indicates the boundary of the target volume, and the displacement field is indicated with *arrows in red*

3.3.2 Preprocessing MRI Volumes

Statistical Parametric Mapping (SPM) software,[1] distributed by Wellcome Trust Centre for Neuroimaging, London, which gives accurate results in brain volumes with tumors, is used for standard operations such as: rigid registration, segmentation, and smoothing. Specifically, the following preprocessing operations are applied to the data before the execution of the deformable registration:

- Follow-up volume is registered to the baseline volume using co-register function of SPM8.
- White matter (WM) and gray matter (GM) segmentations ($P > 0.5$) are obtained for both volumes using SPM8.
- Tumors in both volumes are segmented using the Tumor-cut algorithm [5].
- For each of the volumes, Tumor, WM and GM segmentations are combined using: $\Omega_{\text{Tumor}} \cup \Omega_{\text{WM}} \cup \Omega_{\text{GM}}$.
- Each combined binary volume is smoothed by smooth function of the SPM8 with a Gaussian kernel having $8\times8\times8$ mm full width at half maximum.
- Finally, binary maps are converted to isotropic voxels ($1\times1\times1$ mm).

3.3.3 Results

Sample slices of the result obtained on tumor patient data are shown in Fig. 7. Intense displacement on the hemisphere with tumor, due to the mass effect, can be observed. At the bottom of the sub-figure on the right, displacement of the sulci due to the increased cerebrospinal fluid (CSF) pressure can be seen. Also, the increase in the CSF pressure results slight displacements at the ventricles of the healthy hemisphere, on the top. Displacement field, overlayed on a sample axial slice of the reference MRI in high resolution, is given in Fig. 8. The mass effect around the

[1] http://www.fil.ion.ucl.ac.uk/spm/

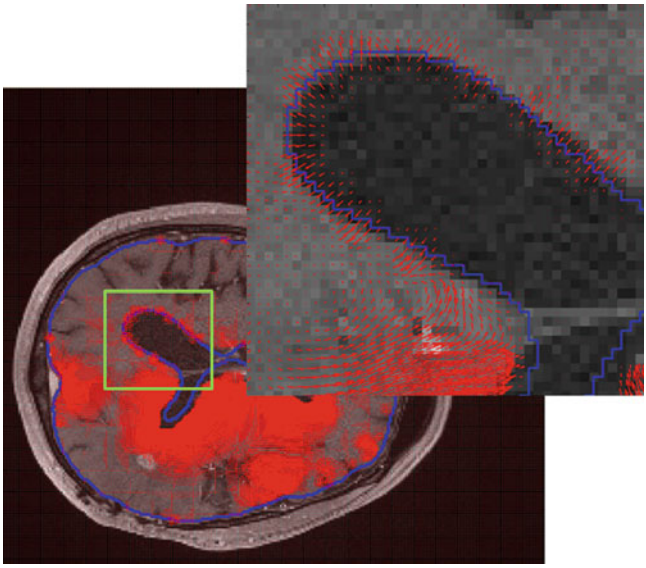

Fig. 8 Displacement field (*in red*) overlayed on a sample MRI slice of the reference volume, with the boundary of the target volume indicated with the *blue contour*. A closer look to the ventricle of the hemisphere without tumor

tumor is clearly observed. A closer look to the ventricle at the hemisphere without tumor depicts the displacement due to the expansion of the ventricle. When we focus on the displacement around the tumor as in Fig. 9, the displacement caused by the mass-effect (at the top) and the tumor growth (on the right) can be observed. The vectors at the bottom-left of the tumor explains the local shrinkage of the tumor as a tissue displacement.

4 Discussion and Conclusions

A method to register the brain tissues in baseline and follow-up MRI volumes using finite deformation models is presented. Implementations on synthetic and patient data, with only minimal user interaction, provide promising results, which might have relevant use in clinical problems. Publicly available state-of-the-art algorithms for the rigid registration and tissue/tumor segmentation are able to provide highly accurate outputs, which is a necessity to obtain an accurate displacement field. Accuracy of the method could be increased by improving the data term, such as by adding vessel correspondences or manual landmarks.

Acknowledgments This work was partially supported by TUBA-GEBIP (Turkish Academy of Sciences) and EU FP7 Grant No: PIRG03-GA-2008-231052.

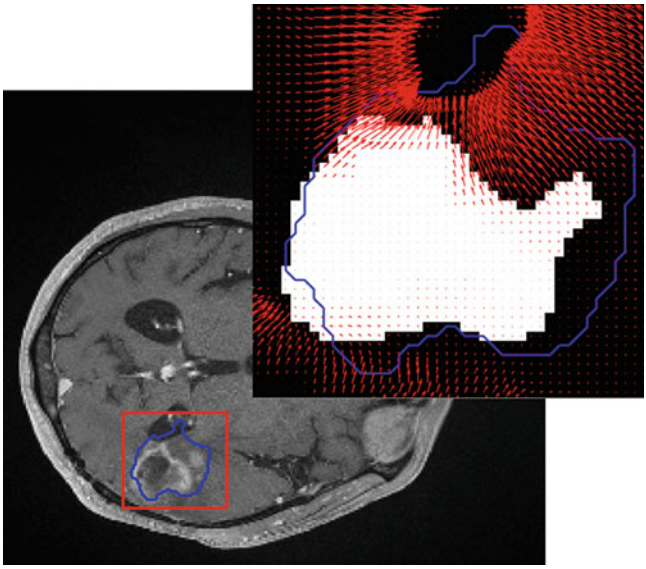

Fig. 9 A closer look to the tumor where the baseline tumor volume is labeled with *white color*, the follow-up tumor boundary is indicated with *blue contour* and the displacement field is overlayed with *red arrows*

References

1. Bower, A.F.: Applied Mechanics of Solids. Taylor and Francis Group, LLC (2010)
2. Clatz, O., Sermesant, M., Bondiau, P.Y., Delingette, H., Warfield, S., Malandain, G., Ayache. N.: Realistic simulation of the 3d growth of brain tumors in mr images coupling diffusion with biomechanical deformation. IEEE Trans. Med. Imag. **24**(10), 1334–1346 (2005)
3. Davatzikos, C.: Spatial transformation and registration of brain images using elastically deformable models. Comput. Vis. Image Understand. **66**(2), 207–222 (1997)
4. Demir, A., Unal, G., Karaman, K.: Anatomical landmark based registration of contrast enhanced t1-weighted mr images. In: Proceedings of the 4th International Conference on Biomedical Image Registration, pp. 91–103. Springer, Berlin, Heidelberg, WBIR'10 (2010)
5. Hamamci, A., Kucuk, N., Karaman, K., Engin, K., Unal, G.: Tumor-cut: Segmentation of brain tumors on contrast enhanced mr images for radiosurgery applications. IEEE Trans. Med. Imag. **31**(3), 790–804 (2012)
6. Hogea, C., Biros, G., Abraham, F., Davatzikos, C.: A robust framework for soft tissue simulations with application to modeling brain tumor mass effect in 3D MR images. Phys. Med. Biol. **52**(23), 6893 (2007)
7. Joldes, G.R., Wittek, A., Miller, K.: Suite of finite element algorithms for accurate computation of soft tissue deformation for surgical simulation. Med. Image Anal. **13**(6), 912–919 (2009)
8. Konukoglu, E., Clatz, O., Bondiau, P.Y., Delingette, H., Ayache, N.: Extrapolating glioma invasion margin in brain magnetic resonance images: suggesting new irradiation margins. Med. Image Anal. **14**(2), 111–125 (2010)
9. Miller, K., Chinzei, K.: Mechanical properties of brain tissue in tension. J. Biomech. **35**(4), 483–490 (2002)

10. Mohamed, A., Davatzikos, C.: Finite element modeling of brain tumor mass-effect from 3D medical images. In: Proceedings of the 8th International Conference on Medical Image Computing and Computer-Assisted Intervention - Volume Part I, pp. 400–408. Springer, Berlin, Heidelberg, MICCAI'05 (2005)
11. Niethammer, M., Hart, G., Pace, D., Aylward, S.: Geometric metamorphosis. In: MICCAI (2011)
12. Pedregal, P.: Variational Methods in Nonlinear Elasticity. Society for Industrial and Applied Mathematics, Philadelphia, PA, USA (2000)
13. Periaswamy, S., Farid, H.: Elastic registration with partial data. In: Proceedings of Workshop on Biomedical Image Registration WBIR03, pp. 102–111 (2003)
14. Prastawa, M., Bullitt, E., Gerig, G.: Simulation of brain tumors in MR images for evaluation of segmentation efficacy. Med. Image Anal. **13**(2), 297–311 (2009)
15. Reuter, M., Rosas, H.D., Fischl, B.: Highly accurate inverse consistent registration: a robust approach. NeuroImage **53**(4), 1181–1196 (2010)
16. Wittek, A., Miller, K., Kikinis, R., Warfield, S.K.: Patient-specific model of brain deformation: Application to medical image registration. J. Biomech. **40**(4), 919–929 (2007)
17. Wittek, A., Hawkins, T., Miller, K.: On the unimportance of constitutive models in computing brain deformation for image-guided surgery. Biomech. Model. Mechanobiology **8**, 77–84 (2009)
18. Yanovsky, I., Le Guyader, C., Leow, A., Toga, A.W., Thompson, P.M., Vese, L.: Unbiased volumetric registration via nonlinear elastic regularization. In: Pennec, X. (ed.) 2nd MICCAI Workshop on Mathematical Foundations of Computational Anatomy, New York, États-Unis (2008)

Heterogeneous Biomechanical Model on Correcting Brain Deformation Induced by Tumor Resection

Yixun Liu and Nikos Chrisochoides

Abstract In this paper we present a non-rigid registration method to align pre-operative MRI (preMRI) with resected intra-operative MRI (iMRI) to compensate for brain deformation during tumor resection. This method formulates the registration as a three-variable (point correspondence, deformation field and resection region) functional minimization problem, in which point correspondence is represented by a fuzzy assign matrix, deformation field is represented by a piece-wise linear function regularized by the strain energy of a heterogeneous biomechanical model, and resection region is represented by a maximal connected tetrahedral mesh. A Nested Expectation and Maximization framework is developed to simultaneously resolve these three variables. This method accommodates a heterogeneous biomechanical model as the regularization term to realistically describe the underlying deformation field and allows the removal of the tetrahedra from the model to simulate the tumor resection. A simple two tissue heterogeneous model (ventricle plus the rest of the brain) is used to evaluate this method on 14 clinical cases. The experimental results show the effectiveness of this method in correcting the deformation induced by resection. The comparison between the homogeneous model and the heterogeneous model demonstrates the statistical significance of the improvement brought by the heterogeneous model (P-value 0.04)

Y. Liu
Department of Computer Science, Old Dominion University, Norfolk, USA

Radiology and Imaging Sciences, National Institutes of Health
e-mail: yixun.liu@nih.gov

N. Chrisochoides (✉)
Department of Computer Science, Old Dominion University, Norfolk, USA
email: nikos@cs.odu.edu

A. Wittek et al. (eds.), *Computational Biomechanics for Medicine: Models, Algorithms and Implementation*, DOI 10.1007/978-1-4614-6351-1_11,

© Springer Science+Business Media New York 2013

1 Introduction

Brain shift severely compromises the fidelity of image-guided neurosurgery (IGNS). Most studies use a biomechanical model to estimate the brain shift based on sparse intra-operative data after the dura is opened [1–3]. Very few studies in the literature address brain deformation during and after tumor resection. The difficulty originates from the fact that resection creates a cavity, which renders the biomechanical model defined on pre-operative MRI inaccurate due to the existence of the additional part of the model corresponding to the resection region. In this work, the model accuracy will be improved by (1) removing the tetrahedra in the model corresponding to the resection region and (2) building a heterogeneous biomechanical model, which is facilitated by our multi-tissue mesh generation method [4].

In [5], Miga et al. investigated tissue retraction and resection using sparse operating room (OR) data and a finite element model. They developed a two-step method: (1) remove tissue volume by manual deletion of model elements that coincide with the targeted zone and then (2) apply boundary conditions to the new surfaces created during the excision process. Determining the cavity is challenging because a portion of it will be filled by surrounding tissues [6]. Our method eliminates the manual removal step by treating the resection region as a variable, which is able to be automatically resolved by a Nested Expectation and Maximization (EM) framework, an extension of traditional EM optimization [7]. Based on the bijective Demons algorithm, Risholm et al. presented an elastic FEM-based registration algorithm and evaluated it on the registration of 2D pre- with intra-operative images, where a superficial tumor has been resected [8]. Ding et al. [6] presented a semi-automatic method based on postbrain tumor resection and laser range data. Vessels were identified in both pre-operative MRI and laser range image; then the robust point matching (RPM) method [9] was used to force the corresponding vessels to exactly match each other under the constraint of the bending energy of the whole image. RPM uses thin-plate splines (TPS) as the mapping function. The basis function of TPS is a solution of the biharmonic [10], which does not have compact support and will therefore lead to, in real application, unrealistic deformation in the region far away from the matching points. In other words, RPM is not suitable for estimating deformation using sparse data. We use a heterogeneous biomechanical model to realistically simulate the underlying movement of the brain, which extends our previous work using a homogeneous model [11].

In this work, we target the specific feature point-based non-rigid registration (NRR) problem, which can be stated as:

Given a heterogeneous patient-specific brain model, a source point set in pre-operative MRI and a target point set in intra-operative MRI, find point correspondence, deformation field and resection region.

To resolve this problem, the three variables are incorporated into one cost function, which is minimized by a Nested EM strategy. The deformation field is represented by a displacement vector defined on the mesh nodes, the correspondence

between two point sets is represented by a correspondence matrix, and the resection region is represented by a connected submesh.

2 Method

In this section, we first develop the cost function step by step from a simple point-based non-rigid registration cost function to the three-variable cost function and then present a Nested Expectation and Maximization framework to resolve it.

2.1 Cost Function

Given a source point set $S = \{s_i\}_{i=1}^{N} \in \Re^3$ and a target point set $T = \{t_i\}_{i=1}^{N} \in \Re^3$, with known correspondence, i.e., s_i corresponding to t_i, the point-based non-rigid registration problem can be formulated as:

$$\bar{u} = \arg\min_{u} \left(\int_{\Omega} R(u) \mathrm{d}\Omega + \lambda \sum_{s_i \in \Omega} \|s_i + u(s_i) - t_i\|^2 \right) \tag{1}$$

where the first term is regularization or smoothing energy, and the second term is similarity energy. u is the deformation field and λ controls the trade-off between these two energies. Ω is the problem domain, namely the segmented brain. The removed tumor influences Ω and therefore influences both terms in Eq. (1). We extend Eq. (1) to (2) by specifying the regularization term with the strain energy of a linear elastic model, removing the limitation of correspondence between S and T, and accommodating tumor resection.

$$(\bar{u}, \bar{c}_{ij}, \bar{\Omega}') = \arg\min_{u, c_{ij}, \Omega'} \left(\int_{\Omega - \Omega'} \sigma(u)\varepsilon(u) d(\Omega - \Omega') + \lambda_1 \sum_{s_i \in \Omega - \Omega'} \|s_i + u(s_i) - \sum_{t_j \in \Omega_R} c_{ij} t_j\|^2 \right) + \lambda_2 \iiint_{\Omega'} \mathrm{d}x\mathrm{d}y\mathrm{d}z \tag{2}$$

where variable Ω' represents the resection region, and variable c_{ij} reflects the degree to which point s_i corresponds to t_j. The c_{ij} is defined as in RPM [9] with soft assignment. The classic Iterative Closest Point (ICP) method [12] treats the correspondence as a binary variable and assigns the value based on the nearest-neighbor relationship. However, this simple and crude assignment is not valid for non-rigid registration, especially when large deformation and outliers are

involved [13]. We define a range Ω_R, a sphere centered at the source point with radius R, and only take into account: (1) the target points, which are located in Ω_R of the source point, and (2) the source points, which have at least one target point in Ω_R. Thus, with this simple extension of RPM, our method is capable of eliminating outliers existing in both point sets. The first two terms come from the extension of Eq. (1), and the last term is used to prevent too much regions from being rejected.

The homogeneous model employed in the regularization term in Eq. (2) is further extended to the following heterogeneous model:

$$(\bar{u}, \bar{c}_{ij}, \bar{\Omega}') = \arg\min_{u, c_{ij}, \Omega'} \left(\sum_{\Omega_i \in \Omega - \Omega'} \int_{\Omega_i} \sigma_i(u) \varepsilon_i(u) d\Omega_i + \lambda_1 \sum_{s_i \in \Omega - \Omega'} ||s_i + u(s_i) - \sum_{t_j \in \Omega_R} c_{ij} t_j||^2 \right) + \lambda_2 \iiint_{\Omega'} \mathrm{d}x\mathrm{d}y\mathrm{d}z \tag{3}$$

where $\cup \Omega_i = \Omega - \Omega'$, $i = 1 \ldots n$.

Remark: If $n = 1$, $\Omega' =$ Empty, and $c_{ij} = 1$ then Eq. (3) is reduced to Eq. (1), which means the proposed method can be viewed as a general point-based NRR method characterized by (1) employing a heterogeneous biomechanical model as the regularization, (2) accommodating incomplete data, and (3) without correspondence requirement.

Equation (3) is approximated by Eq. (4) using finite element method:

$$J(U, C, M_{\mathrm{Rem}}) = \sum U^{\mathrm{T}} K_i U + \lambda_1 (HU - D(C))^{\mathrm{T}} W (HU - D(C)) + \lambda_2 |M_{\mathrm{Rem}}| \tag{4}$$

where $U^{\mathrm{T}} K_i U$ approximates $\int_{\Omega_i} \sigma_i(u) \varepsilon_i(u) d\Omega_i$ as in [14, 15]. C is a point correspondence matrix with entries c_{ij}. The equation to calculate c_{ij} will be given later. The entries of the vector D are defined as: $d_i(c_{ij}) = s_i - \sum_{t_j \in \Omega_R} c_{ij} t_j, \forall s_i \in M \backslash M_{\mathrm{Rem}}$, where M is the non-resected mesh that approximates Ω, and M_{Rem} is the removed mesh that approximates Ω'. The first term of Eq. (4) is the strain energy assembled on all elements in $M \backslash M_{\mathrm{Rem}}$, the second term is similarity energy defined on all source points $s_i \in M \backslash M_{\mathrm{Rem}}$, and the third term prevents too much tetrahedral from being rejected.

W in the second term is a weighted matrix of size $3|S| \times 3|S|$. W is a block-diagonal matrix whose 3×3 submatrix W_k is defined as $\frac{m}{|S|} S_k^{\mathrm{avg}}$, where m is the number of the vertices of the mesh. $\frac{m}{|S|}$ makes the matching term independent of the numbers of the vertices and the registration (source) points. S_k^{avg} is the average stiffness tensor for the k-th registration point. S_k^{avg} makes the registration point behavior like an elastic node of the finite element model. Assume the k -th registration point is located in the tetrahedron defined by vertices c_i, $i \in [0:3]$. S_k^{avg} is calculated by $S_k^{\mathrm{avg}} = \sum_{i=0}^{3} h_i K_{c_i}$, where K_{c_i} is a 3×3 sub-matrix of the global

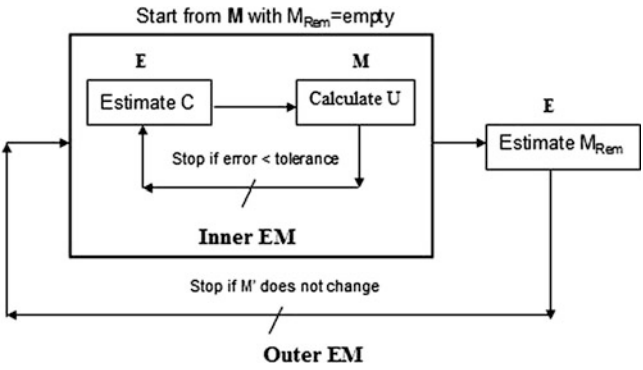

Fig. 1 Nested expectation and maximization framework

stiffness matrix K. h_i is the interpolation factor, the element of the global linear interpolation matrix H [16].

Finding C and M_{Rem} is equivalent to outlier rejection. We developed a Nested Expectation and Maximization method to iteratively reject point and element outliers.

2.2 Nested Expectation and Maximization

The Expectation and Maximization (EM) algorithm [7] is a general algorithm for maximum-likelihood [17] estimation of the model parameter (unknowns) in the presence of missing or hidden data. EM proceeds iteratively to estimate the model parameters. Each iteration of the EM algorithm consists of two steps: The E step and the M step. In the E step, the missing data is estimated given the observed data and current estimate of the model parameters. In the M step, the likelihood function is maximized under the assumption that the missing data is known. The estimate of the missing data from the E step is used in lieu of the actual missing data. Convergence is assured since the algorithm is guaranteed to increase the likelihood at each iteration [7].

The proposed Nested EM framework is shown in Fig. 1. The inner EM is used to resolve $\langle U, C \rangle$ with M_{Rem} fixed, and the outer EM is used to resolve M_{Rem}. M_{Rem} is approximated as a collection of tetrahedra located in a region of the model, which corresponds to the resection region in the intra-operative MRI. M_{Rem} is initialized as empty and updated at each iteration of the outer EM. If all the tetrahedra contained in the resection region are collected, the outer EM stops.

$[U, C]$=*PtOutlierRejection*$(M, M_{Rec}, S, T, \epsilon, r)$

Input: M: non-resected mesh, M_{Rec}: resected mesh, S: source points, T: target points, ϵ: tolerance, r: annealing rate, R: search ragne, S: source points, T: target points
Output: U: displacement vector, C: correspondence matrix

1: $U \Leftarrow I$
2: **repeat**
3: Transform S based on U: $S \Leftarrow U(S)$
4: E step:
// outlier rejection for S
5: $S \Leftarrow S \setminus \{s_i |$ if no target points in Ω_R for $s_i\}$
// outlier rejection for T
6: $S \Leftarrow T \setminus \{t_i |$ if no source points list it within $\Omega_R\}$
7: Estimate correspondence C
8: M step:
9: Solve U
10: $change \Leftarrow \|U_i - U_{i-1}\|$ between successive iterations
11: Decrease R: $R \Leftarrow R \times r$
12: **until** $change < \epsilon$

Alg 1. Feature point outlier rejection (inner EM)

2.2.1 Inner EM

Inner EM is used to resolve $\langle U, C \rangle$ given M_{Rem}.

For each source point s_i, assume its correspondences are subject to Gaussian distribution, so c_{ij} can be estimated (E step) by Eq. (5).

$$c_{ij} = \frac{c'_{ij}}{\sum_{k=1}^{m} c'_{ik}}, c'_{ij} = \frac{1}{R\sqrt{2\pi}} \mathrm{e}^{\frac{-(t_j - s_i)^2}{2R^2}}, \forall t_j \in \Omega_R, j = 1 \ldots m \tag{5}$$

Once C is estimated, U can be resolved by solving the minimization equation obtained by setting the derivative of functional (4) to zero, i.e., $\mathrm{d}J/\mathrm{d}U = 0$. The last term can be ignored because it becomes a constant. The resolved U is used to warp S closer to T, and then the correspondence C is estimated again. The pseudo code of the inner EM is presented in Algorithm 1.

2.2.2 Outer EM

Outer EM is used to find M_{Rem}. In M step, $\langle U, C \rangle$ is resolved by the inner EM. In E step, M_{Rem} is resolved by an element outlier rejection algorithm. M_{Rem} is approximated by a collection of tetrahedron outliers, which fall in the resection region of the intra-operative MRI. The resection region does not need to be identified

$[M_{Rem}, S]$=*EleOutlierRejection*(M, M_{Rem}, U, BGI)

Input: M: non-resected mesh, M_{Rem}: removed mesh,
U: displacement vector, BGI: background image
Output: M_{Rem}: new removed mesh, S: new source points
1: Obtain deformed resected mesh $M_{Def} \Leftarrow U(M \setminus M_{Rem})$
2: Find all elements M_1 completely contained in the background image BGI and constitute the largest connected mesh with M_{Rem}
3: Map M_1 in M_{Def} to M_2 in $M \setminus M_{Rem}$
4: $S \Leftarrow S \setminus \{s_i | s_i \in M_2\}$
5: $M_{Rem} \Leftarrow M_{Rem} \cup M_2$
6: Scale Young's modulus for the elements across the boundary

Alg 2. Element outlier rejection

in the intra-operative MRI, and it is in fact impossible to distinguish the resection region from the background. The Background Image *BGI* including the resection region and the background can be very easily segmented by a simple threshold segmentation method. However, we cannot determine if a tetrahedron is an outlier based only on whether it is located in the *BGI* because this tetrahedra might happen to fall in the background rather than the resection region. To make the element outlier rejection algorithm robust, we utilize the fact that the resection region is a collection of tetrahedra, which not only fall in the *BGI* of intra-operative MRI but also connect with each other and constitute a maximal connected submesh. The collection of the outliers proceeds iteratively, and at each iteration, more specifically the E step of outer EM, additional outliers will be added into M_{Rem} if they fall in the *BGI* and connect with the maximal connected submesh identified in previous iteration.

The element outlier rejection algorithm is presented in Algorithm 2.

The outer EM iteratively rejects element outliers using Algorithm 2 and computes $\langle U, C \rangle$ using Algorithm 1 until no additional element outliers are detected. Algorithm 3 presents the whole pseudo code of the Nested EM algorithm.

3 Results

We conducted experiments on 14 clinical cases using MRI data, which were acquired with the protocol: T1-weighted magnetization-prepared rapid gradient echo (MPRAGE) sagittal images with [dimension $= 256 \times 256 \times 176$, in plane resolution $= 1.0 \times 1.0$ mm, thickness $= 1.0$ mm, FOV $= 256 \times 256$].

Figure 2a shows the multi-tissue mesh we used to build the heterogeneous model.

Figure 2b shows the result of element outlier rejection produced by Algorithm 2 and the deformation field of the heterogeneous model. A portion of the brain is cut

$[U, M_{Rem}, C]$=*NEMNRR*$(preMRI, iMRI)$

Input: $preMRI$: pre-operative MRI, $iMRI$: intra-operative MRI
Output: U: displacement vector
1: Segment brain on $preMRI$ and do mesh generation to produce M
2: Segment background image BGI on $iMRI$
3: Canny edge detection on $preMRI$ to get S
4: Canny edge detection on $iMRI$ to get T
5: Input R, ϵ, and r
6: Initiate $M_{Rem} \Leftarrow \varnothing$
7: **repeat**
8: M step: $U, C \Leftarrow$*PtOutlierRejection*$(M, M_{Rem}, S, T, \epsilon, r, R)$
9: E step: $M_{Rem}, S \Leftarrow$*EleOutlierRejection*(M, M_{Rem}, U, BGI)
10: **until** M_{Rem} does not change

Alg 3. Nested expectation and maximization

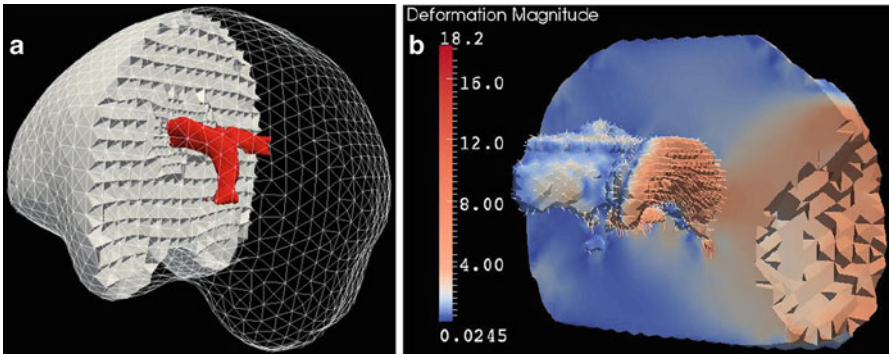

Fig. 2 **(a)** Multi-tissue mesh: brain and ventricle. **(b)** Deformation field of resected heterogeneous model

off to expose the ventricle and its deformation field. The largest deformation reaches 18.2 mm, still in the effective range of the linear elastic biomechanical model. The larger deformation occurs in the region near the resection, and the ventricle on the tumor side is squeezed inward as the arrows show.

Figure 3 shows the results of point outlier rejection produced by Algorithm 1. Comparing to the edges before outlier rejection, most point outliers are removed after outlier rejection.

Figure 4 shows the results of the Nested EM method. We superimpose edges detected on iMRI onto preMRI and warped preMRI, respectively, to illustrate the improvement of the boundary matching after registration.

To quantitatively evaluate the proposed method, Hausdorff Distance (HD) [18] is employed as the measurement of the registration accuracy. We use outlier rejected edge points in preMRI and iMRI to calculate HD before non-rigid registration

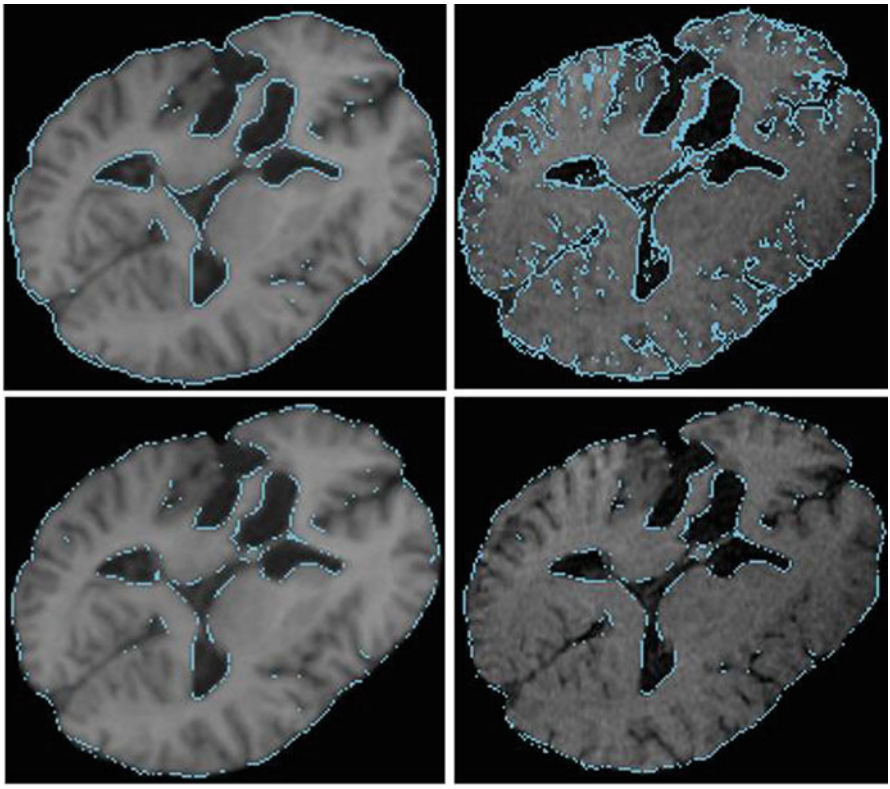

Fig. 3 Point outlier rejection. The *blue* points are edge detected by canny edge detection. The top two figures are edge points before outlier rejection. The *bottom* two figures are remaining edge points after outlier rejection

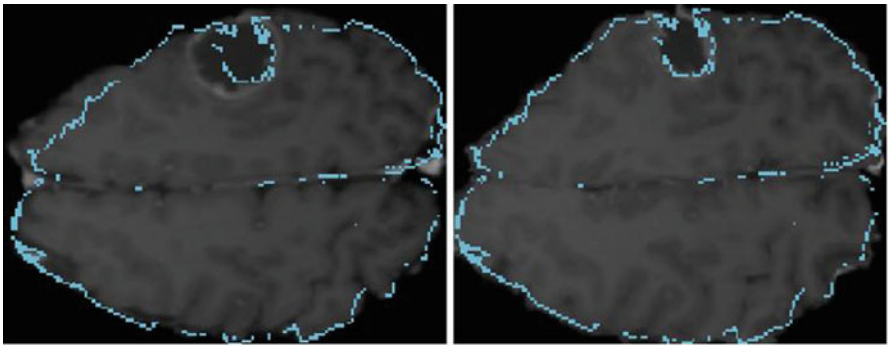

Fig. 4 Qualitative evaluation regarding canny edges. The *blue points* are edge detected by canny edge detection on iMRI. The detected edge points are superimposed on the preMRI (*left*) and warped preMR (*right*)

(after rigid registration) and use outlier rejected edge points in iMRI and warped preMRI to calculated the HD after registration. Both the homogeneous model and the heterogeneous model are used for the registration. As shown in Table 1, both models can significantly improve the accuracy.

We also conducted experiments to compare the homogeneous model and the heterogeneous model. To specifically measure the influence of the model on the registration, we employ the multi-tissue mesh, as shown in Fig. 2a, in both models. As a result, the influence of the discrepancy of the geometry and topology between the single mesh and the multi-tissue mesh can be eliminated. The only difference between the two models is the biomechanical attributes of the ventricle. The homogeneous model uses Young's modulus $E = 3,000\,\text{Pa}$, Poisson's ratio $\nu = 0.45$ for all tetrahedra, and the heterogeneous model replaces Young's modulus with $E = 10\,\text{Pa}$ and Poisson's ratio with $\nu = 0.1$ for the ventricle [19]. We compared the two models regarding edge points with HD as the measurement. The evaluation results show the magnitude improvement brought by the heterogeneous model is not large, but statistically significant (Two tailed t test, P-value 0.04).

4 Conclusion and Future Work

We present a novel non-rigid registration method to compensate for brain deformation induced by tumor resection. This method does not require the point correspondence to be known in advance and allows the input data to be incomplete.

This method uses strain energy of the biomechanical model to regularize the solution. To improve the fidelity of the simulation of the underlying deformation field, we build a heterogeneous model based on a multi-tissue mesher. To resolve the deformation field with unknown correspondence and resection region, we develop a Nested EM framework, which can effectively resolve these three variables simultaneously.

The heterogeneous model, embedded in the proposed registration method, can incorporate as many tissues as possible. In this work, we use a simple two-tissue model to perform the evaluation. Compared to rigid registration, the proposed method can significantly improve the accuracy. Compared to the homogeneous model, the improvement of the accuracy brought by the heterogeneous model is statistically significant. We believe as more tissues are incorporated into the model, such as the falx of the brain, the improvement of the accuracy will become more noticeable.

Table 1 Quantitative evaluation of Nested EM NRR regarding edge points using HD for 14 cases

	1	2	3	4	5	6	7	8	9	10	11	12	13	14
Rigid	8.31	9.27	15.43	11.70	11.49	9.85	12.69	2.12	10.34	13.30	14.28	13.64	13.60	15.26
Homo	1.17	1.12	1.54	1.22	1.62	1.50	1.54	2.12	1.54	1.88	3.81	3.96	2.19	2.95
Hete	1.13	1.06	1.33	1.14	1.58	1.32	1.95	1.41	1.50	1.85	2.96	3.66	2.14	2.18
Homo-Hete	0.04	0.06	0.21	0.08	0.04	0.18	−0.41	0.71	0.04	0.03	0.85	0.30	0.05	0.77

"*Rigid*" denotes the error after rigid registration, "*Homo*" denotes the error after non-rigid registration using a homogeneous model, "*Hete*" denotes the error after non-rigid registration using a heterogeneous model, and the "*Homo-Hete*" denotes the improvement brought by the heterogeneous model. The unit of the error is mm. $\lambda_1 = 1.0$. $R = 10.0\,\text{mm}$

Acknowledgements This work was supported in part by NSF grants CCF-1139864, CCF-1139864, and CSI-1139864, as well as by the John Simon Guggenheim Foundation and the Richard T. Cheng Endowment.

References

1. Miga, M.I., Paulsen, K.D., Lemery, J.M., Eisner, S.D., Hartov, A., Kennedy, F.E., Roberts, D.W.: Model-updated image guidance: initial clinical experiences with gravity-induced brain deformation. IEEE Trans. Med. Imag. **18**(10), 866–74 (1999)
2. Ferrant, M., Nabavi, A., Macq, B., Jolesz, F., Kikinis, R., Warfield, S.: Registration of 3-d intraoperative mr images of the brain using a finite-element biomechanical model. IEEE Trans. Med. Imag. **20**(12), 1384–97 (2001)
3. Skrinjar, O., Nabavi, A., Duncan, J.: Model-driven brain shift compensation. Med. Image Anal. **6**(4), 361–73 (2002)
4. Liu, Y., Foteinos, P., Chernikov, A., Chrisochoides, N.: Multitissue mesh generation for brain images. In: International Meshing Roundtable, **19**, pp. 367–384 (2010)
5. Miga, M.I., Roberts, D., Kennedy, F., Platenik, L., Hartov, A., Lunn, K., Paulsen, K.: Modeling of retraction and resection for intraoperative updating of images. Neurosurgery **49**(1), 75–84 (2001)
6. Ding, S., Miga, M.I., Noble, J.H., Cao, A., Dumpuri, P., Thompson, R.C., Dawant, B.M.: Semiautomatic registration of pre- and post brain tumor resection laser range data: method and validation. IEEE Trans. Biomed. Eng. **56**(3), 770–80 (2009)
7. Dempster, A.P., Laird, N.M., Rubin, D.B.: Maximum likelihood from incomplete data via the em algorithm. J. R. Stat. Soc. Ser. B **39**, 1–38 (1977)
8. Risholm, P., Melvær, E.L., Mørken, K., Samset, E.: Intra-operative adaptive fem-based registration accommodating tissue resection. Medical Imaging 2009: Image Processing 7259(1), pp. 72 592Y–72 592Y–11. SPIE (2009)
9. Haili, C., Rangarajan, A.: A new point matching algorithm for nonrigid registration. Comput. Vis. Image Underst. **89**(2–3), 114–141 (2003)
10. Bookstein, F.L.: Principal warps: thin-plate splines and the decompostion of deformations. IEEE Trans. Pattern Anal. Mach. Intell. **11**(6), 567–585 (1989)
11. Liu, Y., Yao, C., Zhou, L., Chrisochoides, N.: A point based non-rigid registration for tumor resection using IMRI. In: 2010 IEEE International Symposium on Biomedical Imaging: From Nano to Macro, pp. 1217–1220 (2010)
12. Besl, P.J., McKay, N.D.: A method for registration of 3-d shapes. IEEE Trans. Pattern Anal. Mach. Intell. **14**(2), 239–256 (1992)
13. Rangarajan, A., Chui, H., Bookstein, F.L.: The softassign procrustes matching algorithm. In: Information Processing in Medical Imaging, pp. 29–42. Springer, New York (1997)
14. Bathe, K.: Finite Element Procedure. Prentice Hall, New Jersey (1996)
15. Hughes, T.J.R.: The Finite Element Method: Linear Static and Dynamic Finite Element Analysis, pp. 207–208. Dover Publications, Mineola (2000)
16. Clatz, O., Delingette, H., Talos, I.-F., Golby, A., Kikinis, R., Jolesz, F., Ayache, N., Warfield, S.: Robust non-rigid registration to capture brain shift from intra-operative MRI. IEEE Trans. Med. Imag. **24**(11), 1417–1427 (2005)
17. John, A.: R. a. fisher and the making of maximum likelihood 1912–1922. Stat. Sci. **12**(3), 162–176 (1997)
18. Hausdorff, F.: Set Theory, 2nd edn. Chelsea Publishing, New York (1962)
19. Wittek, A., Miller, K., Kikinis, R., Warfield, S.K.: Patient-specific model of brain deformation: application to medical image registration. J. Biomech. **40**(4), 919–929 (2007)

Intra-operative Update of Neuro-images: Comparison of Performance of Image Warping Using Patient-Specific Biomechanical Model and BSpline Image Registration

Ahmed Mostayed, Revanth Reddy Garlapati, Grand Roman Joldes, Adam Wittek, Ron Kikinis, Simon K. Warfield, and Karol Miller

Abstract This paper compares the warping of neuro-images using brain deformation predicted by means of patient-specific biomechanical model with the neuro-image registration using BSpline-based free form deformation algorithm. Deformation fields obtained from both algorithms are qualitatively compared and overlaps of edges extracted from the images are examined. Finally, an edge-based Hausdorff distance metric is defined to quantitatively evaluate the accuracy of registration for these two algorithms. From the results it is concluded that the patient-specific biomechanical model ensures higher registration accuracy than the BSpline registration algorithm.

A. Mostayed (✉) • R.R. Garlapati • G.R. Joldes • A. Wittek
Intelligent Systems for Medicine Laboratory, The University of Western Australia, Perth, Australia
e-mail: mostayed@mech.uwa.edu.au; revanth@mech.uwa.edu.au; grandj@mech.uwa.edu.au; adwit@mech.uwa.edu.au

R. Kikinis
Surgical Planning Laboratory, Brigham & Women's Hospital, Harvard Medical School, Boston, MA, USA
e-mail: kikinis@bwh.harvard.edu

S.K. Warfield
Computational Radiology Laboratory, Children's Hospital, Harvard Medical School, Boston, MA, USA
e-mail: Simon.Warfield@childrens.harvard.edu

K. Miller
Intelligent Systems for Medicine Laboratory, The University of Western Australia, Perth, Australia

Institute of Mechanics and Advanced Materials, Cardiff School of Engineering, Cardiff University, Wales, UK
e-mail: kmiller@mech.uwa.edu.au

A. Wittek et al. (eds.), *Computational Biomechanics for Medicine: Models, Algorithms and Implementation*, DOI 10.1007/978-1-4614-6351-1_12,
© Springer Science+Business Media New York 2013

1 Introduction

In a neurosurgical procedure the aim of a surgeon is to resect as much diseased tissues as possible while preserving healthy tissues. Sophisticated pre-operative imaging techniques have been developed over the past decade to aid neurosurgeons with improved visualization [1]. However, surgical interventions (craniotomy, for example) tend to distort the pre-operative anatomy and often lead to misalignment between the actual position of pathology and its position determined from pre-operative images [2]. In addition, constraints of the operating room restrict the contrast and resolution of intra-operative images. These barriers, in principle, can be overcome by aligning high quality pre-operative scans to intra-operative ones. Accurate alignment demands that the pre-operative image is non-rigidly registered with the intra-operative image.

The field of non-rigid registration of medical images has evolved in two separate streams. One way to register the pre-operative image with the intra-operative image is to use some intensity-based similarity criterion and derive a non-linear warp function, which then can be used for warping the pre-operative image. In this approach images are often treated as fluids or elastic bodies subjected to elastic deformation [3]. The similarity criterion acts as the driving force of the deformation. The BSpline-based free form deformation (FFD) algorithm [4] is considered as a state-of-the-art non-rigid registration algorithm belonging to this category. However, BSpline registration algorithm may often produce physically implausible deformation field [5].

On the other hand it is shown in [2, 6–10] that the craniotomy-induced brain shift can be predicted by non-linear biomechanical models. These models take into account the mechanical behaviour of different classes of brain tissue (ventricle, parenchyma, and tumour) and do not need a similarity criterion to drive the numerical computation. In fact, the need for a target image (intra-operative image in this case) can be eliminated and numerical computation can be carried out with only the knowledge of the displacement of few points on the brain surface near craniotomy.

In this work, the non-rigidly registered pre-operative images obtained using deformations within the brain predicted by means of both a biomechanical model [2, 6] and a BSpline algorithm implemented in 3D Slicer (www.slicer.org) are analyzed and compared. For five different patients undergoing surgery, the accuracy of registration is compared both qualitatively and quantitatively. The deformation fields obtained from each registration algorithm are qualitatively compared. Also the amount of overlap between edge contours obtained from the registered pre-operative image and the edge contours of the intra-operative image is compared for both registration algorithms. Finally, a novel edge-based Hausdorff distance (HD) measure is used to compare the results quantitatively.

2 Registration Methods

2.1 Image Data

Five surgery cases involving tumour resection were analysed in this work. They were used for biomechanical model-based warping in previous studies carried out in [2] and [6]. For each case a high resolution, high quality pre-operative image and a low resolution intra-operative image were available. For the purpose of this paper the preoperative image for each case is registered with its corresponding intra-operative image using both the biomechanical model and the BSpline registration algorithm. The pre-operative images have a resolution of $256 \times 256 \times 124$ voxels and the intra-operative images have a resolution of $256 \times 256 \times 60$ voxels. Voxel size for the pre-operative image is $0.9375 \times 0.9375 \times 1.3\,\text{mm}^3$ and for the intra-operative image $0.8594 \times 0.8594 \times 2.5\,\text{mm}^3$.

2.2 Image Warping Using Intra-operative Brain Deformations Predicted from Patient-Specific BiomechanicalModel

Construction of patient-specific finite element mesh. A three-dimensional (3D) surface model of each patient's brain was created from segmented pre-operative magnetic resonance image (MRI). A brain mesh was constructed from the surface model with 8-noded hexahedral and 4-noded tetrahedral elements. The meshes were generated using IA-FEMesh (University of Iowa [11]) and HyperMesh (commercial FE mesh generator by Altair of Troy, MI, USA).

Loading and boundary conditions. The displacements were applied on the exposed part (due to craniotomy) of the brain surface. In [12] it is suggested that for this type of loading the unknown deformation field within the brain very weakly depends on the constitutive model. The displacements for loading the models were determined from the segmented pre-operative and intra-operative cortical surfaces. The correspondence between pre-operative and intra-operative cortical surface was determined by applying the Vector-Spline regularization algorithm [13] to the surface curvature maps. In order to define the boundary condition for the unexposed nodes on the brain surface, a contact interface was defined between the rigid skull model and that part of the brain. The frictionless sliding contact proposed in [14] is used which prevents the brain from penetrating the skull.

Mechanical properties. According to [12] if geometric nonlinearity is considered, the results of prediction of deformation field within the brain shift are only weakly affected by the constitutive model of the brain tissue. Therefore, a simple Neo-Hookean model was used [15]. The Young's modulus of 3,000 Pa was selected for parenchyma [16]. The Young's modulus for tumour was assigned two times larger than for parenchyma. Poisson's ratio 0.49 was chosen for the parenchyma and tumour following [2].

Algorithm. An efficient algorithm for integrating the equations of solid mechanics has been developed by Joldes et al. [17–19]. The computational efficiency of this algorithm is achieved by using—(1) Total Lagrangian (TL) formulation [17] for updating the calculated variables; and (2) Explicit Integration in the time domain combined with mass proportional damping. In the TL formulation, all the calculated variables (such as displacements and strains) are referred to the original configuration of the analysed continuum [18]. The decisive advantage of this formulation is that all derivatives with respect to spatial coordinates can be pre-computed [17]. In explicit time integration, the displacement at time $t + \Delta t$(where Δt is the time step) is solely based on the equilibrium at time t. Therefore, no matrix inversion and iterations are required when solving nonlinear problems. Application of explicit time integration scheme reduces the time required to compute the brain deformations by an order of magnitude in comparison with implicit integration typically used in commercial finite element codes [2].

Image warping. At first the pre-operative image is aligned with the intra-operative image using rigid registration. In order to obtain the warped pre-operative image, the coordinate of each voxel of the discrete image grid has to be mapped onto the original (un-deformed) pre-operative image grid. To perform such mapping, the deformed (when predicting the deformation within the brain) and un-deformed (corresponding to the pre-operative brain geometry) brain meshes are first re-meshed by Delaunay tessellation. Then the enclosing tetrahedral element for each voxel is found using the Quick–Hull algorithm [20]. The coordinate of a particular voxel in the original pre-operative image grid is determined by using the shape functions of its enclosing tetrahedron. The intensity value of the voxel is interpolated from the intensity value of its neighbours by using tri-cubic interpolation [21]. All these tasks are performed using an in-house code programmed in MATLAB^{TM}.

2.3 BSpline Registration

BSplines are bell-shaped functions that were introduced by Schoenberg [22] for interpolation. Due to their minimal local support they have become a strong tool for modelling 3D deformable shapes. BSplines are useful for both interpolation and approximation of scattered data. Free-form-deformation (FFD) based on BSpline algorithm is widely used for non-rigid image registration [3]. The initial algorithm proposed by Rueckert et al. [4] was based on the multi-level BSpline approximation algorithm (MBA) developed by Lee et al. [23] for scattered data interpolation. The basic idea of FFD is to deform an object by manipulating an underlying mesh of control points. The resulting deformation controls the shape of the 3D object and produces a smooth transformation. The FFD algorithm maximizes the mutual information [24] between the pre-operative and intra-operative image to obtain the warping transform. A regular grid of control points with equal spacing is required.

For highly localized non-rigid deformations, which can be expected in neurosurgery, a high resolution control grid needs to be used. The resolution also defines the number of degrees of freedom (DoF) of the transformation, for example a $10 \times 10 \times 10$ grid of control points yields a transformation with $3 \times 10 \times 10 \times 10$ DoFs in 3D.

The BSpline transform for the analysed neurosurgery cases were obtained by the BSpline registration module of 3D Slicer v3.6. The initial size of the BSpline grid was $10 \times 10 \times 10$. Fifty histogram bins and 10,000 spatial samples were used to calculate the marginal and joint entropies [25]. Total number of iterations was selected as 20. The similarity criterion of this Slicer module is based on Mattes mutual information [25].

3 Qualitative Comparison

3.1 Deformation Field

The deformation fields predicted by the biomechanical model and the deformation field obtained from the BSpline transform are compared in Fig. 1. These deformation fields are three dimensional. However, for clarity, only arrows representing 2D vectors (x and y component of displacement) are shown overlaid on the un-deformed pre-operative slices. Each of these arrows represents the displacement of a voxel of the pre-operative image domain.

The deformation fields predicted by the biomechanical model is very similar to the one calculated from the BSpline registration for case 1. For this case the maximum deformation of the surface of the brain was approximately 4 mm. However, for case 2 deformation predicted by the biomechanical model significantly differs from that obtained using BSpline registration. For this case the maximum deformation of the brain surface was around 8 mm. For cases 3 and 5, the maximum deformation of the brain surface was between 4 and 5 mm. For these two cases, the deformation fields from the biomechanical model and BSpline registration are similar in the craniotomy and tumour areas, but look significantly different in other parts of the brain. For case 4, the deformation fields predicted using the two methods differ significantly near the craniotomy.

3.2 Canny Edges

Plot of deformation vectors provides useful estimate of the nature of non-rigid transform between two images. However, to obtain a qualitative assessment of the degree of alignment after registration, one must examine the overlap of corresponding anatomical features of the intra-operative and registered pre-operative

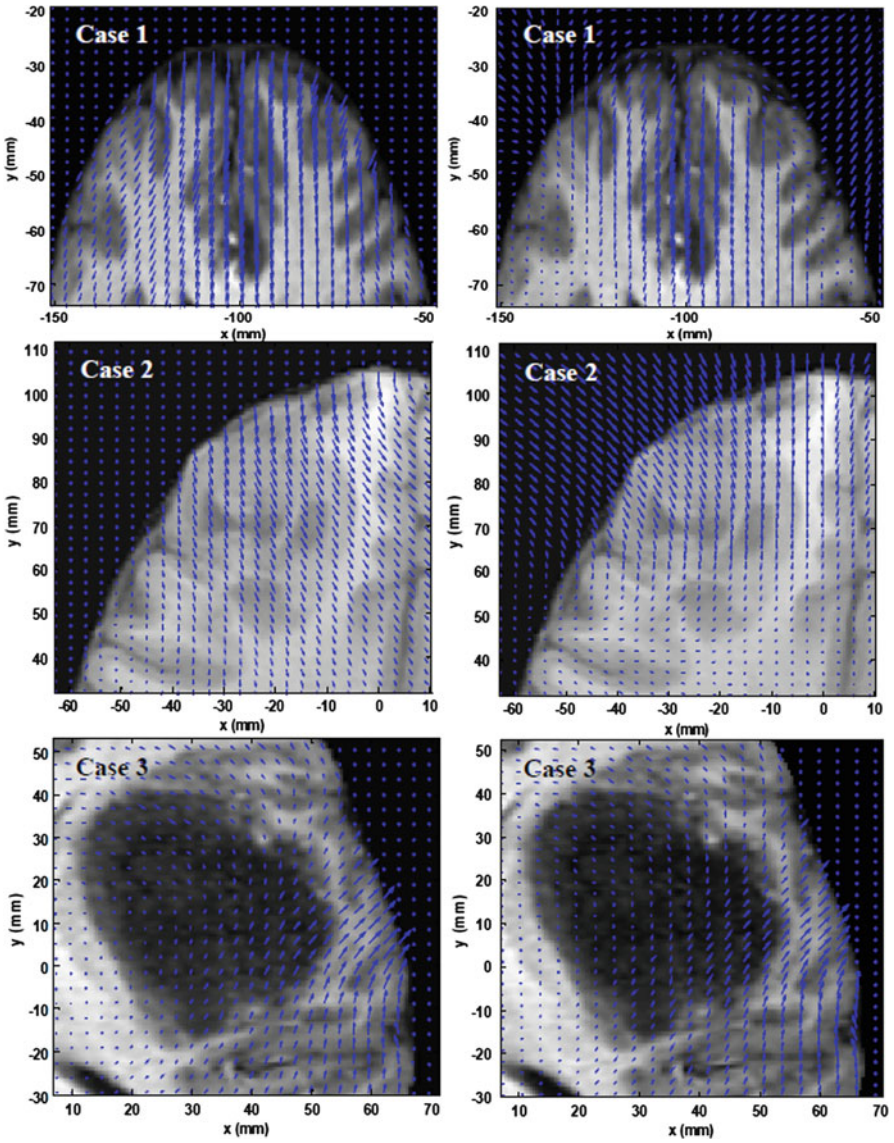

Fig. 1 The predicted deformation fields overlaid on an axial slice of pre-operative image. An arrow represents a 2D vector consisting of the x (R–L) and y (A–P) components of displacement at a voxel centre. Left column: deformation field predicted by biomechanical warping. Right column: deformation field derived from BSpline registration transform. The predicted deformation fields overlaid on an axial slice of pre-operative image. Left column: deformation field predicted by biomechanical warping. Right column: deformation field derived from BSpline registration transform

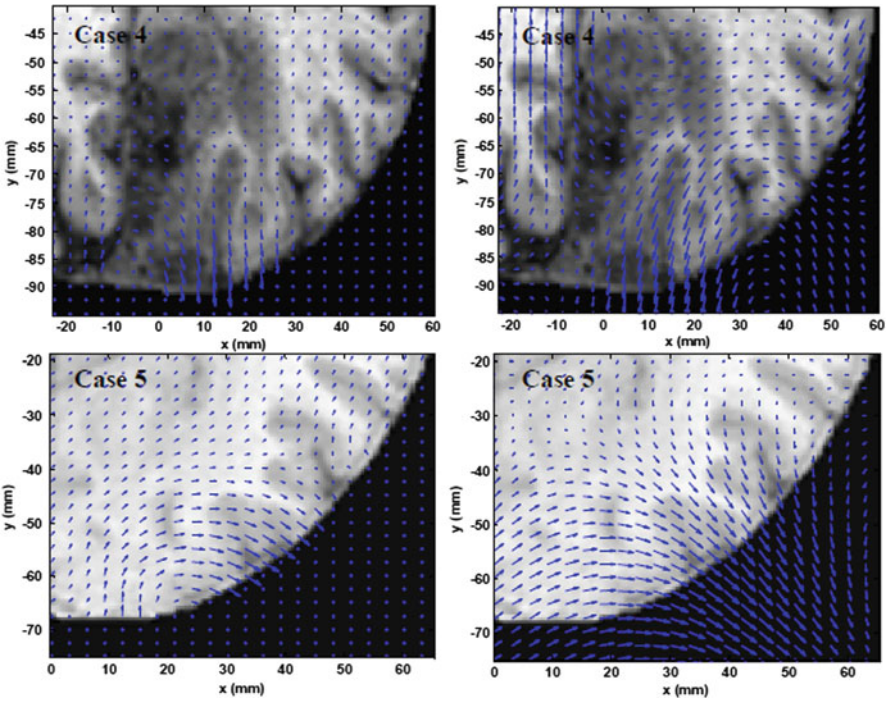

Fig. 1 (continued)

image. For this purpose tumours and ventricles in both registered pre-operative and intra-operative images can be segmented and their surfaces can be compared [6]. Image segmentation is time consuming, not fully automated and not suitable for comparing a large number of image pairs [26]. Therefore in this study, we use edges detected from an image. Such edges are regarded as useful and easily recognizable features, and they can be detected using techniques that are totally automated and fast. Hence, Canny edges [27] obtained from the intra-operative and registered pre-operative image slices are labelled in different colours and overlaid (Fig. 2). In Fig. 2 intra-operative edges are labelled with blue and pre-operative edges are represented with red and their overlap pixels are labelled in green.

From Fig. 2 we can see that misalignments between the edges detected from the intra-operative images and the edges from the pre-operative images updated to the intra-operative brain geometry are much lower for the biomechanics-based warping than for BSpline registration. The edges obtained from the images warped with both registration algorithms are similar for cases 1, 4, and 5. It is related to the fact that the deformation fields predicted using our biomechanical model and BSpline registration are very similar for these three cases. However, as indicated by visual inspections, for case 2, misalignment between the edges obtained from the intra-operative image and edges from the pre-operative image registered using

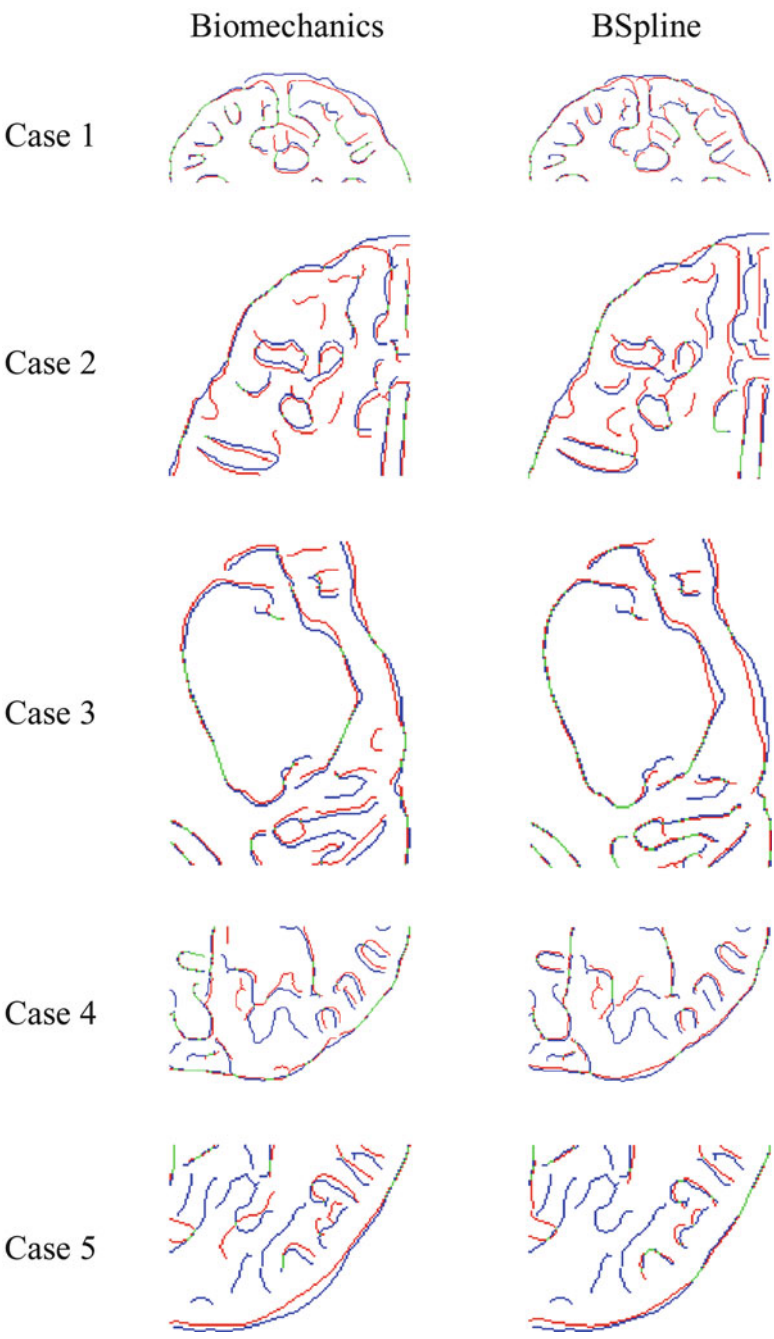

Fig. 2 Canny edges extracted from intra-operative and the registered pre-operative image slices overlaid on each other. Blue colour represents the non-overlapping pixels of the intra-operative slice and red colour represents the non-overlapping pixels of the pre-operative slice. Green colour represents the overlapping pixels. Left column: edges of the deformed pre-operative image obtained by applying biomechanical warping. Right column: edges of the deformed pre-operative image obtained by applying BSpline registration algorithm

BSpline algorithm can be observed. For this case there was a large intra-operative brain shift and the deformation field obtained using BSpline algorithm significantly differ from deformation predicted using biomechanical model. It is an indication that the BSpline registration algorithm cannot perform as well as the biomechanics warping if large deformation is involved. In Sect. 4 the misalignment between edges is quantified using a novel edge-based Hausdorff distance measure [28].

4 Quantitative Comparison

4.1 Edge-based Hausdorff Distance

We begin the section with a definition of the traditional point-based Hausdorff distance (HD) between two intensity images $\mathbf{I}$ and $\mathbf{J}$. Let I and be J the binary edge images derived from $\mathbf{I}$ and $\mathbf{J}$, respectively, and $\mathbf{A} = \{a_1, \cdots, a_n\}$ and $\mathbf{B} = \{b_1, \cdots, b_n\}$ are the set of non-zero points corresponding the non-zero pixels on the edge images, then the directed distance between them $h(\mathbf{A}, \mathbf{B})$ is defined as the maximum distance from any of the points in the first set to the second one:

$$h(\mathbf{A}, \mathbf{B}) = \underset{a \in \mathbf{A}}{\operatorname{argmax}} \left[\underset{b \in \mathbf{B}}{\operatorname{argmin}} \|a - b\|_2 \right] \tag{1}$$

$$h(\mathbf{B}, \mathbf{A}) = \underset{b \in \mathbf{B}}{\operatorname{argmax}} \left[\underset{a \in \mathbf{A}}{\operatorname{argmin}} \|b - a\|_2 \right] \tag{2}$$

The HD between the two sets $H(\mathbf{A}, \mathbf{B})$ is defined as the maximum of these two directed distances:

$$H(\mathbf{A}, \mathbf{B}) = \max\left(h(\mathbf{A}, \mathbf{B}), h(\mathbf{B}, \mathbf{A})\right) \tag{3}$$

The proposed directed distance between two sets of edges is defined as

$$h_e(\mathbf{A}^e, \mathbf{B}^e) = \underset{a_i^e \in \mathbf{A}^e}{\operatorname{argmax}} \left[\underset{b_j^e \in \mathbf{B}^e}{\operatorname{argmin}} \left\| a_i^e - b_j^e \right\| \right] \tag{4}$$

where $\mathbf{A}^e = \{a_1^e, \cdots, a_m^e\}$ and $\mathbf{B}^e = \{b_1^e, \cdots, b_n^e\}$ are two sets of edges.

The quantity $\|a_i^e - b_j^e\|$ in Eq. (4) is nothing but the point-based Hausdorff distance between two point sets $\mathbf{M} = \{m_1 \cdots, m_p\}$ and $\mathbf{T} = \{t_1 \cdots, t_q\}$ representing edges a_i^e and b_i^e, respectively,

$$\left\| a_i^e - b_j^e \right\| := d(a_i^e - b_j^e) = \max\left(h(\mathbf{T}, \mathbf{M}), h(\mathbf{M}, \mathbf{T})\right) \tag{5}$$

Now the edge-based Hausdorff distance is defined as

$$H_e(\mathbf{A}^e, \mathbf{B}^e) = \max\left(h_e(\mathbf{A}^e, \mathbf{B}^e), h_e(\mathbf{B}^e, \mathbf{A}^e)\right) \tag{6}$$

Fig. 3 Overlaid edges before (left) and after (right) round-trip consistency. Blue colour represents the non-overlapping pixels of the intra-operative slice and red colour represents the non-overlapping pixels of the pre-operative slice. Green colour represents the overlapping pixels

Pre-processing. Some pre-processing of the extracted edges was required before the edge-based Hausdorff distance could be calculated. Some small misalignments between the edges detected from two images are inevitable even after the registration. The pre-processing step finds the pixels of one image that are most likely to have correspondence with the other image. For each non-zero pixel involved in the binary edge image, A, the closest non-zero pixel in the other image, B, is found. The same procedure is repeated from this pixel in image B to find the closet non-zero pixel in image A. One would reach the starting point, if the images were perfectly aligned. However, in reality, the images are not perfectly aligned. Hence, we often end up at a point that is different from the starting point in image A. The distance between the starting point and end point in image A is termed the "round-trip distance". The pixels that have a round trip distance greater than a prescribed threshold (referred to as "round-trip threshold") are excluded (see Fig. 3), as they are less likely to have correspondence with any pixel in the other image. The higher the threshold; the lower the consistency between the pixels. However, excessively low value of this threshold can cause removal of important feature points. Hence, it is crucial to select an optimal threshold that maximizes the consistency and minimizes the number of features removed. Throughout this paper a threshold of 1.5 mm is used. The round-trip consistency procedure tends to generate artefacts by eliminating points in the interior of an edge which results in several broken edges. Such edge pixels are recovered by applying morphological filters [21]. Any edge shorter than 5 mm was removed from the images before maximizing the consistency using round-trip consistency criterion as their dimension is insignificant compared to the relevant brain dimension.

Methodology. For the quantitative evaluation of registration accuracy, each image volume was cropped into a region-of-interest (ROI) which encloses the tumour. These ROI sub-volumes were re-sliced (in the axial plane) with a slice thickness of 1.45 mm and the in-plane resolution was increased to $0.5 \times 0.5\,\text{mm}^2$. This was done to improve the precision of Canny edge detection [27] used in a slice-by-slice registration accuracy evaluation process. The proposed edge-based Hausdorff distance (HD) was used to calculate the misalignment between slice pairs. The directed distances for all edge pairs [see Eq. (4)] are recorded and the edge-based

Hausdorff distance values at different percentile of directed distances are plotted (see Fig. 4). The *P*th percentile HD, "D", between two images means that "*P*" percent of edge pairs have a Hausdorff distance below D.

4.2 Results

The percentile vs. Hausdorff distance (HD) curve provides an estimation of the percentage of edges that were successfully registered in the registration process (Fig. 4). As accuracy of the edge detection is limited within the image resolution, an alignment error twice the in-plane resolution of the intra-operative image (which is 0.8594 mm for the five cases considered) cannot be avoided. Hence, for five cases analysed here, any edge pair having HD value less than 1.7 mm can be considered successfully registered. It is obvious from Fig. 4 that biomechanical warping was able to successfully register more edges than the BSpline registration for all five cases.

Percentile of edges successfully registered by two registration algorithms (i.e. warping using biomechanical model and BSpline registration) for each analysed case is listed in Table 1. It can be clearly seen from this table that the percentile of successfully registered edge is higher for image warping using biomechanical model than for BSpline registration.

For all five cases, the percentiles vs. HD curves tend to rise steeply around 90 percentile. Hence, it can be safely assumed that edge pairs that do not have any correspondence (outliers) are between 91 and 100 percentile. The 90-percentile HD values for five cases are listed in Table 2.

5 Discussions

From the results presented in Sects. 3 and 4 it is evident that application of the intra-operative deformation predicted using patient-specific biomechanical model [2, 6] to warp pre-operative images ensures higher registration accuracy than BSpline-based image registration [4]. Biomechanical models are especially effective in neurosurgery cases where intra-operative brain shift is large. Another distinctive advantage of the biomechanical algorithm is that it does not need the intra-operative image at all to compute deformation. Only the displacement of a limited number of points on the exposed (during craniotomy) intra-operative brain surface is required. Such displacement can be determined from 3D ultrasound or 3D laser range imaging [29].

For image warping using the intra-operative brain deformation predicted from patient-specific biomechanical model, the required amount of intra-operative data points is reduced to a few hundred compared to few millions for BSpline registration (Table 3).

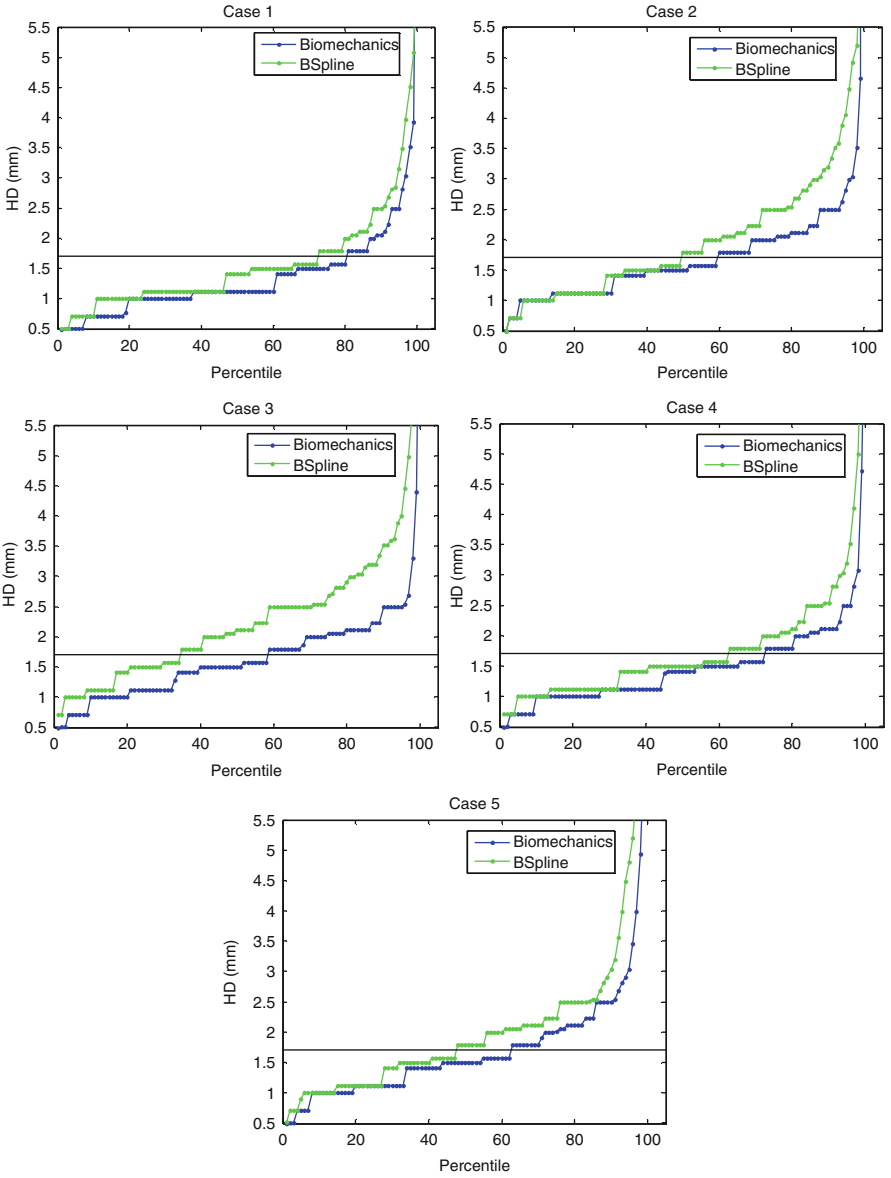

Fig. 4 The plot of Hausdorff distance between intra-operative and registered pre-operative images against the percentile of edges. The horizontal line is the 1.7 mm mark

Table 1 Percentile of edges successfully registered for five patient specific cases

	Percentile of edges successfully registered	
Case	Biomechanics	BSpline
'1'	80	72
'2'	59	49
'3'	58	34
'4'	72	62
'5'	62	47

Table 2 90 percentile Hausdorff distance values for five patient specific cases

	Non-rigid registration algorithm	
Case	Biomechanics	BSpline
'1'	2.06 mm	2.49 mm
'2'	2.49 mm	3.19 mm
'3'	2.49 mm	3.52 mm
'4'	2.11 mm	2.54 mm
'5'	2.49 mm	3.03 mm

Table 3 Number of points of intra-operative geometry required for numerical computation

	Data requirement (No. of points)	
Case	Biomechanics	BSpline
'1'	322	3.932×10^6
'2'	328	3.932×10^6
'3'	171	3.932×10^6
'4'	134	3.932×10^6
'5'	63	3.932×10^6

The presented results of comparison of warping of neuro-images using brain deformation predicted by means of patient-specific biomechanical model with the BSpline-based neuro-image registration were obtained using the BSpline algorithm implemented in 3D Slicer. An alternative implementation and alternative algorithms for image-based alignment should be evaluated in future work.

Acknowledgements The first author is a recipient of the SIRF scholarship and acknowledges the financial support of the University of Western Australia. The financial support of National Health and Medical Research Council (Grant No. APP1006031) is gratefully acknowledged. This investigation was also supported in part by NIH grants R01 EB008015 and R01 LM010033 and by a research grant from the Children's Hospital Boston Translational Research Program. In addition, the authors also gratefully acknowledge the financial support of Neuroimage Analysis Center (NIH P41 EB015902), National Center for Image Guided Therapy (NIH U41RR019703) and the National Alliance for Medical Image Computing (NAMIC), funded by the National Institutes of Health through the NIH Roadmap for Medical Research, Grant U54 EB005149. Information on the National Centers for Biomedical Computing can be obtained from http://nihroadmap.nih.gov/bioinformatics.

References

1. Warfield, S.K., Haker, S.J., Talos, I.F. et al.: Capturing intraoperative deformations: research experience at Brigham and Women's hospital. Med. Image Anal. **9**, 145–162 (2005)
2. Wittek, A., Miller, K., Kikinis, R. et al.: Patient specific model of brain deformation: Application to medical image registration. J. Biomech. **40**, 919–929 (2007)
3. Holden, M.: A review of geometric transformations for nonrigid body registration. IEEE Trans. Med. Imag. **27**, 111–128 (2008)
4. Rueckert, D., Sonoda, L.I., Hayes, C. et al.: Nonrigid registration using free-form deformations: Application to breast MR images. IEEE Trans. Med. Imag. **18**, 712–721 (1999)
5. Schnabel, J.A., Tanner, C., Castellano-Smith, A.D.: Validation of nonrigid image registration using finite-element methods: application to breast MR images. IEEE Trans. Med. Imag. **22**, 238–247 (2003)
6. Wittek, A., Joldes, G., Couton, M. et al.: Patient-specific non-linear finite element modelling for predicting soft organ deformation in real-time; Application to non-rigid neuroimage registration. Progr. Biophys. Mol. Biol. **103** 292–303 (2010)
7. Miller, K., Wittek, A., Joldes, G. et al.: Modelling brain deformations for computer-integrated neurosurgery. Int. J. Numer. Meth. Biomed. Eng. **26** 117–138 (2010)
8. Paulsen, K.D., Miga, M.I., Kennedy, F.E. et al.: A computational model for tracking subsurface tissue deformation during stereotactic neurosurgery. IEEE Trans. Biomed. Eng. **46**, 213–225 (1999)
9. Miga, M.I.: Development and quantification of a 3D brain deformation model for model-updated image-guided stereotactic neurosurgery. PhD. thesis, Dartmouth College, Thayer School of Engineering, Hanover (1998)
10. Miga, M.I., Paulsen, K.D., Hoopes, P.J. et al.: In vivo modeling of interstitial pressure in the brain under surgical load using finite elements. ASME J. Biomech. **122**, 354–363 (2000)
11. Grosland, N.M., Shivanna, K.H., Magnotta, V.A. et al.: IA-FEMesh: an open-source, interactive, multiblock approach to anatomic finite element model development. Comput. Meth. Programs Biomed. **94**, 96–107 (2009)
12. Wittek, A., Hawkins, T., Miller, K.: On the unimportance of constitutive models in computing brain deformation for image-guided surgery. Biomech. Model. Mechanobiology **8**, 77–84 (2009)
13. Joldes, G.R., Wittek, A., Miller, K.: Cortical surface motion estimation for brain shift prediction. In: Computational Biomechanics for Medicine IV Workshop (MICCAI 2009). London, UK, p. 50–59 (2009)
14. Joldes, G., Wittek, A., Miller, K. et al.: Realistic and efficient brain-skull interaction model for brain shift computation. In: Computational Biomechanics for Medicine III (MICCAI 2008 Associated Workshop), p. 95–105 (2008)
15. Joldes, G., Wittek, A., Couton, M. et al.: Real-time prediction of brain shift using nonlinear finite element algorithms. Medical Image Computing and Computer Assisted Intervention (MICCAI 2009), London, LNCS 5762, p. 300–307 Springer, Berlin (2009)
16. Miller, K., Chinzei, K.: Mechanical properties of brain tissue in tension. J. Biomech. **35**, 483–490 (2002)
17. Miller, K., Joldes, G.R., Lance, D. et al.: Total Lagrangian explicit dynamics finite element algorithm for computing soft tissue deformation. Communications. In Numerical Methods in Engineering vol. **23**, 121–134 (2007)
18. Joldes, G., Wittek, A., Miller, K.: Computation of intra-operative brain shift using dynamic relaxation. Comput. Meth. Appl. Mech. Eng. **198**, 3313–3320 (2009)
19. Joldes, G.R., Wittek, A., Miller, K.: Suite of finite element algorithms for accurate computation of soft tissue deformation for surgical simulation. Med. Image Anal. **13**, 912–919 (2009)
20. Barber, C.B., Dobkin, D.P., Huhdanpaa, H.T.: The quickhull algorithm for convex hulls. ACM Trans. Math. Softw. 22, 469–483 (1996)
21. Gonzalez, R.C., Woods, R.E., Eddins, S.L.: Digital Image Processing using Matlab. Gatesmark Publishing (2009)

22. Schoenberg, I.J.: Contributions to the problem of approximation of equidistant data by analytic functions. Q. Appl. Math. **4**, 45–99 (1946)
23. Lee, S., Wolberg, G., Shin, S.Y.: Sacttered data interpolation with multilevel B-Splines. IEEE Trans. Visual. Comput. Graph. **3**, 228–244 (1997)
24. Wells III, W.M., Viola, P., Atsumi, H. et al.: Multi-modal volume registration by maximization of mutual information. Medical Image Analysis 1, 35-51 (1996)
25. Mattes, D., Haynor, D.R., Vesselle, H. et al.: Nonrigid multimodality image registration. In: Proceedings of SPIE 4322, 1609 (2001)
26. Fedorov, A., Billet, E., Prastawa, M. et al.: Evaluation of Brain MRI alignment with the Robust Hausdorff distance measures. In: The 4th International Symposium on Visual Computing 2008, LNCS, p. 594–603 (2008)
27. Canny, J.: A computational approach to edge detection. IEEE Trans. Pattern Anal. Mach. Intell. **8**, 679–698 (1986)
28. Garlapati, R.R., Joldes, G.R., Wittek, A., et al.: Objective evaluation of accuracy of intra-operative neuroimage registration. In: Computational Biomechanics for Medicine VII (MICCAI Associated Workshop) (accepted) (2012)
29. Ji, S., Fan, X., Roberts, D.W. et al.: Cortical surface strain estimation using stereovision. In: Medical Image Computing and Computer Assisted Intervention (MICCAI 2011), Toronto. LNCS 6891, p. 412–419 Springer, Berlin (2011)

Part IV
Musculoskeletal System, Muscles and Injury Biomechanics

Trabecular Bone Poroelasticity for MicroCT-Based FE Models

Clara Sandino and Steven K. Boyd

Abstract A useful mathematical model that describes the mechanical behavior of bone is the poroelastic model. So far, numerical studies of trabecular bone poroelasticity have considered the tissue as a homogeneous porous structure. The objective of this study was to develop a methodology for creating large-scale finite element models that predict the poroelastic response of trabecular bone, including the tissue micro-architecture. $1\,cm^3$ cubes of bovine trabecular bone were scanned using micro-computed tomography. Finite elements models were developed using different voxel and sample sizes. Strain equivalent to 1% of deformation was applied at three different rates and confined and unconfined conditions were simulated. Stress distributions in the bone phase were similar under confined and unconfined conditions. The fluid velocity and the pore pressure in the marrow were higher under confined than under unconfined conditions. The trabecular bone stiffness was higher under confined compared to under unconfined conditions, increasing with increments in the strain rate. Variations in the sample size were more significant in the predicted stiffness than variations in the voxel size. This study included both the poroelasticity and the micro-architecture of trabecular bone to predict changes in the mechanical response of trabecular tissue under time-dependent loading conditions.

C. Sandino (✉) • S.K. Boyd
Schulich School of Engineering, University of Calgary, Calgary, Canada

Roger Jackson Centre for Health and Wellness Research, University of Calgary, Calgary, Canada

McCaig Institute for Bone and Joint Health, University of Calgary, Calgary, Canada
e-mail: csandino@kin.ucalgary.ca; skboyd@ucalgary.ca

A. Wittek et al. (eds.), *Computational Biomechanics for Medicine: Models, Algorithms and Implementation*, DOI 10.1007/978-1-4614-6351-1_13,

© Springer Science+Business Media New York 2013

1 Introduction

The poroelastic properties of trabecular bone play a critical role in the biomechanical response of bone tissue. Trabecular bone gives supporting strength to the ends of the weight-bearing bones, and this strength is related to the strain rate due to its poroelastic nature [4, 9]. Additionally, the inter-trabecular porous space is connected to the modularity cavity and is saturated with marrow, fat, and blood vessels. The marrow contains stem cells, which can differentiate into different phenotypes in order to generate tissue [3].

Trabecular bone poroelasticity has been studied at the macroscopic level [5]. At this level, trabecular bone tissue, which is formed by an interconnected structure of rods and plates saturated with marrow, is considered as a homogeneous material with specific properties describing its poroelastic behavior. Most of the studies have been focused on determining trabecular bone poroelastic properties [8, 11]. The study of Nauman et al. [11] demonstrated that the permeability of trabecular bone ranges over three orders of magnitude depending on the porosity and the anatomical site.

The introduction of the micro-computed tomography (μCT) technology makes it possible to obtain 3D reconstructions with enough resolution to differentiate bone from marrow [10]. From these reconstructions, finite element (FE) models can be developed to study the distribution of stresses and strains throughout the tissue. So far, most of the bone studies using FE models based on μCT images have used the linear elastic formulation [14]. The poroelastic response of trabecular bone, taking into account its specific micro-architecture, has not been studied before to our knowledge.

The objective of this study is to develop a methodology for creating μCT-based large-scale FE models that introduce the effect of the microstructure of the tissue in the study of the poroelasticity of trabecular bone. This kind of models will allow to determine the distribution of mechanical stimuli not only in the bone phase but also in the marrow, as well as the contribution of the marrow to the biomechanical response of the trabecular bone.

2 Methods

2.1 Mathematical Description of the Model

The Biot formulation [2] of the constitutive equations for a linear isotropic poroelastic material states:

The constitutive equation for the porous solid is:

$$\sigma_{ij} + \alpha p\, \delta_{ij} = 2G\varepsilon_{ij} + \frac{2G\nu}{1-2\nu}\varepsilon_{kk}\delta_{ij} \tag{1}$$

where σ_{ij} is the stress tensor, p is the pore pressure, ε_{ij} is the strain tensor, δ_{ij} Kronecker delta, α is the Biot coefficient of effective stress, G is the shear modulus, and ν is the Poisson's ratio.

The constitutive equation for the fluid is:

$$2G\zeta = \frac{\alpha(1-2\nu)}{1+\nu}\left(\sigma_{kk} + \frac{3}{B}p\right) \tag{2}$$

where ζ is the variation of fluid content per unit volume of porous media, σ is the stress, p is the pore pressure, α is the Biot coefficient of effective stress, B is the Skempton pore pressure coefficient, G is the shear modulus, and ν is the Poisson's ratio.

The Biot and the Skempton coefficients can be expressed in terms of the Bulk modulus and the pore volume fraction as:

$$\alpha = 1 - \frac{K}{K_s} \tag{3}$$

$$B = \frac{\alpha K_{\mathrm{f}}}{[\alpha - \phi(1-\alpha)]K_{\mathrm{f}} + \phi K} \tag{4}$$

where ϕ is the pore volume fraction, K is the bulk modulus, K_f is the bulk modulus of the fluid, and K_s is the bulk modulus of the solid.

The Darcy's law, expressed as:

$$q = -\frac{k}{\mu}(\nabla p - \rho_{\mathrm{f}} g) \tag{5}$$

where q is the rate of fluid volume crossing a unit area of porous solid, ∇p is the pressure gradient, k the intrinsic permeability having dimension of length squared, μ the fluid viscosity, and $\rho_f g$ is the body force per unit volume of fluid with ρ_f the fluid density.

The equilibrium equation is:

$$\frac{\mathrm{d}\sigma}{\mathrm{d}x} = -\rho g \tag{6}$$

where ρg is the body force per unit volume of the bulk material, and ρ is the bulk density defined as $\rho = (1-\phi)\rho_s + \phi\rho_f$, where ρ_s and ρ_f are the densities of the solid and the fluid phase, respectively.

The continuity equation is defined as:

$$\zeta + \frac{\mathrm{d}q}{\mathrm{d}x} = \gamma \tag{7}$$

where ζ is the variation of fluid content per unit volume of porous media and γ is the source density (the rate of injected fluid volume per unit volume of the porous solid).

Fig. 1 2D μCT slice of a $1\,cm^3$ sample of bovine trabecular bone. Bone shown in gray and marrow shown in black

2.2 *Specimen Preparation and* μCT *Scanning and Segmentation*

$1\,cm^3$ cubes of bovine trabecular bone were cut using an IsoMet 5000 linear precision saw (Buehler, Canada). The cubes were scanned using μCT (Scanco Medical μCT 35 Brüttisellen, Switzerland; 70 kVp, 114 μA, 400 ms integration time) resulting in an isotropic voxel size of 20 μm. The 3D images were smoothed using a Gaussian filter (sigma = 0.8, support = 1.0) and segmented using a threshold of 22.0% of the maximum value (Fig. 1). Between the cutting and the scanning, the samples were wrapped in gauze wet with saline solution and stored at −30°C.

2.3 *FE Models*

Eight-node hexahedral FE meshes were obtained directly from the 3D images using the voxel-based method. Each element corresponds to one voxel. Bone and marrow were simulated using the poroelastic formulation describe in Sect. 2.1. Material properties are listed in Table 1. A uniform displacement equivalent to uniaxial deformation of 1% was applied on the nodes of the top fixing the nodes of the bottom. Three different strain rates were used: 0.1%, 1%, and 10% strain per second. Confined and unconfined fluid conditions were simulated. For the unconfined system, the pore pressure was set as zero on the nodes of the walls. Models were solved in Abaqus (Simulia, USA) using transient consolidation analysis. Principal stresses and strains, pore pressure, fluid velocity, and total reaction force were computed. In order to compare the samples of different sizes, the apparent stiffness (total reaction force/area) was determined.

Table 1 Material properties [7]

Property	Bone	Marrow
Young's modulus (MPa)	17,000	2
Poisson's ratio	0.3[a]	0.17
Porosity	0.04[b]	0.8
Permeability (m/s)	9.64×10^{-14}[c]	9.64×10^{-11}
Solid bulk modulus (MPa)	17,660[d]	2,300[e]
Fluid bulk modulus (MPa)	2,300[e]	2,300[e]

[a]Cowin [5]; [b]Schaffler and Burr [12]; [c]Johnson et al. [6]; [d]Smit et al. [13]; [e]Anderson [1]

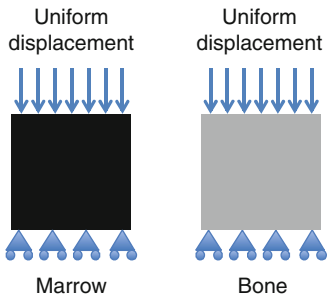

Fig. 2 Schematic representation of FE models

2.4 Investigations into Poroelastic Behavior

With the purpose of understanding the effect of the poroelastic formulation on the response of trabecular bone under compressive strain, and to determine the critical size and resolution that should be used to model the poroelasticity of trabecular bone, three studies were conducted:

2.4.1 Effect of Loading Conditions and Material Properties

1 mm^3 cubes with homogeneous material properties were simulated. Separated models for bone and marrow were created (Fig. 2).

2.4.2 Effect of Voxel Size

1 mm^3 cubic sections of trabecular bone with voxel size of 40 and 80 µm were simulated (Fig. 3).

2.4.3 Effect of Sample Size

1 and 8 mm^3 cubic sections of trabecular bone with voxel size of 80 µm were simulated (Fig. 4).

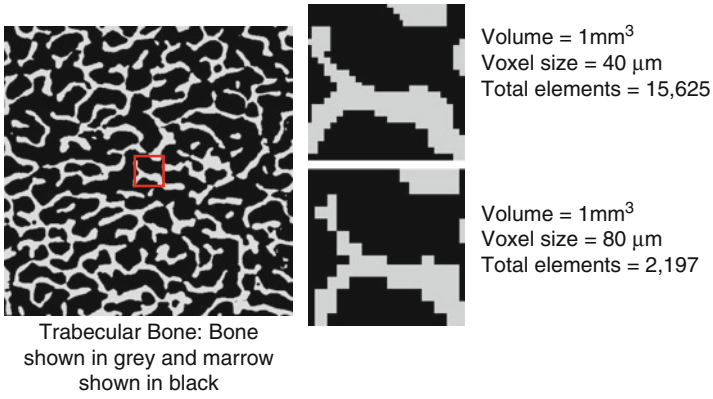

Fig. 3 1 mm^3 samples reconstructed using 40 and 80 µm

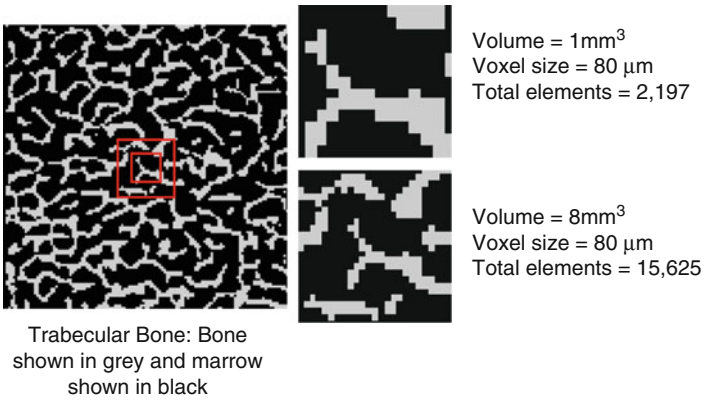

Fig. 4 1 and 8 mm^3 samples reconstructed using 80 µm

3 Results

The distribution of von Mises stress of the bone phase was similar under confined and unconfined conditions, with maximal values consistently 600 MPa. The fluid velocity of the marrow phase was 5.88% higher under confined than under unconfined conditions with maximal values of 1.8×10^{-2} and 1.7×10^{-2} mm/s, respectively. The pore pressure of the marrow phase was more than two orders of magnitude higher under confined than under unconfined conditions achieving maximal values of 130 and 0.32 MPa, respectively (Fig. 5).

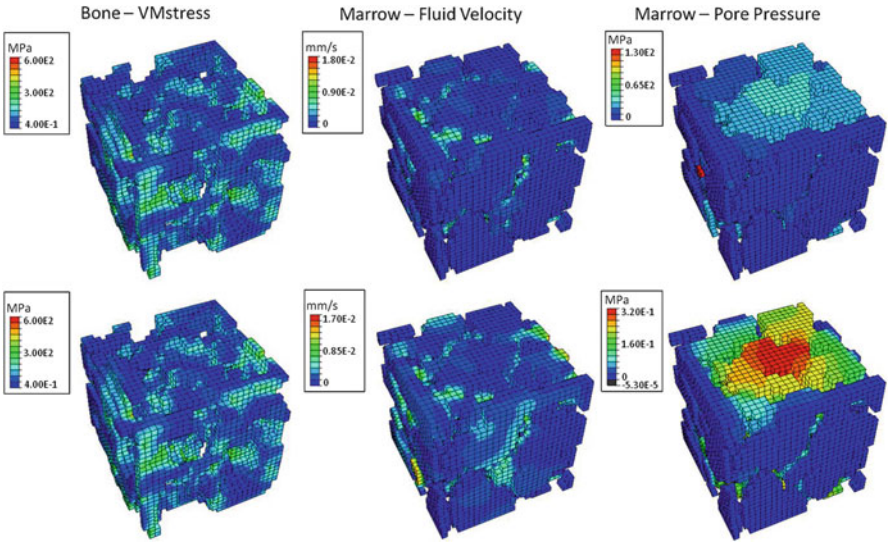

Fig. 5 Mechanical stimuli distribution predicted in the 8 mm^3 sample reconstructed using 80 µm when 1% of total deformation was applied in 1 s. Confined conditions are shown in the top and unconfined in the bottom

3.1 Study of the Effect of Loading Conditions and Material Properties

The stiffness of bone was 2.27%, 2.07%, and 1.22% higher under confined versus unconfined boundary conditions when 0.001, 0.01, and 0.1/s strain rates were applied, respectively. Moreover, it augmented 0.05% under confined conditions and 1.08 under unconfined conditions when the strain rate was increased (Fig. 6, left). Similarly, the marrow stiffness was 42.22%, 16.96%, and 4.57% higher under confined versus unconfined conditions when 0.001, 0.01, and 0.1/s strain rates were applied, respectively. It increased 7.19% under confined conditions and 45.78% under unconfined conditions, when the strain rate was increased (Fig. 6, right).

3.2 Study of the Effect of Voxel Size

The predicted apparent stiffness of trabecular bone (composed by bone and marrow) was about 26 MPa. Increasing the strain rate caused a positive increment of 0.23% and 0.31% in the stiffness under confined and unconfined conditions, respectively. Changing the boundary conditions from unconfined to confined produced positive

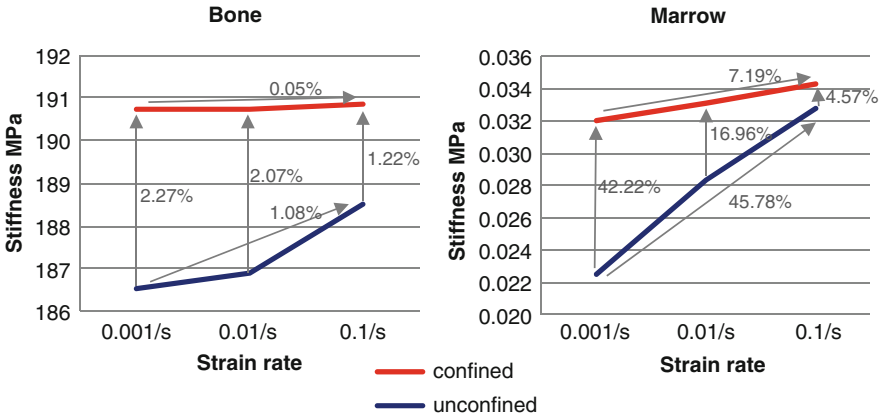

Fig. 6 Stiffness of 1 mm^3 cubic samples simulated using bone and marrow poroelastic properties separately. Gray arrows indicate the increase in stiffness due to variations in both the loading and the boundary conditions

Fig. 7 Apparent stiffness of 1 mm^3 samples reconstructed using 40 and 80 µm. Gray arrows indicate the effect of the resolution used for the reconstruction on the stiffness

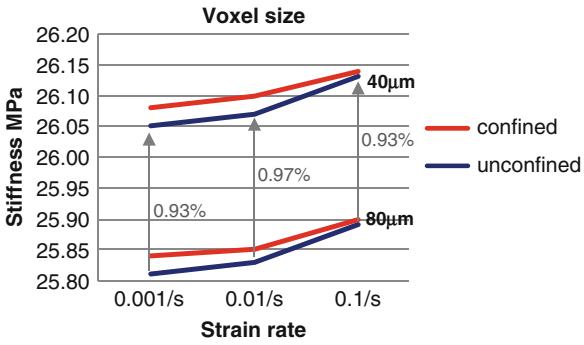

increments of stiffness no greater than 0.11%. These variations were similar for the samples reconstructed using 40 and 80µm. Reducing the resolution of the reconstruction to 80µm decreased the stiffness less than 1% (Fig. 7).

3.3 Study of the Effect of Sample Size

The computed apparent stiffness of trabecular bone was about 25.8 MPa for the 1mm^3 and 25.0 MPa for the 8mm^3 sample. Reducing the sample size from 8 to 1mm^3 increased the stiffness no more than 3.5%. Similar than in the previous study, the increase in strain rate caused an increment of 0.23% and 0.31% under confined and unconfined conditions, respectively. The stiffness varied by less than 0.11% between the confined and the unconfined cases. These variations were similar for the 1 and 8mm^3 samples (Fig. 8).

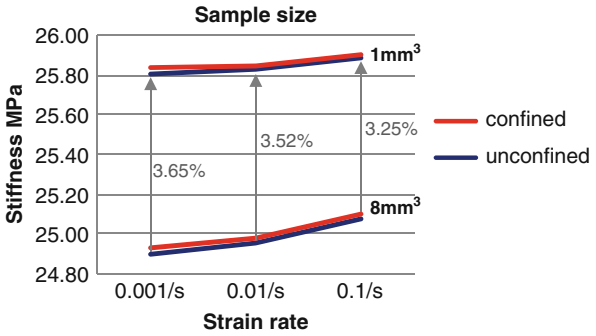

Fig. 8 Apparent stiffness of 1 and 8 mm^3 samples reconstructed using 80 µm. Gray arrows indicate the effect of the sample size on the stiffness

4 Discussion

An approach to study the poroelasticity of trabecular bone including the specific microarchitecture of bone had been presented. In this approach, bone and marrow were discretized and simulated as poroelastic materials. The variation in the stiffness due to different boundary conditions and strain rates was studied separately for the bone and the marrow phases. By definition, the stiffness of a poroelastic material is higher under confined rather than unconfined conditions, because the fluid cannot flow out of the sample. Similarly, the stiffness increases under high strain rates, because the fluid within the pores has less time to flow within or out of the sample, increasing the pore pressure. Due to the complexity of the poroelastic equations, it is difficult to quantify this variation analytically. Poroelastic modeling is of great value to understand the contribution of the bone and the marrow phases to the trabecular bone mechanical response. In this study, apparent stiffness of 186.5, 0.022, and 26.05MPa were predicted for the bone, the marrow, and the trabecular bone models, respectively, when 0.001/s strain rate was simulated under unconfined conditions. When the strain rate was increased and the boundary conditions were modified, the maximum increase computed for the stiffness of the trabecular bone was about 0.31%. This result suggests that modeling the bone poroelasticity may not be cost-effective if the unique goal is to predict bone strength. However, poroelastic modeling allows predicting fluid velocity and pore pressure which are of great interest in the study of bone biological processes (i.e., bone regeneration).

One of the major difficulties investigating trabecular bone poroelasticy is the size of the models. In order to model a $4 \times 4 \times 4$mm sample with a resolution of 20µm, 8 million voxels are needed. The total number of voxels can be reduced by increasing the voxel size or decreasing the sample size. In this study, it was predicted that decreasing the sample size has a higher effect (about 3%) than increasing the voxel size (about 1%) when reducing the total number of voxels for the same sample. A sample of bovine trabecular bone was used in this study; the effect of the voxel and the sample size on the biomechanical response may be different for human bone, especially for osteoporotic bone, where the variation of the microstructure of bone is significant. Furthermore, bovine bone tends to be

younger (i.e., more collagen content) than human osteoporotic bone, and this may be an important difference in the poroelastic properties. Ongoing studies are being conducted to apply the proposed large-scale FE poroelastic approach to the study of human bone strength and bone regeneration. These studies include experimental tests for validation.

5 Conclusion

μCT-based FE models were developed to introduce bone microstructure for the study of the poroelasticity of trabecular bone. This methodology can be used to create large-scale models, to study the contribution of the marrow to the bone mechanical response, and to predict the biomechanical response of the tissue under mechanical loading.

Acknowledgements Dr. Dennis Coombe is acknowledged for some discussions. This work was supported by funding from the Natural Science and Engineering Research Council of Canada and Alberta Innovates-Health Solutions.

References

1. Anderson, C.B.: In: Baumeister, T. (ed.) Marks' Standard Handbook for Mechanical Engineers, pp. 3.48–3.76. MacGraw-Hill, New York (1967)
2. Biot, M.A.: General theory of three-dimensional consolidation. J. Appl. Phys. **12**, 155–164 (1941)
3. Caplan, A.I.: Mesenchymal stem cells. J. Orthop. Res. **9**, 641–650 (1991)
4. Carter, D.R., Hayes, W.C.: The compressive behavior of bone as a two-phase porous structure. J. Bone Joint Surg. Am. **59**, 954–962 (1977)
5. Cowin, S.C.: Bone poroelasticity. J. Biomech. **32**, 217–238 (1999)
6. Johnson, M.W., Chakkalakal, D.A., Harper, R.A., Katz, J.L., Rouhana, S.W.: Fluid flow in bone in vitro. J. Biomech. **15**, 881–885 (1982)
7. Lacroix, D., Prendergast, P.J.: A mechano-regulation model for tissue differentiation during fracture healing: analysis of gap size and loading. J. Biomech. **35**, 1163–1171 (2002)
8. Lim, T.H., Hong, J.H.: Poroelastic properties of bovine vertebral trabecular bone. J. Orthop. Res. **18**, 671–677 (2000)
9. Linde, F., Norgaard, P., Hvid, I., Odgaard, A., Soballe, K.: Mechanical properties of trabecular bone. Dependence on strain rate. J. Biomech. **24**, 803–809 (1991)
10. Muller, R., Hildebrand, T., Ruegsegger, P.: Non-invasive bone biopsy: a new method to analyze and display the three-dimensional structure of trabecular bone. Phys. Med. Biol. **39**, 145–164 (1994)
11. Nauman, E.A., Fong, K.E., Keaveny, T.M.: Dependence of intertrabecular permeability on flow direction and anatomic site. Ann. Biomed. Eng. **27**, 517–524 (1999)
12. Schaffler, M.B., Burr, D.B.: Stiffness of compact bone: effects of porosity and density. J. Biomech. **21**, 13–16 (1988)

13. Smit, T.H., Huyghe, J.M., Cowin, S.C.: Estimation of the poroelastic parameters of cortical bone. J. Biomech. **35**, 829–835 (2002)
14. van Rietbergen, B., Majumdar, S., Pistoia, W., et al.: Assessment of cancellous bone mechanical properties from micro-FE models based on micro-CT, pQCT and MR images. Technol. Health Care **6**, 413–420 (1998)

Using Multibody Dynamics to Design Total Knee Replacement Implants

John L. Williams and Said T. Gomaa

Abstract Computational mechanics methods, such as finite element analysis or multibody dynamics, are usually employed toward the end of the design phase of a total joint implant system. It is of greater benefit, however, to utilize these methods early in the design process as a benchmarking tool to compare competitive products, as a screening tool to eliminate poor design concepts, and as a means to virtually test selected designs to determine if they meet the functional requirements prior to cadaver testing in an experimental knee rig. The use of a purpose-written commercial multibody dynamics program has provided computational advantages for this purpose in an industrial setting, saving an unprecedented amount of time required for addressing design questions, prior to prototype manufacturing and testing. Such methods can be successfully employed to deal with challenging and clinically motivated design questions. This paper illustrates the use of computational mechanics as an enabling technology to discover design-related factors that contribute to unsatisfactory functional performance in some patients. As an illustrative example, it is demonstrated that the sagittal design of the femoral component of a total knee replacement is responsible for the observed phenomenon of paradoxical anterior motion in knee bending activities and that minor design modifications can reduce or eliminate and even reverse paradoxical anterior displacement.

J.L. Williams (✉)
Biomedical Engineering, University of Memphis, Memphis, TN, USA
e-mail: john.williams@memphis.edu

S.T. Gomaa
DePuy, a Johnson & Johnson Company, Warsaw, IN, USA
e-mail: sgomaa@its.jnj.com

A. Wittek et al. (eds.), *Computational Biomechanics for Medicine: Models, Algorithms and Implementation*, DOI 10.1007/978-1-4614-6351-1_14,
© Springer Science+Business Media New York 2013

1 Introduction

Paradoxical anterior motion has been clearly demonstrated to occur in total knee replacement (TKR) subjects by in vivo fluoroscopy. The term "paradoxical" describes the observed anterior sliding of the femur on the tibia while the subject bends the knee whereas the femur is expected to roll back as it does in a healthy knee. It has been reported to occur to varying degrees in most TKR devices. Paradoxical anterior motion has been observed in both posterior cruciate-retaining and posterior cruciate substituting TKR designs [1]. During weight-bearing knee flexion posterior "rollback" of the femur occurs between 0° and 30° of flexion, but beyond 30° the medial side of a TKR femoral component typically moves anteriorly with knee flexion while the lateral side stays in a relatively fixed posterior position relative to the tibial component. Some of the negative consequences of this paradoxical movement are: limited maximum flexion, difficulty getting out of a chair, ascending and especially descending stairs, accelerated wear of the tibial insert and the feeling of instability described as "walking on ice" [2]. Although the phenomenon has been observed in most single-leg knee bending fluoroscopic studies for some time, the exact cause of this undesirable kinematic outcome has only recently been discovered [3–5]. In this paper we demonstrate that paradoxical anterior sliding is caused by a common design aspect of TKR femoral components. We compare multibody dynamics simulations of a double leg squat of several posterior cruciate retaining total knee implant designs using measurements of the tibio-femoral "contact positions" similar to those published in fluoroscopic studies, in order to examine the nature and extent of paradoxical anterior motion in relation to the sagittal curvature of the femoral and tibial component contact surfaces.

2 Materials and Methods

2.1 Multibody Dynamics Model

A commercial multibody dynamics virtual knee simulator (LifeMOD^{TM}/KneeSIM, LifeModeler, Inc., San Clemente, CA, USA) was used to simulate a double-leg deep knee bend in a manner similar to the "Purdue Knee Simulator." Details of the KneeSIM program and many model parameters have been described elsewhere [6]. The model included tibio-femoral and patello-femoral contact, ligaments (MCL, LCL, and PCL), capsular tissues, and quadriceps and hamstring muscles (Fig. 1).

The MCL, LCL, and PCL and capsular stiffness properties were modeled with point-to-point elements (multiple elements for the capsule, two elements for the MCL, and single element for the PCL and LCL). Ligament lengths were calculated using the distance between the attachments. Ligament force was calculated from the relation: $F = k\varepsilon L - cv$, where k is the stiffness, e is the strain, L is the original "free length," c is the damping, and v is the velocity. The ligament stiffness (slope

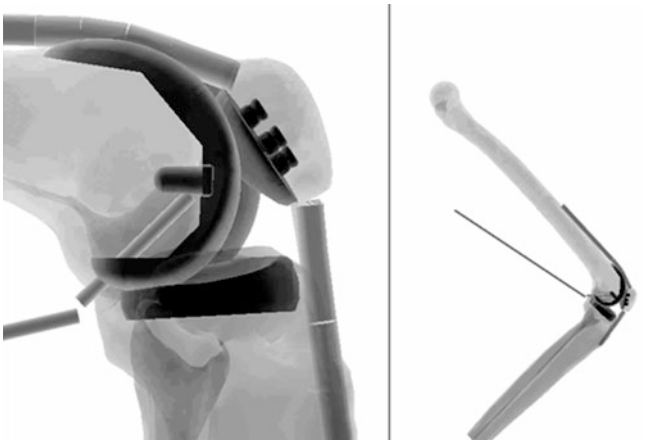

Fig. 1 Model of an implanted left knee in a squat simulation. The quadriceps and hamstrings muscles and the posterior cruciate ligament and wrapping patellar tendon and ligament are shown. The capsular tissues and the collateral ligaments are not shown, but are present in the model

of the force-strain curve) values—1,900 N (PCL), 3,800 N (MCL), 3,800 N (LCL), and 8,900 N (capsule)—were based on comparisons to literature values and on comparisons of model simulations to implanted cadaver knee experiments. An initial pre-tension of 44 N was applied to each of the ligaments.

Flexion/extension at the hip and ankle joints, and abduction/adduction, varus/valgus and axial rotation at the ankle joint were unconstrained while a constant vertical load of 463 N (equal to half of the body weight of a 95 kg subject) was applied at the hip. A proportional/derivative (PD) feedback control system was applied to the quadriceps and hamstrings muscle forces to maintain a user-input knee flexion angle history. The PD controller compared the instantaneous knee flexion angle during the simulation to the desired (input) knee flexion angle. The error was then multiplied by a Pgain resulting in a quadriceps/hamstrings muscle tension force. The derivative gain (Dgain) was a fixed percentage of the Pgain and was applied as a damping force to the error rate. The force applied to the hamstrings was proportional to the product of the error and quadriceps force. The systems were subjected to one 9-s cycle of knee bending up to 120° of flexion. The anterior–posterior (AP) positions of the lowest points on the femoral lateral and medial condyles closest to the tibial tray (the same measure used in fluoroscopy studies) were recorded relative to the dwell points of the inserts. Model validation, in the sense of evidence that the model is suitable for the tasks at hand, has been addressed by several studies [6], including comparisons with the ASTM F1223–89 laxity test and comparisons with in vitro knee cadaver testing and in vivo fluorosocopic data [7].

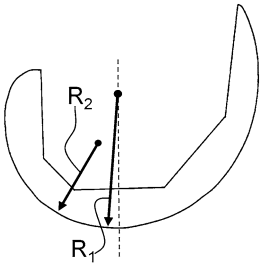

Fig. 2 Lateral view of a para-sagittal cross-section of a generic femoral component showing a radius of curvature in the posterior condylar region decreasing from R_1 to R_2. The angle where the change in curvature occurs was measured from the vertical axis

2.2 Intact Commercial Designs

Reverse-engineered models of commercially available fixed-bearing cruciate-retaining total knee implant systems (NexGen®, Zimmer, Warsaw, IN, USA; Biomet Vanguard™, Biomet, Warsaw, IN, USA) were imported into the model without modification to the design of the tibial insert or femoral components. These were among many such simulations performed on a wide variety of commercial designs to determine if multibody dynamics could predict the fluoroscopically observed paradoxical anterior motion.

2.3 Influence of Femoral Contact Geometry on Kinematics

In order to isolate the influence of the femoral condyle geometry from tibial insert geometry, simulations were performed for a generic perfectly flat tibial insert. For this purpose, we report simulation results of reverse-engineered models of fixed-bearing cruciate-retaining total knee implants: the anterior–posterior positions of the condylar lowest points (CLP) on the femoral condyles closest to the tibial tray (the same measure used in fluoroscopy studies) were recorded relative to the equilibrium position in full extension. For the flat inserts the CLP coincided with the "contact points" or centers of pressure (COP) of the calculated tibio-femoral contact areas.

2.4 Theoretical Designs

Several theoretical TKR models were designed to further explore the relationship between design and kinematics. The anterior geometry (trochlear and patello-femoral surfaces) and patella of the theoretical designs were identical in all of these theoretical models. The tibio-femoral contact surfaces of the femoral components were designed to have multi-radial curvatures in the para-sagittal planes (polycentric designs) (Fig. 2).

Two cases are presented: in the first the para-sagittal radius decreased from 35 mm at full extension to 25 mm at 30° of flexion, and in the second the radius increased from 25 to 30 mm at 30° of flexion. Simulations with these two femoral designs were performed using both a generic perfectly flat tibial insert and an insert with curvature in the para-sagittal and para-coronal planes in order to isolate the influence of the femoral condyle geometry from that of the tibial insert geometry. Both inserts had the same antero-posterior dimensions. In addition to the CLP, we report translations of the calculated COP of the medial and lateral tibio-femoral contact patches. More extensive simulations using curved tibial inserts and numerous variations in the femoral sagittal radius of curvature change can be found in a recent patent application [3].

3 Results and Discussion

3.1 Commercial Designs

In all commercial designs analyzed in this fashion we noted that the onset of paradoxical anterior motion occurred at angles that corresponded approximately with the flexion angles at which the femoral para-sagittal radius abruptly decreased (Table 1, Figs. 3 and 4).

Table 1 Magnitude and angle of discrete femoral radius reduction as determined from reverse-engineered components

Knee system	Medial	Lateral
NexGen®	35 % at 37°	50 % at 16°
Vanguard™	35 % at 20° and 20 % at 90°	35 % at 20° and 20 % at 90°
Scorpio®	6 % at 75°	6 % at 75°

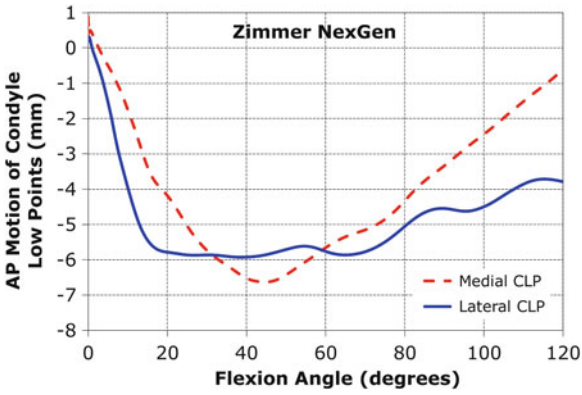

Fig. 3 Antero-posterior (+ANT) translation (mm) of the lowest condyle points (CLP) of a Zimmer NexGen TKR, as a function of knee flexion angle during a lunge simulation (medial condyle: dashed line; lateral condyle: solid line)

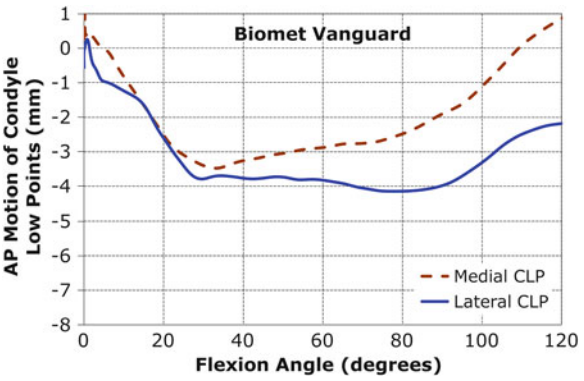

Fig. 4 Antero-posterior (+ANT) translation (mm) of the lowest condyle points (CLP) of a Biomet Vanguard TKR, as a function of knee flexion angle during a lunge simulation

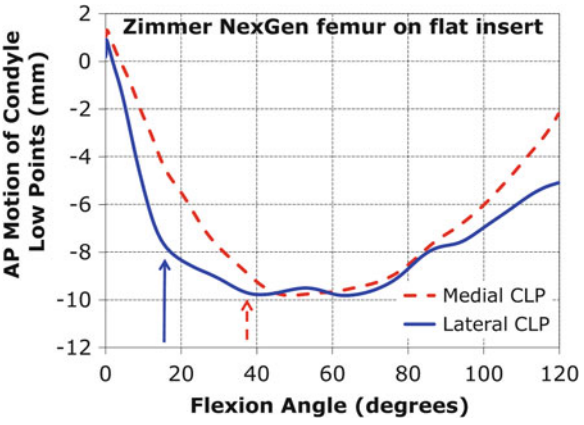

Fig. 5 Antero-posterior (+ANT) motion (mm) of the condyle low points (CLP) relative to the tibial tray during flexion from 0 to 120° for a design with a polycentric sagittal femoral curve. The medial and lateral condyles in this design have different sagittal curvatures and the radius decrease occurs at knee flexion angles shown by arrows (see Table 1)

3.2 Influence of Femoral Contact Geometry on Kinematics

Posterior translation of the medial and lateral tibio-femoral "contacts" of NexGen®, Vanguard™, and Scorpio® either ceased or slowed at flexion angles between 16 and 75° (Figs. 5, 6, and 7). Paradoxical anterior motion started at about 40° for NexGen® (Fig. 5), 90° for Vanguard™ (Fig. 6) and almost imperceptibly at about 70° for Scorpio® (Fig. 7).

3.3 Theoretical Designs

For the theoretical design with a femoral radius reduction on a flat insert: the tibio-femoral lowest points (CLP) coincided with the COP and both translated posteriorly from 0 to 120°, but the rate of "rollback" slowed at 30° of flexion (Fig. 8).

For the design with a femoral radius reduction on a curved insert: the tibio-femoral lowest points (CLP) translated posteriorly from 0 to 30°, after which the

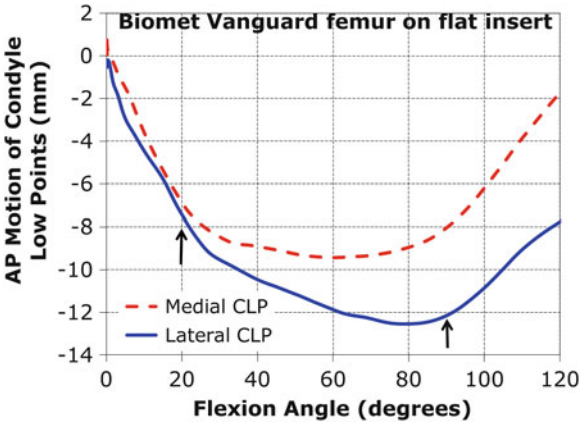

Fig. 6 Antero-posterior (+ANT) motion (mm) of the condyle low points (CLP) relative to the tibial tray during flexion from 0 to 120° for a design with a polycentric sagittal femoral curve. The medial and lateral condyles in this design have the same sagittal geometry in the tibio-femoral contact regions and the radius decrease occurs at knee flexion angles indicated by arrows (see Fig. 2 and Table 1)

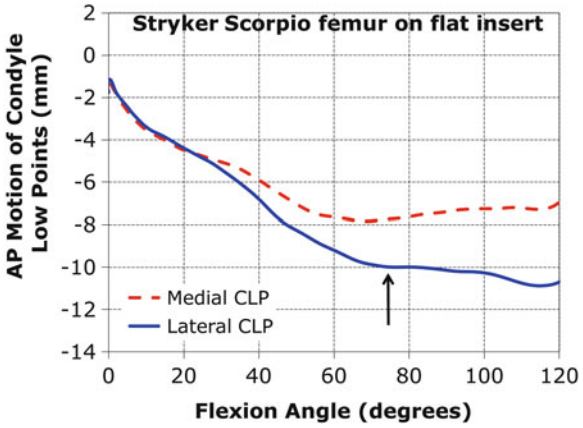

Fig. 7 Antero-posterior (+ANT) motion (mm) of the condyle low points (CLP) relative to the tibial tray during flexion from 0 to 120° for a design with a polycentric sagittal though nearly constant femoral curve. The medial and lateral condyles in this design have the same sagittal geometry in the tibio-femoral contact regions and the slight radius decrease observed in the reversed-engineering component occurs at knee flexion angle marked by the arrow (see Table 1)

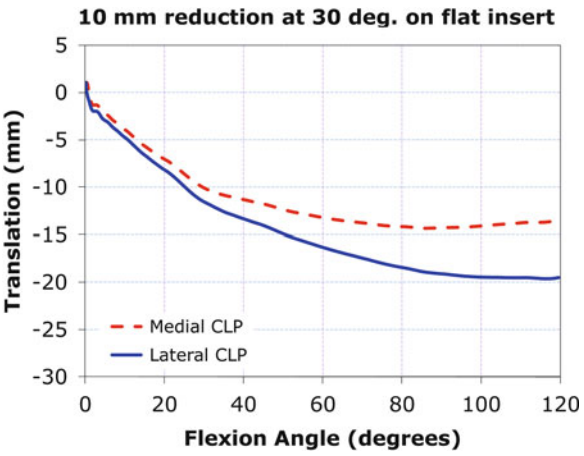

Fig. 8 Theoretical femoral design with a 10 mm reduction in sagittal radius at approximately 30° of knee flexion. Antero-posterior (AP, +ANT) translations (mm) of the condyle lowest points (CLP) and centers of pressure (COP) relative to the tibial tray with a flat insert

medial side translated anteriorly while the lateral side rolled back at a slower rate (Fig. 9). The COP showed similar "rollback" behavior to that of the CLP. Due to the sagittal curvature of the insert, the COP translated posteriorly faster than the CLP. Since contact was made between the insert and the reduced radius at an earlier flexion angle than for a flat insert, "rollback" of the COP was correspondingly slowed earlier in the flexion cycle. For the design with a femoral radius increase on a flat insert: both CLP and COP translated posteriorly continuously and a slight acceleration of "rollback" could be seen at 30° (Fig. 10).

For the design with a femoral radius increase from 25 to 30 mm at 30° on a curved insert: CLP "rollback" accelerated after 30°, especially on the lateral side, while COP "rollback" preceded CLP rollback due to the additional curvature of the insert (Fig. 11). At approximately 105° the lateral condyle of the femur with the increasing radius rode up onto the posterior lip of the curved insert and reached the edge of the flat insert. At that point the COP of the lateral side remained on the rim, while the CLP continued past the physical boundary of the inserts (Figs. 10 and 11).

4 Discussion and Conclusion

4.1 Commercial Designs

NexGen® and Vanguard™ are multi-radius (polycentric) designs, whereas Scorpio® is a single-radius design. Manufacturing, polishing, and/or reverse engineering tolerances may result in radius variations slightly different from original design intent. Despite differences in both the femoral and the tibial component para-sagittal plane curvatures between these implants, the onset of paradoxical anterior motion was approximately related to the flexion angle at which the para-sagittal

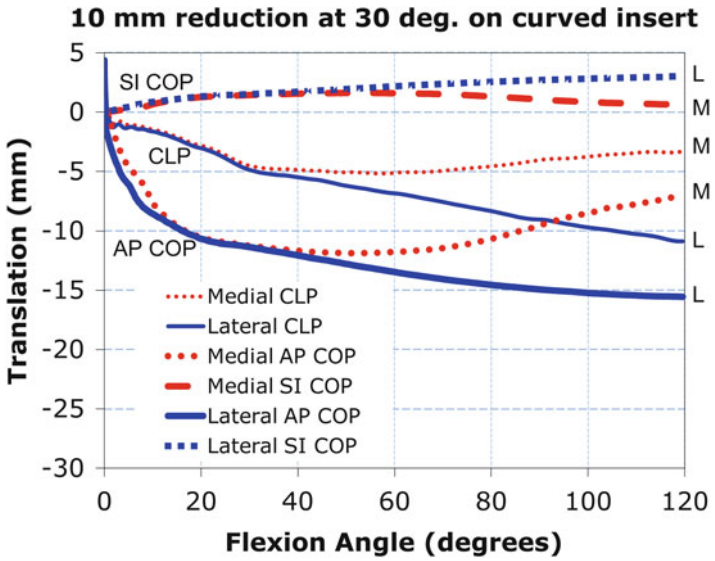

Fig. 9 Theoretical femoral design with a 10 mm reduction in sagittal radius at approximately 30° of knee flexion. Theoretical femoral design with a 100 mm reduction in sagittal radius at approximately 30° of knee flexion. Antero-posterior (AP, +ANT) translations (mm) of the condyle lowest points (CLP) and centers of pressure (COP), and supero-inferior (SI, +SUP) translations (mm) of the COP relative to the tibial tray with a curved insert

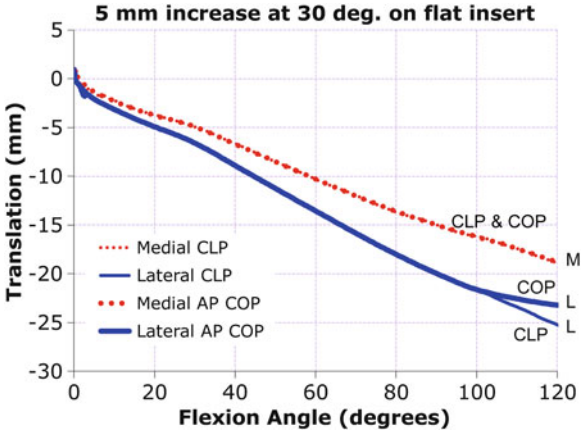

Fig. 10 Theoretical femoral design with a 5 mm increase in sagittal radius at approximately 30° of knee flexion. Antero-posterior (AP, +ANT) translations (mm) of the condyle lowest points (CLP) and centers of pressure (COP) relative to the tibial tray with a flat insert

femoral radius of curvature at the contact points decreased abruptly relative to the radius at the contact points in extension. These findings suggest the principal cause of paradoxical anterior motion is a 30–50 % discrete decrease in the femoral condyle para-sagittal radius at flexion angles between 20 and 40°. It should be noted that the flexion angle in the simulations can only be approximately synchronized with the angle at which the radius of curvature change is observed in the implant

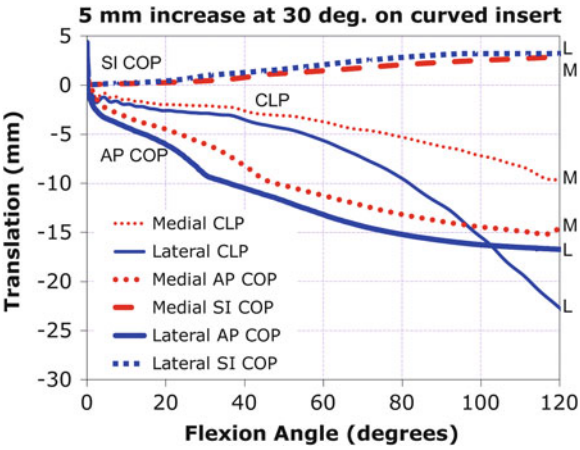

Fig. 11 Theoretical femoral design with a 5 mm increase in sagittal radius at approximately 30° of knee flexion. Antero-posterior (AP, +ANT) translations (mm) of the condyle lowest points (CLP) and centers of pressure (COP), and supero-inferior (SI, +SUP) translations (mm) of the COP relative to the tibial tray with a curved insert

component, due to the fact that R_1 and R_2 have different centers of curvature and that the centers of curvature for polycentric designs are located in positions that differ from the Grood and Suntay origin used in the simulations.

4.2 Influence of Femoral and Tibial Contact Geometry on Kinematics

These deep knee bending simulations indicate that the primary cause of paradoxical anterior motion in posterior cruciate retaining TKRs is the discrete reduction in posterior condylar radius of curvature in the para-sagittal plane of the femoral component. While the radius of curvature of the bearing surface on the tibial side can influence the kinematics as well, the femoral curvature appears to dominate the onset of paradoxical anterior motion. Designs with a nearly constant radius of curvature (single radius design) over the bearing surfaces of the femoral condyles in the para-sagittal planes appear to be less susceptible, or even immune, to paradoxical anterior motion.

The results for AP motion of the lowest condylar points are similar to what has been reported for cruciate-retaining total knee implants in a single-leg deep knee bend [1]: in a deep knee bend, PCL-retaining total knees pivot on the lateral side, rather than the medial, in association with paradoxical anterior motion. Due to the different sagittal curvatures of the inserts, the AP movements of the COP (true contact points) in the medial and lateral compartments are different from those of the lowest condylar points. We have provided results for the latter because they correspond with what has most frequently been reported in fluoroscopic studies. The results of these simulations suggest that inserts with less sagittal plane conformity not only have greater posterior motion in early flexion but also have more undesired anterior motion past 30–40° of flexion. Paradoxical anterior sliding is likely to

occur independently of the insert sagittal radius. The results further suggest that paradoxical anterior sliding is associated with a reduction in the condylar radius in the sagittal plane, which causes slippage at the contacts between the condyles and insert. Patients may achieve improved "rollback" and deeper flexion with a lower conformity design but may still suffer from a sense of instability due to paradoxical anterior sliding.

4.3 Conclusions

This paper focused on the application of multibody dynamics in understanding a clinically motivated question and determining a design parameter associated with the clinical challenge. In this case the designs were all posterior cruciate retaining TKR designs. The same problem of paradoxical anterior sliding occurs in posterior cruciate substituting designs and is related to the same design factors. The remedy may therefore be similar; however, this has to be carefully coordinated with the timing of the cam-post engagement so as not to engage the cam and post at the wrong time or cause large transfer of load to the cam mechanism.

One study has reported that patients with TKR designs based on a single radius design do not suffer from paradoxical anterior motion of the femur [8] lending support to conclusions drawn from these simulation results.

Although the insert design can moderate the severity of paradoxical anterior motion, these results for theoretical designs point to the reduction in femoral para-sagittal radius as the trigger for paradoxical anterior motion and suggest a simple design modification to alleviate or eliminate it, or even to potentially enhance rollback in deep flexion. Further examples of how even a 1 mm increase in the femoral sagittal radius of curvature can enhance femoral rollback have been published elsewhere [3].

Finally, it should be recognized that although paradoxical anterior motion can be dealt with by making small changes to the radial curvature of the femoral component, it is not at all clear how such changes affect knee kinematics in load-bearing activities other than deep knee bending.

References

1. Dennis, D.A., Komistek, R.D., Colwell Jr., C.E., Ranawat, C.S., Scott, R.D., Thornhill, T.S., Lapp, M.A.: In vivo anteroposterior femorotibial translation of total knee arthroplasty: a multicenter analysis. Clin. Orthop. Relat. Res. **356**, 47–57 (1998)
2. Blaha, J.D.: The rationale for a total knee implant that confers anteroposterior stability throughout range of motion. J. Arthroplasty **19**(4 Suppl 1), 22–26 (2004)
3. Williams, J.L., Gomaa, S.T., Armacost, J.M.: Orthopaedic femoral component having controlled condylar curvature. US Utility Patent Application US20090326667 (A1) (Dec 31, 2009). http://www.google.com/patents/US20090326667. Accessed 19 Jul 2012

4. Williams, J.L.: Proposed causation and treatment of paradoxical anterior translation in knee prosthesis designs. In: Transactions of the 55th Annual Meeting of the Orthopaedic Research Society 34: Paper no. 2073, Orthopaedic Research Society, Rosemont, IL (2009)
5. Williams, J.L.: Polycentric versus single axis sagittal femoral geometry and paradoxical anterior translation in total knee implants. Paper no. BioMed2009–83011: pp. 5–6. In: ASME Conf Proc/ASME 2009 4th Frontiers in Biomedical Devices, ASME, New York, NY. http://dx.doi.org/10.1115/BioMed2009--83011 (2009)
6. Innocenti, B., Pianigiani, S., Labey, L., Victor, J., Bellemans, J.: Contact forces in several TKA designs during squatting: a numerical sensitivity analysis. J. Biomech. **44**, 1573–1581 (2011)
7. Gomaa, S.T., Williams, J.L.: Kinematics of total knee replacement: indirect comparison of virtual knee simulation and in vivo fluoroscopy during deep knee bending. In: Transactions of the 53rd Annual Meeting of the Orthopaedic Research Society 32. Paper no. 1830, Orthopaedic Research Society, Rosemont, IL (2007)
8. Streicher, R.M., Banks, S., Schmalzried, T., Reilly, D.: Knee kinematics of two different sagittal design implants. J. Bone Joint Surg. Br. 86-B(Suppl IV), **452** (2004)

Using Tagged MRI to Quantify the 3D Deformation of a Cadaver Brain in Response to Angular Acceleration

A.K. Knutsen, W.T. Wang, J.E. McEntee, J. Zhuo, R. Gullapalli, J.L. Prince, P.V. Bayly, J.B. Butman, and D.L. Pham

Abstract A quantitative three-dimensional (3D) description of the deformation of brain tissue during acceleration of the skull is necessary to provide understanding of the underlying mechanisms of traumatic brain injury. Tagged magnetic resonance imaging (MRI) allows for the noninvasive measurement of the deformation of biological tissue. In this study, tagged MRI with harmonic phase (HARP) analysis was used to quantify the 3D deformation during angular acceleration of a gelatin phantom and the head of a human cadaver specimen. Two-dimensional results from the gelatin phantom showed good agreement with previously published results. Two-dimensional strains in the cadaver brain were lower in magnitude than previously reported results from a similar experiment in the live human brain. Strains on the inferior–superior axis were measured and shown to be of similar magnitude to the strain components in the plane formed by the anterior–posterior and left–right axes. Future studies will involve the acquisition of 3D deformation fields in live humans and additional cadaver specimens.

A.K. Knutsen (✉) • W.T. Wang • J.E. McEntee • D.L. Pham
Center for Neuroscience and Regenerative Medicine, Henry M. Jackson Foundation for the Advancement of Military Medicine, Bethesda, USA
e-mail: andrew.knutsen@nih.gov

J. Zhuo • R. Gullapalli
Magnetic Resonance Research Center, University of Maryland School of Medicine, Baltimore, USA

J.L. Prince
Department of Electrical and Computer Engineering, Johns Hopkins University, Baltimore, USA

P.V. Bayly
Department of Mechanical Engineering and Materials Science, Washington University in St. Louis, Saint Louis, USA

J.B. Butman
Clinical Center, National Institutes of Health, Bethesda, USA

A. Wittek et al. (eds.), *Computational Biomechanics for Medicine: Models, Algorithms and Implementation*, DOI 10.1007/978-1-4614-6351-1_15,

© Springer Science+Business Media New York 2013

1 Introduction

Traumatic brain injury, a serious health concern that affects approximately 1.4 million people per year in the USA [1], occurs in response to the rapid, nonrigid deformation of brain tissue. However, the deformation of the brain in response to specific loading conditions is poorly understood. Previous studies have quantified brain deformation under acceleration by performing craniotomies on primates [2–4] and have used high speed X-ray to image implanted opaque radiotracers in dogs, primates, and cadavers [5–8]. Such studies involve invasive procedures and provide low spatial resolution of displacements and strain. Computational simulations have also been used to analyze loading conditions that would otherwise be difficult to examine experimentally [9–13]. Computational models must be validated using experimental results to ensure accuracy of the model under known conditions. In general, models are validated by experiments conducted using cadaver specimens. However, the quantitative relationship between the brain response to acceleration in live and post mortem tissue is largely unknown.

Tagged magnetic resonance imaging (MRI) [14, 15] with harmonic phase (HARP) analysis [16] is an approach used to quantify the spatial and temporal deformation of biological tissue. Tagged MRI is noninvasive and does not use ionizing radiation, making it advantageous to imaging live humans. Tagged MRI has been used previously to study brain deformation during angular [17] and linear [18, 19] acceleration in the human brain. These studies employed a segmented acquisition approach where one line in the spatial frequency domain (k-space) was acquired repeatedly during a single repetition (acceleration) of the head. The identical motion was then repeated up to 144 times in order to build up the time series of images at an image plane in the brain.

For 2D strain estimation, standard tagged MRI [14] requires that two sets of tag lines be applied in orthogonal and complimentary directions (i.e., horizontal and vertical tag lines), either within the same image (grid tags) or during two separate (line tags) acquisitions. Complimentary spatial modulation of magnetization (CSPAMM) [20] improves tagging contrast over time, and slice-following CSPAMM (SF-CSPAMM) [21] allows motion to be tracked through the imaging plane. zHARP [22] is an extension of SF-CSPAMM where 3D displacement fields can be computed within a single imaging plane. A downside to these advanced acquisition techniques is that each requires four acquisitions, with two acquisitions for each tag line direction, to form a complete data set. Temporal resolution is governed by the amount of time necessary to acquire a single line of k-space and by the number of lines of k-space being acquired during a single repetition of the motion.

The primary objective of this study is to establish the feasibility of computing a 3D deformation field in the brain. Secondary objectives are to compare the deformation field obtained in the human cadaver brain to previously obtained results in live humans, reduce the number of repetitions necessary to acquire a single image set relative to previous experiments, and compare the grid tag, CSPAMM, and

zHARP pulse sequences. Results obtained using the grid tag pulse sequence will serve as the gold standard based on previously published results [23].

To accomplish these objectives, zHARP and CSPAMM images were acquired and analyzed to compute the 3D deformation (2D for CSPAMM) of the brain in response to angular acceleration of the head at multiple locations in a human cadaver specimen. By reducing resolution in the phase-encode direction, acquiring multiple lines of k-space in rapid succession (e.g., using a segmented echo-planar imaging approach) and employing parallel imaging techniques (e.g., generalized autocalibrating partially parallel acquisitions (GRAPPA) [24]), the number of repetitions required for each acquisition was reduced to a more manageable number. The same experimental setup was used to image a gelatin phantom. Grid tags, CSPAMM, and zHARP images were acquired and analyzed, and the results were compared to those obtained by Bayly et al. ([23]–Fig. 7).

2 Methods

2.1 Head Rotation

The MRI-compatible head rotation device used in this study was provided by Dr. Phil Bayly at Washington University and has been used in previous studies [17, 23]. The device (Fig. 1) uses an off-axis counterweight to apply a torque, accelerating the head at approximately $260\,\mathrm{rad/s^2}$. Rotation is initiated by release of a latch, which allows the head cradle to rotate approximately 35° about a central axis. Release of the latch triggers a TTL pulse to the scanner, beginning the image acquisition. The receive coil used in the previous studies is not compatible with the current scanners. Instead, a four-channel flexible receive coil was attached to a custom-made support structure that fits over the head rotation device (Fig. 1).

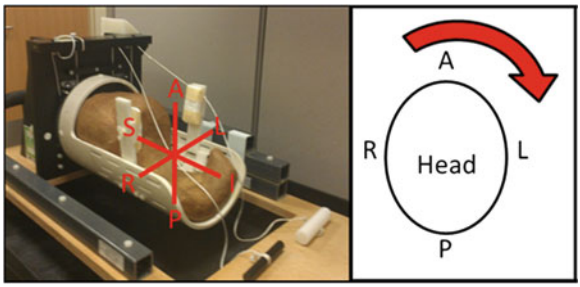

Fig. 1 MRI-compatible head rotation device: pulling the cable releases a latch, causing the head cradle to rotate approximately 35° about its center axis at approximately $260\,\mathrm{rad/s^2}$. As the latch is released, a signal is sent to the scanner which starts the MRI pulse sequence. The rotation occurs in the plane formed by the anterior (*A*)-posterior (*P*) and left (*L*)-right (*R*) axes

2.2 Gelatin Phantom Experiment

A gelatin phantom was constructed using 96 g of Knox brand gelatin (Knox, Camden, NJ) powder mixed with 1.8 L of water that was heated to approximately 80°C in a cylindrical container (inner diameter = 11.4 cm; length = 18 cm) (see Bayly et al. [23]). The mixture was allowed to cool at room temperature for 30 min and then placed in a refrigerator to solidify for approximately 12 h. Because the stiffness of the gel is dependent on temperature, the solidified gel was placed at room temperature approximately 3 h prior to the experiment to equilibrate to room temperature. The exact stiffness of the gel was not measured, so it cannot be directly compared to a numerical simulation, as in Bayly et al. [23]. However, a similar deformation response is expected, and a qualitative comparison can be made.

Three consecutive transverse image slices were acquired using zHARP. Acquisition of the second slice was repeated using grid tags and CSPAMM. Images were acquired using a Siemens 3.0 T Biograph mMR and Siemens 3.0 Telsa Verio (Siemens, Munich, Germany). The imaging parameters used were: gradient echo acquisition, field of view (FOV) = $240 \times 240\,\text{mm}^2$, matrix size = 128×64, tag spacing = 8 mm, slice thickness = 8 mm, number of time frames = 60. For zHARP, echo time (TE)/repetition time (TR) = 2.15 ms/9.3 ms, segments = 2, GRAPPA factor = 2; total repetitions = 72; for grid tags, matrix size = 128×96, TE/TR = 1.99 ms/7.86 ms, segments = 2; GRAPPA = 2, total repetitions = 27; for CSPAMM, TE/TR = 4.17 ms/7.10 ms, segments = 4, EPI factor = 4, total repetitions = 68.

2.3 Human Cadaver Head Experiment

A human cadaver was obtained from the Maryland State Anatomy Board, Department of Health and Mental Hygiene in Baltimore, Maryland. The specimen was imaged at 60 h post death. The specimen was rigidly attached to the head rotation device during the experiment. Four consecutive transverse image slices were acquired using zHARP. The acquisition of the second and fourth slices was repeated using CSPAMM. The imaging parameters used were: gradient echo acquisition, FOV = $240 \times 240\,\text{mm}^2$, matrix size = 128×64, tag spacing = 12 mm, slice thickness = 8 mm, TR/TE = 2.15 ms/9.3 ms, segments = 2, GRAPPA factor = 2, number of time frames = 60, total repetitions = 72. Additionally, standard clinical scans (T1-weighted, T2-weighted, and FLAIR MRI images) were acquired. Scans were read by a neuroradiologist and determined to be within normal limits.

2.4 Motion Tracking and Strain Estimation

Figure 2 provides a visual description of the processing steps for image combination and motion tracking. A total of four image sets are necessary for both CSPAMM and

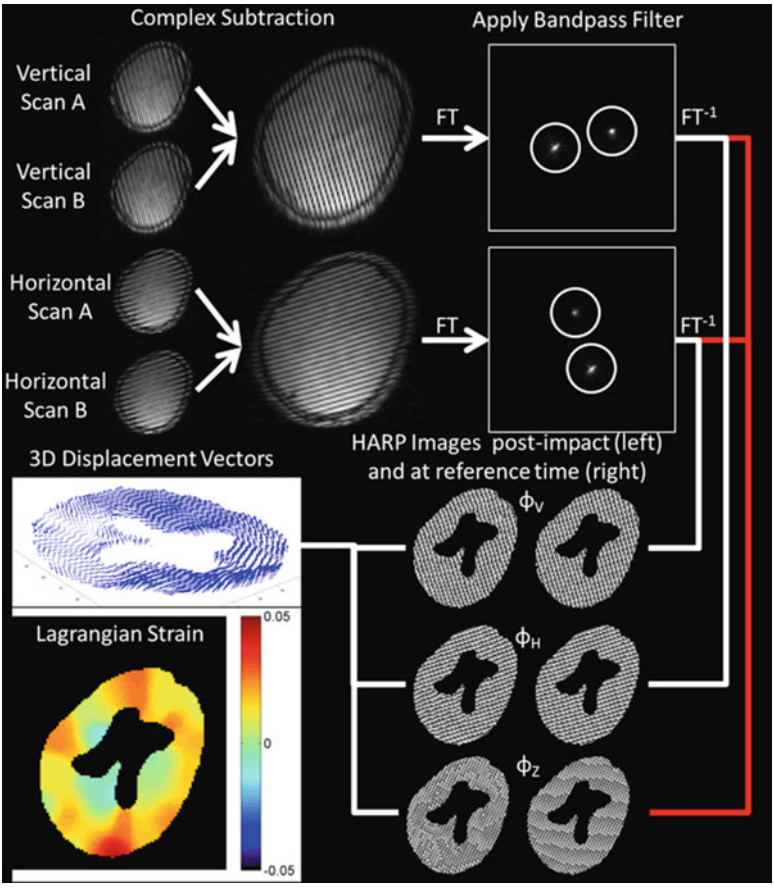

Fig. 2 For CSPAMM and zHARP pulse sequences, four sets of tagged images (two with both horizontal and vertical tag lines) are acquired to compute 2D (CSPAMM) or 3D (zHARP) deformation fields. Tag lines move with the deforming material. The A and B scans for each direction are combined using complex subtraction, transformed into the spatial frequency domain using a Fourier transform, and a bandpass filter is applied about the center of each of the spectral peaks in k-space. HARP images are created from the filtered k-space images using peak combination [26]. The spatial position of constant HARP values are tracked between time frames using the HARP images in the horizontal (ϕ_H) and vertical (ϕ_V) directions. After computing the in-plane displacements, through plane displacements are computed using the third set of HARP images (ϕ_Z). Lagrangian strain is computed from the spatial derivatives of the displacement field

zHARP—A and B scans with tag lines applied in both the vertical and horizontal directions—and a single image set for grid tags. For zHARP, the A and B scans were combined using complex subtraction. For CSPAMM, the images A and B scans were combined using MICSR, which only uses image magnitudes [25].

After a 2D Fourier transform, a bandpass filter with a radius of 12 voxels centered at each of the spectral peaks was applied. HARP images were created

by computing the angle between the real and imaginary components of the inverse Fourier transform of the bandpass filtered images. HARP images represent the phase of the dominant harmonic components of the tagged images [26]. For CSPAMM, peak combination was applied to reduce phase errors in the HARP images [27]. For zHARP, peak combination is required to form the third set of HARP images, which are used to determine the z-component of displacement.

A tracking algorithm similar to the approach described in Liu et al. [28] was implemented using in-house software written in Matlab (Mathworks, Natick, MA). Tagged images were rigidly registered to the reference image. HARP images were unwrapped using a quality path-guided unwrapping algorithm [29]. HARP values are constant over time, so the spatial location between each time frame was tracked using a Newton–Rhapson iterative minimization approach [16]. Because of different frame rates between the grid tags, CSPAMM, and zHARP for the gel phantom, third order b-spline functions were fit to displacement components for each tracked point, and the functions were evaluated at a temporal resolution of 6 ms.

Lagrangian strain ($\boldsymbol{E}$), a dimensionless measure of deformation that is independent of rigid-body rotation and translation, was calculated using the approach described in Filas et al. [30]. Briefly, second order polynomial functions were fit in the least squares sense to local regions of reference and corresponding deformed coordinates, and derivatives were computed from the fits.

$$E = \frac{1}{2}\left(F^T \cdot F\right)$$

Here, $\boldsymbol{F}$ is the deformation gradient tensor, which is given by

$$F = \frac{\mathrm{d}x}{\mathrm{d}X} = I + \frac{\mathrm{d}u}{\mathrm{d}X}$$

where $\boldsymbol{I}$ is the identity tensor, $\boldsymbol{X}$ are the reference coordinates (i.e., the reference time frame), $\boldsymbol{x}$ are the deformed coordinates (i.e., subsequent time frames), and $\boldsymbol{u}$ are the displacement vectors. The center of rotation was identified using the displacement vectors and then used to transform $\boldsymbol{E}$ from Cartesian to Cylindrical coordinates.

3 Results

3.1 Gelatin Phantom

A subset of tagged images obtained during deformation from the experiments is shown in Fig. 3. Radial circumferential shear strain ($E_{R\theta}$), as a function of time post trigger is shown in Fig. 4 for grid tags, CSPAMM, and zHARP acquisitions, respectively, from 258 to 348 ms post trigger. Impact occurs at approximately 250 ms post trigger, lasting for approximately 50 ms. Consistent with previous

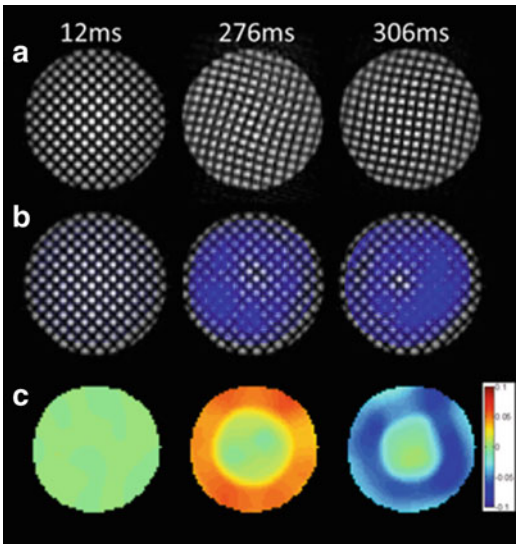

Fig. 3 (**a**) Tagged images (using grid tags), (**b**) displacement vectors, and (**c**) radial-circumferential strain maps 12 ms, 276 ms, 306 ms post trigger

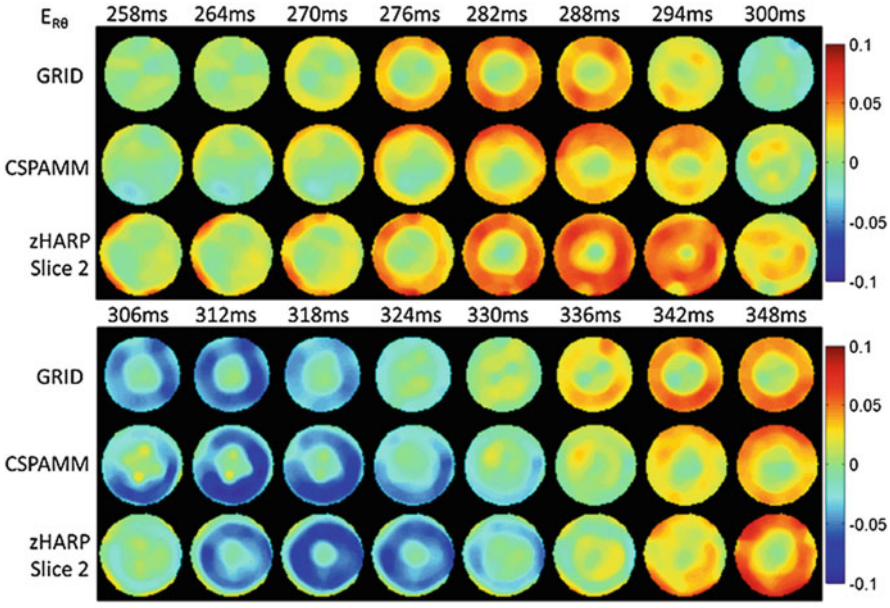

Fig. 4 Radial circumferential Lagrangian shear strains obtained in a gelatin phantom using grid tags, CSPAMM, and zHARP. Impact occurred at approximately 250 ms post trigger

results, radial circumferential shear strains dominate the deformation. Through plane strains (E_{ZZ}—along the I/S axis) are shown in Fig. 5 for the three consecutive slices acquired using zHARP. As expected, the magnitude of E_{ZZ} post impact is generally an order of magnitude less than $E_{R\theta}$.

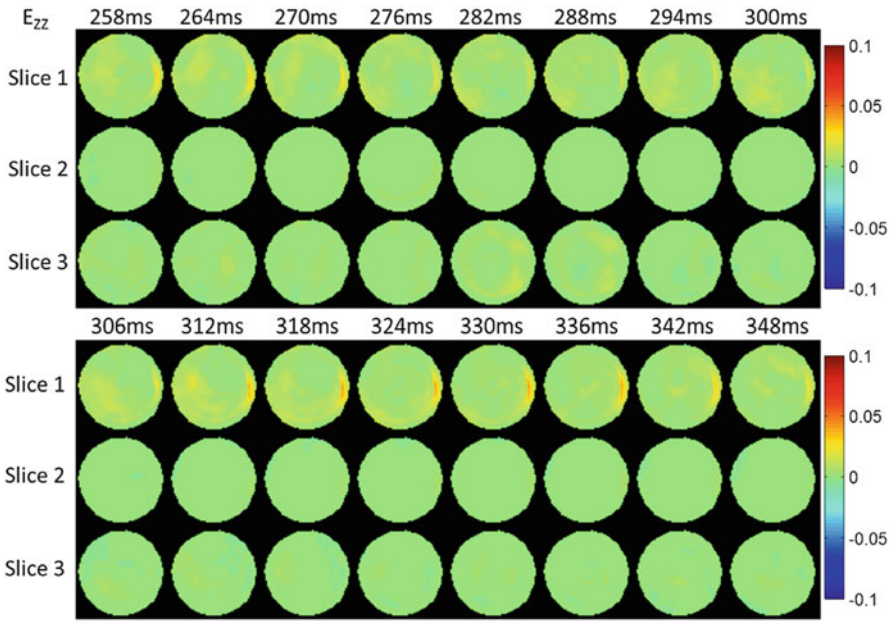

Fig. 5 Through plane (E_{ZZ}—along the I/S axis) strains obtained in a gelatin phantom in three consecutive 8 mm slices using zHARP. Impact occurred at approximately 250 ms post trigger

3.2 Human Cadaver Head

Four consecutive transverse slices were acquired using zHARP (Fig. 6). Radial circumferential ($E_{R\theta}$) shear strain fields as a function of time post trigger are shown in zHARP (Fig. 7) and CSPAMM (Fig. 8) acquisitions. Through plane strains (E_{ZZ}—along the I/S axis) are shown in Fig. 9. The fraction of the area of the brain with strain above defined thresholds (0.02, 0.04, and 0.06 strain) as a function of time post trigger is shown in Fig. 10 for the zHARP images.

4 Discussion

4.1 Measurement of Deformation in the Gelatin Phantom

Results obtained for the gelatin phantom agree qualitatively with previous results ([23]—Fig. 7). Additionally, results compare well between the three methods used for acquisition. The temporal response of the gelatin is slightly different for each of the three responses. The stiffness of the gel, which affects the deformation, is dependent on temperature. Grid tags was acquired first, CSPAMM second, and

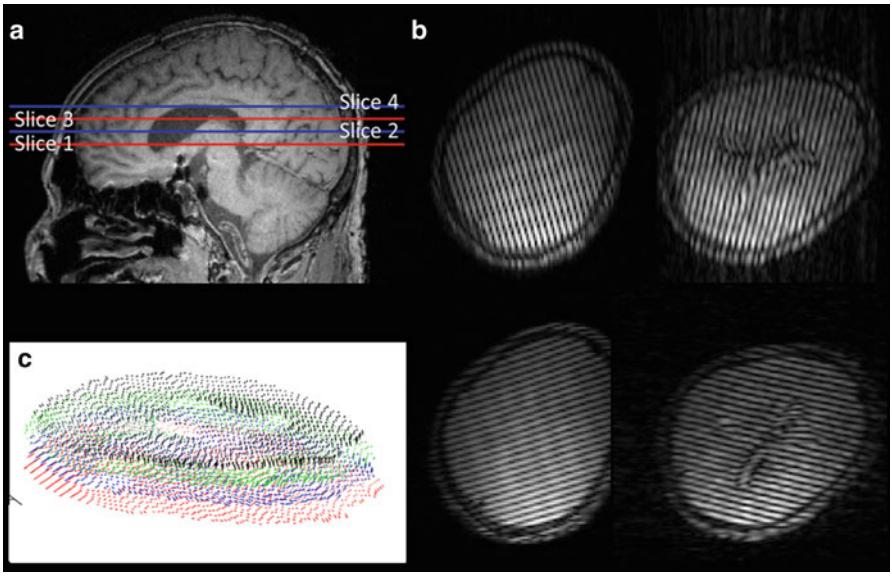

Fig. 6 (**a**) The location of the four transverse zHARP slices overlaid on a sagittal T_1-weighted image. The acquisition of slices two and four was repeated using CSPAMM. (**b**) zHARP images with tag lines in the vertical and horizontal directions shown at the first time point and at 276 ms post trigger. (**c**) A 3D displacement field of all four slices at 276 ms post trigger

zHARP last. Approximately 30–45 min elapsed between each of these acquisitions, so the temperature could have risen as a result of scanning and equilibration with room temperature. An increase in temperature corresponds to a decrease in stiffness. Additionally, the amount of time that elapsed between the application of the tags and the acquisition of the first image is different for each of the three sequences. The timing of the trigger is recorded in the DICOM file but is rounded to the nearest 2.5 ms, which provides some uncertainty in the timing between the three sequences. Still, the general consistency of the results and similarity to previously published experimental and simulation results provide confidence and validation to the experimental setup and analysis procedures.

4.2 Measurement of Deformation in the Cadaver Brain

Using the zHARP pulse sequence and analysis, a 3D deformation field was computed throughout a 3.2 cm slab in a human cadaver brain. The area fraction of the radial circumferential Lagrangian strains estimated during angular acceleration of the cadaver head (Fig. 10) show that the strains are lower in magnitude than those seen in the live human brain ([17]—Fig.12). The specimen obtained for this experiment was imaged at approximately 60 h post mortem. Ideally, the experiment

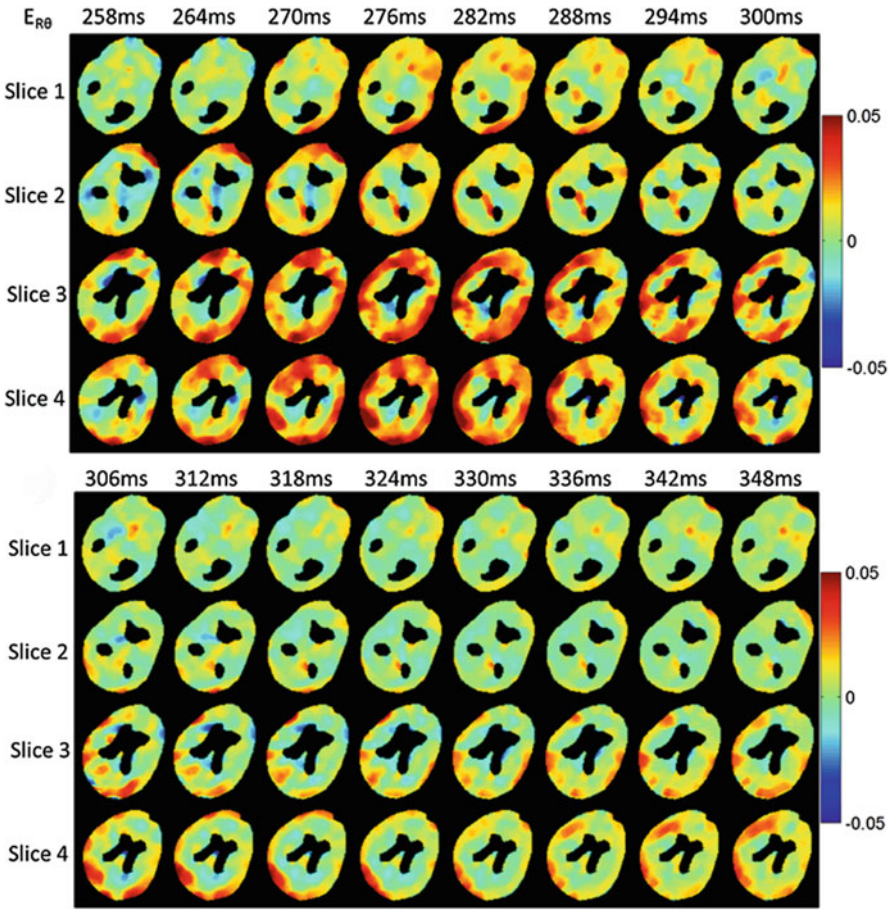

Fig. 7 Radial circumferential Lagrangian shear strains obtained using zHARP for each of the four slices from 258 to 348 ms post trigger. Impact occurred at approximately 250 ms post trigger

would have been carried out as soon as possible after death. Studies comparing in vivo and in situ tissue in the rat [31] and porcine [32, 33] brain showed that material properties remain constant for approximately 6 h post mortem and then begin to increase in stiffness. Similar to previous results, the area fraction of the radial-circumferential shear strain component showed a larger peak than the other two in-plane strain components.

Radial-circumferential shear strains measured using zHARP and CSPAMM (processed using MICSR) are qualitatively similar for the two slices where both sequences were acquired. However, some spatial and temporal local differences exist, which should be investigated in future experiments. Strain in the through plane direction contained higher magnitudes and more spatial variability than the other strain components. Experimental results previously obtained under similar loading

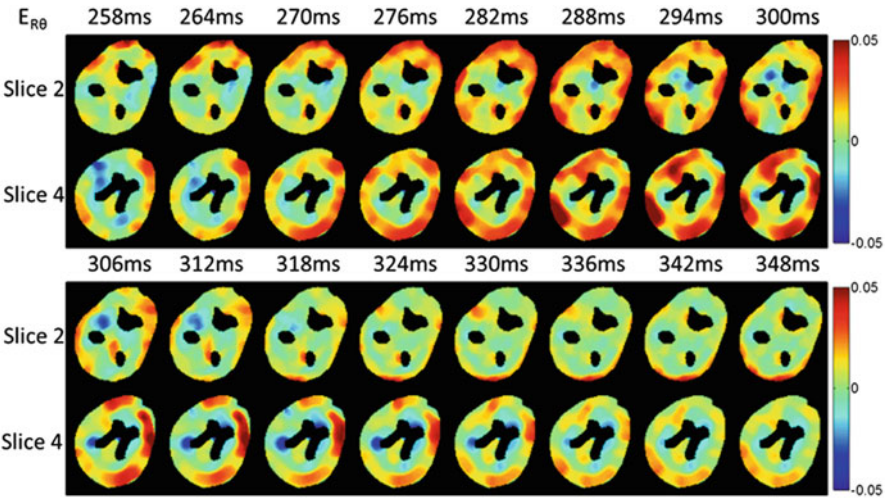

Fig. 8 Radial circumferential Lagrangian shear strains obtained using CSPAMM as a function of time post trigger. Impact occurred at approximately 250 ms post trigger

conditions were limited to 2D deformation fields, making direct comparison of the through plane strain components impossible.

The loading conditions applied during angular acceleration of the head are well below the point where injury could potentially occur. This is necessary for experiments to more directly compare these results with those obtained in living human subjects. The advantage of using post mortem tissue is that loading conditions at levels too great for live humans can be studied. Additionally, the acceleration can be repeated as many times as necessary, so that the whole brain can be imaged. In comparison in live humans, the number of repetitions is limited by what is safe and tolerable to the subject.

4.3 Reduction in the Number of Repetitions

Previous studies performed using this same device required 144 repetitions of the head acceleration motion to acquire a set of images from a single transverse plane in the brain. In the gelatin phantom, the same acquisition was replicated in 27 repetitions. The number of repetitions necessary to acquire a single acquisition using CSPAMM or zHARP is less than for grid tags because the number of phase encode steps can be substantially reduced. However, the acquisition must be repeated four times to create a single image set. The CSPAMM pulse sequence is implemented with a segmented EPI acquisition, which allows multiple phase encode lines to be acquired at high temporal resolution. Work is being done to add this capability to the zHARP pulse sequence.

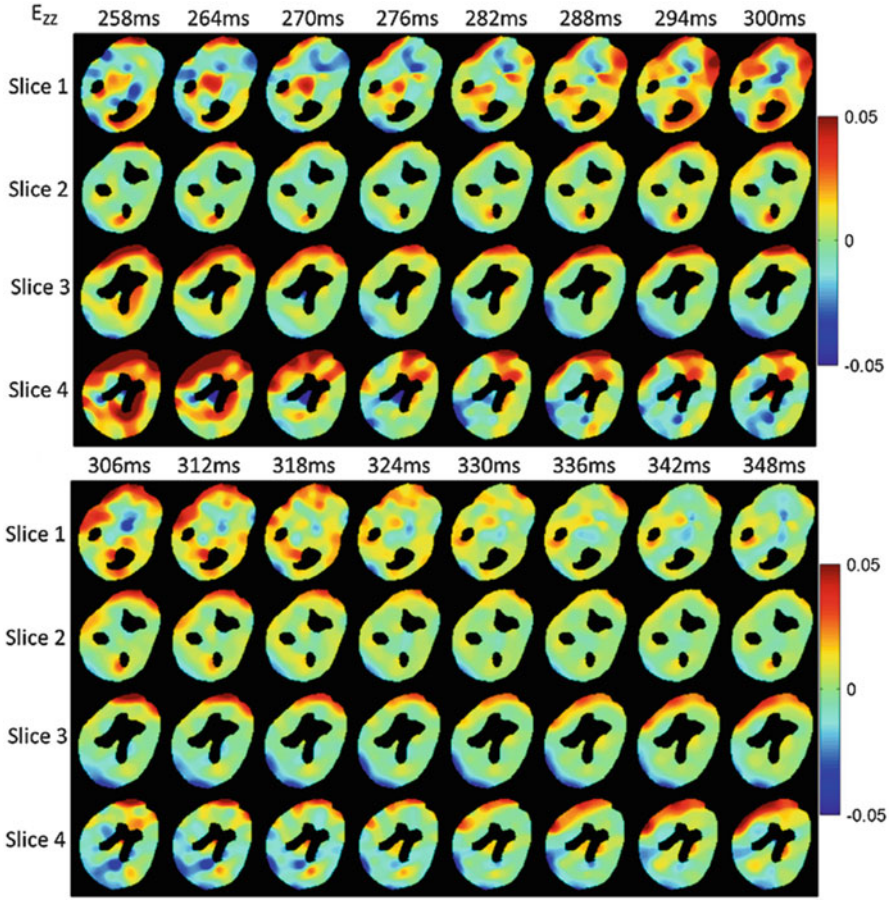

Fig. 9 Through plane (E_{ZZ}) Lagrangian strains obtained using zHARP for each of the four slices from 258 to 348 ms post trigger. Impact occurred at approximately 250 ms post trigger

If an EPI factor of 4 (i.e., four lines of k-space are acquired per repetition) is used with a GRAPPA factor of 2, then a 128×48 matrix could be acquired in nine repetitions for a single acquisition (36 for a single image set), which would allow for a large number of slices to be acquired relatively quickly in the brain.

4.4 Future Directions

Only a single specimen was analyzed in this study. In future studies, additional specimens will be analyzed, ideally within a shorter time frame post mortem. Additionally, increased levels of acceleration will be studied in addition to $260\,\mathrm{rad/s^2}$.

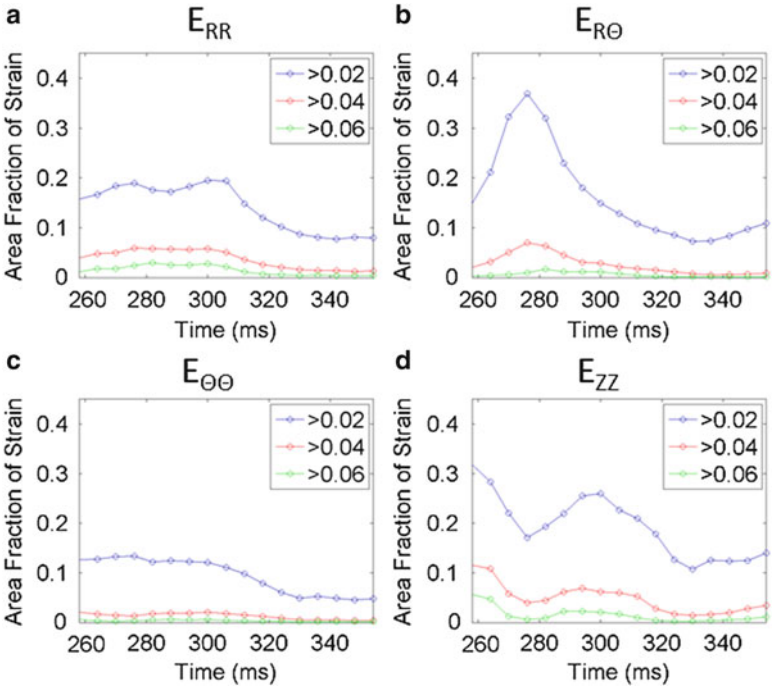

Fig. 10 The area fraction of (a) E_{RR}, (b) $E_{R\theta}$, (c) $E_{\theta\theta}$, and (d) E_{ZZ} as a function of time post trigger

Three-dimensional deformation fields have not yet been obtained in live human studies for comparison with post mortem results. Future studies will use zHARP to acquire 3D deformation fields in live human subjects.

The experimental and analysis methods presented in this paper extend on previous approaches by acquiring 3D deformation fields, reducing the number of repetitions necessary to acquire a single image, and demonstrating the ability to acquire high quality strain maps in post mortem tissue. Knowledge of the quantitative relationship between the live and post mortem human brain in response to acceleration will improve the understanding of response of the live human brain, thanks to the different loading conditions and degree of acceleration that can be applied to the post mortem brain.

Acknowledgments This work was funded by the Department of Defense in the Center for Neuroscience and Regenerative Medicine pilot grant (Pham) and National Institutes of Health grant NS 055951 (Bayly).

References

1. Langlois, J.A., Rutland-Brown, W., Wald, M.M.: The epidemiology and impact of traumatic brain injury: a brief overview. J. Head Trauma Rehabil. **21**(5), 375–8 (2006)
2. Shelden, C.H., et al.: The lucite calvarium—a method for direct observation of the brain. J. Neurosurg. **1**, 67–75 (1944)
3. Pudenz, R.H., Shelden, C.H.: The lucite calvarium—a method for direct observation of the brain. J. Neurosurg. **3**, 487–505 (1946)
4. Gosch, H.H., Gooding, E., Schneider, R.C.: Distortion and displacement of the brain in experimental head injuries. Surg. Forum 20, 425–426 (1969)
5. Hodgson, V.R., Gurdjian, E.S., Thomas, L.M.: Experimental skull deformation and brain displacement demonstrated by flash x-ray technique. J. Neurosurg. **25**(5), 549–52 (1966)
6. Shatsky, S.A., et al. Traumatic distortions of the primate head and chest: correlation of biomechanical, radiological and pathological data. In: Proceedings 18th Stapp Car Crash Conference, Ann Arbor (1974)
7. Stalnaker, R.L., et al. Head impact response. In: Proceedings of the 21st Stapp Car Crash Conference (1977)
8. Zou, H., Schmiedeler, J.P., Hardy, W.N.: Separating brain motion into rigid body displacement and deformation under low-severity impacts. J. Biomech. **40**(6), 1183–91 (2007)
9. Zhang, L., et al.: Recent advances in brain injury research: a new human head model development and validation. Stapp Car Crash J. **45**, 369–94 (2001)
10. Ivancevic, V.G.: New mechanics of traumatic brain injury. Cogn. Neurodyn. **3**(3), 281–93 (2009)
11. Kimpara, H., et al.: Investigation of anteroposterior head-neck responses during severe frontal impacts using a brain-spinal cord complex FE model. Stapp Car Crash J. 50, 509–44 (2006)
12. Cloots, R.J., et al.: Biomechanics of traumatic brain injury: influences of the morphologic heterogeneities of the cerebral cortex. Ann. Biomed. Eng. **36**(7), 1203–15 (2008)
13. Kimpara, H., Iwamoto, M.: Mild traumatic brain injury predictors based on angular accelerations during impacts. Ann. Biomed. Eng. **40**(1), 114–26 (2012)
14. Zerhouni, E.A., et al.: Human heart: tagging with MR imaging–a method for noninvasive assessment of myocardial motion. Radiology **169**(1), 59–63 (1988)
15. Axel, L., Dougherty, L.: MR imaging of motion with spatial modulation of magnetization. Radiology **171**(3), 841–5 (1989)
16. Osman, N.F., et al.: Cardiac motion tracking using CINE harmonic phase (HARP) magnetic resonance imaging. Magn. Reson. Med. **42**(6), 1048–60 (1999)
17. Sabet, A.A., et al.: Deformation of the human brain induced by mild angular head acceleration. J. Biomech. **41**(2), 307–15 (2008)
18. Feng, Y., et al.: Relative brain displacement and deformation during constrained mild frontal head impact. J. R. Soc. Interface **7**(53), 1677–88 (2010)
19. Bayly, P.V., et al.: Deformation of the human brain induced by mild acceleration. J. Neurotrauma **22**(8), 845–56 (2005)
20. Fischer, S.E., et al.: Improved myocardial tagging contrast. Magn. Reson. Med. **30**(2), 191–200 (1993)
21. Fischer, S.E., et al.: True myocardial motion tracking. Magn. Reson. Med. **31**(4), 401–13 (1994)
22. Abd-Elmoniem, K.Z., et al.: Three-dimensional magnetic resonance myocardial motion tracking from a single image plane. Magn. Reson. Med. **58**(1), 92–102 (2007)
23. Bayly, P.V., et al.: Magnetic resonance measurement of transient shear wave propagation in a viscoelastic gel cylinder. J. Mech. Phys. Solids **56**(5), 2036–2049 (2008)
24. Griswold, M.A., et al.: Generalized autocalibrating partially parallel acquisitions (GRAPPA). Magn. Reson. Med. **47**(6), 1202–10 (2002)
25. NessAiver, M., Prince, J.L.: Magnitude image CSPAMM reconstruction (MICSR). Magn. Reson. Med. **50**(2), 331–42 (2003)

26. Osman, N.F., McVeigh, E.R., Prince, J.L.: Imaging heart motion using harmonic phase MRI. IEEE Trans. Med. Imag. **19**(3), 186–202 (2000)
27. Ryf, S., et al.: Peak-combination HARP: a method to correct for phase errors in HARP. J. Magn. Reson. Imag. **20**(5), 874–80 (2004)
28. Liu, X., Prince, J.L.: Shortest path refinement for motion estimation from tagged MR images. IEEE Trans. Med. Imag. **29**(8), 1560–72 (2010)
29. Spottiswoode, B.S., et al.: Tracking myocardial motion from cine DENSE images using spatiotemporal phase unwrapping and temporal fitting. IEEE Trans. Med. Imag. **26**(1), 15–30 (2007)
30. Filas, B.A., et al.: A new method for measuring deformation of folding surfaces during morphogenesis. J. Biomech. Eng. **130**(6), 061010 (2008)
31. Vappou, J., et al.: Assessment of in vivo and post-mortem mechanical behavior of brain tissue using magnetic resonance elastography. J. Biomech. **41**(14), 2954–9 (2008)
32. Garo, A., et al.: Towards a reliable characterisation of the mechanical behaviour of brain tissue: The effects of post-mortem time and sample preparation. Biorheology **44**(1), 51–8 (2007)
33. Prevost, T.P., et al.: Dynamic mechanical response of brain tissue in indentation in vivo, in situ and in vitro. Acta Biomater. **7**(12), 4090–101 (2011)

Identification of Tongue Muscle Fibre Group Contraction from MR Images

Yikun Wang, Thiranja P. Babarenda Gamage, Poul M.F. Nielsen, Oliver Röhrle, and Martyn P. Nash

Abstract The tongue is made up of a collection of interwoven families of muscle fibres, but little is known about the function of each of these muscle groups during physiological motions of the tongue. Magnetic resonance imaging (MRI) tissue tagging has been used to observe internal tongue tissue deformation, and estimate possible contractile patterns of the tongue muscles. However, the complex fibrous arrangement and the limited field of view from 2D planar images make it difficult to identify muscle movements in 3D space. This casts doubt on the empirical conclusions drawn from these studies. Here we present a computational modelling framework to estimate the contractile properties of the different muscle groups in the tongue by combining a generic tongue model with anatomical and strain data derived from tagged MR images. Tongue propulsion during dry swallowing was simulated and results were compared with previously published data. The model predicated model results by using empirical conclusion showed that, the co-activation of single intrinsic muscles (transversus, verticalis) cannot explain the most dominate expansion in the posterior tongue body. Contact between the tongue and upper palate and simultaneous contraction with more muscles may also result in anterior–posterior expansion.

Y. Wang (✉) • T.P.B. Gamage
Auckland Bioengineering Institute, University of Auckland, New Zealand
e-mail: yikun.wang@auckland.ac.nz

P.M.F. Nielsen • M.P. Nash
Auckland Bioengineering Institute, University of Auckland, New Zealand

Department of Engineering Science, University of Auckland, New Zealand

O. Röhrle
Institut für Mechanik (Bauwesen), Universität Stuttgart, Germany

A. Wittek et al. (eds.), *Computational Biomechanics for Medicine: Models, Algorithms and Implementation*, DOI 10.1007/978-1-4614-6351-1_16,

© Springer Science+Business Media New York 2013

1 Introduction

The tongue is a dexterous organ consisting of a collection of muscles organised into functionally distinct fibre families. The 11 fibre families within the tongue may be classified into three types: the intrinsic muscles, including transversus (*t*), verticalis (*v*), superior longitudinalis (*sl*), inferior longitudinalis (*il*); the extrinsic muscles which contains genioglossus anterior (*ga*), genioglossus posterior (*gp*), styloglossus (*s*), hyoglossus (*h*), and external muscle fibre groups such as geniohyoid (*g*), digastric (*d*), and mylohyoid (*m*). The deformed shape of the tongue is determined from co-activations of one, or multiple, intrinsic and extrinsic muscles [6]. Napadow et al. [13] and Gilbert et al. [6] suggested that treating the multiple muscles within the tongue as a single entity is essential for studying tongue configurations in various physiological activities, such as mastication and speaking.

The literature regarding muscle activation levels during tongue motion is sparse, and the physiological roles of the different muscle groups in the tongue are poorly understood. Magnetic resonance imaging tissue tagging (tagged MRI) provides an approach to monitor the movements of internal material points within the tongue tissue. Tagged MRI makes it possible to fully characterise deformation of the tongue during different activities by tagging and tracking material points within the tongue body. For example, Napadow et al. [11, 12] and Felton et al. [4] studied the deformation of the tongue in-vivo during phonetic and food intake tasks and provided a quantitative description of the internal tissue movements during these activities. They also attempted to explain the different muscle activation patterns by combining muscle motion derived from MR images with muscle fibre spatial distributions and orientations.

This study reports on the development of an anatomically based large deformation mechanics FE tongue model, which includes all 11 muscle fibre families. This model provides a generic platform for studying tongue motion by allowing the activation levels of one or more muscle fibre families to be prescribed. This framework has been applied to identify the optimal placement of motion sensors for tracking tongue movements [19]. The combination of such a model with in-vivo tagged MRI experimental data and inverse modelling techniques for revealing the muscle activation patterns makes it possible to estimate the structure–function relationships for the different muscle families. Previous work by Pelteret and Reddy [16] has shown the potential of this approach where particles' motions on the surface of the mid-sagittal line was used to determine possible activation patterns. In this study, we present an inverse modelling technique that allows the contractile activation properties of the different fibre families within the tongue to be identified using quantitative strain measurements derived from tagged MRI data during a predetermined tongue movement as previously reported by Napadow et al. [12]. We also aimed to test the empirical conclusions drawn by Napadow et al. [12].

2 Method

2.1 Data from MR Images

This study was based on deformation data derived from a set of tagged MR images from the mid-sagittal plane of the tongue in seven subjects, taken during propulsion under dry swallowing condition [12]. The mid-sagittal area of the tongue for each subject's images were divided into four non-overlapping regions, with each region including several muscle fibre families. The average local axial strains were derived for each region by tracking the deformation of the MRI tags. For each region, the mean $\pm$ standard derivation axial strains were recorded for the anterior–posterior and superior–inferior directions. The reported experimental data are shown in Table 1.

The MR images were obtained using a 1.5 Tesla Siemens Vision MRI system, and an anterior neck coil with an ultrafast asymmetric gradient echo pulse sequence (TurboFlash). The imaging parameters were defined as follows: image slice thickness, 10 mm; effective spatial resolution, 1.33×1.33 mm; and the matrix size, 80×128.

The observations by Napadow et al. [12] in Table 1 indicated that during tongue propulsion in dry swallowing, the tongue expanded along the anterior–posterior and superior–inferior directions. Since contraction of the muscle fibre groups is the only driving force leading to tongue deformation, Napadow et al. [12] postulated that the geometrical arrangements of the different tongue muscles would greatly influence the resultant shape of the tongue. Based on these observations, Napadow et al. [12] concluded that the anterior–posterior and superior–inferior expansions were most likely due to contraction of the transversus or verticalis intrinsic muscles (both of which according to classical anatomy are believed to align orthogonally in the coronal image plane, as shown in Fig. 1a and c, respectively). They also hypothesised that the retrograde motion in propulsion was a consequence of activation of the styloglossus (shown in Fig. 1b). We set out to test these hypotheses using our quantitative model of tongue mechanics.

Table 1 Measured axial strain data (mean $\pm$ standard deviation; $* P < 0.01$) taken from Napadow et al. [12] estimated within four predefined regions in the tongue during dry swallowing. AP and SI denote the anterior–posterior and superior–inferior directions, respectively

	Region 1	Region 2	Region 3	Region 4
AP	0.034 ± 0.053	0.065 ± 0.081	$0.173 \pm 0.045 *$	$0.064 \pm 0.044 *$
SI	$0.083 \pm 0.067 *$	0.050 ± 0.093	$0.098 \pm 0.050 *$	0.008 ± 0.058

Fig. 1 Distributions and orientations of transversus, styloglossus and verticalis muscles within the FE model of the tongue. The vectors in the FE mesh illustrate the distribution of fibre orientations, and the length of the vectors represents the local volume fraction. The colours of orthogonal axes outside the tongue model indicate the superior (*blue*), posterior (*green*) and lateral (*red*) directions (these colours do not relate to the fibre groups). (**a**) Transversus, (**b**) Styloglossus, (**c**) Verticalis

2.2 Modelling Tongue Mechanics

We constructed a nonlinear hyperelastic model of the tongue based on a FE representation of its geometrical shape, which was embedded with the fibrous architecture of the different muscle groups. The geometric data used to fit our tongue model were digitised from the female Visible Human data set [17]. The FE mesh consisted of 64 hexahedral elements (interpolated using tricubic Hermite basis functions), which connected 120 FE nodes (2,880 geometric degrees of freedom), as illustrated in Fig. 1. The eleven muscle fibre families were embedded in the geometrical model by fitting FE fields to describe the tongue's interior fibrous architecture.

The mechanical response of the tongue was described as a nonlinear hyperelastic material (Mooney–Rivilin material model) with multiple fibre reinforcement, contributing to the passive and active stress components [5]. The total 2nd Piola–Kirchhoff stress tensor, denoted $\mathbf{S}_{\text{tissue}}$, at each point in the tongue was calculated as a linear superposition of the mechanical response of the ground matrix (connective tissues, fat), denoted $\mathbf{S}_{\text{matrix}}$, plus a sum of stress contributions from the different muscle families, as indicated in Eq. (1).

$$\mathbf{S}_{\text{tissue}} = \mathbf{d}_{\text{matrix}}\mathbf{S}_{\text{matrix}} + 2\sum_{i\in\mathscr{F}}\left[\frac{d_i}{\lambda_i^2}\sigma_i\left(\alpha_i,\lambda_i,\sigma_i^{\max}\right)\right]\mathbf{a}_i\otimes\mathbf{a}_i, \tag{1}$$

where $\mathscr{F} = \{t, v, sl, \ldots\}$ is the set containing all indices of the muscle fibre groups (see Introduction for definitions), $\lambda_i^2 = \mathbf{a}_i \cdot \mathbf{C}\,\mathbf{a}_i$ is the squared fibre stretch (where $\mathbf{C}$ is the right Cauchy–Green deformation tensor), $\alpha_i \in [0,1]$ is the activation parameter for muscle fibre group i, and $\sigma_i^{\max}$ is the maximal contractile stress that can be generated by the fibres in muscle group i [1, 7, 8]. The volume fractions for each fibre family (denoted d_i, where i is the muscle fibre family index), represented

the local proportions of each fibre family at each point in the tongue, and were modelled as separate fields fitted to data from Wilhelms-Tricarico [20] and $\mathbf{d}_{\text{matrix}}$ is the volume fraction of the remaining substances, i.e. the ground matrix. The fibre orientations for each fibre family (denoted $\mathbf{a}_i$) were represented as spatially varying vector fields, each with three independent components that were fitted using tricubic Hermite basis functions interpolated over the geometric tongue mesh. No anatomical evidence is available in the literature which shows interaction between different muscle fibre groups during activation. Therefore, we assumed that the different muscle fibre groups were independent and did not directly interact.

The stress term of the ground matrix was modelled as a Mooney–Rivilin material, $\mathbf{S}_{\text{matrix}} = 2(c_1 + c_2 tr(\mathbf{C}))\mathbf{I} - 2c_2\mathbf{C} + p\mathbf{C}^{-1}$. Incompressibility constraints were also included, which involved the introduction of a linearly interpolated hydrostatic pressure field within the tongue as defined in Nash and Hunter [14]. The total fibre stress was defined in terms of the fibre stretch, maximal contractile stress, and activation parameter for each muscle fibre group using:

$$\sigma_i(\alpha_i, \lambda_i, \sigma_i^{\max}) = \sigma_i^{\max}\left[\mathbf{f}_i^{\text{passive}}(\lambda_i) + \alpha_i \mathbf{f}_i^{\text{active}}(\lambda_i)\right], \tag{2}$$

where $\mathbf{f}_i^{\text{passive}}$ and $\mathbf{f}_i^{\text{active}}$ are normalised length–force relationships for the passive and active behaviour of skeletal muscle tissues, respectively, as defined in Blemker et al. [1].

The material parameters in this study were selected based on data in the literature. The overall shear modulus of the tongue body was estimated by Cheng et al. [2] to be (2.67 ± 0.29) kPa (mean $\pm$ standard deviation). For a Mooney–Rivilin material, the shear modulus can be represented as $2(c_1 + c_2)$. We assumed that the ground matrix contributed approximately 40% of the overall passive shear response (with the remainder due to the passive fibre components), and thus we defined $c_1 = 0.375$ kPa and $c_2 = 0.175$ kPa. Titze [18] reported a maximum active fibre stress of 100 kPa for the human laryngeal muscles, whereas De Groot and Van Leeuwen [3] reported a maximum active fibre stress in a chameleon tongue of 200 kPa. We assumed that the maximum active stress of the human tongue lies within this range, and thus set $\sigma_i^{\max} = 150$ kPa for all muscle groups.

2.3 Estimation of Contractile Parameters

The mechanics of the tongue depends on the levels of activation for each muscle fibre group. We aimed to reproduce the measured in-vivo deformation patterns using our FE model by independently varying the fibre activation levels for different muscle groups. This section describes the parameter estimation approach used to address this complex inverse problem to identify the muscle group activation levels.

As the data reported by Napadow et al. [12] was based on a group of 7 subjects, the observations can be considered as being representative of the underlying tongue

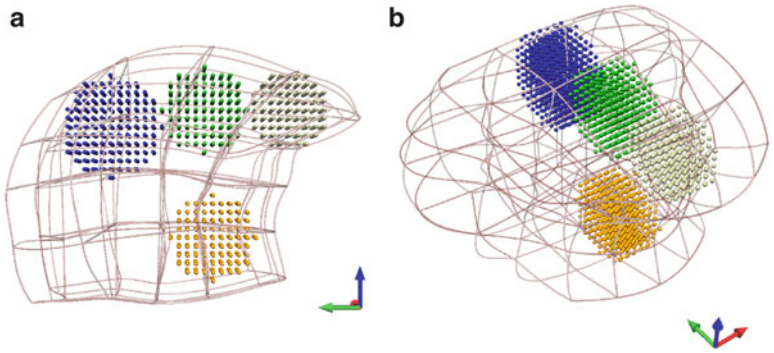

Fig. 2 The *white, green, blue and golden sets* of material points within the tongue were used to represent regions 1, 2, 3 and 4, respectively, in Fig. 1 of Napadow et al. [12]

motion during dry swallowing. To verify Napadow et al. [12]'s conclusion regarding which muscle families were activated during dry swallowing, we compared results from activating only these muscles in our model to the experimental data collected by Napadow et al. [12] (Table 1). To compare the deformation of the tongue model with the experimental data, four sets of material points were defined within the reference (undeformed) tongue model, as shown in Fig. 2 (c.f. Fig. 1 of [12]). Within each region, the material points were uniformly distributed (1.3 mm spacing) throughout a 10 mm thick mid-sagittal plane to mimic the MR image resolution. For deformed configurations, strain tensors were evaluated at each material point, and the average predicted strain components for each of the four regions were compared with the experimental data in Table 1.

In order to quantify the similarity between model predictions and experimental data, we compared the average axial strains for each region using the following two objective functions:

$$f_1 = \sum_{i=1}^{4} (E_{\mathrm{AP}}^{(i,\mathrm{experiment})} - E_{\mathrm{AP}}^{(i,\mathrm{model})})^2 + \sum_{i=1}^{4} (E_{\mathrm{SI}}^{(i,\mathrm{experiment})} - E_{\mathrm{SI}}^{(i,\mathrm{model})})^2, \tag{3}$$

$$f_2 = \sum_{i=1}^{4} \left(\frac{E_{\mathrm{AP}}^{(i,\mathrm{experiment})} - E_{\mathrm{AP}}^{(i,\mathrm{model})}}{\sigma_{\mathrm{AP}}^{(i,\mathrm{experiment})}} \right)^2 + \sum_{i=1}^{4} \left(\frac{E_{\mathrm{SI}}^{(i,\mathrm{experiment})} - E_{\mathrm{SI}}^{(i,\mathrm{model})}}{\sigma_{\mathrm{SI}}^{(i,\mathrm{experiment})}} \right)^2, \tag{4}$$

where superscript i denotes the region index, AP and SI denote the anterior–posterior and superior–inferior directions, respectively, and σ denotes the standard deviations of the measurements. The difference between the objective functions is that f_2 takes into account the variance of the experimental measurements as a weighting factor on the strain comparison.

Note that the model predicted axial strains depend on the activation level vector $\boldsymbol{\alpha}$, where $\boldsymbol{\alpha} = (\alpha_t, \alpha_v, \alpha_{sl}, \ldots)$. Finding a configuration of the tongue model that

best matches the given experiment data can thus be formulated as an optimisation problem over the parameter domain,

$$\hat{\boldsymbol{\alpha}} = \operatorname{argmin} f_j(\boldsymbol{\alpha}), \tag{5}$$

subject to the constraints $\mathbf{0} \leq \boldsymbol{\alpha} \leq \mathbf{1}$, where j indicates the choice of objective function defined by Eq. (3) (for $j = 1$) or Eq. (4) (for $j = 2$).

The parameter estimation procedure was implemented using the optimisation toolbox package in Matlab R2009b. In our implementation, we restricted the range of permissible parameters $\boldsymbol{\alpha}$ to $[0.001, 1.0]$. A trust-region-reflective algorithm was used to solve the optimisation problem. If the objective function values for two consecutive iterations, i.e., $f_1^{(k)}$ and $f_1^{(k+1)}$, differed by less than 10^{-5}, then the optimisation algorithm was terminated.

In this study, we tested the conclusions of Napadow et al. [12] using computational experiments to quantitatively identify the levels of activation of the muscles involved in swallowing. Activations of two different combinations of muscle groups were used in the analysis to investigate the validity of these conclusions. Two deformation cases were considered: in case A we activated only the transversus and styloglossus muscles; and in case B we activated only the verticalis and styloglossus muscles. Each case included one intrinsic and extrinsic muscle. This reduced $\boldsymbol{\alpha}$ to two components, $\boldsymbol{\alpha} = (\alpha_s, \alpha_t)$ in case A, and $\boldsymbol{\alpha} = (\alpha_s, \alpha_v)$ in case B. The remaining muscle groups were not activated ($\alpha_{sl,il,ga,gp,h,g,d,m} = 0$). For each case, the inverse procedure was performed using several different pairs of initial values for $\boldsymbol{\alpha}$, including $(0.1, 0.9)$, $(0.5, 0.5)$ and $(0.9, 0.1)$, to ensure that the algorithm reached the global optimal solution.

3 Results

The optimal activation levels were determined by matching FE model predicted tongue strains to the experimental data of Napadow et al. [12]. Table 2 shows the optimal solutions found using objective function f_1 for the two muscle combination cases.

Table 2 Parameter estimation results using objective function f_1. Case A denotes activation of styloglossus and transversus muscles and Case B denotes activation of styloglossus and verticalis muscles. $f_1(\hat{\boldsymbol{\alpha}})$ denotes the objective function value at the optimal solutions

	$\hat{\boldsymbol{\alpha}}$	$f_1(\hat{\boldsymbol{\alpha}})$
Case A	$(0.317, 0.317)$	0.051
Case B	$(0.920, 0.079)$	0.091

Table 3 Optimal results using the f_1 objective function for Case A (styloglossus and transversus muscle activation). The data are means of axial strains in four predefined regions within the model. AP and SI represent the anterior–posterior and superior–inferior directions, respectively

Case A	Region 1	Region 2	Region 3	Region 4
AP	0.0248	0.0705	−0.0293	−0.0002
SI	0.0744	0.0397	0.0282	0.0568

Table 4 Optimal results using the f_1 objective function for Case B (styloglossus and verticalis muscle activation). The data are means of axial strains in four predefined regions within the model. AP and SI represent the anterior–posterior and superior–inferior directions, respectively

Case B	Region 1	Region 2	Region 3	Region 4
AP	−0.0705	−0.0489	−0.0370	−0.0012
SI	−0.0043	0.0037	0.0049	−0.0003

The corresponding strains, at the optimum activation levels $\hat{\boldsymbol{\alpha}}$ identified for each case using f_1, are shown in Tables 3 and 4. A positive value represents extension, while a negative value indicates tissue compression. When comparing Table 3 with Table 1, the average axial strains in regions 1 and 2 compared well with the experimental data in terms of sign and the approximate order of magnitude with the main difference occurred within region 3. Table 1 shows the posterior region of the tongue in propulsion is expanding in AP direction. However, the optimal model predictions in Table 3 show that the posterior region (region 3) contracted in the AP direction (−0.0293). Thus, the model predicted axial strains for each region had an opposite sign to those measured experimentally.

In Napadow et al. [12]'s data (Table 1), the average axial strains along AP and SI directions in region 3 are the most significant data ($p < 0.001$). Thus, the above results suggested that the optimal solutions were not consistent with the experimental data, since none of the model predications showed similar predicted deformations to those informed by experimental data at posterior regions.

Parameter identification using the two deformation cases with f_2 resulted in optimal solutions with zero activation levels for the two muscle groups involved. In other words, the f_2 function rejected case A and B as possible pairs of activated muscles to achieve the recorded configuration data for the propulsion of the tongue.

4 Discussion

MRI has been extensively applied in tissue deformation analysis. However for measurements of the tongue, most studies have only used a limited number of images in an effort to reduce tongue motion during scanning. The complex nature of the tongue's fibre arrangements have also added to the challenges of understanding the synergy between tongue motion and muscular activation patterns. The parameter estimation procedure proposed above demonstrates the feasibility of estimating the activation levels of different selected muscular families by combining movement information derived from MR images and a 3D anatomically based mechanical model.

Two objective functions, f_1 and f_2, have been used to quantify the similarity between model and experimental data during the optimisation procedure. f_1 equally weighted each average strain component. By comparing the model results and experimental data, we concluded that o-contraction of styloglossus and verticalis muscles was unlikely to cause tongue propulsion due to the unmatched signs of all regional axial strains. The styloglossus and transversus muscles could drive the deformation to closely match the experimental data in regions 1 and 2. The most reliable experimental data were recorded in region 3; however, the model predicts totally different movements compared with the data of Napadow et al. [12].

When using the objective function f_2, the components of the average axial strains were weighted by the inverse of the standard deviations of the corresponding experimentally determined strain components. Small standard deviations indicate that the experimentally determined strain values across the seven subjects were concentrated around the computed mean (E) and hence were more reliable estimates. In f_2, comparatively small standard deviations correspond to a higher weight. When estimating the parameters using f_2, both of the estimated activation levels for case A and B were all zeros, which shows how activating the pairs of muscles groups (for cases A and B) could not produce the large positive axial strain recorded in the anterior–posterior direction for region 3 of the experiments.

Using the objective functions f_1 and f_2 for cases A and B revealed that the deformation in the posterior region (region 3) predicted by the model was fundamentally different to the experimental observation presented in Table 1. The axial strain for each muscle in the tongue is directly influenced by the muscle's fibre orientation which, along with the active stress component, defines the resultant orientation of the active stress field. Consequently, the local fibre direction cannot be ignored. Within our model, the direction of the transversus muscle in the posterior region of the tongue, around the mid-sagittal plane, is oriented in the anterior–posterior direction, while the verticalis fibre rotates towards the direction of axial plane. Thus, the axial strain in AP direction may only show a compression-like deformation (negative sign of strain), when activating one of the intrinsic muscles. In short, the fibrous structure of transversus and verticalis muscle in the posterior of the tongue can only lead to contraction along the anterior–posterior direction.

A recent diffusion tensor MRI (DTMRI) study by Kim et al. [10] on the fibrous arrangement of the tongue tissue confirmed a similar anatomical description to the model presented here. Kim et al. [10] observed that the anterior portion of the intrinsic transversus and verticalis muscles were orientated parallel to the coronal image plane. However, both gradually rotated almost into the transverse image plane (axial image plane) in the posterior side of the tongue. The empirical conclusion by Napadow et al. [12] is based on the classical definition of those fibre arrangements and a 2D image with limited viewing angle. In classical anatomy, the transversus and verticalis fibre are believed to orthogonally interdigitated, producing a woven texture pattern with the verticalis muscle arranging itself along the superior–inferior direction and the transversus muscle passing from the lateral to medial direction, throughout the entire upper tongue body. This may have misled the analysis of the tissue movement in the posterior region. Thus, the empirical conclusion by Napadow et al. [12], regarding the contraction of a single intrinsic muscle with the styloglossus muscle, may be insufficient to explain the posterior expansion in AP direction.

It is natural to consider whether more muscles could be activated simultaneously to form propulsion of the tongue. Felton et al. [4] reconstructed principal strains on the mid-sagittal, anterior and posterior coronal planes of the tongue using tagged MRI techniques during the propulsive phase. They reported that the activated muscles may include the hyoglossus, genioglossus, transversus, verticalis and styloglossus muscles, and there is a strong possibility that other structures might be involved. For instance, the tongue may interact with surrounding oral structures such as the palate. Ono et al. [15] and Kennedy et al. [9] studied the intra-oral pressures patterns during swallowing and showed significant tongue interaction with the upper palate and generate contact pressures systematically from anterior to posterior on the upper palate. This implies an external loading (force) applied from the superior direction on the tongue dorsum.

While these comparisons indicate possible tongue muscle activation levels during swallowing, the results were limited to analysing the contributions of only two muscle groups. Furthermore the optimal solution only gives a possible mathematical agreement between the model and experimental data, whose physiological significance needs to assessed. Consequently an estimation procedure with more comprehensive parameter selection is necessary.

5 Conclusion

An anatomically realistic biophysical model of the tongue was developed to determine whether activation levels of two different pairs of muscle fibre families were involved in propulsion of the tongue during dry swallowing. This involved optimising muscle activation levels such that the difference between model predicted and experimentally measured axial strains in four regions of the tongue using tagged MRI [12] were minimised. The model predicted strains at the optimal

activation levels were then compared with the measurements of Napadow et al. [12]. The results showed that the empirical conclusion of Napadow et al. [12] based on co-contraction of a single intrinsic muscle (transversus or verticalis muscle) and styloglossus muscles was not sufficient to explain the major expansion in the AP direction at the posterior of the tongue during the propulsive phase. Future work will look at extending the identification framework to include more than two muscle fibre families, and employing a systematic approach to assess which combinations of muscles improve model predictions. Contact boundary conditions will also be included in the modelling framework in order to simulate the interaction between the tongue body and the upper palates to better reproduce the physiological conditions of tongue propulsion.

Acknowledgments Yikun Wang would like to acknowledge support from the New Zealand Foundation for Research in Science and Technology under contract NERF UOAX0406. The authors tender their thanks to Prof. Jules Kieser from The University of Otago and the late Prof. Andrew Pullan from The University of Auckland for valuable discussions on anatomy of the tongue and model development.

References

1. Blemker, S.S., Pinsky, P.M., Delp, S.L.: A 3D model of muscle reveals the causes of nonuniform strains in the biceps brachii. J. Biomech. **38**(4), 657–665 (2005)
2. Cheng, S., Gandevia, S.C., Green, M., Sinkus, R., Bilston, L.E.: Viscoelastic properties of the tongue and soft palate using MR elastography. J. Biomech. **44**(3), 450–454 (2011)
3. De Groot, J.H., Van Leeuwen, J.L.: Evidence for an elastic projection mechanism in the chameleon tongue. Proc. R. Soc. B Biol. Sci. **271**(1540), 761–770 (2004)
4. Felton, S.M., Gaige, T.A., Reese, T.G., Wedeen, V.J., Gilbert, R.J.: Mechanical basis for lingual deformation during the propulsive phase of swallowing as determined by phase-contrast magnetic resonance imaging. J. Appl. Physiol. **103**(1), 255–265 (2007)
5. Gerard, J.M., Ohayon, J., Luboz, V., Perrier, P., Payan, Y.: Non-linear elastic properties of the lingual and facial tissues assessed by indentation technique: Application to the biomechanics of speech production. Med. Eng. Phys. **27**(10), 884–892 (2005)
6. Gilbert, R.J., Napadow, V.J., Gaige, T.A., Wedeen, V.J.: Anatomical basis of lingual hydrostatic deformation. J. Exp. Biol. **210**(23), 4069–4082 (2007)
7. Holzapfel, G.A.: Nonlinear Solid Mechanics: A Continuum Approach for Engineering Science. Springer, New York (2002)
8. Holzapfel, G.A., Gasser, T.C., Ogden, R.W.: A new constitutive framework for arterial wall mechanics and a comparative study of material models. J. Elasticity **61**(1), 1–48 (2000)
9. Kennedy, D., Kieser, J., Bolter, C., Swain, M., Singh, B., Waddell, J.N.: Tongue pressure patterns during water swallowing. Dysphagia **25**(1), 11–19 (2010)
10. Kim, S., Barnett, A.S., Pierpaoli, C., Chi-Fishman, G.: Three-dimensional mapping of lingual myoarchitecture by diffusion tensor mri. NMR Biomed. **21**(5), 479–488 (2008)
11. Napadow, V.J., Chen, Q., Wedeen, V.J., Gilbert, R.J.: Intramural mechanics of the human tongue in association with physiological deformations. J. Biomech. **32**(1), 1–12 (1999a)
12. Napadow, V.J., Chen, Q., Wedeen, V.J., Gilbert, R.J.: Biomechanical basis for lingual muscular deformation during swallowing. Am. J. Physiol. Gastrointest. Liver Physiol. **277**(3), 695–701 (1999b)

13. Napadow, V.J., Kamm, R.D., Gilbert, R.J.: A biomechanical model of sagittal tongue bending. J. Biomech. Eng. **124**(5), 547–556 (2002)
14. Nash, M.P., Hunter, P.J.: Computational mechanics of the heart. J. Elasticity 61(1), 113–141 (2000)
15. Ono, T., Hori, K., Nokubi, T.: Pattern of tongue pressure on hard palate during swallowing. Dysphagia 19(4), 259–264 (2004)
16. Pelteret, J.-P.V., Reddy, B.D.: Computational model of soft tissues in the human upper airway. Int. J. Numer. Meth. Biomed. Eng. **28**(1), 111–132 (2012)
17. Spitzer, V., Ackerman, M.J., Scherzinger, A.L., Whitlock, D.: The visible human male: a technical report. J. Am. Med. Informat. Assoc. **3**(2), 118–130 (1996)
18. Titze, I.R.: Mechanical stress in phonation. J. Voice **8**(2), 99–105 (1994)
19. Wang, Y.K., Nash, M.P., Pullan, A.J., Kieser, J.A., Röhrle, O.: Model-based identification of motion sensor placement for tracking propulsion and elongation of the tongue. Biomech. Model. Mechanobiology (2012). doi: 10.1007/s10237-012-0407-6
20. Wilhelms-Tricarico, R.: Geometric representation of a human tongue for computational biomechanical modeling. 2005. Retrieved June 2010, http://webpages.charter.net/reinerwt/JSHLRmanuscript.pdf

Finite Element Analysis of Thorax Responses Under Quasi-Static and Dynamic Loading

Jikuang Yang, Fang Wang, Guibing Li, and Xiaoqing Jiang

Abstract This study aimed at investigation of the response of the human thorax under various loading conditions. For this purpose an FE thorax model was developed based on the human anatomical structures. The human thorax consists of ribs, thoracic vertebrae and intervertebral discs, a sternum, costal cartilages and internal organs. Material properties used in this study were based on the published literature. The FE model was used to simulate the phenomenon of thorax compression. The simulations were carried out in different configurations, including the three-point bending of single rib and frontal impacting with a cylinder to a complete thorax at low speed. The results from simulations were compared with the impact responses obtained from biological tests, such as 3-point bending tests and rib structural tests. The entire thorax model was then tested by simulation of volunteer test. The responses predicted by the simulation showed a good biofidelity.

1 Introduction

Thorax injuries are often observed in vehicle traffic accidents. The number of fatalities and serious injuries ranked the second in reported passenger vehicle crashes [1]. It is also indicated that thoracic injuries occurred in vehicle–pedestrian collisions, especially for collisions with MPV and mini bus. It is therefore necessary to have a good understanding of the thoracic injury mechanism to reduce the injury risk in vehicle accidents. The dynamic responses and injury mechanisms

J.K. Yang (✉)
State Key Laboratory of Advanced Design and Manufacturing for Vehicle Body, Hunan University, Changsha, China

Department of Applied Mechanics, Chalmers University of Technology, Sweden
e-mail: jikuang.yang@chalmers.se; jikuangyang@hnu.edu.cn

F. Wang • G.B. Li • X.Q. Jiang
State Key Laboratory of Advanced Design and Manufacturing for Vehicle Body, Hunan University, Changsha, China

A. Wittek et al. (eds.), *Computational Biomechanics for Medicine: Models, Algorithms and Implementation*, DOI 10.1007/978-1-4614-6351-1_17,
© Springer Science+Business Media New York 2013

have been widely studied by using biological material, mechanical dummies, and mathematical model. Recent years, many studies have carried out by using human body FE models for dynamic responses and injury mechanisms of the thorax in frontal or lateral loading [2]. An FE model of the 50th percentile adult males was developed by Emmanuel Lizee et al. for predicting dynamic responses of a driver in car frontal and side impact [3]. In a study by Gordon R. Plank et al. [4], a coupled FE model of the human thorax with a Hybrid III dummy (replaced Hybrid III thorax) was used in simulations of an out-of-position driver during airbag deployment. Shah et al. [5] used a human thorax FE model [6] developed by Wang to predict modes of loading that are most likely to produce aortic ruptures. Jesse et al. [7] developed a full human model to simulate the human thoracic dynamic responses and injuries associated with frontal impact, side impact, and belt loading.

Since 1997 the EC funded the HUMOS and HUMOS2 [8, 9] projects developed a series of FE human models with aims at prediction of injury risks for victims involved in road traffic accidents. In addition, TOYOTA developed a series FE models (THUMS) of human body in order to estimate injuries in traffic accidents involved occupant and pedestrian [10].

The aim of this study was to simulate dynamic responses of the thorax and rib fractures under different load conditions by using an FE human thorax model developed at Hunan University based on the anatomical structures [11, 12].

2 Method and Materials

An FE thorax model was developed based on a mid-size adult male. Basic geometry data of the thorax model was based on medical data. The validity of the model was evaluated by simulation of the experimental tests using biological specimens. The solver for the simulation used here is LS-DYNA with the Hyperworks as the pre & post-processor. A study was carried out for understanding of the thorax responses to low speed collisions.

2.1 Anatomy-Based Human Thorax FE Model

Basic geometry data of the human thorax FE model was based on computed tomography (CT) scanner sections of a lying individual from a medical university, the subject is average in size and in weight. Each slice was 1 mm thick. Figure 1 shows a slice of the intermediate sternum location.

The thorax FE model consists of ribs, thoracic vertebrae and intervertebral discs, a sternum, costal cartilage and internal organs. Each rib is different in length, shape, and orientation, and the ribs are classified as true (1–7), false (8–10) or floating (11–12). True ribs connect between the vertebrae and sternum; false ribs connect

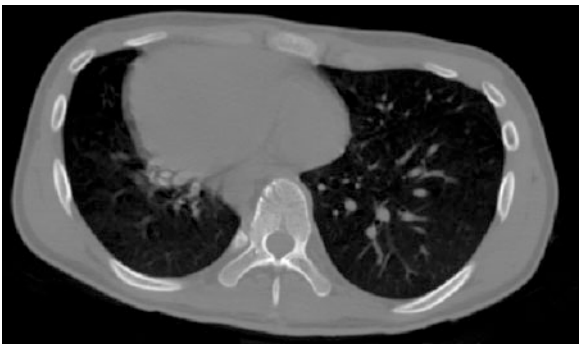

Fig. 1 Image for the anatomic data of thorax

between the vertebrae and the rib immediately above it; and floating ribs connect only to the vertebrae.

The thoracic vertebra body consists of outer cortical bone and the inner cancellous bone. The cortical bone was modeled as isotropic elastic plastic material using shell elements while the cancellous bone was modeled as the same material using 8-node solid elements. Each intervertebral disc composes of nucleus pulpous (NP) and its surrounding components—annulus fibrosus (AF). They were all represented with 8-node solid elements.

The ribs, costal cartilages, and the sternum were modeled in the same way as thoracic vertebra; outer cortical bone modeled using shell elements while the cancellous bone modeled using 8-node solid elements.

The soft tissues filling in the ribcage, the abdomen and the pelvis cavity are also represented in the model. The different organs, like the heart, spleen, lung, stomach, liver, and intestines, were modeled with solid elements; the muscles and adipose tissues covering the ribcage and the abdominal organs were represented by a layer of solid elements and a layer of shell elements.

There are several spinal ligaments and muscles. All of the ligaments were modeled with bi-linear spring elements that can only carry loads in tension and the muscles were modeled with beam elements. Figure 2 shows the frontal and back views of the FE human thorax model.

2.2 Material Properties

The material models for the skeleton structure were considered as either elastic-plastic or linear elastic. In the modeling of the internal organs, the linear visco-elastic material law (LS-DYNA material type MAT_06) was used. The visco-elastic law defined by a compressibility module k and a relaxation function in shear:

$$G(t) = G_0 + (G_0 - G_i)^* \exp(-\beta t), \tag{1}$$

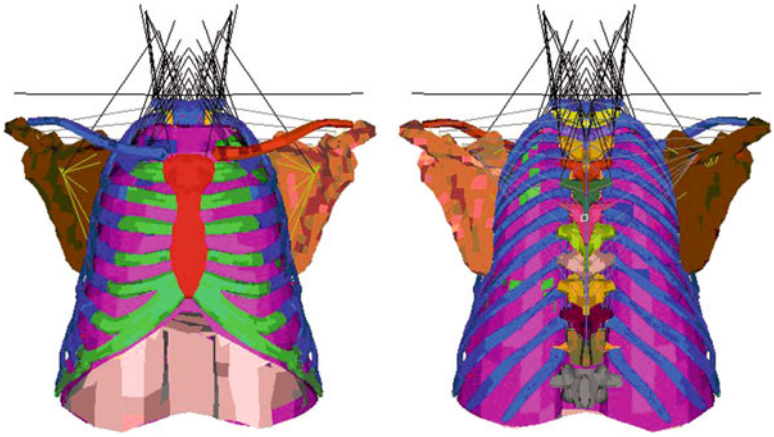

Fig. 2 The frontal (L) and dorsal (R) views skeleton of the FE human thorax model

Table 1 Material definition of the model skeleton components

	Material Model	Density (kg/m^3)	E (MPa)	Poison Ratio	Yield Stress (MPa)	K (MPa)	Reference
Vertebra solid	Elastic	2,500	11,000	0.3	–	–	[13]
Vertebra shell	Elastic	2,500	100	0.3	–	–	[7]
Disc Nucleus Pulposus	Elastic	1,040	2,300	0.3	–	–	[7]
Disc Anulus Fibrosus	Elastic	1,040	300	0.3	–	–	[7]
Sternum trabecular	Elastic	1,000	0.05	0.3	–	–	[7]
Sternum cortical	Elastic	2,000	9,600	0.3	–	–	[7]
Rib Cartilage trabecular	Elastic	1,000	70	0.3	–	–	[13]
Rib Cartilage cortical	Elastic-Plastic	2,000	49	0.3	4.84	15.6	[13]
Rib trabecular	Elastic-Plastic	1,000	40	0.3	1.8	32	[14]
Rib cortical	Elastic-Plastic	2,000	10,000	0.3	90	1,800	[7]

E = Young's modulus, k = bulk modulus

where G_0 = short-term shear modulus, G_i = long-term shear modulus, β = decay constant.

All of the material parameters used in the current model is given in Tables 1 and 2.

Table 2 Material definition of the model soft tissues component

Tissues	Material Model	Density kg/m^3	k (MPa)	Shear Modulus		β (decay constant)	Reference
				G_0(MPa)	G_i(MPa)		
Heart	Vi-elastic	1,000	8.3	0.00384	0.001	0.25	Wang [6];
Lungs	Vi-elastic	1,000	3.333	0.00715	0.00415	0.25	
Spleen	Vi-elastic	1,000	0.25	0.054	0.04	0.25	Stephane [9];
Liver	Vi-elastic	1,000	0.166	0.045	0.036	0.25	
Kidney	Vi-elastic	1,000	0.166	0.045	0.036	0.25	Jesse et al. [7];
Stomach	Vi-elastic	1,000	0.25	0.054	0.04	0.25	
Intestine	Vi-elastic	1,000	0.025	0.036	0.027	0.25	Jay and Gopal [13]

k = bulk modulus

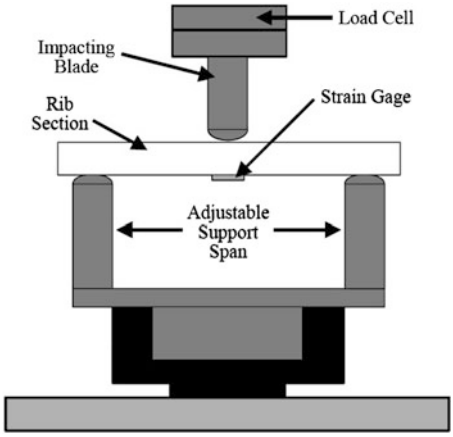

Fig. 3 Apparatus used for human rib three-point bending

2.3 Simulation of Rib Fracture

Rib fractures are common thoracic injuries that can result in mortality and severe morbidity. For good understanding of biomechanical properties of the human rib, a large number of experiments have been performed using cadaver rib specimens—including shearing tests [15], 3-point bending tests [15–19], and tension coupon tests [20]. Based on the test data, the material properties, such as the elastic modulus, yield stress, yield strain, ultimate stress, and ultimate strain were determined within certain ranges from the resulting stress versus strain curves. In 1976 Granik and Stein performed on 10 human rib specimens from the 6th and 7th ribs. Afterwards more experimental studies [17–19] were conducted using cadaver specimens of different ribs by other researchers. Of all the rib tests, attention was paid to the 3-point bending properties. Strain was measured by placing a strain gage at the center of the tension side of the rib section. The Young's modulus was calculated by using linear elastic beam equations.

Kallieris et al. [21] investigated the correlation between rib deflection and applied force by performing 3-point bending quasi-static and dynamic tests on the 6th and 7th ribs obtained from PMHSs as presented in Fig. 3. Each rib specimen was placed on between two supports with distance 0.1 m. Rib specimens were loaded till the material failure at velocities of 2 m/s and 4 m/s in the dynamic tests and at 0.02 m/s in quasi-static tests. The 3-point bending tests were simulated with FE models of the ribs from ribcage of the thorax model. According to the configuration in Kallieris tests the impactor was modeled as a rigid sphere with a radius equal to 0.013 m and a weight of 2.35 kg. The cortical failure strains are defined based on the strain rate from literature [22].

Zuoping Li et al. [22] performed quasi-static noninjurious (0.002 m/s for all) and dynamic injurious (1 m/s for R2 and 0.5 m/s for L4 and L10) experiments using the 2nd, 4th, and 10th human rib to record the structural behavior and fracture tolerance of individual ribs under anterior–posterior bending loads as seen in frontal

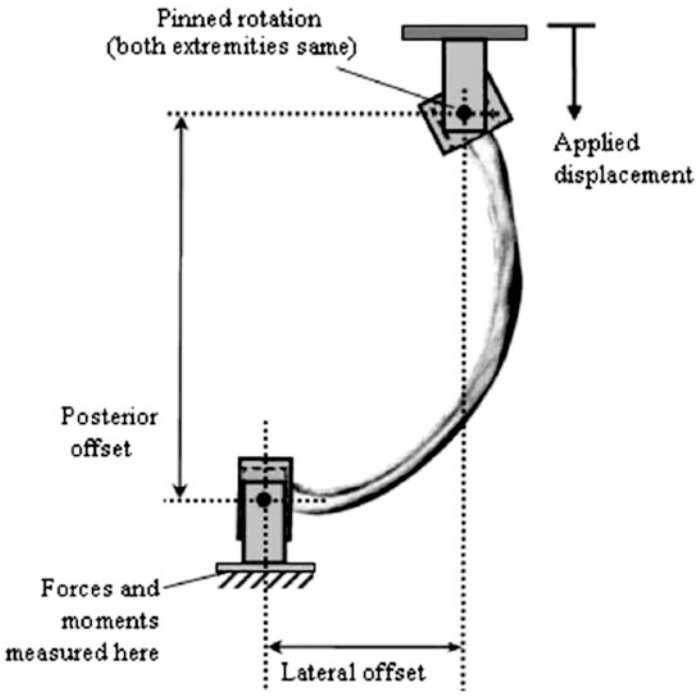

Fig. 4 Setup of rib structural test [22]

impact, which demonstrated in Fig. 4. Reaction forces at the posterior extremity, the displacement time history at the anterior extremity, and the cortical bone strain were measured.

In the simulation study, the configuration of FE rib model was defined based on the setup of the experimental loading and boundary conditions [22] in the corresponding rib structural test (Fig. 4). The anterior and posterior extremities were modeled by spherical FE joints with free rotation permitted in the loading plane only. The displacement of anterior extremity was prescribed at a constant velocity equal to those applied during the experiments. The resultant joint force at the posterior extremity was output for comparison with the measured reaction forces for each rib.

2.4 Whole Thorax FE Model Simulation

Many frontal blunt impact tests have been conducted to determine the force-deflection corridors of the human chest. It has been suggested that blunt impacts are a better test method when assessing the stiffness of the chest compared to sled tests [13]. In the 1970s a total of 35 frontal chest pendulum impact tests

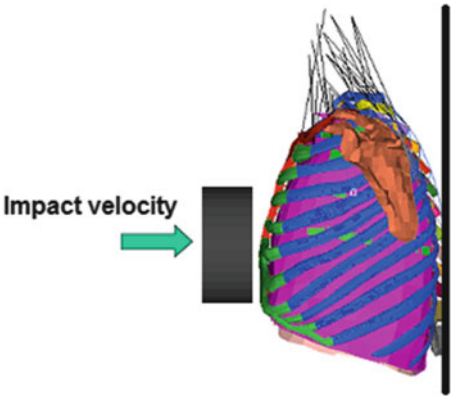

Fig. 5 Initial condition for hub loading

have been conducted [23, 24]. In these tests, the subjects were positioned in a sitting posture on a flat surface of a rigid table with a free-back configuration. The impactor was centered on the sternum in the mid-sagittal plane at the level of the fourth intercostals space and the load was delivered by an unpadded flat wooden impactor with rounded edges and a diameter of 152 mm. These tests were analyzed by Neathery [25, 26]. There was also another series of experiments performed by Patrick [27] at Ford. In Patrick's tests, the volunteer was fixed-back and the posterior of the chest movement was essentially zero during the tests. A cylinder simulating a steering wheel hub (diameter: 152 mm, mass: 10 kg) impacted to the anterior surface of the thorax of a volunteer at an initial velocity of 3.4–4.6 m/s. Each test was synchronized on high-speed film and the displacement of the impactor and the forces by load cell were measured to calculate force-deflection curves.

In this study the entire thorax model was simulated according to Patrick's tests. Figure 5 shows the setup of simulation of thoracic impactor test performed by Patrick [27].

The force-deflection response was reconstructed by using the thorax model under every initial speed in the tests (initial velocity: 3.4 m/s for 3 times, 4.2 m/s and 4.6 m/s for 1 time). The impactor force was output as a contact load between the impactor surface and the anterior surface of the thorax. Impactor displacement was calculated from node displacement, and thoracic deflection was calculated from changes in the distance between nodes on the anterior and posterior surfaces of the thorax.

3 Results

3.1 Analysis of the Rib Fractures

The force-deflection histories from quasi-static, low rate, and high rate (Fig. 6-abc) loading simulations were plotted against the experimental corridors achieved by Kallieris [21].

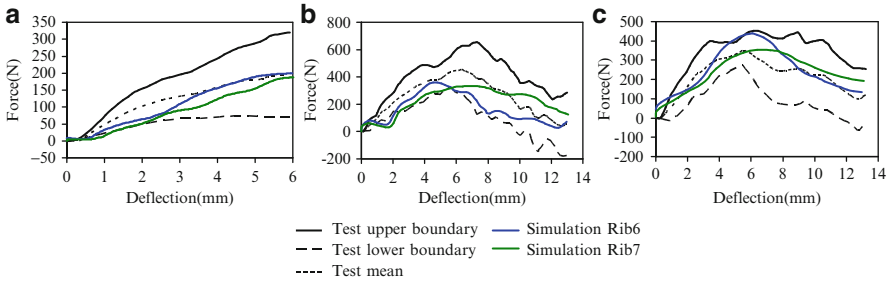

Fig. 6 Three-point bending loading simulation comparing with Kallieris tests. (**a**) Quasi-static 0.02 m/s, (**b**) Dynamic 2 m/s, (**c**) Dynamic 4 m

Table 3 Static and dynamic results from experiments (Exp) and FE simulation (Sim) for the 2nd, 4th, and 10th ribs

		Static Data		Dynamic Data	
Subject	Model	Displacement (mm)	Resultant Reaction force (N)	Fracture Time (ms)	Resultant Reaction force (N)
419m-Rib 2R	Exp	10	57.1	18.9	90.7
	Sim	10	72.8	22.0	143.7
413m-Rib 4L	Exp	14	51.9	82	123.4
	Sim	14	46.8	102.3	128.0
412m-Rib 10L	Exp	16	41.2	122	87.6
	Sim	16	40.5	120.8	96.1

In simulation of the rib 3-point bending tests (Fig. 6), the forces after reaching their maximum value show a decreasing tendency due to fracture of the rib in dynamic tests which finds a good agreement with the test. It is possible that the material of the cortical bone is modeled with a damage model, and applying a damage model with failure parameters allowed showing the ribs fracture, and consequently, more biofidelic force-deflection curves would be obtained. Meanwhile in the quasi-static test simulation, the force increases with the deflection within the range showed in the literature, just like the test output. In dynamic test simulations the ribs' material strain rate dependency also could be demonstrated.

Differences are seen when comparing the computational and experimental resultant reaction force of the rib structural static tests [22] as well as the fracture time and the reaction force at the fracture moment of the structural dynamic tests [22] as shown in Table 3.

The force-displacement curves of the structural test simulation with second, fourth, and tenth rib FE model comparing with the test data under dynamic loading are shown in Fig. 7. It could be seen that in the simulation of the ribs at different velocities, the results represent almost the same tendency as in the test. Also, the differences of rib fracture time between simulations and tests in the comparison curves reflect what is shown in Table 3.

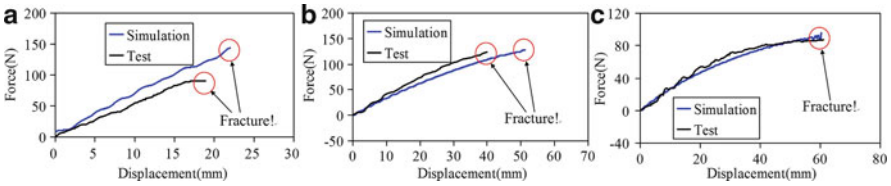

Fig. 7 The structural loading simulation comparing with the Zuoping Li tests. (**a**) Rib2 at 1 m/s. (**b**) Rib4 at 0.5 m/s, (**c**) Rib10 at 0.5 m/s

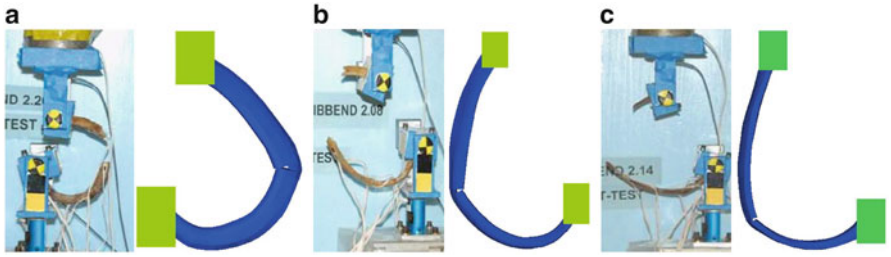

Fig. 8 The rib fracture locations of simulations comparing with the Zuoping Li tests. (**a**) Rib2 at 1 m/s, (**b**) Rib4 at 0.5 m/s, (**c**) Rib10 at 0.5 m/s

Figure 8 compares the fracture locations between the FE simulations and Zuoping Li et al. [22] tests under dynamic loading conditions. The FE models predict closer fracture locations to the posterior extremity of the rib bone than that of the experimental locations, it is considered due to that there are some age-dependent differences in material properties of human body tissues among the subjects from which the experimental bony sections and the FE model geometry are obtained, which is also reported by Zuoping Li et al. [22] and Qing Zhou et al. [28]. Moreover, the variation of the rib cortical thickness, the accuracy of the cortical geometry captured, and the material properties chosen for the FE model also have effect on the biomechanical responses [21, 29].

3.2 Results of the Thorax FE Model Simulation

Figure 9 shows the observed state of the thoracic geometry after impactor contact at the highest velocity of 4.6 m/s, it shows the thoracic deflection of 0 mm, 20 mm, 40 mm and 60 mm. In this case, maximum thoracic deflection was 59.8 mm, which is also shown in Fig. 10c.

The following results are based upon the limited number of impact simulation and range of velocities.

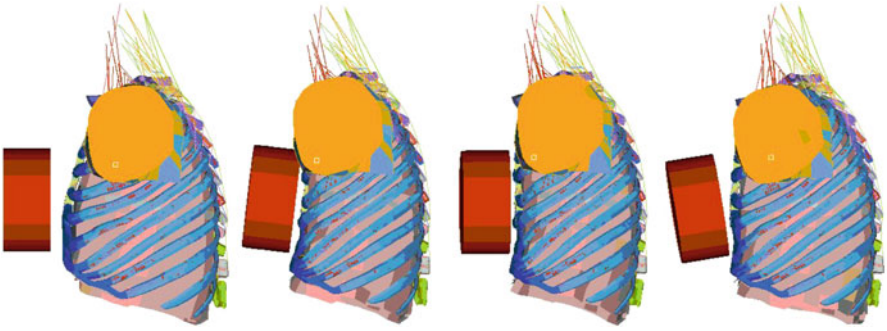

Fig. 9 Kinematics of the thorax model for a 4.6 m/s frontal chest impact with a 10 kg mass pendulum

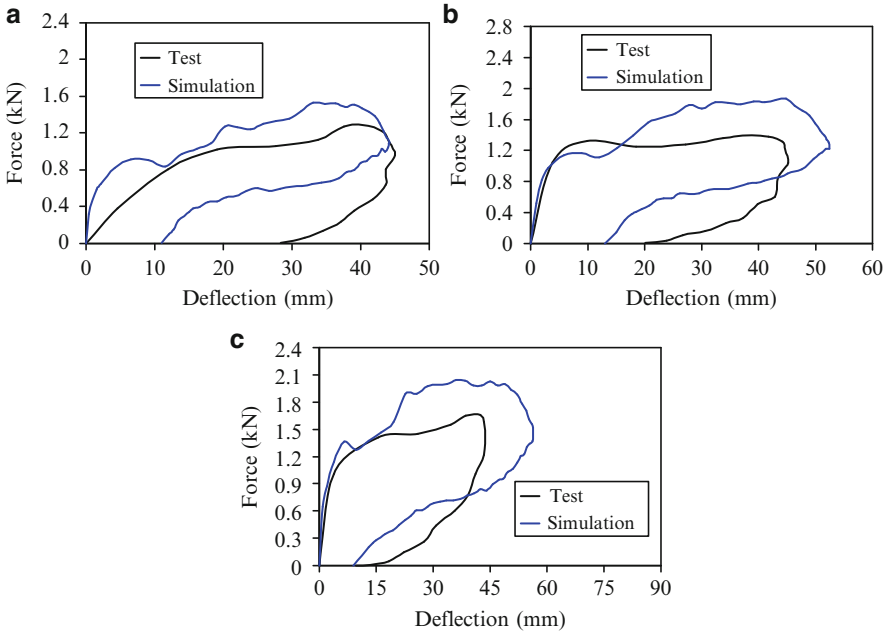

Fig. 10 The comparison of force-deflection time history curves between test and simulation. (**a**) 3.4 m/s (**b**) 4.2 m/s (**c**) 4.6 m/s

In the test, force increases initially with deflection, reaches an initial peak or plateau before continuing up to a maximum peak, but the same phenomenon was not so distinctly represented in the simulation results (Fig. 10).

The maximum force of 2.03 kN occurred at the maximum impact velocity of 4.6 m/s in simulations and that is 1.67 kN at 4.6 m/s in the tests (Figs. 10 and 11a).

The maximum deflection of the impact varies linearly with impact velocities based on the simulation, which does not agree with the test result. Actually, the

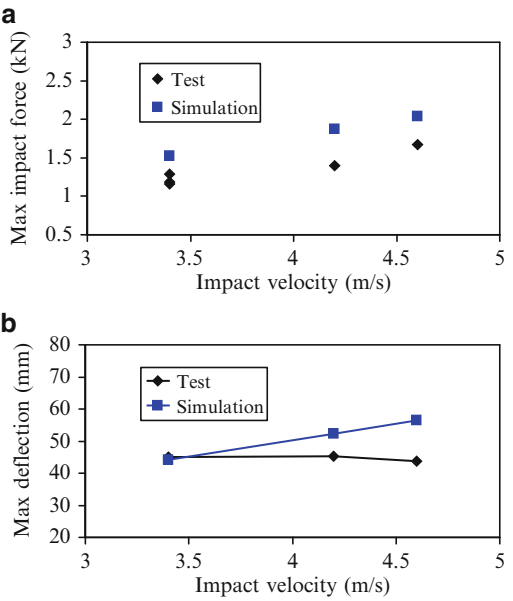

Fig. 11 The comparison of peak values between test and simulation. (**a**) force vs. impact velocity (**b**) deflection vs. impact velocity

maximum chest compression in the tests was essentially the same, 4.37–4.57 cm (Figs. 10 and 11b).

The maximum force of the impact varies linearly with impact velocities based on the simulation, which agreed with the test result (Fig. 11a).

4 Discussions

The human rib FE models were used to simulate the 3-point bending tests performed by Kallieris et al. [21] and the structural quasi-static and dynamic tests carried out by Zuoping Li et al. [22]. The former simulation results well reflect the test data and the latter results just obtain an acceptable agreement with the results from structural tests. There are some factors causing the differences between the results of the simulations and tests, which would also be the focus of coming research.

For simulations of the frontal pendulum impact, the maximum impact force predicted by the FE model was 22%–34% higher than that obtained from experiments. While the maximum deflection as a function of impact velocity was not exactly the same as that of the tests. The maximum chest compression in the tests was essentially the same (Figs. 10 and 11b), but based on the simulation the maximum deflection of the impact varies linearly with impact velocities. Moreover, it is very difficult to imagine that during the analysis of the Patrick tests [27], discrepancies were found when comparing the initial energy with the integrated energy of the force-displacement curves. It is therefore necessary and important to obtain more

information about the tests and adjust the responses of the human thorax FE model to determine the fidelity of the correlations. However, giving the viscoelasticity and strain rate dependency of the human bone material, it seems like that the simulation results make more sense.

The number of the volunteer tests reported in the literature is limited. The material constitutive laws and material properties chosen in this study were, in general, consistent with previous studies designed to develop the 50th percentile male models. For the reason, various scaling and compromising methods, mainly on the material properties, have been used on the model.

Among the experimental results available in the literature, different authors reported many rib fractures. In order to account for this phenomenon, a failure plastic strain is introduced in the rib material law. More research is also needed to increase the accuracy of predictability for thoracic injuries so that the human chest injury mechanisms can be better understood.

5 Conclusions

The simulations of dynamic response of the human thorax under impact load were carried out by using an FE human thorax model based on the anatomical structures. This model includes a detailed description of the bony skeleton, chest, and abdominal internal organs.

The responses predicted by the rib model matched reasonably well with experimental data obtained from rib three-point bending tests and rib structural tests. The whole thorax simulation of a series of hub loading volunteer tests showed some discrepancy comparing with the test results. The model is expected to be applied for the injury prediction of rib fractures under the reported loading conditions in biological tests.

References

1. Shin, J., Untaroiu, C., Lessley, D. et al.: Thoracic Response to Shoulder Belt Loading: Investigation of Chest Stiffness and Longitudinal Strain Pattern of Ribs. Society of Automotive Engineers, SAE 2009–01–0384 (2009)
2. Yang, K.H., Hu, J.W., White, N.A. et al.: Development of numerical models for injury biomechanics research: a review of 50 Years of Publications in the Stapp Car Crash conference. 50th Stapp Car Crash J. 50, 429–490 (2006)
3. Lizee, E., Rohin, S., Song, E. et al.: Development of a 3D Finite Element Model of the Human Body. Society of Automotive Engineers, SAE 983152 (1998)
4. Plank, G.R., Kleinberger, M., Eppinger, R.H.: Analytical Investigation of Driver Thoracic Response to Out of Position Airbag Deployment. Society of Automotive Engineers, SAE 983165 (1998)
5. Shah, C.S., Yang, K.H., Hardy, W. et al.: Development of a Computer Model to Predict Aortic Rupture Due to Impact Loading. Society of Automotive Engineers, SAE 2001–22–0007 (2001)

6. Wang, H-C.: Development of a side impact finite element human thoracic model, Doctoral Dissertation, Wayne State University, US, 1995.
7. Ruan, J., EI-Jawahri, R., Li, C. et al.: Prediction and analysis of human thoracic impact responses and injuries in cadaver impacts using a full human body finite element model. 47th Stapp Car Crash J. **47**, 299–321 (2003)
8. Vezin, P., Verriest, J.P.: Development of a set of numerical human models for safety. In: Proceedings of the 19th International Technical Conference on the Enhanced Safety of Vehicles, Washington D.C, US, Paper No. 05–0163 (2005)
9. Robin, S.: HUMOS: human model for safety – a joint effort towards the development of refined human-like car occupant models. In: Proceedings of the 17th International Technical Conference on the Enhanced Safety of Vehicles, Amsterdam, The Netherlands, Paper No. 01 - 0297 (2001)
10. Iwamoto, M., Kisanuki, Y., Watanabe, I. et al.: Development of a finite element model of the total human model for safety (THUMS) and application to injury reconstruction. In: Proceedings of the International Research Council on the Biomechanics of Impacts (IRCOBI) Conference, Munich, Germany, pp. 31–42 (2002)
11. Yang, J.K., Xu, W., Otte, D.: Brain injury biomechanics in real world vehicle accident using mathematical models. Chin. J. Mech. Eng. **32**(4), 81–86 (2008)
12. Yang, J.K., Yao, J.F.: Development and validation of a human neck FE model in impact loading condition. J. Hunan Univ. Natural Sci. **30**, 40–46 (2003) (In Chinese)
13. Zhao, J., Narwani, G.: Development of a human body finite element element model for restraint system R&D application. In: Proceedings of the 19th International Technical Conference on the Enhanced Safety of Vehicles, Washington D.C, US, Paper No. 05 - 0399 (2005)
14. Kimpara, H., Lee, J.B., Yang, K.H. et al.: Development of a three-dimensional finite element chest model for the 5th percentile female. 49th Stapp Car Crash J. **49**, 251–269 (2005)
15. Sacreste, J., Brun-Cassan, F., Fayon, A. et al.: Proposal for a thorax tolerance level in side impacts based on 62 tests performed with cadavers having known bone condition. 26th Stapp Car Crash J. 155–171 (1982)
16. Stein, I.D., Granik, G.: Rib structure and bending strength: an autopsy study. Calcif. Tissue Int. **20**, 61–73 (1976)
17. Stitzel, J.D., Cormier, J.M., Barretta, J.T. et al.: Defining regional variation in the material properties of human rib cortical bone and its effect on fracture prediction. 47th Stapp Car Crash J. **47**, 243–265 (2003)
18. Cormier, J.M., Stitzel, J.D., Duma, S.M. et al.: Regional variation in the structural response and geometrical properties of human ribs. In: Proc. 49th Association for the Advancement Automotive Conference, Boston, US, pp. 153–170 (2005)
19. Yoganandan, N., Pintar, F.A.: Biomechanics of human thoracic ribs. J. Biomech. Eng. **120**, 100–104 (1998)
20. Kemper, A.R., McNally, C., Kennedy, E.A., et al.: Material properties of human rib cortical bone from dynamic tension coupon testing. 49th Stapp Car Crash J. **49**, 199–230 (2005)
21. Kallieris, D., Schonpflug, M., Yang, J. et al.: Report on Injury Mechanisms Database/Version B (2004)
22. Li, Z., Kindig, M.W., Subit, D. et al.: Influence of mesh density, cortical thickness and material properties on human rib fracture prediction. Med. Eng. Phys. **32**, 998–1008 (2010a)
23. Kroell, C.K., Schneider, D.C., Nahum, A.M.: Impact tolerance and response of the human thorax. 15th Stapp Car Crash J. 84–134 (1971)
24. Kroell, C.K., Schneider, D.C., Nahum, A.M.: Impact tolerance and response of the human thorax . 18th Stapp Car Crash J. 383–457 (1974)
25. Neathery, R.F.: Analysis of chest impact response data and scaled performance recommendations. 18th Stapp Car Crash J. 459–493 (1974)
26. Kent, R., Lessley, D., Sherwood, C.: Thoracic response to dynamic, non-impact loading from a hub, distributed belt, diagonal belt, and double diagonal belts. 48th Stapp Car Crash J. 495–519 (2004)

27. Patrick, L.M.: Impact force-deflection of the human thorax. 25th Stapp Car Crash J. 471–496 (1981)
28. Zhou, Q., Rouhana, S.W., Melvin, J.W.: Age effects on thoracic injury tolerance. 40th Stapp Car Crash J. 137–148 (1996)
29. Li, Z., Kindig, M.W., Kerrigan, J.R. et al.: Rib fractures under anterior-posterior dynamic loads: experimental and finite element study. J. Biomech. **43**(2), 228–324 (2010b)